UNIVERSIDADE FEDERAL DO ESPÍRITO SANTO
CENTRO TECNOLÓGICO
PROGRAMA DE PÓS-GRADUAÇÃO EM ENGENHARIA MECÂNICA

BRUNO FURTADO DE MOURA

A PROCESS OF TECHNOLOGY APPROPRIATION: ELECTRICAL RESISTANCE TOMOGRAPHY FOR MULTIPHASE PATTERN MEASUREMENTS

VITÓRIA
2020

BRUNO FURTADO DE MOURA

A PROCESS OF TECHNOLOGY APPROPRIATION: ELECTRICAL RESISTANCE TOMOGRAPHY FOR MULTIPHASE PATTERN MEASUREMENTS

Thesis presented to the Graduate Program in Mechanical Engineering of Federal University of Espírito Santo, as part of the requirements to obtain the title of Doctor of Science in Mechanical Engineering.

Advisor: Prof. Márcio Ferreira Martins, Ph.D.
Co-Advisor: Prof. Francisco Hernán Sepúlveda Palma, Ph.D.

VITÓRIA
2020

BRUNO FURTADO DE MOURA

A PROCESS OF TECHNOLOGY APPROPRIATION: ELECTRICAL RESISTANCE TOMOGRAPHY FOR MULTIPHASE PATTERN MEASUREMENTS

Thesis presented to the Graduate Program in Mechanical Engineering of Federal University of Espírito Santo, as part of the requirements to obtain the title of Doctor of Science in Mechanical Engineering.

Approved in April 15th, 2020.

EXAMINING BOARD

Prof. Márcio Ferreira Martins
Ph.D., Advisor
Universidade Federal do Espírito Santo (UFES)

Prof. Francisco Hernán Sepúlveda Palma
Ph.D., Co-Advisor
Universidad de Santiago de Chile (Usach)

Prof. Rogério Ramos
D.Sc., Committee President
Universidade Federal do Espírito Santo (UFES)

Prof. Luiz Affonso Henderson Guedes de Oliveira
D.Sc., External Committee Member
Universidade Federal do Rio Grande do Norte (UFRN)

Júlio César Sampaio Dutra
D.Sc., External Committee Member
Universidade Federal do Espírito Santo (UFES)

Prof. Humberto Belich Júnior
D.Sc, Internal Committee Member
Universidade Federal do Espírito Santo (UFES)

Prof. Wellington Betencurte da Silva, D.Sc.
D.Sc., Internal Committee Member
Universidade Federal do Espírito Santo (UFES)

Abstract

Electrical Impedance Tomography (EIT) is a soft-field tomography technique for imaging in industrial and medical applications. The method consists of injecting a bidirectional known current through electrodes inside a domain and measuring the subsequent voltages at the boundaries formed due to these injections, considering only non-ionizing radiation, unlike hard-field tomography. These measurements are acquired by a data acquisition system and are used to solve an inverse problem. The result is a distribution of the conductivities inside the domain. Thus, the image is formed by differences in electrical conductivity that may be present in this distribution. The present work aims to develop a data acquisition system and reconstruction software focused on multiphase flow measurement. A low-cost EIT system is developed, capable of 30.61 images/s with a signal-to-noise ratio of 57.47 dB. Further, the performance of the system is evaluated and it is drawn new guidelines from a validated model to develop the next version of the hardware. To extend the frequency response of the system, the parasitic capacitances, which are unavoidable and usually unwanted capacitance that exists between the parts of an electronic component or circuit, must be compensated or eliminated from the circuits. Methods to directly measure these quantities are scarce and limited. Therefore, a technique to statistically estimated with Maximum a Posterior and Markov Chain Monte Carlo method is presented in this work as an alternative. Since there is a concern in estimating sharp images by determining the position of the boundary, a new statistical and recursive application based on the particle filter is presented to estimate the conductivities inside the domain. The results demonstrated the capability of reconstructing fast-moving inclusions properly.

Keywords: Electrical Impedance Tomography, Data Acquisition Design, Instrumentation, Multiphase Flow, Measurement, Error Analysis, Parasitic Capacitance Estimation, Maximum a Posteriori Estimate, Markov Chain Monte Carlo, Particle Filter, Shape Estimation, Elliptic Contours, Image Processing.

Co-Authorship Statement

The author wrote the thesis under the supervision of Dr. Márcio Ferreira Martins and co-supervision of Dr. Francisco Hernán Sepúlveda Palma at "Universidade Federal do Espírito Santo" and part-time at "Universidad de Santiago de Chile". The author is responsible for the computational simulation, conducted experiments, the analysis of the data, and conclusion. Other contributions are from Dr. Jorge Acevedo Cabello, Dr. Rogério Ramos.

Contributions:

Bruno F. de Moura Initiation of the research topic; Developed the methodology; Development of the experimental apparatus; Development of the computational routines; Wrote the thesis.

Márcio F. Martins Initiation of the research topic; Provided funding and resources for the present project; Guided on the methodology, development of the computational routines; Reviewed the chapters.

Francisco H. S. Palma Guided on the methodology, development of the experimental apparatus; Reviewed the chapters.

Jorge Cabello Acevedo Guided on the methodology, development of the computational routines; Reviewed the chapters.

Rogério Ramos Guided on the methodology, provided funding and resources for the present project; Reviewed the chapters.

Contents

List of Figures

List of Tables

Nomeclature

Abbreviations

AC	Alternated Current
ADC	Analog-to-Digital Converter
$ASIR$	Auxiliary Sequential Importance Resampling
BEM	Boundary Element Method
$CMRR$	Common-Mode Rejection Ratio
DC	Direct Current
$EIDORS$	Electrical Impedance Tomography and Diffuse Optical Tomography Reconstruction Software
EIT	Electrical Impedance Tomography
EKF	Extended Kalman Filter
ERT	Electrical Resistance Tomography
FEM	Finite Element Method
GCV	Generalized Cross-Validation
GIC	General Impedance Converter
$GNOSIR$	Gauss-Newton Optimization Sequential Importance Resampling
IP	Image Processing

KF	Kalman Filter
LBP	Linear Back-Projection
MAE	Mean Absolute Error
MAP	Maximum a Posteriori
MC	Monte Carlo
$MCMC$	Markov Chain Monte Carlo
$NOSER$	Newton's One Step Error Reconstructor
PF	Particle Filter
RMS	Root Mean Square
SIR	Sequential Importance Resampling
SIS	Sequential Importance Sampling
$SPICE$	Simulation Program with Integrated Circuit Emphasis
SNR	Signal-to-Noise Ratio
UKF	Unscented Kalman Filter
$VCCS$	Voltage-Controlled Current Source

Latin Symbols

A	Coefficient matrix of a system of equations
A_g	Gain from the instrumentation amplifier
A_M	Stiffness matrix
Aol	Open-loop gain of a operational amplifier
B	Magnetic induction, [T]

B_{LBP}	Linear Back-Projection operator
B_M	Matrix component of the stiffness matrix
b	Vector of a system of equations
C	Capacitance, $[F]$
C_M	Matrix component of the stiffness matrix
D	Electric displacement, $[C/m^2]$
D_M	Matrix component of the stiffness matrix
$\tilde{d}$	Dimension of the state vector
E	Electric field, $[V/m]$
$E(.)$	Expected or mean value
e_l	Electrode
F	Forward problem
f	Frequency, $[Hz]$
$f(.)$	Function
$f_k(.)$	System transition function
G_m	Transconductance, $[A/V]$
$g(.)$	Reference signal, $[V]$
H	Magnetic field strength, $[A/m]$
h	Voltages calculated with the forward problem, $[V]$
$h(.)$	Reference signal, $[V]$
$h_k(.)$	Observation model, $[V]$
I	Current, $[A]$

I_M	Current vector to solve the forward problem, $[A]$
I_{patt}	Current vector containing the injection pattern, $[A]$
$Im(.)$	Imaginary number
$\tilde{I}$	Identity matrix
IP	In-phase signal, $[V]$
J	Jacobian
J_t	Total current density, $[A/m^2]$
$\hat{J}$	Covariance of the jitter noise
j	Imaginary number, $\sqrt{-1}$
j_{bound}	Boundary current density, $[A/m^2]$
$\hat{K}$	Roughening tuning parameter
k_{adp}	Electrode index from adaptive protocol
L	Number of electrodes
L_G	Inductance, $[H]$
$\hat{L}$	Function of the roughening process
l	Index notation
$\hat{l}$	Interval between the maximum and minimum samples in the roughening process
MAE	Mean absolute error
N	Number of nodes
$N(.)$	Normal distribution
N_{meas}	Number of measurements

N_{meas}	Number of measurements
N_s	Number of samples
n	Normal component
n_s	Index notation
$\tilde{n}$	Number
P	Number of particles
$\hat{P}$	Covariance of the posterior density
p	Orthogonal vector
$p(.)$	Probability
$p(.\|.)$	Conditional probability
QD	Quadrature signal, [V]
R	Resistance, [Ω]
RMS	RMS error
$Re(.)$	Real number
r	Gain setting resistor in the Howland current source
r_a	Radius related to the x-axis, [m]
r_b	Radius related to the y-axis, [m]
$\tilde{r}$	Residual in the conjugate gradiente algorithm
S	Area, [m^2]
SNR	Signal-to-noise ratio, [dB]
$STD(.)$	Standard deviation
T	Tolerance

T_m	Time interval of the wave, $[s]$
t	Time, $[s]$
U	Boundary voltage, $[V]$
u	Electric potential, $[V]$
u_{sol}	Solution vector of the forward problem, $[V]$
V	Voltage, $[V]$
$\not{V}$	Volume, $[m^3]$
v	Arbitrary function for the weak form
$\hat{v}$	Noise from the state variables
$\hat{w}$	Weight
$\hat{w}_k$	System white-noise
X	Reactance, $[\Omega]$
X_{dep}	Dependent variable
x	Cartesian coordinate, $[m]$
x_c	Cartesian coordinate of the center of the ellipse, $[m]$
x_{sol}	Solution of the system of equations
$\hat{x}$	Parameters vector
Y	Admittance $[S]$
Y_{ind}	Independent variable
y	Cartesian coordinate, $[m]$
y_c	Cartesian coordinate of the center of the ellipse, $[m]$
Z	Impedance, $[\Omega]$

z	Observations, $[V]$
$\hat{z}$	Observations from the model, $[V]$
$\bar{z}$	Contact impedance, $[\Omega \cdot m^2]$

Greek Symbols

α	Regularization parameter
α_{lw}	Landweber gain
α_{vf}	Void fraction
β	Ratio between residuals in the conjugate gradient
β_{fb}	Feedback ratio in the Howland current source
γ	Admittivity, $[S/m]$
Δ	Variation
δ	Dirac delta
$\delta\Omega$	Boundary contour
ϵ	Permittivity $[F/m]$
θ	Angle, $[rad]$
λ_{max}	Maximum eigenvalue of the approximated Hessian
μ	Permeability, $[H/m]$
ρ	Angular orientation of the axis of the ellipse, $[rad]$
ρ_c	Charge density, $[C/m^3]$
Σ	Covariance matrix of the process
σ	Electrical conductivity, $[S/m]$

σ_{rough}	Standard deviation of the roughening process
Φ	Phase, [^{o}]
ϕ	Basis function
φ	Sensitivity parameter
χ	Characteristic function of the element
Ω	Domain
ω	Frequency, [rad/s]

Subscripts

0	Initial
c	Current
$calc$	Calculated
cp	Continuous phase
dp	Dispersed phase
exp	Experimental
eq	Equivalent
gbw	Gain-bandwidth
hom	Homogeneous
i	Index notation
inc	Inclusion
j	Index notation
k	Iteration

$\tilde{k}$	Iteration
L	Load
l	Index notation
$likelihood$	Likelihood
MAP	Maximum a Posteriori
mc	Mixture conductivity
$meas$	Measured
out	Output
opt	Optimization
$patt$	Pattern
$prior$	Prior
ref	Reference
RMS	Root mean square
s	Sampling
sig	Signal
sys	System
$true$	True value

Superscripts

d	Driving pattern
k	Electrodes from the optimal drive protocol
m	Measurement pattern

ohm	Ohmic
P	Peak
$sour$	Source
T	Transpose
$+$	Positive
$-$	Negative

Terminology

Admittivity	Quantifies the conductance of the material or the complex conductivity. Represent the sum of the electrical conductivity and the permittivity $\gamma = \sigma + j\omega\epsilon$ or, in terms of circuit elements, $\frac{1}{R+jX}$.
Attenuation	The reduction in the strength of a signal.
Bandwidth	Difference between the upper and lower frequencies in a continuous band.
Bidirectional Current	Current that flows in two directions, positive and negative, periodically.
Common-Mode Voltage	Signal that is present on both lines of a differential measurement.
Conductivity	Represent the real part of the complex admittivity.
Coupling Circuit	Circuit that effectively removes the DC voltage from the signal.
Current Divider	Circuit that effectively attenuates the input current.
Difference Imaging	Linear one-step reconstruction from a reference point.
Driven Shield	Prevention of external fields from affecting the signal in noise form.
Dynamic Imaging	Recursive reconstruction of state variables.
Dynamic Range	Ratio of the largest and the small value that a signal can have in a system.

Feedback	Feed of a portion of the output signal into the input.
Floating Source	The voltage signal is not connected to any absolute reference or any common ground.
Gain	Output increase in voltage related to the input of the circuit.
Hard-Field	Type of tomography where the diffusion of the signal are straight, depending only of the material along the path, regardless of the position.
Impedance	Complex resistance to the electrical conductance of the material. in terms of circuit elements, $Z = R + jX$.
Inclusion	Object that presents an admittivity different from the medium.
Injection	The act of input an electrical current into the sensors, or the electrodes.
Inverting Input	Negative input of a amplifier.
Leakage	Gradual transfer of current across a boundary normally viewed as insulating.
Noise	Irregular and unwanted fluctuations present on a transmitted electrical signal that corrupts it.
Non-inverting Input	Positive input of a amplifier.
On-resistance	Non-linear resistance present in CMOS circuits.
Open-loop gain	Gain a amplifier presents when no feedback is provided between input and output.
Parasitic Capacitance	Unavoidable and usually unwanted capacitance that exists between the parts of an electronic component or circuit.
Pattern Identification	The identification of the multiphase flow pattern form due to the flow of different phases.
Permeability	Quantifies the resistance of a material against the formation of a

	magnetic field.
Permitivity	Represent the imaginary part of the admittivity.
Phase	Angle of the periodic signal. From the Ohm's law, the phase and the relationship with the impedance is $\phi = arctan(\frac{X}{R})$
Protocol	The scheme, i.e. the procedure, that the electrical currents are set on the electrodes and the forming voltages on the boundaries are measured in the sensors.
Reactance	Imaginary resistance to the electrical conductance of the material X. For capacitive reactances $X = \frac{1}{j\omega C}$
Resistance	Real resistance to the electrical conductance of the material R.
Ripple	Residual periodic variation of the DC voltage.
Roll-off	The frequency response that systems may present.
Settling Time	Time required to the output signal to reach a certain error band.
Shunt	Creation of a low-resistance path that directs electrical current.
Signal Delay	Length of time that takes the input to reach the output.
Soft-Field	Type of tomography where the diffusion of the signal strength depends not only on the spatial disposition, but also to the distance between the source and detector.
Static Imaging	Iterative reconstruction that initiates without a reference image.
Tomography	Cross-sectional imaging methodology by using a penetrating wave.
Transconductance	Electrical characteristic which relates the current through the output of a circuit to the voltage in the input of a circuit.
Trim	Adjust an electrical component by a precision potentiometer, more commonly resistors.
Void-Fraction	The fraction of the channel cross-sectional area that is occupied by

	the gas phase.
Voltage Divider	Circuit that effectively attenuates the input voltage.

Chapter 1

Introduction

In the 1990s, the introduction of methods of tomography begins to rise in popularity. From the success in the medical field [1, 2, 3], the tomography methods begin to being applied to industrial processes. The standard methods available involve ionizing radiation [4, 5], such as x-ray and gamma-ray, which is undesirable regarding the hazard and risk of the process. From the perspective of eliminating the methods involving this type of radiation than other types of tomography are still being developed nowadays.

Three types merit attention: the Electrical Resistance Tomography (ERT) or, generally, the Electrical Impedance Tomography (EIT); the Electrical Capacitance Tomography (ECT); and the Electromagnetic Tomography (EMT) [6]. These methods are used to estimate the field of electrical conductivities (the real and imaginary components), the permittivity when there is no real component, and the permeability respectively.

Other common classifications are the soft-field and the hard-field. The first refers to the diffusion of the signal strength depends not only on the spatial disposition but also of the distance between the source and detector. Differently, the path of transmitting the signal for hard-field methods is straight, depending only on the material along the path, regardless of the position [7]. Therefore, the ERT or EIT, ECT, and EMT are soft-field, whilst the x-ray and gamma-ray tomography are hard-field.

The process of developing an operational system is a continuous and iterative process with several steps that involve an absorptive capacity of the technology that leads to innovation [8]. Cohen and Levinthal [9] introduce the term absorptive capacity, which is the ability to absorb and

Table 1.1: Different EIT system in the literature.

Organization	Type	Purpose
Aberdeen [12]	ERT	Industrial
Cape Town [13]	ERT	Industrial
Dartmouth [14]	ERT	Medical
ITS [15]	ERT, ECT	Industrial
Kyung Hee [16, 17]	EIT	Medical
Kuopio [18]	EIT	Industrial
Leeds, UMIST [19, 20]	EIT	Industrial
Oxford Brooks [21]	EIT	Medical
Sheffield [22, 23]	ERT, EIT	Medical
Tianjin [24]	EIT	Medical
Timpel [25]	EIT	Medical
Xi'an's Military University [26, 27]	EIT	Medical

utilize external knowledge and it is a critical process to the innovative capabilities. The success of the extension of the appropriation is close related to the reconfiguration of the internal knowledge to such process, the combination of the knowledge of different autonomous groups and its prior related knowledge [10]. Therefore, it is important to establish a multidisciplinary team with different skills when developing any complex system. The final result is the appropriation of technology to some extent. Some of the instruments of appropriation are legal, such as patents, trademarks, and copyrights; other instruments are strategic, such as product complexity and secrecy [11].

Several groups of researchers have developed the system and appropriated the technology for research and commercial reasons. Some of the systems developed for medical and industrial objectives are included in Table 1.1.

1.1 Objectives

Considering the above arguments, the main objective of this thesis is the appropriation of EIT technology, to perform multiphase flow measurements, such as pattern identification. From the appropriation perspective, this thesis is mainly concerned with:

- The development of a low-cost EIT system to be tested in a flow loop.

- The evaluation of the errors in the system for further adjustment.
- The establishment of guidelines for the development of the next version of the system, to achieve superior accuracy and temporal resolution.
- The development of a method to estimate the parasitic capacitances present in the system.
- The development of a recursive algorithm to estimate the boundaries of the air phase b.

1.2 Thesis Outline and Contributions

The major points concerning each chapter, which are like article format, are described below:

- Chapter 2
  The complete literature survey is presented in this chapter. It is shown the developments concerning the applications of EIT, the forward modeling and accuracy, the inverse problem, and the errors in reconstruction, the acquisition system design, and considerations of the errors.
- Chapter 3
  The chapter named "Design of a Low-Cost Acquisition System to Reconstruct Images through Electrical Resistance Tomography" presents the article submitted to the journal "IEEE Latin America Transactions" and accepted on February 14th, 2020. It consists of the development of a low-cost EIT system for measurements in multiphase flow. The prototype was soldered in a universal board and the first version that was capable of 1 image after 20 s. After adjustments in the demodulation subsystem, the system was capable of performing 30 images/s, which was a significant improvement for the design. The main contribution of the paper is the appropriation of a low-cost technology, which can be used to perform investigations in multiphase flow and other applications.
- Chapter 4
  The chapter named "Modeling and Errors Assessment of an Electrical Impedance Tomography Data Acquisition System" presents the article submitted to the journal "Measurement" on March 13th, 2020. From this point, it was important to analyzes the system performance more deeply, enumerate the modifications that would improve the next version, and establish a methodology for these improvements. Therefore, the chapter consists of the evaluation of measurements in the data acquisition system and the modeling of

the errors to use as a guideline to develop a newer version. After investigating the literature, it was noticed that this methodology to develop an EIT system is not presented comprehensively. Therefore, the chapter provides this information.

- Chapter 5

  The chapter named "Estimating the Parasitic Capacitances of an Electrical Impedance Tomography Data Acquisition by MAP and MCMC" presents the article submitted to the journal "International Journal of Electronics and Communications" on March 31th, 2020. It was concluded that the parasitic capacitances presented a major role in the systematic errors in the DAQ system. Methods to estimate the parasitic capacitances are scarce in the literature and compensation methods utilize a trial-and-error to calibrate these quantities. Therefore, a technique to estimate the parasitic capacitances is presented as an alternative to other methods. The chapter consists of applying statistical Bayesian inference, by Maximum a Posteriori and Markov Chain Monte Carlo method to the determination of the parasitic capacitances present in the data acquisition design.

- Chapter 6

  The chapter named "A Novel Algorithm Combining Gauss-Newton Optimization with Image Processing and Particle Filter for Recursive Shape Determination in Electrical Impedance Tomography" presents the article submitted to the journal "Inverse Problem in Science and Engineering" on November 18th, 2019. For multiphase flow, it is important to define the contour of the inclusions to calculate the void-fraction correctly since deterministic methods often utilize a smooth prior. The chapter consists of proposing a new application of the particle filter combining the Gauss-Newton optimization and image processing for estimating the shape of the boundaries of an inclusion recursively. The filter can estimate fast-moving objects in the domain by improving the election of the proposal distribution.

References

[1] L. A. Shepp and J. B. Kruskal. Computerized tomography: The new medical x-ray technology. *The American Mathematical Monthly*, 85(6):420–439, 1978.

[2] H Griffiths and Z Zhang. A dual-frequency electrical impedance tomography system. *Physics in Medicine and Biology*, 34(10):1465–1476, 1989. doi: 10.1088/0031-9155/34/10/009.

[3] Christopher John Solomon and Robert John Ott. Gamma ray imaging with silicon detectors - a compton camera for radionuclide imaging in medicine. *Nuclear Instruments and Methods in Physics Research Section A: Accelerators, Spectrometers, Detectors and Associated Equipment*, 273(2):787 – 792, 1988. doi: https://doi.org/10.1016/0168-9002(88)90097-6.

[4] D Toye, P Marchot, M Crine, and G L'Homme. Modelling of multiphase flow in packed beds by computer-assisted x-ray tomography. *Measurement Science and Technology*, 7(3):436–443, 1996. doi: 10.1088/0957-0233/7/3/027.

[5] S A Tjugum, B T Hjertaker, and G A Johansen. Multiphase flow regime identification by multibeam gamma-ray densitometry. *Measurement Science and Technology*, 13(8):1319–1326, 2002. doi: 10.1088/0957-0233/13/8/321.

[6] D.S. Holder. *Electrical Impedance Tomography: Methods, History and Applications*. Series in Medical Physics and Biomedical Engineering. CRC Press, 2004. ISBN 9781420034462.

[7] Manuchehr Soleimani. Super-sensing through industrial process tomography. *Philosophical Transactions of the Royal Society A: Mathematical, Physical and Engineering Sciences*, 374(2070):20150445, 2016. doi: 10.1098/rsta.2015.0445.

[8] J. Lienig and H. Bruemmer. *Fundamentals of Electronic Systems Design*. Springer International Publishing, 2017. ISBN 9783319558400.

[9] Wesley M. Cohen and Daniel A. Levinthal. Absorptive capacity: A new perspective on learning and innovation. *Administrative Science Quarterly*, 35(1):128–152, 1990.

[10] D. Hislop. integration processes and the appropriation of innovations. *European Journal of Innovation Management*, 6(3):159–172, 2003. doi: 10.1108/14601060310486235.

[11] Anna Arbussà and Germà Coenders. Innovation activities, use of appropriation instruments and absorptive capacity: Evidence from spanish firms. *Research Policy*, 36(10):1545 – 1558, 2007. doi: https://doi.org/10.1016/j.respol.2007.04.013.

[12] J J A van Weereld, D A L Collie, and M A Player. A fast resistance measurement system for impedance tomography using a bipolar DC pulse method. *Measurement Science and Technology*, 12(8):1002–1011, 2001. doi: 10.1088/0957-0233/12/8/303.

[13] A. J. Wilkinson, E. W. Randall, J. J. Cilliers, D. R. Durrett, T. Naidoo, and T. Long. A 1000-measurement frames/second ERT data capture system with real-time visualization. *IEEE Sensors Journal*, 5(2):300–307, April 2005. ISSN 1530-437X. doi: 10.1109/JSEN.2004.842445.

[14] A. Hartov, R. A. Mazzarese, F. R. Reiss, T. E. Kerner, K. S. Osterman, D. B. Williams, and K. D. Paulsen. A multichannel continuously selectable multifrequency electrical impedance spectroscopy measurement system. *IEEE Transactions on Biomedical Engineering*, 47(1):49–58, 2000.

[15] Industrial tomography systems ltd. https://www.itoms.com/, 2020. Accessed: 2020-20-04.

[16] Tong In Oh, Eung Je Woo, and David Holder. Multi-frequency EIT system with radially symmetric architecture: KHU mark1. *Physiological Measurement*, 28(7):S183–S196, 2007. doi: 10.1088/0967-3334/28/7/s14.

[17] Tong In Oh, Hun Wi, Do Yub Kim, Pil Joong Yoo, and Eung Je Woo. A fully parallel multi-frequency EIT system with flexible electrode configuration: KHU mark2. *Physiological Measurement*, 32(7):835–849, jun 2011. doi: 10.1088/0967-3334/32/7/s08.

[18] J. P. Kaipio T. Savolainen and M. Vauhkonen P. A. Karjalainen. An electrical impedance tomography measurement system for experimental use. *Review of Scientific Instruments*, 3605(1):49–58, 1996.

[19] Fraser Dickin and Mi Wang. Electrical resistance tomography for process applications. *Measurement Science and Technology*, 7(3):247–260, mar 1996. doi: 10.1088/0957-0233/7/3/005.

[20] Mi Wang, Yixin Ma, N. Holliday, Yunfeng Dai, R. A. Williams, and G. Lucas. A high-performance EIT system. *IEEE Sensors Journal*, 5(2):289–299, April 2005. ISSN 1530-437X. doi: 10.1109/JSEN.2005.843904.

[21] Q S Zhu, C N McLeod, C W Denyer, F J Lidgey, and W R B Lionheart. Development of a real-time adaptive current tomograph. *Physiological Measurement*, 15(2A):A37–A43, 1994. doi: 10.1088/0967-3334/15/2a/005.

[22] B H Brown and A D Seagar. The Sheffield data collection system. *Clinical Physics and Physiological Measurement*, 8(4A):91–97, nov 1987. doi: 10.1088/0143-0815/8/4a/012.

[23] A J Wilson, P Milnes, A R Waterworth, R H Smallwood, and B H Brown. Mk3.5: a modular, multi-frequency successor to theMk3a EIS/EIT system. *Physiological Measurement*, 22 (1):49–54, feb 2001. doi: 10.1088/0967-3334/22/1/307.

[24] C. Tan, S. Liu, J. Jia, and F. Dong. A wideband electrical impedance tomography system based on sensitive bioimpedance spectrum bandwidth. *IEEE Transactions on Instrumentation and Measurement*, 69(1):144–154, 2020.

[25] Timpel s. a. http://www.timpel.com.br/pt/, 2020. Accessed: 2020-20-04.

[26] X. Shi, W. Li, F. You, X. Huo, C. Xu, Z. Ji, R. Liu, B. Liu, Y. Li, F. Fu, and X. Dong. High-precision electrical impedance tomography data acquisition system for brain imaging. *IEEE Sensors Journal*, 18(14):5974–5984, July 2018. ISSN 1530-437X. doi: 10.1109/JSEN.2018.2836336.

[27] W. Li, J. Xia, G. Zhang, H. Ma, B. Liu, L. Yang, Y. Zhou, X. Dong, F. Fu, and X. Shi. Fast high-precision electrical impedance tomography system for real-time perfusion imaging. *IEEE Access*, 7:61570–61580, 2019.

Chapter 2

Literature Survey

Electrical Impedance Tomography (EIT) is a technique that is getting attention from researchers nowadays. Through the injection of electrical current into a specific domain and the measurement of the subsequent voltages formed, it is possible to obtain a reconstructed image of the information of the resistive and reactive part of the conductivity distribution, as shown in Figure 2.1. Its attractiveness comes from the characteristic of being non-intrusive, as the electrodes are attached to the boundaries of the domain in question [1], relatively low-cost, due to the characteristics of the application [2], ionizing radiation-free, since the injection of the acquisition system considers only electrical current, and high temporal resolution, as it is possible to acquire over 1000 images per second [3, 4].

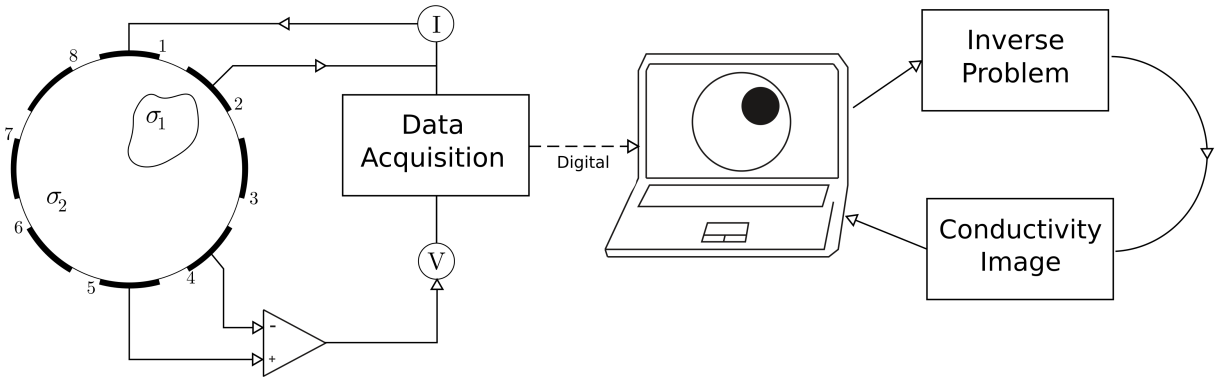

Figure 2.1: The EIT method, from the acquisition of measuments to the reconstruction.

2.1 Review of the Literature

2.1.1 EIT Applications

The method has been applied in some areas of knowledge. In the medical field, EIT becomes available for clinical application, especially for monitoring the ventilation process [5]. This technique is well suited to studying pulmonary activity because of the movement of air results in significant conductivity changes within the thorax [6, 7]. The ventilation cycle and perfusion of cardiac function are observed with EIT in Figure 2.2. The implementation of EIT for imaging the brain activity is also under investigation. Despite the difficulties in measuring with accuracy the voltages due to the contact impedances of the electrodes [8], the first images of this activity in rat specimens have been recorded by researchers, shown in Fig. 2.3 [9, 10]. In industrial envi-

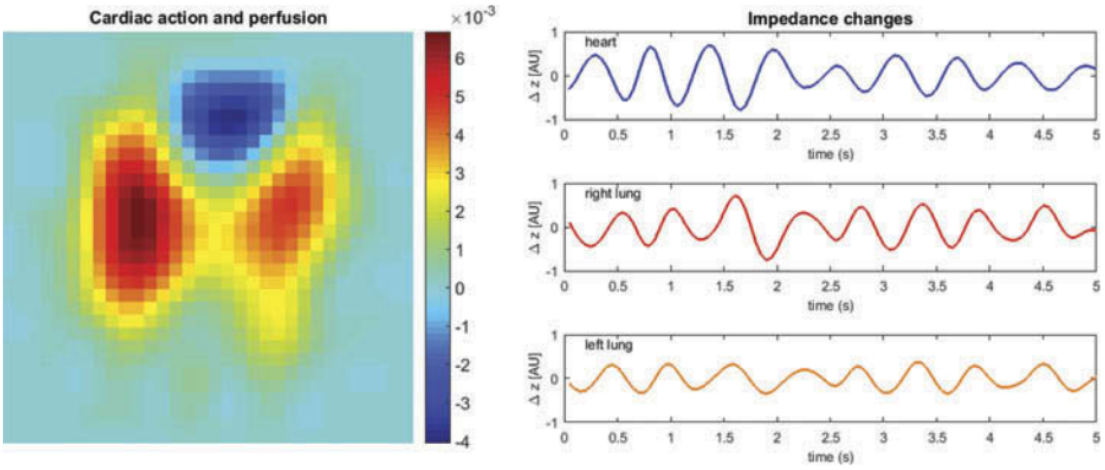

Figure 2.2: EIT image of the cardiac and perfusion and its impedance changes in time [5].

ronment, one of main applications is concentrated in multiphase flow applications [11]. There is interest in characterization of the flow pattern, since it is essential to determine this pattern when in need of optimization, design and operation industrial processes. Parvareh et al.[12] combine the use of EIT and computational fluid dynamics simulation for flow pattern identification. Ramskill and Wang [13] evaluate the frequency of conductivity change to characterize the horizontal flow regime of water and air. Through this information, it is possible to determine if it is a bubble or plug flow regime. Work has been also concentrated in measuring void-fraction or volume fraction since the image of the section plane in question can be used to evaluate the area of each phase [14, 15]. The void fraction or volume fraction can be determined by the Maxwell relationship, Eq. 2.1 [14, 15].

$$\alpha_{vf} = \frac{2\sigma_{cp} + \sigma_{dp} - \sigma_{mc} - \frac{\sigma_{mc}\sigma_{dp}}{\sigma_{cp}}}{\sigma_{mc} - \frac{\sigma_{dp}}{\sigma_{cp}}\sigma_{mc} + 2(\sigma_{cp} - \sigma_{dp})} \tag{2.1}$$

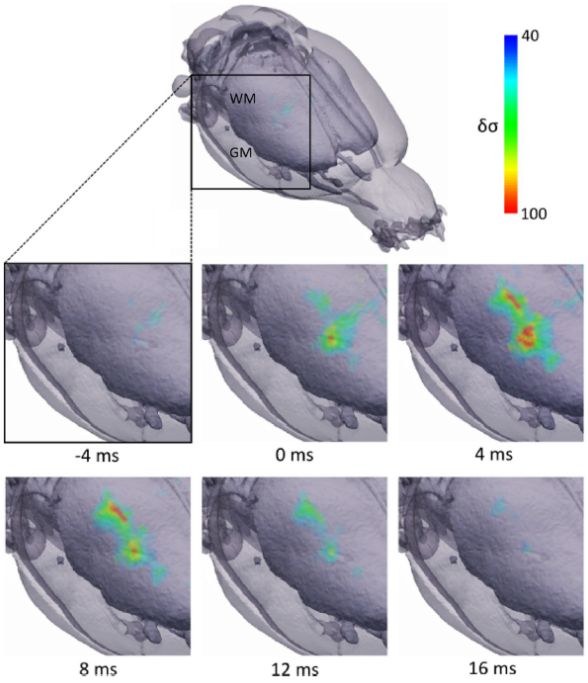

Figure 2.3: EIT recording of the brain activity of an anesthetized rat [10].

where σ_{cp} is the conductivity of the aqueous continuous phase (water), σ_{dp} is the conductivity of the dispersed phase (air or oil), σ_{mc} is the mixture conductivity obtained from EIT and α_{vf} is the local void fraction of the dispersed phase.

The information regarding the volume-fraction or void-fraction can be used in combination with other types of measurement. Meng et al. [16] use the information of the EIT, identifying the flow pattern and calculating void fraction, with a Venturi meter to calculate the mass flow rate. Wang et al. [17] utilize EIT in combination with an electromagnetic flow meter, a gradiomanometer flow-mixture density meter, and extra sensors to obtain measurements regarding the flow-rate of multiphase flow, with oil, gas, and water. The information about the patterns is obtained as well, Fig. 2.4. Dong et al. [18] utilize two planes of EIT to measure the flow rate of multiphase flow.

2.1.2 Injection Pattern

The EIT method relies on injecting currents and measuring voltages to solve an inverse problem. The current is injected through electrodes by a data acquisition system, and this system also measures the boundary voltages at the electrodes. To estimate the electrical conductivities, it is important to determine the strategy of injection of this current inside the domain. Each of these patterns has its strong points and weakness, such as the region of sensibility, number of independent measurements, hardware complexity.

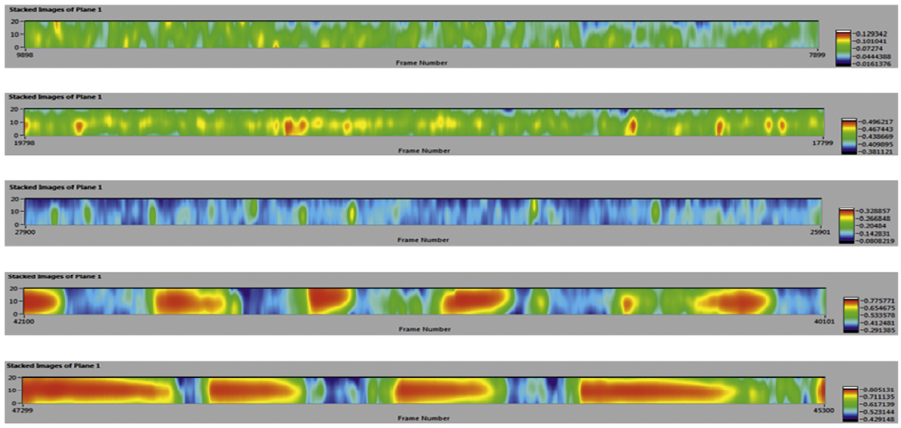

Figure 2.4: Example of a flow pattern visualization by EIT technique. A set of images are stacked to build an axial image [17].

2.1.2.1 Reciprocity Theorem

The principle of measuring electrical impedance is based on Ohm's law. This impedance is obtained by applying a known voltage or current and measuring the response of current or voltage resultant in the electrodes. This procedure is done to different electrodes. The resultant impedance is known as mutual impedance Z [19]. For a four-electrode system, Fig. 2.5, the reciprocity theorem, derived from the divergence theorem, is given [19]:

$$\Delta Z = \frac{V_{12}}{I_{43}} = \frac{V_{43}}{I_{12}} \tag{2.2}$$

Thus, considering that the current is the same for all cases, it can be stated that:

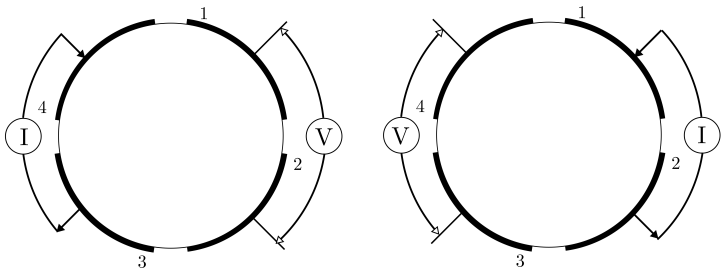

Figure 2.5: Four electrode system. Measurements occurs first for the injection in the left electrodes, then in the right.

$$I_{12} = I_{43} \rightarrow V_{43} = V_{12} \tag{2.3}$$

Therefore, not all measurements are independent of each other. It is important to provide the maximum number of independent measurements to assure a good resolution of the image.

2.1.2.2 Adjacent Protocol

The first pattern utilized to such a method is the adjacent protocol or the neighboring pattern. Initially utilized by Brown and Seagar [20] in the Sheffield system presented on the work, the adjacent protocol applies a current through two neighboring electrodes, and the voltage is measured by subsequent electrodes, which are not injecting current [19, 21]. This procedure repeats until all electrode pairs have passed through the process of injecting current, Figure 2.6. It is common to avoid measurements in the injecting electrode to prevent the contact impedance

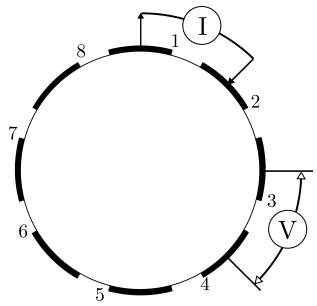

Figure 2.6: Adjacent protocol.

problems due to the polarization effect [21]. Due to reciprocity, Eq. 2.3, the protocol present a total number of independent measurements of:

$$N_{meas} = \frac{L(L-3)}{2} \tag{2.4}$$

The adjacent protocol is commonly chosen due to the hardware simplicity required to implement, a high number of independent measurements (a total of 104 measurements considering a 16 electrode system). Further, the adjacent protocol is sensitive to changes in the conductivity near the boundaries of the vessel [19, 21, 22].

2.1.2.3 Opposite Protocol

The opposite protocol, proposed by Hua et al. [23], utilizes differential voltage measurement, considering neighbors electrodes, although, differently from the adjacent pattern, the injection occurs with geometrical opposite electrodes in the clockwise direction. It is shown in Fig. 2.7 the strategy. Due to reciprocity, Eq. 2.3, the number of independent measurements of the opposite protocol is:

$$N_{meas} = \frac{L(L-4)}{2} \tag{2.5}$$

The opposite protocol is known to be less sensitive to noise, although there is a decreased resolution due to a decreased number of independent measurements compared to the adjacent

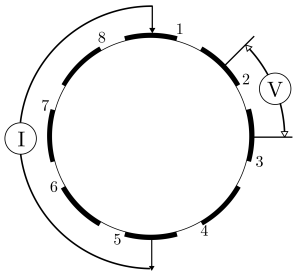

Figure 2.7: Opposite protocol.

protocol (a total of 96 considering a 16 electrode system). Further, the opposite protocol presents greater sensitivity in the middle of the vessel since the current injects passes through the central region [21, 22, 23].

2.1.2.4 Diagonal Protocol

The diagonal protocol, also known as the cross method, the injections occurs from electrodes separated by large distances [21]. It is shown in Fig. 2.8. Considering a 16 electrode system, the protocol proceeds as follows: The reference for the current and voltage are the electrode 1 and 2 respectively. The injection proceeds to electrodes 3, 5, ..., 15. The voltages are measured in each electrode, excluding the ones that are injecting currents. In the next moment, the current and voltage reference is changed to electrode 4 and 3 respectively. The injection proceeds now on electrodes 6, 8, ..., 16, and 2. The voltages are measured in each electrode as before. The protocol displays a total of 7 injections, 13 measurements, and 2 cycles, totalizing $91 \times 2 = 182$ measurements, from which 104 are independent [21].

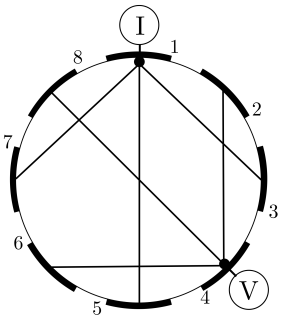

Figure 2.8: Diagonal protocol.

2.1.2.5 Metal Wall Protocol

The reconstruction of images on a metallic vessel introduces several new variables into the method. Aw et al. [24] presents a comprehensive review of these questions. In that frame-

work, the metal wall protocol is developed for use in processes that present metallic walls in its pipelines and vessels. The strategy utilizes the large conductive boundary to be the reference electrode, the ground node [19, 21]. Therefore, the protocol utilizes a two-electrode measurement strategy, as opposed to the four-electrode method. The large area used to sink the current reduces the common-mode compared to the adjacent strategy and acts also as a shield, reducing the interference problems [21]. The metal wall protocol is shown in Fig. 2.9.

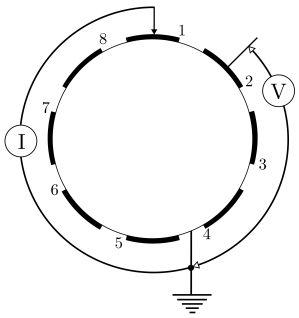

Figure 2.9: Metal wall protocol.

2.1.2.6 Adaptive Protocol and Optimal Drive Protocols

Gisser et al. [25] and Isaacson [26] utilizes the definition of distinguishability, which is the ability of a pattern of currents to distinguish between two conductivities, to search the optimal drive protocols. The optimal current is obtained by maximizing by the distinguishability to obtain the optimal drive protocol, Eq. 2.6.

$$I_{opt} = argmax_I \frac{\|(V_{exp} - V(\sigma))I\|}{\|I\|} \tag{2.6}$$

The resulting pattern is defined the adaptive method, which depends on currents related to $cos(k_l\theta)$ and $sin(k_l\theta)$. Cheney et al. [27] utilize this method, which consists in considering the currents to be:

$$I_l^{k_l} = \begin{cases} cos(k_{adp}\theta_l), & k_{adp} = 1, 2, ..., L/2 \\ sin(k_{adp} - L/2)\theta_l, & k_{adp} = (L/2) + 1, ..., L - 1 \end{cases} \tag{2.7}$$

$$\theta_l = \frac{2\pi l}{L} \quad l = 1, 2, ..., L. \tag{2.8}$$

This adaptive pattern injects currents and measures voltages from all the electrodes except one, which is the reference grounded electrode, varying from I to $-I$. This pattern obtains better estimations, although it is necessary to use multiple adjustable current sources, increasing the

system complexity [1, 19]. Further, Demidenko et al [28] demonstrate by defining the total variance statistical criterion for optimal patterns that the trigonometric or adaptive protocol is a special case and there are different optimal patterns, to estimate conductivity and resistivity.

2.1.3 Model

2.1.3.1 Maxwell's Equation

The forward problem is modeled through the analysis of the Maxwell's equations, which describes the electromagnetic field in a body, Eq. 2.9-2.12 [29, 30, 31].

$$\nabla \cdot D = \rho_c \tag{2.9}$$

$$\nabla \cdot B = 0 \tag{2.10}$$

$$\nabla \times E = -\frac{\partial B}{\partial t} \tag{2.11}$$

$$\nabla \times H = J_t + \frac{\partial D}{\partial t} \tag{2.12}$$

Where E is the electric field, H is the magnetic field, B is the magnetic induction, D is the electric displacement, J_t is the total current density described by the sum of the source current and ohmic current $J_t = J^{sour} + J^{ohm}$, and the ρ_c is the charge density. Considering a linear isotropic medium, Eq. 2.13-2.15 are valid.

$$D = \epsilon E \tag{2.13}$$

$$B = \mu H \tag{2.14}$$

$$J_t = \sigma E \tag{2.15}$$

Where ϵ is the permittivity, μ is the permeability, and σ is the conductivity of the medium.

Assuming the hypothesis of a quasi-static approximation it is possible to simplify further the set of equations. It considers that the currents time-dependency is neglected. This approach is adequate considering that the frequencies of the alternate currents are sufficiently small [31]. Therefore, the time-dependent derivatives from Eq. 2.11 and 2.12 becomes zero. The current source J^{sour} is considered zero inside the domain. Since $\nabla \times E = 0$, there is an electric potential u in a form that Eq. 2.16 is true.

$$E = -\nabla u \tag{2.16}$$

Taking the divergence of Eq. 2.12 in Eq. 2.17,

$$\nabla \cdot J_t = \nabla \cdot (\nabla \times H) = 0. \tag{2.17}$$

Substituting Eq. 2.15 in Eq. 2.17,

$$\nabla \cdot \sigma E = 0. \tag{2.18}$$

Thus, using Eq. 2.16 in 2.18

$$\nabla \cdot \sigma \nabla u = 0. \tag{2.19}$$

Therefore, the problem reduces into solving the Laplace equation for the electric potential inside the body.

2.1.3.2 Boundaries Condition and Complete Electrode Model

Through the years, the boundary conditions were a matter of discussion, as the first assumed to describe the phenomenon was not fully accurate. The first attempt to describe the injection through the electrodes was to model the current density j as a continuous current around the body, represented by $sin(k_{adp}\theta)$ or $cos(k_{adp}\theta)$. This model is called the Continuous Model [29], which is described in Eq. 2.20.

$$\sigma \frac{\partial u}{\partial n} = j_{bound} \tag{2.20}$$

where n is the normal component. Its characteristic is of being an easy model to be implemented numerically. However, its drawback is the overestimation of the results, around 25 percent for the resistivity [29].

Since it was a consensus that it was necessary an accurate model describe fully and with superior precision those injections to reconstruct images with the highest resolution as possible, modifications were necessary to improve the currently existing modeling in the literature. The first

modification was to treat the problem as discrete because the electrodes are not manufactured continually. In its main conception, there are spaces between each electrode that is responsible for injecting and measuring the currents. Its name is due to these gaps that exist between the discontinuities of the electrodes. This model is called the Gap Model, shown in 2.21.

$$j_{bound} = \begin{cases} \frac{I_l}{|e_l|}, & l = 1, 2, ..., L. \\ 0, & in \quad \partial\Omega \setminus \partial\Omega \cup_{l=1}^{L} e_l. \end{cases} \tag{2.21}$$

where $|e_l|$ is the area of the electrode, I is the current, $\partial\Omega$ is the boundary, L is the number of electrodes, e_l is the l-esimal electrode in the boundary $\partial\Omega$. Despite the slight improvement, the boundary condition still presents flaws in the correct modeling of the phenomenon, overestimating the value [29].

The model still does not account for the shunt effect that happens in the electrode. This effect happens because of the low resistance path of the current that the metal exhibit within its area when injecting a current through an electrode. Thus, the Shunt Model combines the improvements of the Gap Model and adds the shunt effect to the electrodes, which is described in Eq. 2.22-2.23.

$$\int_{e_l} \sigma \frac{\partial u}{\partial n} dS = I_l \quad l = 1, 2, ..., L. \tag{2.22}$$

$$\sigma \frac{\partial u}{\partial n} = 0 \quad in\, \partial\Omega \setminus \partial\Omega \cup_{l=1}^{L} e_l. \tag{2.23}$$

Additionally, the condition that the potential is constant on each electrode is given in Eq. 2.24.

$$u = U_l \quad on\, e_l \tag{2.24}$$

Since the model is no longer a standard Neumann problem, two conditions for existence and uniqueness of the solution are necessary. Thus, the conservation of charges confers existence, Eq. 2.25

$$\sum_{l=1}^{L} I_l = 0 \tag{2.25}$$

and setting a reference voltage by Eq. 2.26 confers uniqueness.

$$\sum_{l=1}^{L} U_l = 0 \tag{2.26}$$

Still, the model does not precisely matches the experimental data [29]. Cheng et al. [32] propose the Complete Electrode Model to represent the electrode injection inside the domain, replacing Eq. 2.24. Its feature is to combine all the conditions previously presented and also considering the effect caused by electrochemical conditions. In the surface of the electrode forms a layer that confers an electrochemical resistance, also called contact resistance. This contact resistance imposes a potential drop that must be considered in the electrode. The Complete Electrode Model is widely accepted in the process tomography community to be used as the forward model in EIT [33, 34, 35], and it is given by Eq. 2.27.

$$u + \bar{z}_l \sigma \frac{\partial u}{\partial n} = U_l \quad in\ e_l,\ l = 1, 2, ..., L \tag{2.27}$$

where $\bar{z}$ is the contact impedance of the electrodes.

2.1.3.3 Discretization

To solve the Complete Electrode Model, it is necessary to discretize the domain to evaluate the partial differential equations, as the solution of the problem analytically is not easily accomplished for complex domains. Some types of discretization are available in the literature to solve the set of equations. The most commonly used to solve these equations is the Finite Element Method (FEM) [33, 34, 35]. It presents an advantage when applied to arbitrarily shaped domains, being superior to the Finite Difference Method, although no restriction is imposed on the adoption of this method [36], and the Finite Volume Method [37].

The FEM discretizes the interior of the body after turning into a weak formulation of its boundary value problem. This method splits the domain Ω into a finite number of elements K and nodes N [1, 35, 38, 39]. The elements have the form of triangles or other higher-order elements. The electric potential is approximated by functions that are linear inside the element. The chosen basis is the set of functions ϕ_i that is given the value one on vertex i and zeroes otherwise. This approximation is represented by:

$$u = \sum_{i=1}^{N} u_i \phi_i \tag{2.28}$$

in a form that $\phi_i = (\phi_1, ..., \phi_n)^T \in \mathbb{R}^N$ The Eq. 2.28 is not differentiable, so it is not possible to apply directy into Eq. 2.19. To overcome this requirement, the weak form is derived. Multipling Eq. 2.19 by a function v and integrating over Ω,

$$\int_{\Omega} v \nabla \cdot (\sigma \nabla u) d\forall = 0 \tag{2.29}$$

Using Green's second identity and the vector identity

$$\nabla \cdot (v\sigma\nabla u) = \sigma\nabla u \cdot \nabla v + v\nabla \cdot (\sigma\nabla u) \tag{2.30}$$

Eq. 2.29 becomes

$$\int_{\Omega} \nabla \cdot (v\sigma\nabla u)d\forall - \int_{\Omega} \sigma\nabla u \cdot \nabla v d\forall = 0 \tag{2.31}$$

From the divergence theorem, Eq. 2.32

$$\int_{\Omega} \nabla \cdot (v\sigma\nabla u)d\forall = \int_{\partial\Omega} v\sigma\frac{\partial u}{\partial n}dS = 0 \tag{2.32}$$

Thus, Eq. 2.31 becomes

$$\int_{\Omega} \sigma\nabla u \cdot \nabla v d\forall = \int_{\partial\Omega} \sigma\frac{\partial u}{\partial n}vdS \tag{2.33}$$

For the Laplace Equation 2.19, Eq. 2.33 is the weak form [1, 38, 39, 35]. Rearranging the boundary conditions of Eq. 2.27 as

$$\sigma\frac{\partial u}{\partial n} = \frac{1}{\bar{z}_l}(V_l - u) \tag{2.34}$$

on E_l, considering $\bar{z}_l \neq 0$ and incorporating it into Eq. 2.33 gives

$$\int_{\Omega} \sigma\nabla u \cdot \nabla v d\forall = \sum_{l=1}^{L} \int_{e_l} \frac{1}{\bar{z}_l}(V_l - u)vdS. \tag{2.35}$$

Utilizing $v = \sum_{i=0}^{N} v_i\phi_i$ and Eq. 2.28 gives

$$\sum_{j=1}^{N} \left[\int_{\Omega} \sigma\nabla\phi_i \cdot \nabla\phi_j d\forall\right] u_j + \sum_{l=1}^{L} \left[\int_{e_l} \frac{1}{\bar{z}_l}\phi_i\phi_j dS\right] u_j - \sum_{l=1}^{L} \left[\int_{e_l} \frac{1}{\bar{z}_l}\phi_i dS\right] V_l = 0 \tag{2.36}$$

Considering the known total current from boundaries condition, substituting Eq. 2.34 into Eq. 2.22, it becomes

$$I_l = \int_{e_l} \frac{1}{\bar{z}_l}(V_l - u)dS \tag{2.37}$$

Utilizing $v = \sum_{i=0}^{N} v_i\phi_i$ and Eq. 2.28 gives

$$I_l = \int_{e_l} \frac{1}{\bar{z}_l}V_l - \sum_{i}^{N} \left[\int_{e_l} \frac{1}{\bar{z}_l}\phi_i dS\right] u_i \tag{2.38}$$

Assuming a constant $\bar{z}_l$ on e_l reduces Eq. 2.38 to

$$I_l = \left[\frac{1}{\bar{z}_l}\left|e_l\right|\right] V_l - \sum_{i}^{N} \left[\int_{e_l} \frac{1}{\bar{z}_l}\phi_i dS\right] u_i \tag{2.39}$$

where $|e_l|$ is the length of the electrode in 2D and the area of the electrode in 3D. The conductivity is approximated by choosing the values on each element to be constant. The characteristic function χ_j is one on the jth element and zero elsewhere, thus:

$$\sigma = \sum_{j=1}^{k} \sigma_j \chi_j \tag{2.40}$$

Therefore, a system of equation is formed and must be solved by Eq. 2.36 and 2.39 [1, 38, 39, 35]:

$$A_M u_{sol} = I_M \quad or \quad \begin{bmatrix} B_M & C_M \\ C_M^T & D_M \end{bmatrix} \begin{bmatrix} u \\ U \end{bmatrix} = \begin{bmatrix} 0 \\ I_{patt} \end{bmatrix} \tag{2.41}$$

where $0 \in \mathbb{R}^{1,N}$, $I_{patt} = (I_1, I_2, ..., I_L)^T \in \mathbb{R}^{1,L}$ is the vector containing the injected currents, U is the electric potential and V is the voltage at the electrodes. The matrices B_M, C_M, and D_M are calculated by Eq. 2.42-2.44

$$B_M(i,j) = \sum_{\tilde{k}=1}^{K} \sigma_k \int_{\Omega_{\tilde{k}}} \nabla\phi_i \cdot \nabla\phi_j d\mathcal{V} + \sum_{l=1}^{L} \frac{1}{\bar{z}_l} \int_{e_l} \phi_i \phi_j dS \quad i,j = 1,2,...,N \tag{2.42}$$

$$C_M(i,j) = -\frac{1}{\bar{z}_l} \int_{e_j} \phi_i dS \quad i = 1,2,...,N; j = 1,2,...,L \tag{2.43}$$

$$D_M(i,j) = \begin{cases} 0, & i \neq j \\ \frac{|e_j|}{\bar{z}_j} & i = j \end{cases} \quad i,j = 1,2,...,L \tag{2.44}$$

The Eq. 6.6 can be satisfied by designating in a arbitrary node i $u_i = 0$ [1].

Another approach that is also considered is the Boundary Element Method (BEM). It discretizes the boundary of the domain, utilizing fundamentals solutions in the interior. Because only the boundary is integrated, the complexity of the method reduces and consequently, the computation time reduces. The drawback of such a method is that the interior of the domain must be homogeneous, which limits its application [40]. To overcome this drawback, a solution to this problem could utilize different interfaces corresponding to the conductivities distributions of the different phantoms in the interior of the domain, which reduces the problem into finding the shape of the interfaces [41, 42]. Combining FEM with BEM to calculate the potential voltage in the domain is an option, which could improve the accuracy of the results [43]. Recently, a meshless method is applied to further minimize the computational time, the Method of Fundamental Solutions

[44, 45, 46]. The method uses the fundamental solution to solve the electric potential inside the domain. It is still in development since the solution is obtained for a reduced number of cases and the stability is not guaranteed [44, 45, 46].

2.1.4 Inverse Problem

The problem of the evaluation of the electrical conductivities can be described as a non-linear and ill-posed problem. This condition arises from the propagation of the electrical current through diffusivity in the medium is responsible for the effect called soft-field, caused by the non-linearity of the problem. The inverse problems are distributed in absolute reconstruction, considering non-linear steps; difference reconstruction, considering linear steps; and dynamic reconstruction, based on recursive algorithms. The first two normally involve deterministic problems, while the dynamic reconstructions are statistical. The problem becomes to solve the least-squares problem, Eq. 6.14 [33, 40, 47].

$$\sigma_{calc} = argmin_{\sigma}(\|V_{exp} - V(\sigma)\|^2) \tag{2.45}$$

Consider the forward problem, Eq. 2.46, [33, 40]:

$$V = F(\sigma) \tag{2.46}$$

where F is the forward problem represented by Eq. 2.19, with boundary conditions of Eq. 2.22,2.23,2.25-2.27. By applying the Taylor expansion and neglecting the high order terms, the Eq. 2.47 is given:

$$\delta V = \frac{\partial F}{\partial \sigma}\delta\sigma \tag{2.47}$$

where $J = \frac{\partial F}{\partial \sigma}$ is the Jacobian and $\delta V = V_{exp} - V(\sigma)$.

The inverse problem aims to solve the linearized solution, Eq. 2.48 [33, 40, 47].

$$\delta\sigma = J^{-1}\delta V \tag{2.48}$$

However, the inversion of the matrix is not possible, since the matrix possesses a low rank, which makes it nearly singular matrix. Different inversion methods, such as optimization, and statistical inversion must be utilized to solve the problem.

2.1.4.1 Linear Back-Projection

The first versions of the algorithms to solve such problems uses the linear back-projection (LBP). The implementation by Barber and Brown [48], in their first model of the data acquisition system,

the Sheffield Mark I [20]. The idea behind the algorithm is to approximate the Jacobian through a proposition based on the algorithms utilized in x-ray tomography. By calculating the so-called LBP operator, which is simply a replacement for the Jacobian matrix, combining with a filter and inverting the matrix, shown in Eq. 2.49 [49].

$$\delta\sigma = B_{LBP}\delta V \tag{2.49}$$

where B_{LBP} is the LBP operator. Kotre [50] presents an alternative, which is frequently utilized to reconstruct images, consisting of approximate the inverse of the Jacobian by the transpose matrix, shown in Eq. 2.50.

$$\delta\sigma = J^T\delta V \tag{2.50}$$

Sun et al. [51] reviewed the concepts of the LBP and was able to estimate with superior quality. The developed technique accounted for the effects of the soft-field through an index calculated by the decomposition of the contributions of the positive and negative parts of the effect.

2.1.4.2 Gauss-Newton and Tikhonov Regularization

The use of the LBP, although simple to implement, as it requires only a matrix-vector multiplication, still presents a low quality for the image reconstructed, presenting only qualitative information and others methods were presented in the literature. Since the solution is heavily ill-posed, the minimization on the least-squares sense, Eq. 6.14, is not possible. An approach to solve the minimization contrary to the LBP is to employ a penalizing term which could also be viewed as a form of prior information introduced into the least-squares problem to avoid instabilities in the solution. This term is known as the Tikhonov regularization, Eq. 6.15.

$$\sigma_{calc} = argmin_{\sigma}(\|V_{exp} - V(\sigma)\|^2 + \alpha^2 \left\|\tilde{L}(\sigma - \sigma_{ref})\right\|^2) \tag{2.51}$$

where $\tilde{L}$ is the regularization matrix and the α is the regularization parameter.

In that way, the Gauss-Newton minimization is employed to reconstruct images by the linear approach, which is one of the most used methods. One of the first researchers to implement along with Yorkey [52], Cheney et al. [27] utilized in his algorithm nominated Newton's One Step Error Reconstructor (NOSER), which the linear reconstruction (one-step) is given by Eq. 6.17.

$$\delta\sigma = \left(J^TJ + \alpha^2\tilde{L}^T\tilde{L}\right)^{-1}\left(J^T\delta V + \alpha^2\tilde{L}^T\tilde{L}\left(\sigma_{ref} - \sigma_0\right)\right) \tag{2.52}$$

where J is the jacobian, $\delta\sigma$ is the estimated conductivity, σ_{ref} is a reference conductivity, σ_0 is an initial conductivity. The linear reconstruction is chosen when the true conductivity is close

to the initial estimate [40]. A way to assure this condition is using a reference set of voltages, with known conductivity. The easy to measure the conductivities of fluids makes the method extensively used in tomography for industrial processes. When this condition is not assured, it is common to solve the non-linear iterative method of Gauss-Newton. It consists of updating the Jacobian each iteration. The iteration is given by Eq. 2.53 [40].

$$\sigma_{k+1} = \sigma_k + \left(J_k^T J_k + \alpha^2 \tilde{L}^T \tilde{L}\right)^{-1} \left(J_k^T \delta V + \alpha^2 \tilde{L}^T \tilde{L} \left(\sigma_{ref} - \sigma_k\right)\right) \tag{2.53}$$

2.1.4.3 Landweber

Yang et al. [53] propose an alternative to the Gauss-Newton, the Landweber iteration procedure for Electrical Capacitance Tomography that is also extended to EIT [54]. The method is iterative and based on the steepest gradient descent method. It uses the prior information from the LBP firstly, and, in each iteration, the procedure adds a term to its first estimate, the direction of minimization multiplied by a gain term or a relaxation factor, Eq. 2.54.

$$\delta\sigma_{k+1} = \delta\sigma_k + \alpha_{lw} J^T (\delta V - J\delta\sigma_k) \tag{2.54}$$

$$\delta\sigma = J^T \delta V \tag{2.55}$$

where α_{lw} is the gain related to the maximum eigenvalue of $J^T J$, λ_{max} , by Eq. 2.56.

$$\alpha_{lw} = \frac{2}{\lambda_{max}} \tag{2.56}$$

The iteration process is known to converge to the minimum-norm least-squares solution [55]. One major drawback of the Landweber iteration procedure is that the convergence is poor, as the methods based on the steepest descent tend to converge fast initially and, when close to the minimum, the velocity of convergence gradually decreases. Li and Yang [56] introduced an algorithm with non-linear steps in the Landweber iteration minimization in an attempt to obtain a superior quality image, by updating the jacobian each iteration. It is shown that this step improves the reconstruction of complex forms.

2.1.4.4 Conjugate Gradient

In the same class of the gradient-based algorithms, the conjugate gradient is an iterative option as the main solver of the inverse problem [57]. Since the conjugate gradient is only applicable in symmetric positive-definite matrices, some manipulation is necessary to ensure this condition,

assuring the correct application of the method. The method provides a way to solve N x N linear system. Consider a system of Eq. 2.57

$$Ax_{sol} = b. \tag{2.57}$$

The method aims to minimize the function from Eq. 2.58

$$f(x_{sol}) = \frac{1}{2}x_{sol}Ax_{sol} - bx_{sol} \tag{2.58}$$

by considering the gradient or residual, Eq. 2.60, zero to achieve the Eq. 2.57

$$\nabla f = Ax_{sol} - b \quad or \quad \tilde{r} = Ax_{sol} - b \tag{2.59}$$

The minimization proceeds generating successive vectors p_k in the orthogonal direction that satisfy the condition

$$p_i^T Ap_j = 0 \quad for\ i \neq j \tag{2.60}$$

The method is given by the algorithm in Eqs 2.61:

$$\begin{aligned}
&k = 0 \\
&p_0 = \tilde{r}_0 = b - Ax_{sol(0)} \\
&\\
&\boldsymbol{while}\ \left\|\tilde{r}_{(k)}\right\|_2 < tol \\
&\quad u_{(k)} = Ap_{(k)} \\
&\quad \alpha_k = \tilde{r}_{(k)}^T \tilde{r}_{(k)} / p_{(k)}^T u_{(k)} \\
&\quad x_{sol(k+1)} = x_{sol(k)} + \alpha_{(k)} p_{(k)} \\
&\quad \tilde{r}_{(k+1)} = \tilde{r}_{(k)} - \alpha_{(k)} u_{(k)} \\
&\quad \beta_{(k)} = \tilde{r}_{(k+1)}^T \tilde{r}_{(k+1)} / \tilde{r}_{(k)}^T \tilde{r}_{(k)} \\
&\quad p_{(k+1)} = \tilde{r}_{(k+1)} - \beta_{(k)} p_{(k)} \\
&\quad k = k + 1 \\
&\boldsymbol{end}
\end{aligned} \tag{2.61}$$

To improve further the algorithm from the classical implementation, Wang et al. [58] presented a gradient conjugate method based on Krylov subspaces that showed better results in a minimal number of iterations, proving to be a good candidate for real-time reconstruction.

2.1.4.5 Kalman Filters

The inverse problem can also be seen in the framework of the statistical inversion for dynamic systems. The Kalman Filter (KF) was the first type of filter used to estimate statistically the conductivities field [47, 59, 60]. These pixels represented by the reconstructed conductivities are treated as a state variable and modeled in a Markov chain. The essence of the filter begins by predicting the state based on the previous state aided by a forward problem. The measurement is used then in the sequence to update the state recursively. In the EIT area of research, this type of recursion in a filter is named as dynamic reconstruction [40]. It is important to indicate that the impedance imaging is a non-linear application and the KF is designed to be used to linear systems.

To enable the use of the KF in EIT estimations, the modified version of the filter is the choice for the researchers, the Extended Kalman Filter (EKF), which allows the implementation of linearized models. The EKF utilizes the jacobian originated by the linearization of the model due to a Taylor expansion truncated at the first term. Kaipio et al. [59, 60] were the first group of researchers to successfully implement the EKF in EIT, and in his work, it was argued that it was necessary to apply a spatial regularization to overcome the difficulties of the high dimension problem. In some applications, the resistivity changes may be so fast that the target changes between the injection of the current patterns and thus the data do not correspond to the same target distribution. Since Kalman filter is a causal filter providing estimates for the resistivity distribution at each time based only on the relative past, the estimates exhibit a delay. Vauhkonen et al. [35] accounted for this characteristic and conclude that a fixed-lag smoother provides a better estimation. Trigo et al. [61] utilize the EKF to estimate the conductivities and the unknown impedance contact resistance. Adler et al. [62] propose a temporal reconstruction based on a Kalman filter formulation that considers a group of measurements as a set to reconstruct the image. It is argued that the algorithm is suited to noisy measurements and for rapid changes in the conductivity.

In certain types of applications, prior information is known and a more physical and realistic type of evolution model could present better results. By knowing that in medical applications the conductivity changes in only certain areas, Kim et al. [63] proposes to utilize a kinematic model as an evolutionary model to estimate the conductivity changes dynamically inside two pre-grouped regions. Seppanen et al. [64] model the state evolution with information of the fluid dynamics of the process using the fixed-lag Kalman filter, which is tested experimentally in [34]. Since a homogeneous solution flowing in a pipe would be impossible to reconstruct, as no

conductivities discontinuities caused by different phases were in the domain, it is considered a solution with the two-phase flow, in a manner that the conductivity is related to the concentration of species in the domain. In a later work, this same model is utilized to estimate the velocities inside the pipe [65]. Moura et al. [66] estimates the conductivities of the tissues of the human thorax with the EKF modeled with the Ibrahim time-domain evolution model.

The unscented Kalman filter (UKF) is also considered in the EIT technique. Proposed by Julier and Uhlman [67, 68] to deal with non-linear systems, the UKF also treats the random variable as a Gaussian distribution, but unlikely the EKF, it is specified using a specific number of variables, the sigma points. These points capture the true mean and covariance accurately to the 3rd order of the Taylor expansion series for any nonlinearity. It is argued that the UKF has the same order of computational complexity as the EKF [69]. Ijaz et al [70, 71] compared the EKF with UKF in the EIT technique dealing with state boundaries estimation. The boundaries were modeled as Fourier descriptors and with the aid of the filters, it was possible to estimate recursively the formation of bubbles in a domain. Also, the method was extended to stratified flows. It was shown that the UKF produced images with an error lower than the EKF.

2.1.4.6 Maximum a Posteriori and Markov Chain Monte Carlo Method

On the statistical methods, there are several possibilities to estimate quantities, the maximum a posteriori is a technique that finds the unknown variable that maximizes the posterior distribution. The problem becomes an optimization procedure based on the likelihood and the prior distribution. Adler and Guardo [72] presented a method to reconstruct dynamically the image by MAP. Nissinen et al. [73] evaluate the Bayesian approximation error, based on MAP estimate, and presents improved results by compensating for the errors in the reconstruction. Liu et al. [74] incorporate Bayesian learning to the reconstruction problem, providing images with high spatial accuracy, and avoiding parameter tunning. MCMC is a more computational intensive method that provides the posterior density of the quantity in question. Utilizing the EIT technique, Aykroyd and Cattle estimate the contours of an inclusion by this method [42]. The algorithm utilized is the Metropolis-Hastings, which employs a gaussian transformation kernel to sample to the next step of the chain.

2.1.4.7 Particle Filter

Considering Bayesian methods are the particle filters (PF), which do not rely on Jacobian computation. Those algorithms are a type of sequential Monte Carlo method to solve the Bayes theorem, that for a given state, its noise and observation it is possible to estimate the posterior

density of a state variable sequentially. It was largely underused when presented, which could be explained by the lower computation power available in the past [75]. The proposal distribution is given employing particles and through the calculation of the likelihood function for each particle, and the posterior density is calculated then by the weights provided by the likelihood function.

Its first version, the Sequential Importance Sampling (SIS) filter presented a remarkable flaw, which after some steps of the state update the weights of the particles become zero for all except one particle [75, 76, 77, 78]. This problem is called the degeneracy of the particles. It was the work presented by Gordon et al. [79] that the particle filter has reached its first operational form. By adding a resampling step, in which the particles with the greater weight are chosen and multiplied in detriment of the particles of low weights. The algorithm was then able to estimate without the degeneracy problem and it is called in the literature Sequential Importance Resampling (SIR) filter or bootstrap filter. Although the SIR filter additionally introduces another type of problem, the impoverishment, ways to treat it. Gordon et al. [79] propose the roughening and prior editing. The process which adds noise to the resampled particles is called the roughening. In that form, the diversity from the particles increases, reducing the problem. It is tuned according to the problem in question. The prior editing is a step that calculates the residual to evaluate the quality of the particles, regarding the impoverishment. In the case that the residual is $\|h_k(\sigma) - z\| > 6 \cdot STD(z)$, the iteration is repeated. This threshold works well for univariable measurements and is yet to be tested for multivariate measurements. Xiaolong et al [80] utilize the methods to moves the target away from a "danger zone" when necessary, calling it the sample editing. Both methods, the prior editing and roughening, are extensively used and sometimes critical for the correct application of the filter [81, 82, 83].

Other types of filters have been proposed, such as the Auxiliary Sequential Importance Resampling (ASIR) filter [84]. It is a remarkable alternative to the SIR filter when the particles have all the same weight after the resampling. The filter improves the variability of the particles by drawing a new set of particles exactly after the resampling step, which increases the number of particles in the region of high likelihood. This step considerably increases the processing time also.

The main features that the PF present is its ability to represent the state variable as a density distribution, with mean and standard deviation and its recursive ability, which allows it for being used for tracking purposes [75, 76, 77, 78]. The KF is also used as a tracking algorithm, however, the PF is a method for solving non-linear and non-gaussian problems, while the KF is restricted only to linear and Gaussian problems. Although, the dynamic behavior of the filter is its main

feature, in process tomography applications this recursion is not addressed properly. The choice of the proposal is an extremely important step in the final performance of the filter [77]. The most intuitively, common, and easy to implement proposal is the prior distribution. On the other hand, this type of proposal leads to high variance [77]. It is pointed out that the proposal is problem dependent, therefore a deep knowledge of the problem in question is required for the election of a good proposal. Several comprehensive manners to improve this proposal is given in the literature, based on the EKF [85], the UKF [86], the H_∞ filter [87] and optimization methods for state and parameter estimation [88].

Regarding the contour estimation, Watzenig et al. [89] utilized the PF in electrical capacitance tomography for estimating the contours of a phantom in a domain. Although the author was able to estimate the boundaries of the phantom with good agreement, it was estimated using a stationary reconstruction. The algorithm searched through the entire domain in the first iteration for a particle that provides a sufficient weight. In the next iteration, the search range was decreased and taken from the previous point until it reaches a good convergence. One of the main problems of the PF is the so-called curse of dimensionality [81, 90]. If the number of state variables is sufficiently large, the performance of the filter is known to degrade. To overcome this deficiency it is necessary to perform a dimension reduction by any means. Additionally, Watzenig et al. [89] modeled the phantoms by two different approaches to represent a boundary: by splines and by Fourier descriptors. Therefore, the dimension is reduced, thereby enabling the use of the PF. Wang et al. [91] combined a deterministic method, the Landweber, with PF to estimate the image in electromagnetic tomography. The algorithm uses the minimization procedure of the LBP to provide the initial guess, and the particle generation was directed by the Landweber iteration at each iteration. The procedure does not estimate dynamically as the image is not treated as a state variable.

2.1.4.8 Smooth Priors and Edge-Preserving Priors

To deal with the ill-posedness of the solution, the Tikhonov regularization term is added as prior information, aiding the stabilization of the solution [40, 47, 1]. The commonly choices for the regularization matrix includes the identity matrix (Tikhonov prior) [52], a positive diagonal matrix (the diagonal from $J^T J$, the NOSER prior) [27], approximation of the first and second-order differential operators (Laplace prior) [92], and the inverse of a Gaussian matrix (Gaussian prior) [72].

This regularization matrices consider a smooth and slowly changing prior, therefore the con-

ductivity images estimated do not present sharp boundaries [47]. There are in the literature alternatives to prevent the blur of the images by estimating discontinuities of conductivity properly, such as the Total Variation regularization [93, 94]. Another approach is to include prior knowledge of the physical boundaries into the computational domain [95, 47].

In the statistical framework, Kaipio et al. [96] provides a comprehensive study on considering the priors statistically, and argues that there is an advantage of representation of these priors and the capability of estimate the full statistical information. A way to introduce these priors is the knowledge of the conductivities beforehand in industrial processes. Thus, the problem becomes to estimate the shapes of the inclusion's boundaries. Ijaz et al. [70, 71] use this information to estimate recursively the shapes of open and closed contours in multiphase flow. In the same manner, Watzenig et al. [89] present a method to estimate the boundaries of inclusion inside a vessel, utilizing a high order dimension representation of a closed contour, such as splines and Fourier descriptors.

The regularization parameter or the hyperparameter is a value that is chosen based on a compromise between noise embedded solution and an over smoothed solution. Normally, its election is arbitrary, although a more comprehensive approach could be employed to give a more satisfactory result. Although the regularization parameter is commonly chosen arbitrarily [33, 52, 97, 98], Graham and Adler [38, 99] evaluate several different methods to select the hyperparameter properly, such as the L-curve. The method considers to plot the semi-norm of the regularized solution $log_{10}|\hat{L}\delta\sigma|$ versus the norm of the corresponding residual vector, $log_{10}|J\delta\sigma - \delta V$, [100]. The curve has an L-shape and the selection lies in the corner of the curve. Another method tested is the Generalized Cross-Validation (GCV), which chooses the hyperparameter that minimizes the GCV curve [100], Eq. 2.62.

$$GCV(\lambda) = \frac{\|J\delta\sigma - \delta V\|^2}{tr(\tilde{I} - J(J^T J + \lambda^2 \tilde{L}^T \tilde{L})^{-1} J^T)} \tag{2.62}$$

2.1.5 Jacobian

The Jacobian, also known as the sensibility matrix, informs the variation of voltage through the variation of conductivity, indicating the sensibility that the change of conductivity in the medium influence in an electrode measurement. Each row of the Jacobian is called the sensitivity maps, giving information regarding the sensitivity for each measurement and injection. The deterministic optimizations and the EKF filter relies on the computation of Jacobian.

2.1.5.1 Definition

By the definition, the Jacobian maps the perturbations of the solution to perturbations on the boundary data [30, 31].

$$\Delta\sigma\,|_{\Omega} \rightarrow \Delta V|_{\partial\Omega} \tag{2.63}$$

The Jacobian matrix $J \in \mathbb{R}^{M,K}$, where M is the number of measurements in the pattern.

$$J = \begin{bmatrix} \frac{\partial V_1}{\partial \sigma_1} & \frac{\partial V_1}{\partial \sigma_2} & \cdots & \frac{\partial V_1}{\partial \sigma_K} \\ \frac{\partial V_2}{\partial \sigma_1} & \frac{\partial V_2}{\partial \sigma_2} & & \vdots \\ \vdots & & \ddots & \\ \frac{\partial V_M}{\partial \sigma_1} & \cdots & & \frac{\partial V_M}{\partial \sigma_K} \end{bmatrix} \tag{2.64}$$

The computation from the definition procceeds by perturbing each element by a small amount of $\delta\sigma$ and, from solving the forward problem, the perturbation ∂V on the boundary was calculated.

2.1.5.2 Adjoint Differentiation Method

From the Adjoint problem formulation, the Jacobian is efficiently computed from the dot product of the current and measurement fields with the integrals of the gradient of the shape function over each element [1, 40, 30, 101]. Considering the weak form, Eq. 2.33:

$$\int_{\Omega} \sigma \nabla u \cdot \nabla v d\forall = \int_{\partial\Omega} \sigma \frac{\partial u}{\partial n} v dS \tag{2.65}$$

Considering $v = u$, the Eq. 2.65 becomes:

$$\int_{\Omega} \sigma \left|\nabla u\right|^2 d\forall = \int_{\partial\Omega} \sigma \frac{\partial u}{\partial n} u dS \tag{2.66}$$

The Eq. 2.27 can be written as:

$$u = U_l - \bar{z}_l \sigma \frac{\partial u}{\partial n} \tag{2.67}$$

Substituting Eq. 2.67 in Eq. 2.66

$$\int_{\Omega} \sigma \left|\nabla u\right|^2 d\forall = \sum_{l=1}^{L} \int_{e_l} \left(V_l - \bar{z}_l \sigma \frac{\partial u}{\partial n} \right) \sigma \frac{\partial u}{\partial n} dS \tag{2.68}$$

and Eq. 2.69

$$\int_{e_l} \sigma \frac{\partial u}{\partial n} dS = I_l \tag{2.69}$$

in Eq. 2.68 gives

$$\int_{\Omega} \sigma \left|\nabla u\right|^2 d\forall + \sum_{l=1}^{L} \int_{e_l} \bar{z}_l \left(\sigma \frac{\partial u}{\partial n} \right)^2 dS = \sum_{l=1}^{L} V_l I_l \tag{2.70}$$

The Eq. 2.70 states that the power is dissipated either in the domain or the contact impedance from the electrode. Taking perturbations $\sigma \to \sigma + \delta\sigma$, $u \to u + \delta u$ and $V_l \to V_l + \delta V_l$ considering the current in each electrode to be constant I_l:

$$\int_{\Omega} (\sigma + \delta\sigma) \left|\nabla (u + \delta u)\right|^2 d\not{V} + \sum_{l=1}^{L} \int_{e_l} \bar{z}_l \left((\sigma + \delta\sigma) \frac{\partial (u + \delta u)}{\partial n} \right)^2 dS = \sum_{l=1}^{L} (V_l + \delta V_l) I_l \tag{2.71}$$

Manipulating Eq. 2.71 and ignoring higher order terms gives

$$\int_{\Omega} \delta\sigma \left|\nabla u\right|^2 d\not{V} + 2 \int_{\Omega} \sigma \nabla u \cdot \nabla \delta u \, d\not{V} + 2 \sum_{l=1}^{L} \int_{e_l} \bar{z}_l \left(\sigma \frac{\partial u}{\partial n} \right) \delta \left(\sigma \frac{\partial u}{\partial n} \right) dS = \sum_{l=1}^{L} I_l \delta V_l \tag{2.72}$$

Introducing the boundary condition on the lth electrode E_l, Eq. 2.73

$$\delta \left(\sigma \frac{\partial u}{\partial n} \right) = \frac{1}{\bar{z}_l} (\delta V_l - \delta u) \tag{2.73}$$

Substituting Eq. 2.73 in Eq. 2.72 gives

$$\int_{\Omega} \delta\sigma \left|\nabla u\right|^2 d\not{V} + 2 \int_{\Omega} \sigma \nabla u \cdot \nabla \delta u \, d\not{V} + 2 \sum_{l=1}^{L} \int_{e_l} \sigma \frac{\partial u}{\partial n} \delta V_l \, dS - 2 \sum_{l=1}^{L} \int_{e_l} \sigma \frac{\partial u}{\partial n} \delta u \, dS = \sum_{l=1}^{L} I_l \delta V_l \tag{2.74}$$

Considering the weak formulation, Eq. 2.65, considering $v = \delta u$, Eq. 2.75 is given

$$-2 \int_{\Omega} \sigma \nabla u \cdot \nabla \delta u \, d\not{V} + 2 \sum_{l=1}^{L} \int_{e_l} \sigma \frac{\partial u}{\partial n} \delta u \, dS = 0 \tag{2.75}$$

Summing Eq. 2.75 with Eq. 2.74, the term 2 and 4 from Eq. 2.74 becomes zero.

$$\int_{\Omega} \delta\sigma \left|\nabla u\right|^2 d\not{V} + 2 \sum_{l=1}^{L} \int_{e_l} \sigma \frac{\partial u}{\partial n} \delta V_l \, dS = \sum_{l=1}^{L} I_l \delta V_l \tag{2.76}$$

From Eq. 2.69, the term 2 from Eq. 2.76

$$2 \sum_{l=1}^{L} \int_{e_l} \sigma \frac{\partial u}{\partial n} \delta V_l \, dS = 2 \sum_{l=1}^{L} I_l \delta V_l \tag{2.77}$$

Therefore, the total change in power, Eq. 2.79, is given

$$\sum_{l=1}^{L} I_l \delta V_l = - \int_{\Omega} \delta\sigma \left|\nabla u\right|^2 d\not{V} \tag{2.78}$$

To give the change in voltage, not in power, we simply solve for the special measurement current pattern [101]. The dependence of the potential on a vector of electrode currents $I = (I_1, ..., I_L)^T$

is written $u(I)$. The hypothetical measurement potential, considering the solution of the forward problem for each measurement pattern, is $u(I^m)$. On the other hand, the potential for the drive pattern is $u(I^d)$, the actual forward solution given the driving patterns. Applying $u(I^d) + u(I^m)$ and $u(I^d) - u(I^m)$ to Eq. 2.79 and then subtracting gives

$$\delta V_l = -\int_{\Omega} \delta\sigma \nabla u(I^d) \cdot \nabla u(I^m)\, d\not{V} \tag{2.79}$$

Considering the values to be constant in each element, the discretization from Eq. 2.40, the Jacobian is described in Eq. 2.80

$$\frac{\partial V_l}{\partial \sigma_k} = -\int_{\Omega_k} \nabla u(I^d) \cdot \nabla u(I^m)\, d\not{V} \tag{2.80}$$

2.1.6 Modeling Accuracy and Error

2.1.6.1 Accuracy of the Forward Problem

The accuracy of the model was tested by several researchers. Ider et al. [102] solved by FEM a 2D simulation of a vessel with 1 cm in height filled with NaCl solution. The results presented a good agreement with the model. Further, it was presented as a method to solve 3D forward problems since it was noticed the need to treat appropriately the domain simplification. Ma et al. [103] observed that there are errors regarding the modeling of the 3D domain into a simplified 2D analysis. At some points, over 80% error was observed by this method. Further, results obtained by Fransolet et al. [104] corroborate the need to treat the 3D modeling properly. Additionally, it is observed an error caused by the temperature into the calculated voltages, since the conductivity is highly dependent on the temperature on the electrolyte [105].

2.1.6.2 Errors in the Reconstruction

Considering the reconstruction of the image, Kolehmainen et al. [97] provided a brief review regarding the effect of modeling errors in the static reconstruction, and as well his investigation provided new information.

Contact Impedance The contact impedance (when working with in-vivo measurements) consists of two terms. The first is the electrochemical impedance that exists at the interface between electrode and skin. The second is the skin impedance. Considering the static imaging, the contact impedance must be modeled accurately to obtain good reconstructions, although it is dependent on the injection protocol. The adjacent protocol is insensitive to contact impedance changes, while the adaptive pattern presented high deviations. This occurs since the measurements are

only performed in non-injecting electrodes. Concerning the adaptive protocol, the four-electrode method is superior to the conventional approach. When performing difference imaging reconstruction, assuring that the contact impedance does not change from images, the method is insensitive to these impedances. In the case of changes, spatial or linear variations, there is significant image loss of quality.

Electrode Size It is important to verify errors concerning the electrode size, since complex geometries may present difficulties in modeling large electrodes. When changing the size of the electrodes, initiating from pointlike and increasing the size, it was found that the error is only a little greater than the ones caused by the electronics of the measurement system when the modeling error is small. The errors also increased greatly with the electrode size error. The adjacent method is insensitive to variations in electrode size since the measurements are performed in non-injecting electrodes. The adaptive method estimates poorly the results when this error is present.

Electrode Localization The positioning of the electrode in the model is investigated as well. The absolute reconstruction is very sensitive to this positioning, although it is insensitive when reconstructing with the difference imaging. The localization of the electrode is more important when measuring the signal since it becomes a source of error. A workaround to diminish this error is by considering a stronger regularization, although the effect of blurring occurs strongly.

2.1.7 Acquisition System

The acquisition system development is of the major concern of the researchers since the sensors must acquire a signal with the lowest as possible noise embedded into it to avoid high errors in the reconstruction image. Additionally, each module must achieve sufficient accuracy to avoid errors in the measurements.

2.1.7.1 Architecture

Brown and Seagar [20] developed one of the pioneers' systems, the Sheffield system. The architecture from the system presented the base to the following acquisition system in the literature. It consists of a system composed of the following modules: the sensors, a master clock, a voltage-controlled current source (VCCS), multiplexers, an instrumentation amplifier, a phase-sensitive detector, a sample-and-hold and an analog-to-digital converter (ADC). The block diagram of the system is shown in Fig. 2.10. The master clock is used to control the VCCS, which inputs a

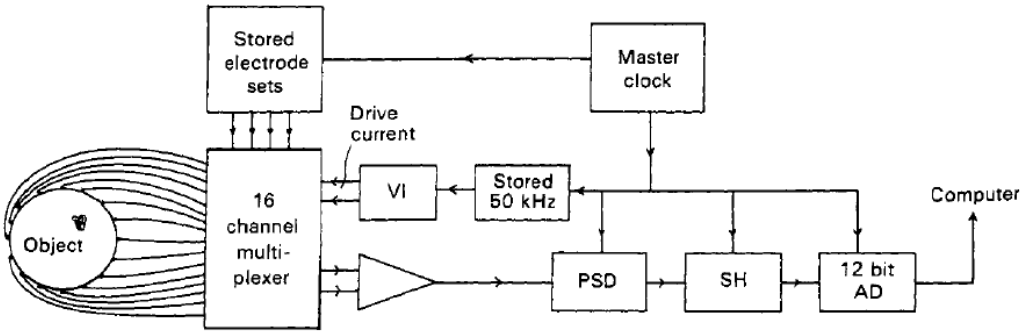

Figure 2.10: The block diagram of one of the first systems [20].

current of 51 kHz in the medium. This clock is also used as a reference to the phase-sensitive detector and controls other modules. The multiplexers have the function of distributing the signal to the working electrode and from the measuring electrodes. It provides a simplification of the hardware necessary since it reduces the number of current sources and voltmeters. The differential voltage is obtained by the instrumentation amplifier (in-amp), which also must reject the common-mode signal. Thus, the common-mode rejection ratio (CMRR) must be large enough in the frequency range of the signal. The phase-sensitive detector must demodulate the signal, to obtain the in-phase value of the signal. The Sheffield system only measured the in-phase signal. The sample-and-hold and ADC are the required modules to transform the signal into a digital value.

The digital demodulation is presented by Dickin and Wang [21] and in a newer version of the Sheffield system, the Sheffield Mk3.5 [106]. The latter presented one of the first versions which could inject current in a range of frequencies (9.6 kHz and 1.2 MHz), the so-called multi-frequencies systems. This Sheffield system is programmable and presents a Howland circuit for the VCCS. There is an absence of multiplexers being fully parallel, contrary to the Mk1 system. Utilizing 8 electrodes, it is capable of measuring 33 frames/s.

Considering that industrial processes require high speeds of acquisition, Wilkinson et al. [4] present its architecture capable of over 1000 frames/s. It consists of injecting pulsed currents through the sensors. The voltage is fed into a differential amplifier, the voltmeter is fully parallel, and a sample-and-hold demodulates the system. A dual-plane system developed by Wang et al. [3] could also obtain, for each plane, numbers in the same order of frames/s. Fast demodulation of the measurement, which is acquired in parallel for the channels, combined with a scheme that decreased the settling time provided the fast acquisition of the system [107]. The system developed by Jia et al. [108] implemented in the acquisition system developed a voltage source

with a current meter. This construction enables high-intensity currents for applications in highly conductive media.

Concerning the modern multi-frequencies systems for medical purposes, after the Sheffield system, it was developed the one from Darthmouth for breast image (Halter et al [109, 110]). This system has a bandwidth of 12.5MHz and over 94dB of signal-to-noise ratio (SNR) until 1 MHz, decaying to 65dB in 10MHz. The main factor that limits the bandwidth is the stray capacitance present in the system. The main reasons to reach this performance are the following guidelines to limit the stray capacitance: maintaining the electronics close to the electrodes to limit the lead length, designing properly the circuit layout, and developing a calibration procedure. The system is fully parallel, thus current can be injected and the voltage can be measured through all electrodes. Considering other designs for a multi-frequency system, Oh et al. [111] present for the second version of their developed system, the KHU Mark2, a system fully parallel, with a CMRR reaching 100dB and an SNR of 80dB. It utilizes a General Impedance Converter (GIC) to cancel the stray capacitance in the VCCS. Shi et al. [112] propose a configuration of 3 in-amps to increases the CMRR of the voltmeter. It is shown by modeling the configuration that the CMRR increases from 60dB to 120dB in 200kHz considering a 0.1% mismatch of the 3 in-amps. The system, aimed for brain image, presented an SNR of 83dB and a CMRR over 75dB. Li et al. [113] develop a system to evaluate changes caused by blood perfusion with a calibration scheme to control the inconsistency between channels. Tan et al. [114] develop a system to obtain complex impedances by injecting currents with a multisinusoidal signal, combining different single-frequency components.

2.1.7.2 Errors in the Instrumentation

The inverse problem requires that the signal is matching as accurately as possible, with low inflicted noise to reconstruct properly the conductivities. Therefore, it is extremely important to provide measurements from the acquisition system assuring certain requirements of accuracy. Jennings and Schneider [115], Boone and Holder [116] provide an extensive review considering the errors when designing an EIT instrumentation. Additionally, McEwan et al. [117] presented a review over multi-frequency systems. Requirements suggested by researchers include a maximum error of 0.02%-0.05% for static imaging and 0.1% for the transconductance measurements of practical dynamic imaging. Jennings and Schneider [115] considers a value of 0.1%.

The ideal problem consists of measuring the voltages from an electrical field developed by current injection. Normally, this procedure is performed by a 4-electrode system, with a medium-

frequency current source (although multi-frequency systems can reach higher frequencies). The ideal 4-electrode injecting and measuring system is described in Fig. 2.11.

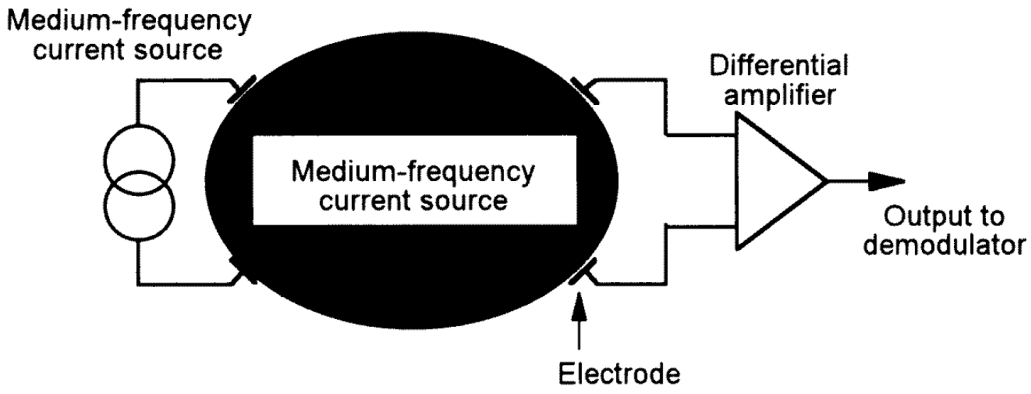

Figure 2.11: The representation of the ideal 4-electrode system [116].

For the real case, it must be accounted that the current source, differential amplifier, and multiplexers are non-ideal. The equivalent circuit presented by Boone and Holder [116] represents the real system in Fig. 2.12.

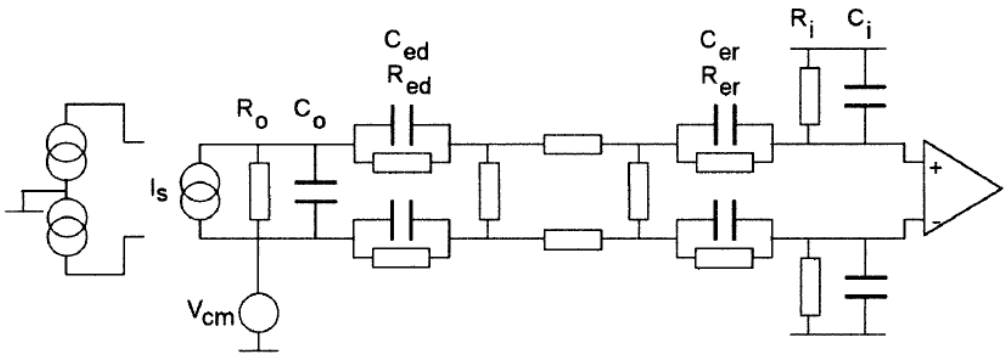

Figure 2.12: The real representation of the measurement system. Adapted from [116].

Current Source The I_s represents the current source, which can be a single or dual, with finite output resistance R_o and capacitance C_o. These impedances cause the current to be shunted (divider effect) before reaching the load. The output resistance affects greater the lower frequencies, while the output capacitance affects more the higher frequencies. The V_{cm} is the undesirable common-mode voltage that arises from the interaction between the current source and the impedances from the system. This value is dependent on the topology of the current source since single-ended topology is more afflicted by common-mode than the floating source.

Additionally, when considering this floating source, the balance between the currents in the dual-source must be good.

Electrodes The electrodes are used to inject current and measure voltage. The skin-electrode interface is represented by the equivalent resistance and capacitance R_{ed} and C_{ed} in parallel respectively. Jennings and Schneider [115] argues that the representation of the impedances in series is more realistic. To model the interface between electrode-electrolyte, Wang [107] utilizes a parallel combination of resistance (charge transfer resistance) and a capacitance (double layer capacitance) and a resistance in series (bulk resistance).

Voltmeter The in-amp have a finite CMRR and input resistance R_i and capacitance C_i. These input resistances and capacitances attenuate the signal (voltage divider effect). Additionally to this effect, the common-mode voltage that needs to be rejected can be as large as 1.3-2.0 times the differential signal. Therefore, if all other circuits elements were ideal, the in-amp would need a total of 60 dB CMRR to achieve 0.1% accuracy [116].

Multiplexers and Cables Additionally, the system can have multiplexers with capacitance and on-resistance, and cables also present resistances and capacitance that must be accounted for, inducing the current and voltage divider effect. The equivalent circuit from Jennings and Schneider [115] considers additional elements, improving the complexity of the analysis.

2.1.7.3 Howland Current Source

The Howland current source is an extensively used circuit to inject current in EIT systems. It was first considered by the work in the Sheffield research group (Bertemes-Filho et al. [118]). Its simplicity and good performance are the main features of this circuit [119]. The design includes inverting and non-inverting configuration, using single or double amplifiers, as shown in Fig. 2.13.

Single Configuration The basic Howland circuit uses a single amplifier with both positive and negative feedback and consists of four resistors, such as Fig. 2.14(a). The drawback of this configuration is the waste of power consumption. A way to reduce this consumption is by splitting resistor R4 in R4a + R4b 2.14(b) [119, 120, 121]. This version is the improved Howland current source. Considering that the balance condition of the resistors is satisfied, Eq. 2.81,

$$\frac{R_3}{R_4} = \frac{R_1}{R_{2A} + R_{2B}} \tag{2.81}$$

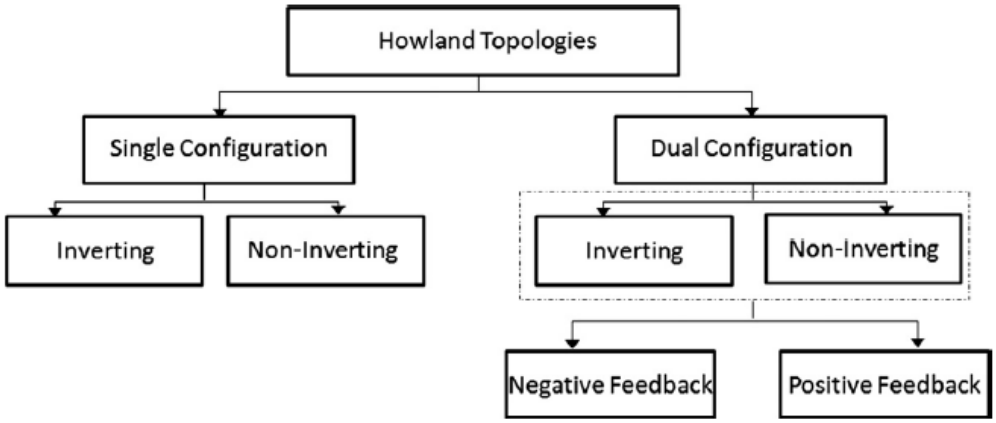

Figure 2.13: Howland circuit topologies [119].

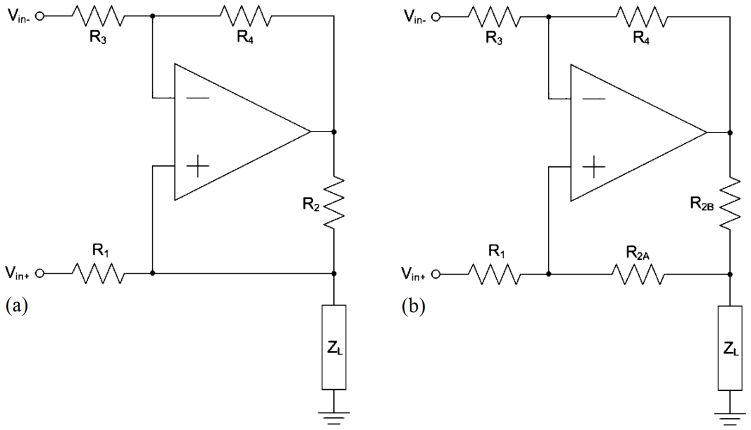

Figure 2.14: (a) Basic Howland circuit and (b) improved Howland circuit. Adapted from [120].

the transcondutance G_m converts the input voltage, V_{in}, into a bidirecional constant current, I_{out}, independent of the load Z_L. The positive and negative transconductances, G_m^+ and G_m^-, are given in Eq. 2.83 and Eq. 2.83.

$$G_m^+ = \frac{I_{out}}{V_{in}+} = \frac{R_{2A} + R_{2B}}{R_1 R_{2B}} \tag{2.82}$$

$$G_m^- = \frac{I_{out}}{V_{in}-} = -\frac{R_4}{R_3 R_{2B}} \tag{2.83}$$

This circuit is stable at low frequencies. At higher frequencies, a pole must be add in order to stabilize the circuit. Thus, small capacitor are connected in parallel with the feedback resistors. Additionally, this VCCS allows the transconductance to be set by a single resistor, considering the conditions are met, Eq. 2.84.

$$if\ R_3 = R_4 \rightarrow G_m^- = -\frac{1}{R_{2B}} \tag{2.84}$$

Tucker et al. [120] perform a comprehensive study of the output accuracy of the improved Howland current source. The model consists of evaluating the non-idealities of the circuit that shunts the current from the load. The linear model is shown in Fig. 2.15. The output impedance is

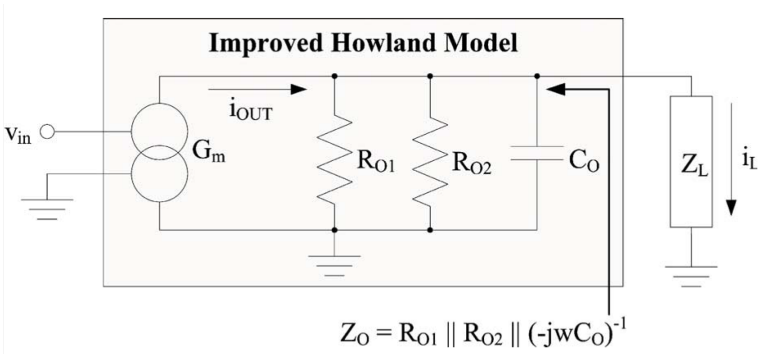

Figure 2.15: Linear model of the improved Howland current source [120].

the parallel combination of R_{o1}, R_{o2}, C_o to ground, forming a current divider with the load. There are inaccuracy caused by these three sources: R_{o1}, the imbalance in the positive and negative feedback paths; R_{o2}, the amplifier finite open-loop gain; C_o, the amplifier finite bandwidth.

Mahnam et al. [122] extends the analysis and provides a comprehensive study to design other topologies of Howland current source, such as the Howland current source with a buffered feedback path. The topology of this VCCS is shown in Fig. 2.16. It presents an improved output impedance compared to the basic and improved Howland current source.

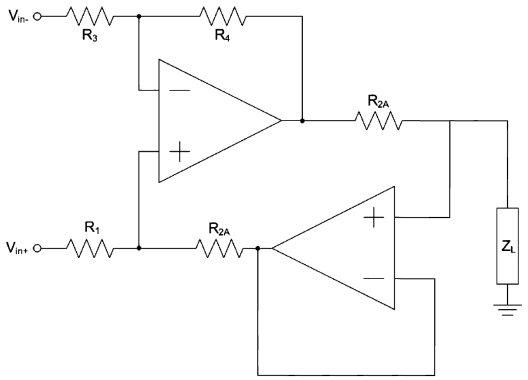

Figure 2.16: Feedback buffered Howland current source. Adapted from [120].

Dual Configuration A topology that is frequently utilized by researchers is studied by Bertemes-Filho et al. [123]. The mirrored modified Howland current source, shown in Fig. 2.17(a), consists of two single-ended modified Howland current source, which uses two signals

with a phase shift of 180 degrees from each other. It shares a unique reference and this configuration significantly reduces the common-mode voltage on the output. The output impedance, as it is shown in the equivalent Norton circuit in Fig. 2.17(b), is increased since the total is the sum of the two single-ended versions.

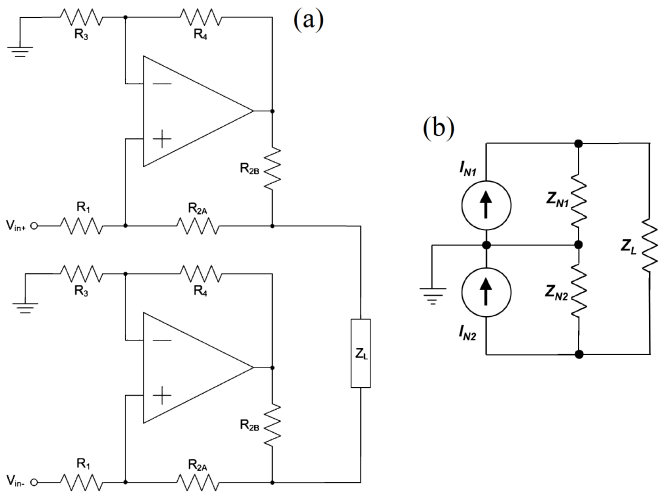

Figure 2.17: (a) Mirrored modified Howland current source and (b) Norton equivalent circuit. Adapted from [123] and [120].

Negative Impedance Converter It is important, especially when developing multi-frequencies systems, to limit the stray capacitance in the circuit. To this matter, a Negative Impedance Converter (NIC) can be designed to synthesize a negative capacitance as the input impedance [124]. The circuit is shown in Fig. 2.18. The theory of such a device is described in [125]. For op-amps, the input impedance of the circuit is given by Eq. 2.85 [126].

$$\frac{V_i}{I_i} = -Z_f \frac{Z_2}{Z_1} = -C_f \frac{R_2}{R_1} \tag{2.85}$$

However, the system suffers from stability and, according to Brownlie [127], if the input impedance is approximated to the element that is necessary to compensate. Hoskins [128] demonstrates using a special case that if the negative input impedance is greater than the element that needs to be compensated, the system becomes unstable as poles on the right part of the complex plane become present. Jimenez-Martin et al. [129] conclude that the method suitable to predict the NIC stability is the use of the Nyquist theorem applied to the Normalized Determinant Function. Segovia-Vargas et al. [130] prove that the design of the NIC can be done by the Normalized Determinant Function, although the accurate linear model of the active devices is required.

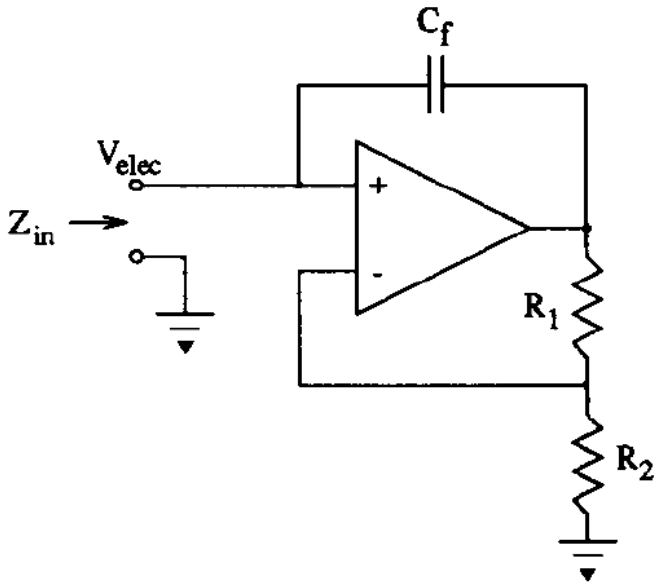

Figure 2.18: Negative impedance converter. Adapted from [124].

Generalized Impedance Converter A VCCS contains both output resistance and output capacitance that limits the accuracy of the output current. A way to deal with these characteristics is considering to include a generalized impedance converter (GIC) into the VCCS circuit. Ross et al. [131] designed a Howland current source with a GIC in parallel.

The GIC is a circuit that synthesizes inductances to cancel the parasitic capacitances in the VCCS. It consists of two amplifiers and a chain of five passive elements, whose types determine the impedance of the element to be synthesized. To produce an inductance, the topology is given in Fig. 2.19(a). The inductance is calculated by the Eq. 2.86.

$$L_G = \frac{R_1 R_3 R_5 C_4}{R_2} \tag{2.86}$$

Considering a ideal case, the capacitance is completely cancelled. This case only occurs when the imaginary part of the parallel impedance is zero. This value is given by Eq. 2.88.

$$Im(Z_{eq}) = \frac{\omega R L_G (R - \omega^2 R L_G C)}{(R - \omega^2 R L_G C)^2 + (\omega L_G)^2} \tag{2.87}$$

where ω is the angular frequency. Choosing the $Im(Z_{eq}) = 0$, the resonance condition is, Eq. 2.89

$$\omega = \frac{1}{\sqrt{L_G C}} \tag{2.88}$$

The equivalent circuit of the current source is given in Fig. 2.19(b). To obtain the maximum output resistance, the equivalent resistance of the circuit must be adjusted to induce the negative

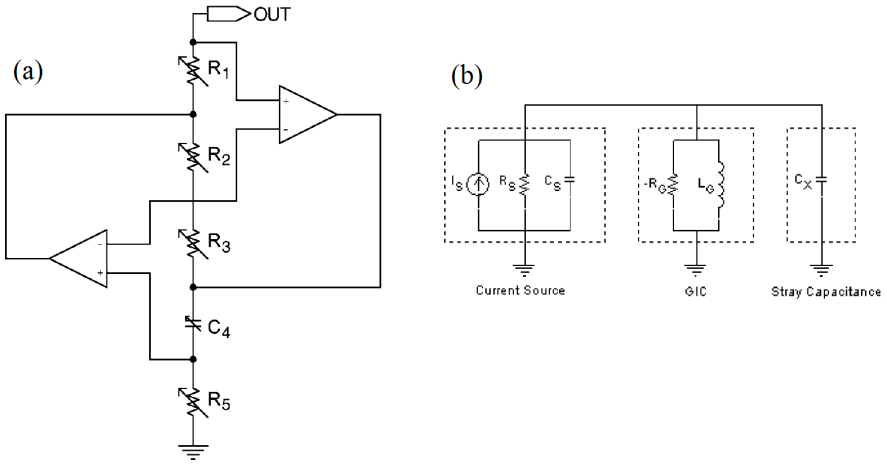

Figure 2.19: (a) Topology of the generalized impedance converter to synthesize the inductance, (b) Model of the current source with GIC and stray capacitance. Adapted from [131].

resistance from the GIC to cancel the output resistance and reaches infinity, Eq. 2.89.

$$R_{eq} = \frac{R_S(-R_G)}{R_S + (-R_G)} \tag{2.89}$$

The inductance to be adjusted, cancelling the stray capacitance and the output capacitance of the current, is given by Eq. 2.90

$$L_G = \frac{1}{\omega^2(C_s + C_x)} \tag{2.90}$$

Calibration Scheme of the Impedance Converters A method to measure the input impedance of the current source is given by Cook et al. [124] which is still in use [132, 133, 111]. It is shown in Fig. 2.20 the circuit for such device.

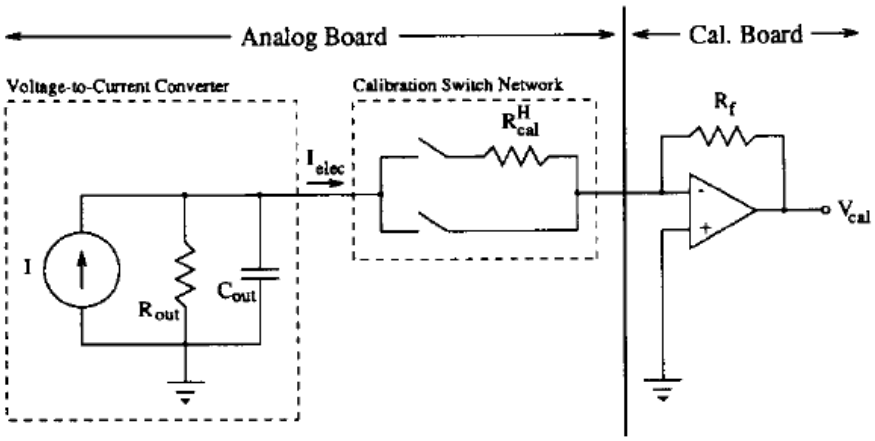

Figure 2.20: Measurement of the input impedance of the current source. [124].

It is defined by the way the current differs by two different known loads, R_{cal}^{H} and R_{cal}^{L}. For simplicity, R_{cal}^{L} = 0. The voltages measured are defined in Eq. 2.91-2.94.

$$V_{cal}^{H} = V_{r}^{H} + jV_{q}^{H} = V_{cal}|_{R_{load}=R_{cal}^{H}} \tag{2.91}$$

$$V_{cal}^{L} = V_{r}^{L} + jV_{q}^{L} = V_{cal}|_{R_{load}=R_{cal}^{L}} \tag{2.92}$$

Therefore,

$$C_{out} = \frac{V_{q}^{L}V_{r}^{H} + V_{r}^{L}V_{q}^{H}}{[(V_{q}^{H})^2 + (V_{r}^{H})^2]\omega R_{cal}^{H}} \tag{2.93}$$

$$R_{out} = \frac{(V_{q}^{H})^2 + (V_{r}^{H})^2}{V_{q}^{L}V_{q}^{H} + V_{r}^{L}V_{r}^{H} - (V_{r}^{H})^2 - (V_{q}^{H})^2} R_{cal}^{H} \tag{2.94}$$

It is noticed that $C_{out} \longrightarrow 0$ and $R_{out} \longrightarrow \infty$ when $V_{r}^{H} = V_{r}^{L}$ and $V_{q}^{H} = V_{q}^{L}$. By arranging digipots in the converter circuits, it is possible to calibrate the output impedance of the current source utilizing an automatic scheme. However the only source of capacitance that is measured is from the current source and a complete mapping of these sources is not possible.

2.1.7.4 Demodulation

To estimate the conductivities from the domain in question, it is necessary information about the voltages on the boundaries. From the output of the instrumentation amplifier, the signal is a sinewave and the information about the amplitude and phase must be demodulated and transferred to the computer. There are several techniques to extract such information. Ruppert et al. [134] provides an extensive review of demodulation techniques that can be extended to the EIT data acquisition system.

RMS-to-DC Converter A practical method to obtain the root mean square (RMS) value of a sinusoidal wave, thus the amplitude, is the RMS-to-DC Conversion method. The operation of the circuit is to compute the RMS, Eq. 2.95, which is a fundamental measurement of the magnitude of an AC signal.

$$V_{RMS} = \sqrt{\frac{1}{T}\int_{0}^{T} V^2(t)\,dt} \tag{2.95}$$

It is easy to show that the RMS voltage value of a sinusoidal wave is Eq. 2.96:

$$V_{RMS} = \frac{V_P}{\sqrt{2}} \tag{2.96}$$

Two ways to obtain this analog value is by the Direct or Explicit Computation and the Indirect or Implicit Computation. Explicit computation uses the most straight-forward way of calculating the RMS value [135]. By performing the operations of squaring, averaging, and square-rooting the signal, it is possible to acquire the signal. The circuit basic idea is shown in Fig. 2.21. Due to

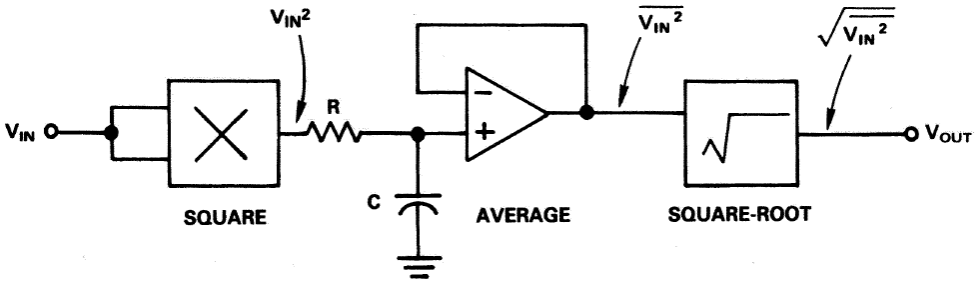

Figure 2.21: The circuit for an explicit computation RMS to DC converter [135].

the increased dynamic range that the process of squaring may inflict (a signal of 10 mV to 1 V, with a dynamic range of 100 to 1, would have a signal of 1mV to 10 V, the dynamic range would be 10000), the method is not frequently employed to perform the measurement. Therefore, the application limited to ranges of 10:1 dynamic range.

The implicit computation is an improved method that uses feedback to perform the square root implicitly, solving Eq. 2.97, as shown in Fig. 2.22.

$$V_{RMS} = \frac{Avg(V(t))^2}{V_{RMS}} \tag{2.97}$$

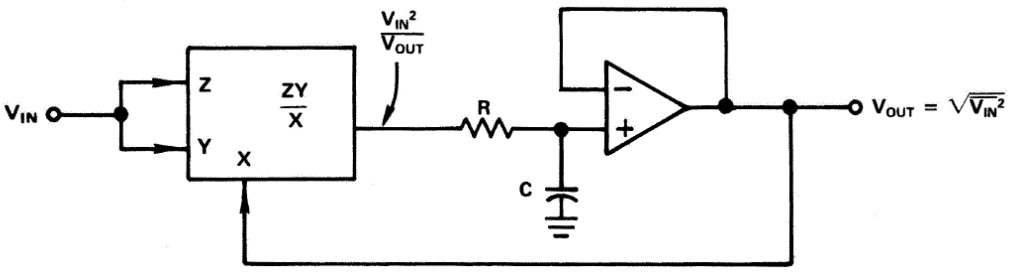

Figure 2.22: The circuit for an implicit computation RMS to DC converter [135].

The simple act of dividing the output of the square by the average of the output turns the application linear, which greatly increases the dynamic range of the device.

Phase-Sensitive Detector Also known as lock-in amplification, the phase-sensitive detector is a technique for measuring the amplitude and phase of a signal when it is affected by Gaussian

noise. Although it can be implemented with an analog circuit, the output is dependent on a low-pass filter that reduces the overall precision of the system [1].

The digital application is described by Smith et al. [136] and it is summarized in Fig. 2.23. Con-

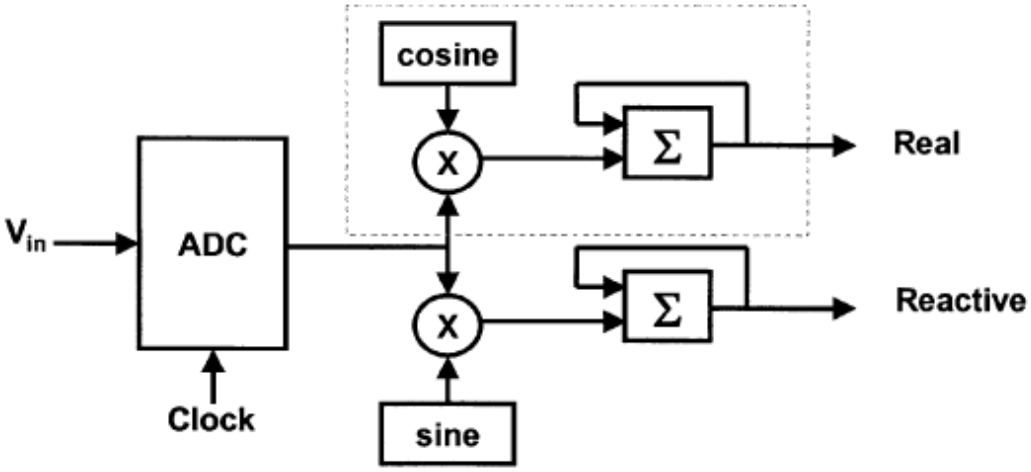

Figure 2.23: Digital phase-sensitive detector [1].

sider that the analogue input signal $V_{in}(t)$ is a sinewave of frequency f_c, amplitude A, truncated at $t = 0$ and at $t = T_m$, the measurement time, and phase relative to a reference Φ_{sig}:

$$V_{in} = \begin{cases} \tilde{A}_{sig} sin(2\pi f_c t + \Phi_{sig}) & if\ 0 \leq t < T_m \\ 0 & otherwise \end{cases} \tag{2.98}$$

where T_m is an multiple of $1/f_c$, consisting in an exact number of cycles of the sinewave. The input signal is digitized by the ADC to form a sampled data sequence $v_{in}(n_s)$ from V_{in}, sampling at frequency f_s multiple of f_c:

$$v_{in}(n_s) = \tilde{A}_{sig} sin\left(\frac{2\pi f_c n_s}{f_s} + \Phi_{sig}\right) \quad n_s = 1, 2, ..., N_s \tag{2.99}$$

where $N_s = T_m f_s$ is the total number of samples.

The reference signal, $h(n_s)$, is a sine waveform of the same frequency of the input signal v_{in}:

$$h(n_s) = \tilde{A}_{ref} cos\left(\frac{2\pi f_c n_s}{f_s} + \Phi_{ref}\right) \quad n_s = 1, 2, ..., N_s \tag{2.100}$$

The sum of the products at the end of the measurement, the in-phase output I, is given by [136, 137, 138]:

$$IP = \sum_{n_s=1}^{N_s} v_{in}(n_s) h(n_s) \tag{2.101}$$

Assuring that T_m is a multiple of $1/f_c$ and $f_s > 2f_c$, Eq. 2.101 is written as Eq. 2.102 [136, 137, 138]:

$$IP = \frac{1}{2}\tilde{A}_{sig}\tilde{A}_{ref}N_s cos(\Phi_{sig} - \Phi_{ref}) \tag{2.102}$$

Consider also $g(n_s)$, which is phase shifted by 90^o:

$$g(n_s) = \tilde{A}_{ref} sin\left(\frac{2\pi f_c n_s}{f_s} + \Phi_{ref}\right) \quad n_s = 1, 2, ..., N_s \tag{2.103}$$

By taking the second sum of products, with v_{in} and $g(n_s)$, the quadrature output QD:

$$QD = \sum_{n_s=1}^{N_s} v_{in}(n_s)g(n_s) \tag{2.104}$$

In the same form, Eq. 2.104 it can be written:

$$QD = \frac{1}{2}\tilde{A}_{sig}\tilde{A}_{ref}N_s sin(\Phi_{sig} - \Phi_{ref}) \tag{2.105}$$

Therefore, from Eqs. 2.101,2.102, 2.104, and 2.105, the amplitude is given by Eq. 2.106.

$$\tilde{A}_{sig}\tilde{A}_{ref} = \frac{2}{N_s}\sqrt{IP^2 + QD^2} \tag{2.106}$$

and the phase is written by Eq. 2.107.

$$\Phi_{sig} - \Phi_{ref} = tan^{-1}\left(\frac{-QD}{IP}\right) \tag{2.107}$$

The reference signals can be obtained by a lookup table and it is common to choose $\tilde{A}_{ref} = 1$ and $\Phi_{ref} = 0$.

2.1.8 Summary

From the literature survey, some conclusions can be drawn that lead to the development of this work.

1. Several works have been done to design the EIT DAQ system, from complex to simple designs, but there is no comprehensive methodology to guide the choices in the process.

2. The measurement of the output impedance necessitates a specific circuit and the measurement of the parasitic capacitances can only be performed to the current source.

3. The recursive algorithms to reconstruct contours fails to reconstruct in the initial states and when there is a fast-moving inclusion.

References

[1] D.S. Holder. *Electrical Impedance Tomography: Methods, History and Applications*. Series in Medical Physics and Biomedical Engineering. CRC Press, 2004. ISBN 9781420034462.

[2] M. Khalighi, B. Vosoughi Vahdat, M. Mortazavi, W. Hy, and M. Soleimani. Practical design of low-cost instrumentation for industrial electrical impedance tomography (eit). In *2012 IEEE International Instrumentation and Measurement Technology Conference Proceedings*, pages 1259–1263, 2012. doi: 10.1109/I2MTC.2012.6229173.

[3] Mi Wang, Yixin Ma, N. Holliday, Yunfeng Dai, R. A. Williams, and G. Lucas. A high-performance EIT system. *IEEE Sensors Journal*, 5(2):289–299, April 2005. ISSN 1530-437X. doi: 10.1109/JSEN.2005.843904.

[4] A. J. Wilkinson, E. W. Randall, J. J. Cilliers, D. R. Durrett, T. Naidoo, and T. Long. A 1000-measurement frames/second ERT data capture system with real-time visualization. *IEEE Sensors Journal*, 5(2):300–307, April 2005. ISSN 1530-437X. doi: 10.1109/JSEN.2004.842445.

[5] Bo Gong, Sabine Krueger-Ziolek, Knut Moeller, Benjamin Schullcke, and Zhanqi Zhao. Electrical impedance tomography: functional lung imaging on its way to clinical practice? *Expert Review of Respiratory Medicine*, 9(6):721–737, 2015. doi: 10.1586/17476348.2015.1103650.

[6] Liangdong Zhou, Bastian Harrach, and Jin Keun Seo. Monotonicity-based electrical impedance tomography for lung imaging. *Inverse Problems*, 34(4), 2018. doi: 10.1088/1361-6420/aaaf84.

[7] Jeffrey Dmytrowich, Tanya Holt, Karen Schmid, and Gregory Hansen. Mechanical ventilation guided by electrical impedance tomography in pediatric acute respiratory distress

syndrome. *Journal of Clinical Monitoring and Computing*, 32(3):503–507, 2018. doi: 10.1007/s10877-017-0048-5.

[8] Lin Yang, Heng Li, Junjie Ding, Weichen Li, Xiuzhen Dong, Zhihong Wen, and Xuetao Shi. Optimal combination of electrodes and conductive gels for brain electrical impedance tomography. *Journal of Clinical Monitoring and Computing*, 17(186):503–507, 2018. doi: 10.1186/s12938-018-0617-y.

[9] Kirill Y. Aristovich, Brett C. Packham, Hwan Koo, Gustavo Sato dos Santos, Andy McEvoy, and David S. Holder. Imaging fast electrical activity in the brain with electrical impedance tomography. *NeuroImage*, 124:204 – 213, 2016. ISSN 1053-8119. doi: https://doi.org/10.1016/j.neuroimage.2015.08.071.

[10] Sana Hannan, Mayo Faulkner, Kirill Aristovich, James Avery, Matthew Walker, and David Holder. Imaging fast electrical activity in the brain during ictal epileptiform discharges with electrical impedance tomography. *NeuroImage: Clinical*, 20:674 – 684, 2018. ISSN 2213-1582. doi: https://doi.org/10.1016/j.nicl.2018.09.004.

[11] Mohadeseh Sharifi and Brent Young. Electrical resistance tomography (ert) applications to chemical engineering. *Chemical Engineering Research and Design*, 91(9):1625 – 1645, 2013. ISSN 0263-8762. doi: https://doi.org/10.1016/j.cherd.2013.05.026.

[12] A. Parvareh, M. Rahimi, A. Alizadehdakhel, and A.A. Alsairafi. CFD and ERT investigations on two-phase flow regimes in vertical and horizontal tubes. *International Communications in Heat and Mass Transfer*, 37(3):304 – 311, 2010. ISSN 0735-1933. doi: https://doi.org/10.1016/j.icheatmasstransfer.2009.11.001.

[13] Nicholas P Ramskill and Mi Wang. Boolean logic analysis for flow regime recognition of gas–liquid horizontal flow. *Measurement Science and Technology*, 22(10):104016, 2011. doi: 10.1088/0957-0233/22/10/104016.

[14] Claudio Olerni, Jiabin Jia, and Mi Wang. Measurement of air distribution and void fraction of an upwards air–water flow using electrical resistance tomography and a wire-mesh sensor. *Measurement Science and Technology*, 24(3):035403, feb 2013. doi: 10.1088/0957-0233/24/3/035403.

[15] Jiabin Jia, Mi Wang, and Yousef Faraj. Evaluation of EIT systems and algorithms for handling full void fraction range in two-phase flow measurement. *Measurement Science and Technology*, 26(1):015305, dec 2014. doi: 10.1088/0957-0233/26/1/015305.

[16] Zhenzhen Meng, Zhiyao Huang, Baoliang Wang, Haifeng Ji, Haiqing Li, and Yong Yan. AirâĂŞwater two-phase flow measurement using a Venturi meter and an electrical resistance tomography sensor. *Flow Measurement and Instrumentation*, 21(3):268 – 276, 2010. ISSN 0955-5986. doi: https://doi.org/10.1016/j.flowmeasinst.2010.02.006.

[17] Mi Wang, Jiabin Jia, Yousef Faraj, Qiang Wang, Cheng gang Xie, Gary Oddie, Ken Primrose, and Changhua Qiu. A new visualisation and measurement technology for water continuous multiphase flows. *Flow Measurement and Instrumentation*, 46:204 – 212, 2015. ISSN 0955-5986. doi: https://doi.org/10.1016/j.flowmeasinst.2015.06.022.

[18] F. Dong, Y. Xu, L. Hua, and H. Wang. Two methods for measurement of gas-liquid flows in vertical upward pipe using dual-plane ert system. *IEEE Transactions on Instrumentation and Measurement*, 55(5):1576–1586, 2006.

[19] Mi Wang. *Industrial Tomography: Systems and Applications*. Woodhead Publishing, Limited, 1st edition, 2015.

[20] B H Brown and A D Seagar. The Sheffield data collection system. *Clinical Physics and Physiological Measurement*, 8(4A):91–97, nov 1987. doi: 10.1088/0143-0815/8/4a/012.

[21] Fraser Dickin and Mi Wang. Electrical resistance tomography for process applications. *Measurement Science and Technology*, 7(3):247–260, mar 1996. doi: 10.1088/0957-0233/7/3/005.

[22] Breckon W R and Pidcock. *Some mathematical aspects of EIT Mathematics and Computer Science in Medical Imaging*, chapter -. Berlin: Springer, 1988.

[23] P. Hua, J. G. Webster, and W. J. Tompkins. Effect of the measurement method on noise handling and image quality of eit imaging. In *Proceedings of the Annual International Conference of the IEEE Engineering in Medicine and Biology Society*, pages 1429–1430, 1987.

[24] Suzanna Ridzuan Aw, Ruzairi Abdul Rahim, Mohd Hafiz Fazalul Rahiman, Fazlul Rahman Mohd Yunus, and Chiew Loon Goh. Electrical resistance tomography: A review of the application of conducting vessel walls. *Powder Technology*, 254:256 – 264, 2014.

[25] D G Gisser, D Isaacson, and J C Newell. Current topics in impedance imaging. *Clinical Physics and Physiological Measurement*, 8(4A):39–46, 1987.

[26] D. Isaacson. Distinguishability of conductivities by electric current computed tomography. *IEEE Transactions on Medical Imaging*, 5(2):91–95, 1986.

[27] M. Cheney, D. Isaacson, J. C. Newell, S. Simske, and J. Goble. NOSER: An algorithm for solving the inverse conductivity problem. *International Journal of Imaging Systems and Technology*, 2(2):66–75, 1990. doi: 10.1002/ima.1850020203.

[28] E. Demidenko, A. Hartov, N. Soni, and K. D. Paulsen. On optimal current patterns for electrical impedance tomography. *IEEE Transactions on Biomedical Engineering*, 52(2): 238–248, 2005.

[29] Erkki Somersalo, Margaret Cheney, and David Isaacson. Existence and uniqueness for electrode models for electric current computed tomography. *SIAM Journal on Applied Mathematics*, 52:1023–1040, 1992. doi: https://doi.org/10.1137/0152060.

[30] Nicholas Polydorides. *Image Reconstruction Algorithms for Soft-Field Tomography*. PhD thesis, University of Manchester Institute of Science and Technology, 2002.

[31] Päivi Vauhkonen. *Image Reconstruction in Three-Dimensional Electrical Impedance Tomography*. PhD thesis, University of Kuopio, 2004.

[32] Kuo-Sheng Cheng, D. Isaacson, J. C. Newell, and D. G. Gisser. Electrode models for electric current computed tomography. *IEEE Transactions on Biomedical Engineering*, 36(9):918–924, 1989. doi: 10.1109/10.35300.

[33] R. Giguère, L. Fradette, D. Mignon, and P.A. Tanguy. ERT algorithms for quantitative concentration measurement of multiphase flows. *Chemical Engineering Journal*, 141(1): 305 – 317, 2008. ISSN 1385-8947. doi: https://doi.org/10.1016/j.cej.2008.01.011.

[34] Aku Seppänen, Lasse Heikkinen, Tuomo Savolainen, Arto Voutilainen, Erkki Somersalo, and Jari P. '. An experimental evaluation of state estimation with fluid dynamical models in process tomography. *Chemical Engineering Journal*, 127(1):23 – 30, 2007. ISSN 1385-8947. doi: https://doi.org/10.1016/j.cej.2006.09.025.

[35] P.J. Vauhkonen, Marko Vauhkonen, and Jari Kaipio. Fixed-lag smoothing and state estimation in dynamic electrical impedance tomography. *International Journal for Numerical Methods in Engineering*, 50:2195 – 2209, 03 2001. doi: 10.1002/nme.120.

[36] Robert P Patterson and Jie Zhang. Evaluation of an EIT reconstruction algorithm using finite difference human thorax models as phantoms. *Physiological Measurement*, 24(2): 467–475, 2003. doi: 10.1088/0967-3334/24/2/357.

[37] Guoya Dong, Richard H Bayford, Shangkai Gao, Yoshifuru Saito, Rebecca Yerworth, David Holder, and Weili Yan. The application of the generalized vector sample pattern matching method for EIT image reconstruction. *Physiological Measurement*, 24(2):449–466, 2003. doi: 10.1088/0967-3334/24/2/356.

[38] Bradley Michael Graham. *Enhancements in Electrical Impedance Tomography (EIT) Image Reconstruction for 3D Lung Imaging*. PhD thesis, University of Ottawa, 2007.

[39] T.J.R. Hughes. *The Finite Element Method: Linear Static and Dynamic Finite Element Analysis.* Series in Medical Physics and Biomedical Engineering. Prentice-Hall, 2004. ISBN 9781420034462.

[40] William R B Lionheart. EIT reconstruction algorithms: pitfalls, challenges and recent developments. *Physiological Measurement*, 25(1):125–142, feb 2004. doi: 10.1088/0967-3334/25/1/021.

[41] Ramani Duraiswami, Georges L. Chahine, and Kausik Sarkar. Boundary element techniques for efficient 2-D and 3-D electrical impedance tomography. *Chemical Engineering Science*, 52(13):2185 – 2196, 1997. doi: https://doi.org/10.1016/S0009-2509(97)00044-4.

[42] Robert G. Aykroyd and Brain A. Cattle. A flexible statistical and efficient computational approach to object location applied to electrical tomography. *Statistics and Computing*, 16(4):363–375, 2006. ISSN 1573-1375. doi: 10.1007/s11222-006-9619-x.

[43] P. Ghaderi Daneshmand and R. Jafari. A 3D hybrid BE-FE solution to the forward problem of electrical impedance tomography. *Engineering Analysis with Boundary Elements*, 37(4):757 – 764, 2013. ISSN 0955-7997. doi: https://doi.org/10.1016/j.enganabound.2013.01.016.

[44] A. Karageorghis and D. Lesnic. The method of fundamental solutions for the inverse conductivity problem. *Inverse Problems in Science and Engineering*, 18(4):567–583, 2010. doi: 10.1080/17415971003675019.

[45] T.E. Dyhoum, D. Lesnic, and R.G. Aykroyd. Solving the complete-electrode direct model of ert using the boundary element method and the method of fundamental solutions. *Electronic Journal of Boundary Elements*, 12(3), 2014.

[46] Marjan Asadzadeh Heravi, Liviu Marin, and Cristiana Sebu. The method of fundamental solutions for complex electrical impedance tomography. *Engineering Analysis with*

Boundary Elements, 46:126 – 139, 2014. doi: https://doi.org/10.1016/j.enganabound.2014.04.022.

[47] M. Vauhkonen, D. Vadasz, P. A. Karjalainen, E. Somersalo, and J. P. Kaipio. Tikhonov regularization and prior information in electrical impedance tomography. *IEEE Transactions on Medical Imaging*, 17(2):285–293, April 1998. ISSN 0278-0062. doi: 10.1109/42.700740.

[48] D C Barber and B H Brown. Applied potential tomography. *Journal of Physics E: Scientific Instruments*, 17(9):723–733, 1984.

[49] Fadil Santosa and Michael Vogelius. A backprojection algorithm for electrical impedance imaging. *SIAM Journal on Applied Mathematics*, 50(1):216âĂŞ243, 1990.

[50] C J Kotre. A sensitivity coefficient method for the reconstruction of electrical impedance tomograms. *Clinical Physics and Physiological Measurement*, 10(3):275–281, 1989. doi: 10.1088/0143-0815/10/3/008.

[51] Benyuan Sun, Shihong Yue, Ziqiang Cui, and Huaxiang Wang. A new linear back projection algorithm to electrical tomography based on measuring data decomposition. *Measurement Science and Technology*, 26(12):125402, 2015.

[52] T. J. Yorkey, J. G. Webster, and W. J. Tompkins. Comparing reconstruction algorithms for electrical impedance tomography. *IEEE Transactions on Biomedical Engineering*, BME-34(11):843–852, 1987.

[53] W Q Yang, D M Spink, T A York, and H McCann. An image-reconstruction algorithm based on landweber's iteration method for electrical-capacitance tomography. *Measurement Science and Technology*, 10(11):1065–1069, 1999. doi: 10.1088/0957-0233/10/11/315.

[54] Huaxiang Wang, Chao Wang, and Wuliang Yin. A pre-iteration method for the inverse problem in electrical impedance tomography. *IEEE Transactions on Instrumentation and Measurement*, 53(4):1093–1096, 2004.

[55] W Q Yang and Lihui Peng. Image reconstruction algorithms for electrical capacitance tomography. *Measurement Science and Technology*, 14(1):R1–R13, dec 2002.

[56] Yi Li and Wuqiang Yang. Image reconstruction by nonlinear landweber iteration for complicated distributions. *Measurement Science and Technology*, 19(9):094014, 2008.

[57] M Wang. Inverse solutions for electrical impedance tomography based on conjugate gradients methods. *Measurement Science and Technology*, 13(1):101–117, 2001. doi: 10.1088/0957-0233/13/1/314.

[58] Qi Wang, Huaxiang Wang, Ziqiang Cui, Yanbin Xu, and Chengyi Yang. Fast reconstruction of electrical resistance tomography (ert) images based on the projected cg method. *Flow Measurement and Instrumentation*, 27:37 – 46, 2012.

[59] Jari P. Kaipio, Erkki Somersalo, Pasi A. Karjalainen, and Marko J. Vauhkonen. Recursive estimation of fast-impedance changes in electrical impedance tomography and a related problem. In Randall Locke Barbour, Mark J. Carvlin, and Michael A. Fiddy, editors, *Computational, Experimental, and Numerical Methods for Solving Ill-Posed Inverse Imaging Problems: Medical and Nonmedical Applications*, volume 3171, pages 208 – 216. International Society for Optics and Photonics, SPIE, 1997.

[60] Jari P. Kaipio, Pasi A. Karjalainen, Erkki Somersalo, and Marko Vauhkonen. State estimation in time-varying electrical impedance tomography. *Annals of the New York Academy of Sciences*, 873(1):430–439, 1999.

[61] F. C. Trigo, R. Gonzalez-Lima, and M. B. P. Amato. Electrical impedance tomography using the extended kalman filter. *IEEE Transactions on Biomedical Engineering*, 51(1): 72–81, 2004.

[62] Andy Adler, Tao Dai, and William R B Lionheart. Temporal image reconstruction in electrical impedance tomography. *Physiological Measurement*, 28(7):S1–S11, 2007. doi: 10.1088/0967-3334/28/7/s01.

[63] K.Y. Kim, B.S. Kim, M.C. Kim, and S. Kim. Dynamic inverse obstacle problems with electrical impedance tomography. *Mathematics and Computers in Simulation*, 66(4):399 – 408, 2004.

[64] A Seppänen, M Vauhkonen, P J Vauhkonen, E Somersalo, and J P Kaipio. State estimation with fluid dynamical evolution models in process tomography - an application to impedance tomography. *Inverse Problems*, 17(3):467–483, 2001. doi: 10.1088/0266-5611/17/3/307.

[65] A Seppänen, A Voutilainen, and J P Kaipio. State estimation in process tomography-reconstruction of velocity fields using EIT. *Inverse Problems*, 25(8):085009, 2009.

[66] F. S. Moura, J. C. C. Aya, A. T. Fleury, M. B. P. Amato, and R. G. Lima. Dynamic imaging in electrical impedance tomography of the human chest with online transition matrix identification. *IEEE Transactions on Biomedical Engineering*, 57(2):422–431, 2010.

[67] Simon J. Julier and Jeffrey K. Uhlmann. New extension of the Kalman filter to nonlinear systems. In Ivan Kadar, editor, *Signal Processing, Sensor Fusion, and Target Recognition VI*, volume 3068, pages 182 – 193. International Society for Optics and Photonics, SPIE, 1997. doi: 10.1117/12.280797. URL https://doi.org/10.1117/12.280797.

[68] S. J. Julier and J. K. Uhlmann. Unscented filtering and nonlinear estimation. *Proceedings of the IEEE*, 92(3):401–422, 2004.

[69] E. A. Wan and R. Van Der Merwe. The unscented kalman filter for nonlinear estimation. In *Proceedings of the IEEE 2000 Adaptive Systems for Signal Processing, Communications, and Control Symposium (Cat. No.00EX373)*, pages 153–158, 2000.

[70] Umer Zeeshan Ijaz, Anil Kumar Khambampati, Jeong Seong Lee, Sin Kim, and Kyung Youn Kim. Nonstationary phase boundary estimation in electrical impedance tomography using unscented kalman filter. *Journal of Computational Physics*, 227(15): 7089 – 7112, 2008. ISSN 0021-9991. doi: https://doi.org/10.1016/j.jcp.2007.12.025.

[71] Umer Zeeshan Ijaz, Soon Il Chung, Anil Kumar Khambampati, Kyung Youn Kim, and Sin Kim. Electrical resistance imaging of a time-varying interface in stratified flows using an unscented kalman filter. *Measurement Science and Technology*, 19(6):065501, 2008. doi: 10.1088/0957-0233/19/6/065501.

[72] A. Adler and R. Guardo. Electrical impedance tomography: regularized imaging and contrast detection. *IEEE Transactions on Medical Imaging*, 15(2):170–179, 1996.

[73] A Nissinen, L M Heikkinen, and J P Kaipio. The bayesian approximation error approach for electrical impedance tomography—experimental results. *Measurement Science and Technology*, 19(1):015501, 2007. doi: 10.1088/0957-0233/19/1/015501.

[74] S. Liu, J. Jia, Y. D. Zhang, and Y. Yang. Image reconstruction in electrical impedance tomography based on structure-aware sparse bayesian learning. *IEEE Transactions on Medical Imaging*, 37(9):2090–2102, 2018.

[75] B. Ristic, S. Arulampalam, and N. Gordon. *Beyond the Kalman Filter: Particle Filters for Tracking Applications*. Artech House, 2003. ISBN 9781580538510.

[76] Arnaud Doucet, Nando de Freitas, and Neil Gordon, editors. *Sequential Monte Carlo Methods in Practice*. Springer New York, first edition, 2001.

[77] Zhe Chen. Bayesian filtering: From kalman filters to particle filters, and beyond. *Statistics*, 182, 01 2003. doi: 10.1080/02331880309257.

[78] M. S. Arulampalam, S. Maskell, N. Gordon, and T. Clapp. A tutorial on particle filters for online nonlinear/non-gaussian bayesian tracking. *IEEE Transactions on Signal Processing*, 50(2):174–188, 2002. doi: 10.1109/78.978374.

[79] N. J. Gordon, D. J. Salmond, and A. F. M. Smith. Novel approach to nonlinear/non-gaussian bayesian state estimation. *IEE Proceedings F - Radar and Signal Processing*, 140(2):107–113, 1993. doi: 10.1049/ip-f-2.1993.0015.

[80] D. Xiaolong, X. Jianying, and G. Weizhong. Bayesian target tracking based on particle filter. *Journal of Systems Engineering and Electronics*, 16(3):545–549, 2005.

[81] Tiancheng Li, Shudong Sun, Tariq Pervez Sattar, and Juan Manuel Corchado. Fight sample degeneracy and impoverishment in particle filters: A review of intelligent approaches. *Expert Systems with Applications*, 41(8):3944 – 3954, 2014. ISSN 0957-4174. doi: https://doi.org/10.1016/j.eswa.2013.12.031.

[82] P. C. P. M. Pardal, H. K. Kuga, and R. V. de Moraes. The particle filter sample impoverishment problem in the orbit determination application. *Mathematical Problems in Engineering*, 2015, 2015.

[83] F. Gustafsson, F. Gunnarsson, N. Bergman, U. Forssell, J. Jansson, R. Karlsson, and P. . Nordlund. Particle filters for positioning, navigation, and tracking. *IEEE Transactions on Signal Processing*, 50(2):425–437, 2002.

[84] Michael K. Pitt and Neil Shephard. *Auxiliary Variable Based Particle Filters*, pages 273–293. Springer New York, New York, NY, 2001.

[85] Li Liang-qun, Ji Hong-bing, and Luo Jun-hui. The iterated extended kalman particle filter. In *IEEE International Symposium on Communications and Information Technology, 2005. ISCIT 2005.*, volume 2, pages 1213–1216, 2005.

[86] Yong Rui and Yunqiang Chen. Better proposal distributions: object tracking using unscented particle filter. In *Proceedings of the 2001 IEEE Computer Society Conference on Computer Vision and Pattern Recognition. CVPR 2001*, volume 2, pages II–II, 2001.

[87] Kiyoshi Nishiyama. Fast and effective generation of the proposal distribution for particle filters. *Signal Processing*, 85(12):2412 – 2417, 2005. doi: https://doi.org/10.1016/j.sigpro.2005.07.030.

[88] L. Fu, Q. Fei, S. Guangming, and Z. Li. Optimization-based particle filter for state and parameter estimation. *Journal of Systems Engineering and Electronics*, 20(3):479–484, 2009.

[89] D Watzenig, M Brandner, and G Steiner. A particle filter approach for tomographic imaging based on different state-space representations. *Measurement Science and Technology*, 18(1):30–40, 2006. doi: 10.1088/0957-0233/18/1/004.

[90] F. Daum and J. Huang. Curse of dimensionality and particle filters. In *2003 IEEE Aerospace Conference Proceedings*, volume 4, pages 1979–1993, 2003. doi: 10.1109/AERO.2003.1235126.

[91] Jingwen Wang and Xu Wang. Application of particle filtering algorithm in image reconstruction of EMT. *Measurement Science and Technology*, 26(7):075303, 2015.

[92] P. Hua, E. J. Woo, J. G. Webster, and W. J. Tompkins. Iterative reconstruction methods using regularization and optimal current patterns in electrical impedance tomography. *IEEE Transactions on Medical Imaging*, 10(4):621–628, 1991.

[93] McLeod C N Borsic A and Lionheart W R B. Total variation regularisation in eit reconstruction. In *2nd World Congress on Industrial Process Tomography*, pages 433–441, 2001.

[94] A. Borsic, B. M. Graham, A. Adler, and W. R. B. Lionheart. In vivo impedance imaging with total variation regularization. *IEEE Transactions on Medical Imaging*, 29(1):44–54, 2010.

[95] A. Borsic, W. R. B. Lionheart, and C. N. McLeod. Generation of anisotropic-smoothness regularization filters for eit. *IEEE Transactions on Medical Imaging*, 21(6):579–587, 2002. doi: 10.1109/TMI.2002.800611.

[96] Jari P Kaipio, Ville Kolehmainen, Erkki Somersalo, and Marko Vauhkonen. Statistical inversion and monte carlo sampling methods in electrical impedance tomography. *Inverse Problems*, 16(5):1487–1522, 2000. doi: 10.1088/0266-5611/16/5/321.

[97] V Kolehmainen, M Vauhkonen, P A Karjalainen, and J P Kaipio. Assessment of errors in static electrical impedance tomography with adjacent and trigonometric current patterns. *Physiological Measurement*, 18(4):289–303, 1997. doi: 10.1088/0967-3334/18/4/003.

[98] Bong Seok Kim, Anil Kumar Khambampati, Yoon Jeong Hong, Sin Kim, and Kyung Youn Kim. Multiphase flow imaging using an adaptive multi-threshold technique in electrical resistance tomography. *Flow Measurement and Instrumentation*, 31:25 – 34, 2013. ISSN 0955-5986. doi: https://doi.org/10.1016/j.flowmeasinst.2012.11.003.

[99] B M Graham and A Adler. Objective selection of hyperparameter for EIT. *Physiological Measurement*, 27(5):S65–S79, 2006.

[100] Per Christian Hansen. Analysis of discrete ill-posed problems by means of the l-curve. *SIAM Rev.*, 34(4):561–580, 1992.

[101] Nick Polydorides and William R B Lionheart. A matlab toolkit for three-dimensional electrical impedance tomography: a contribution to the electrical impedance and diffuse optical reconstruction software project. *Measurement Science and Technology*, 13(12): 1871–1883, 2002.

[102] Y. Z. Ider, N. G. Gencer, E. Atalar, and H. Tosun. Electrical impedance tomography of translationally uniform cylindrical objects with general cross-sectional boundaries. *IEEE Transactions on Medical Imaging*, 9(1):49–59, 1990.

[103] Yixin Ma, Hao Wang, Ling-An Xu, and Changzhen Jiang. Simulation study of the electrode array used in an ert system. *Chemical Engineering Science*, 52(13):2197 – 2203, 1997. ISSN 0009-2509. doi: https://doi.org/10.1016/S0009-2509(97)00045-6.

[104] E Fransolet, M Crine, G L'Homme, D Toye, and P Marchot. Electrical resistance tomography sensor simulations: comparison with experiments. *Measurement Science and Technology*, 13(8):1239–1247, jul 2002. doi: 10.1088/0957-0233/13/8/311.

[105] Y.C. Wu, W.F. Koch, and Kenneth Pratt. Proposed new electrolytic conductivity primary standards for kcl solutions. *Journal of Research of the National Institute of Standards and Technology*, 96:191, 1991.

[106] A J Wilson, P Milnes, A R Waterworth, R H Smallwood, and B H Brown. Mk3.5: a modular, multi-frequency successor to theMk3a EIS/EIT system. *Physiological Measurement*, 22(1):49–54, feb 2001. doi: 10.1088/0967-3334/22/1/307.

[107] M. Wang. Electrode models in electrical impedance tomography. *Journal of Zhejiang University-SCIENCE A*, 6(12):1386–1393, 2005.

[108] Jiabin Jia, Mi Wang, H. Inaki Schlaberg, and Hua Li. A novel tomographic sensing system for high electrically conductive multiphase flow measurement. *Flow Measurement and Instrumentation*, 21(3):184 – 190, 2010. ISSN 0955-5986. doi: https://doi.org/10.1016/j.flowmeasinst.2009.12.002.

[109] Ryan Halter, Alex Hartov, and Keith Paulsen. Design and implementation of a high frequency electrical impedance tomography system. *Physiological measurement*, 25: 379–90, 2004.

[110] R. J. Halter, A. Hartov, and K. D. Paulsen. A broadband high-frequency electrical impedance tomography system for breast imaging. *IEEE Transactions on Biomedical Engineering*, 55(2):650–659, 2008.

[111] Tong In Oh, Hun Wi, Do Yub Kim, Pil Joong Yoo, and Eung Je Woo. A fully parallel multi-frequency EIT system with flexible electrode configuration: KHU mark2. *Physiological Measurement*, 32(7):835–849, jun 2011. doi: 10.1088/0967-3334/32/7/s08.

[112] X. Shi, W. Li, F. You, X. Huo, C. Xu, Z. Ji, R. Liu, B. Liu, Y. Li, F. Fu, and X. Dong. High-precision electrical impedance tomography data acquisition system for brain imaging. *IEEE Sensors Journal*, 18(14):5974–5984, July 2018. ISSN 1530-437X. doi: 10.1109/JSEN.2018.2836336.

[113] W. Li, J. Xia, G. Zhang, H. Ma, B. Liu, L. Yang, Y. Zhou, X. Dong, F. Fu, and X. Shi. Fast high-precision electrical impedance tomography system for real-time perfusion imaging. *IEEE Access*, 7:61570–61580, 2019.

[114] C. Tan, S. Liu, J. Jia, and F. Dong. A wideband electrical impedance tomography system based on sensitive bioimpedance spectrum bandwidth. *IEEE Transactions on Instrumentation and Measurement*, 69(1):144–154, 2020.

[115] D. Jennings and I. D. Schneider. Front-end architecture for a multifrequency electrical impedance tomography system. *Medical and Biological Engineering and Computing*, 39 (3):368–374, May 2001. ISSN 1741-0444. doi: 10.1007/BF02345293.

[116] K G Boone and D S Holder. Current approaches to analogue instrumentation design in electrical impedance tomography. *Physiological Measurement*, 17(4):229–247, nov 1996. doi: 10.1088/0967-3334/17/4/001.

[117] A McEwan, G Cusick, and D S Holder. A review of errors in multi-frequency EIT instrumentation. *Physiological Measurement*, 28(7):S197–S215, jun 2007. doi: 10.1088/0967-3334/28/7/s15.

[118] P Bertemes-Filho, B H Brown, and A J Wilson. A comparison of modified howland circuits as current generators with current mirror type circuits. *Physiological Measurement*, 21(1):1–6, 2000.

[119] Dhouha Bouchaala, Olfa Kanoun, and Nabil Derbel. High accurate and wideband current excitation for bioimpedance health monitoring systems. *Measurement*, 79:339 – 348, 2016. ISSN 0263-2241. doi: https://doi.org/10.1016/j.measurement.2015.07.054.

[120] A. S. Tucker, R. M. Fox, and R. J. Sadleir. Biocompatible, high precision, wideband, improved howland current source with lead-lag compensation. *IEEE Transactions on Biomedical Circuits and Systems*, 7(1):63–70, Feb 2013. ISSN 1932-4545. doi: 10.1109/TBCAS.2012.2199114.

[121] R. A. Pease. AN-1515, a comprehensive study of the howland current source. *National Semiconductor*, 2008.

[122] Amin Mahnam, Hassan Yazdanian, and Mohsen Mosayebi Samani. Comprehensive study of howland circuit with non-ideal components to design high performance current pumps. *Measurement*, 82:94 – 104, 2016. ISSN 0263-2241. doi: https://doi.org/10.1016/j.measurement.2015.12.044.

[123] Pedro Bertemes-Filho, Alexandre Felipei, and Volney Coelho Vincence. High accurate Howland current source: Output constraints analysis. *Circuits and Systems*, 4(7):451–458, 2013. doi: 10.4236/cs.2013.47059.

[124] R. D. Cook, G. J. Saulnier, D. G. Gisser, J. C. Goble, J. C. Newell, and D. Isaacson. Act3: a high-speed, high-precision electrical impedance tomograph. *IEEE Transactions on Biomedical Engineering*, 41(8):713–722, 1994.

[125] J. L. Merrill. Theory of the negative impedance converter. *The Bell System Technical Journal*, 30(1):88–109, 1951.

[126] J.K. Roberge and J. K. *Operational Amplifiers: Theory and Practice*. Massachusetts Institute of Technology. Radiation Laboratory. Wiley, 1975. ISBN 9780471725855.

[127] J. Brownlie. On the stability properties of a negative impedance converter. *IEEE Transactions on Circuit Theory*, 13(1):98–99, 1966.

[128] R. F. Hoskins. Stability of negative-impedance convertors. *Electronics Letters*, 2(9):341–, 1966.

[129] J. L. Jimenez-Martin, V. Gonzalez-Posadas, A. Parra-Cerrada, A. Blanco-Campo, E. Ugarte-MuÃśoz, and D. Segovia-Vargas. Full conditions for the stability analysis of negative impedance converters. In *2012 6th European Conference on Antennas and Propagation (EUCAP)*, pages 135–138, 2012.

[130] Daniel Segovia-Vargas, Jose Jimenez-Martin, Angel Parra-Cerrada, Fernando Albarracin-Vargas, Eduardo Ugarte-Munoz, and Vicente Gonzalez. Stability analysis and design of negative impedance converters: Application to circuit and small antennas. *Radioengineering*, 25:409–418, 09 2016. doi: 10.13164/re.2016.0409.

[131] Alexander S Ross, G J Saulnier, J C Newell, and D Isaacson. Current source design for electrical impedance tomography. *Physiological Measurement*, 24(2):509–516, 2003.

[132] Tong In Oh, Eung Je Woo, and David Holder. Multi-frequency EIT system with radially symmetric architecture: KHU mark1. *Physiological Measurement*, 28(7):S183–S196, 2007. doi: 10.1088/0967-3334/28/7/s14.

[133] Tong In Oh, Kyung Heon Lee, Sang Min Kim, Hwan Koo, Eung Je Woo, and David Holder. Calibration methods for a multi-channel multi-frequency EIT system. *Physiological Measurement*, 28(10):1175–1188, 2007. doi: 10.1088/0967-3334/28/10/004.

[134] Michael G. Ruppert, David M. Harcombe, Michael R. P. Ragazzon, S. O. Reza Moheimani, and Andrew J. Fleming. A review of demodulation techniques for amplitude-modulation atomic force microscopy. *Beilstein Journal of Nanotechnology*, 8:1407–1426, 2017. ISSN 2190-4286.

[135] Dan Sheingold, editor. *RMS-to-DC Application Guide*. Analog Devices, second edition, 1986.

[136] R W M Smith, I L Freeston, B H Brown, and A M Sinton. Design of a phase-sensitive detector to maximize signal-to-noise ratio in the presence of gaussian wideband noise. *Measurement Science and Technology*, 3(11):1054–1062, 1992.

[137] K. Ge and R. Lifeng. Fpga-based digital phase-sensitive demodulator for eit system. In *2007 8th International Conference on Electronic Measurement and Instruments*, pages 4–845–4–848, 2007.

[138] Xuehui Zhang and Huaxiang Wang. Digital phase-sensitive demodulation in electrical capacitance tomography system. In *2008 7th World Congress on Intelligent Control and Automation*, pages 6730–6733, 2008.

Chapter 3

Design of a Low-Cost Acquisition System to Reconstruct Images through Electrical Resistance Tomography

The present chapter has been submitted to the journal "IEEE Latin America Transactions" on September 5th, 2019, and accepted on February 14th, 2020.

3.1 Abstract

Electrical Resistance Tomography (ERT) is a technique employed in the industrial environment that reconstructs images formed by the impedance distributions inside a vessel. The method relies on measures from a data acquisition system, responsible to inject a current inside the vessel and measures the voltage on the boundaries, and sequentially an inverse problem solution. This paper introduces a low-cost design of an acquisition system that can obtain 30 images/s with a signal-to-noise ratio of 57.47 dB and a maximum error of 3.79%, utilizing a simple RMS-to-DC converter demodulation scheme to provide good accessibility to researchers aimed at investigating flow patterns of multiphase flow applications.

Keyword: Electrical Impedance Tomography (EIT), Data Acquisition Design, Instrumentation, Multiphase Flow.

3.2 Introduction

Electrical Resistance Tomography (ERT) is an imaging technique that is widely investigated nowadays. By injecting an electric current into a domain and consequently measuring the resulting voltage, it is possible to reconstruct the electrical conductivity and permittivity of the body. Such readings are used as experimental measures to solve the inverse problem corresponding to this conductivity field [1, 2]. The use of this imaging technique has the advantage of being non-intrusive, relatively low cost, ionizing radiation-free, and high temporal resolution. Nevertheless, the processed images are of poor quality due to the solution of the inverse problem. Even so, the technique has been applied in several areas of knowledge, such as biomedical areas [3, 4] and geological [5, 6]. It is also being widely used in industrial applications [7, 8, 9].

Continuous efforts are being made to improve the design of ERT data acquisition systems. Brown and Seagar [10] have developed one of the pioneering medical applications equipment that has the basic structure of the actual systems: the Sheffield system. Dickin and Wang [11] presented a similar model for industrial applications, but with digital demodulation and adjustable parameters such as current magnitude and frequency. In the third version of Sheffield's system, Wilson et al. [12] improved the design by adding multifrequency injections to the system to the system. Thus one can characterize the human tissue appropriately due to the variation of the electrical properties with the frequency. Wilkinson et al. [13] have developed a system for industrial applications that injects pulse currents and has completely parallel data acquisition, enabling high acquisition rates. Wang et al. [14] proposed a system with two high-speed acquisition planes that allow flow measurement. Further, Jia et al. [15] implemented in the acquisition system a voltage source with a current meter. This construction enables high-intensity currents for applications in highly conductive media.

The development of low-cost ERT systems is desirable to provide easy access to technology by industry and academy. In these systems, one of the components of most interest is the microcontroller and the analog to digital converter (ADC), which can be considered as one of the most important components of the equipment. A low-cost natural choice is the Arduino® microcontroller prototyping platforms [16]. It has the advantage of using simple interfaces between software and hardware. For this reason, Arduino has been used to facilitate the use of microcontrollers in projects in different areas [17, 18, 19]. Some low-cost ERT acquisition systems, such as Tomo [20], use Arduino in their design.

Considering the above assumptions, this paper aims to develop an Arduino-based ERT system

capable of performing multiphase flow pattern identification experiments with a signal-to-noise ratio (SNR) suitable to allow reconstruction of images presenting a satisfactory resolution.

3.3 Hardware Architecture

The developed acquisition system has the following modules: sinewave generator, voltage-controlled Howland current source, multiplexers, sensors, instrumentation amplifier (in-amp), RMS demodulator, low-pass filter, microcontroller from Arduino Due with ADC converter and virtual serial port (via USB), Figure 4.1. The acquisition can be done through 8 or 16 electrodes. The frequency operates in the range of 20-50 kHz. The injection pattern chosen for acquisition is the adjacent pattern. This pattern consists of the injection of the current through neighboring or adjacent electrodes and then to the differential measurement of voltage through the subsequent neighboring electrodes. It should be emphasized that the electrode that injects current in the cycle does not participate in the measuring process. More details are described in [11]. The cycle repeats until all electrodes go through the current injection process. The method presents $L(L-3)$ measurements, with L being the number of electrodes, where half of these measurements are independent [11].

3.3.1 Sinewave Generator and Modified Howland Current Source

The integrated circuit (IC) used as the function generator of the system is the AD9850 module, which uses the Digital Direct Synthesis (DDS) technology to digitally synthesize the sine wave that generates the injection current. Frequencies are digitally controlled by Arduino Due and can reach values greater than 10 MHz, which is sufficient to obtain the medium frequencies required in the method. At the output of the sinewave generator, the signal is conditioned by an amplifier and a coupling capacitor, Figure 3.2. The voltage-controlled current source (VCCS) provides a bidirectional current independent of the load and controlled by the input voltage. The standard Howland current source uses an op-amp with positive and negative feedback [21, 22]. In the design of the current source module implemented in the equipment, a modification with one op-amp and a buffer in the positive feedback is used. This configuration produces a higher output impedance [21], Figure 3.2 for IC2A and IC2B. Since all resistors are equal, from R4 to R7, for the circuit shown in Figure 3.2, the input voltage is related to the output current, Eq. 3.1:

$$I_{out} = \frac{V_{in}}{R8} \tag{3.1}$$

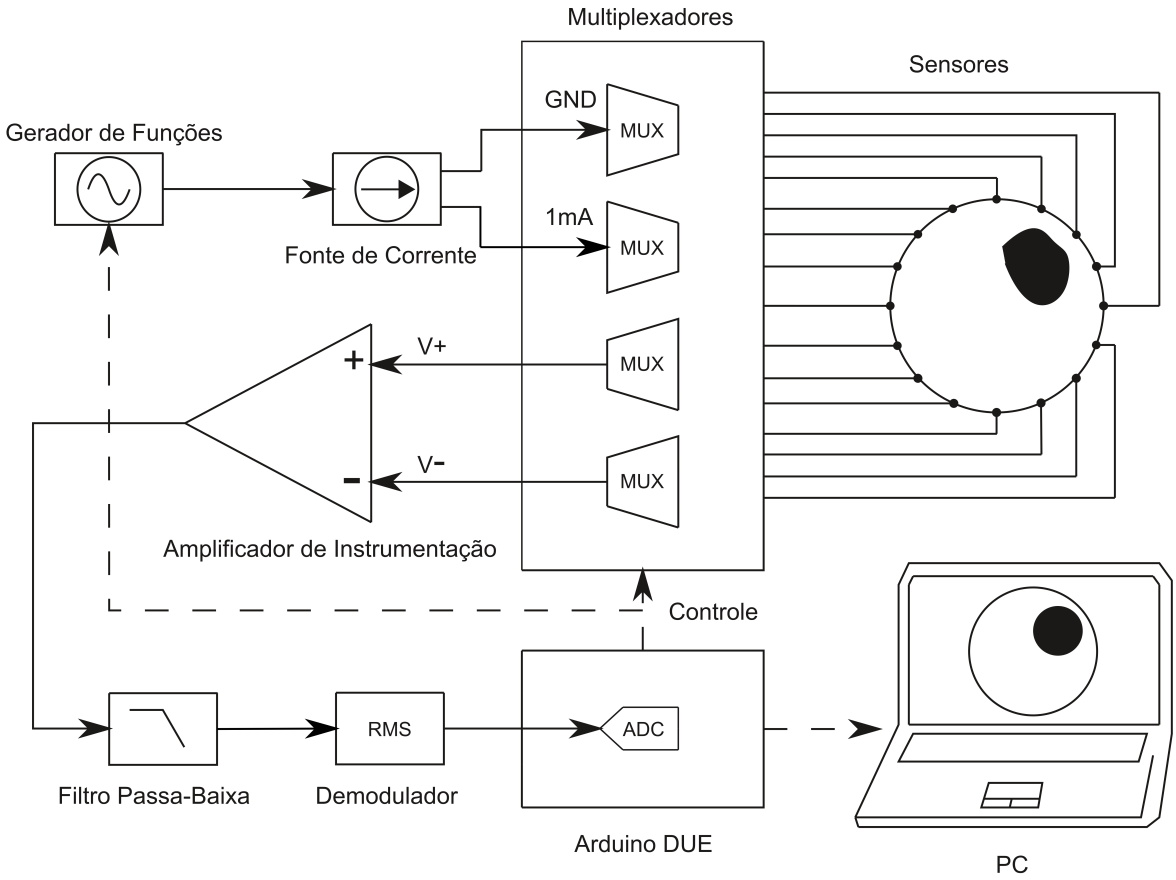

Figure 3.1: Block diagram of the developed tomogram.

where I_{out} is the output current, V_{in} is the input voltage and $R8$ is the adjusting gain resistor of the current.

To increase the output impedance, the resistors must be perfectly matched [21, 22, 23]. Consequently, resistances of 1% or lower tolerance are desirable for positive and negative feedback. The resistors and the input voltage were chosen to form a 1mA RMS current.

3.3.2 Instrumentation Amplifier and Low-Pass Filter

The instrumentation amplifier aims to perform differential measurements on the equipment. The practical effect of this application is to decrease the dynamic range of the signal to be sent to ADC. This is because the signal is significantly smaller and no longer referenced to the ground [24]. With that decrease, the in-amp also amplifies the signal to the condition it according to the need and, at the same time, rejects the common-mode signal appearing naturally in the application. The in-amp is utilized is the INA128, IC4, having a common-mode rejection ratio (CMRR) suitable for the purpose, with a good cost/functionality relationship. The IC4 uses a

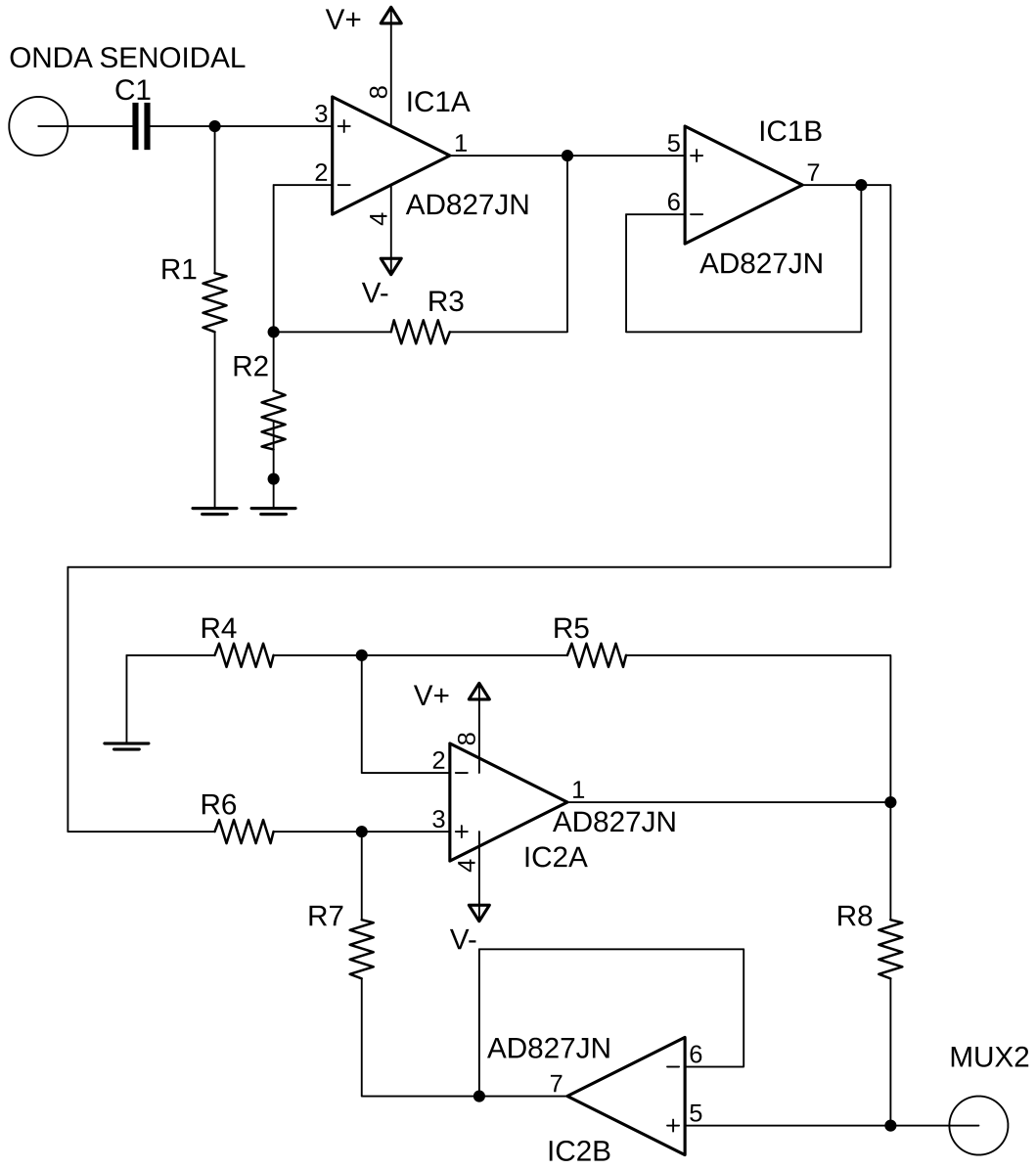

Figure 3.2: Circuit of the sinewave generator and Howland current source signal conditioning.

3 op-amp topology, with buffers in the differential inputs. These buffers have the function of matching and increasing the input impedance, minimally influencing the CMRR [25]. Before the input of the in-amp, the signal passes through coupling capacitors, C2 and C3 (Figure 3.3); then it is applied to the inverter and non-inverter inputs of the in-amp, Figure 3.3. The result at the output is the difference between the signals, Eq. 3.2, which can still be amplified by a factor A_g set by an external resistor, R11, according to the datasheet [26], Eq. 3.3.

$$V_{out} = A_g(V_+ - V_-) \tag{3.2}$$

$$A_g = 1 + \frac{50\,[k\Omega]}{R11} \tag{3.3}$$

The set gain to the electrical conductivity of $74\mu S/cm$ is 5.10.

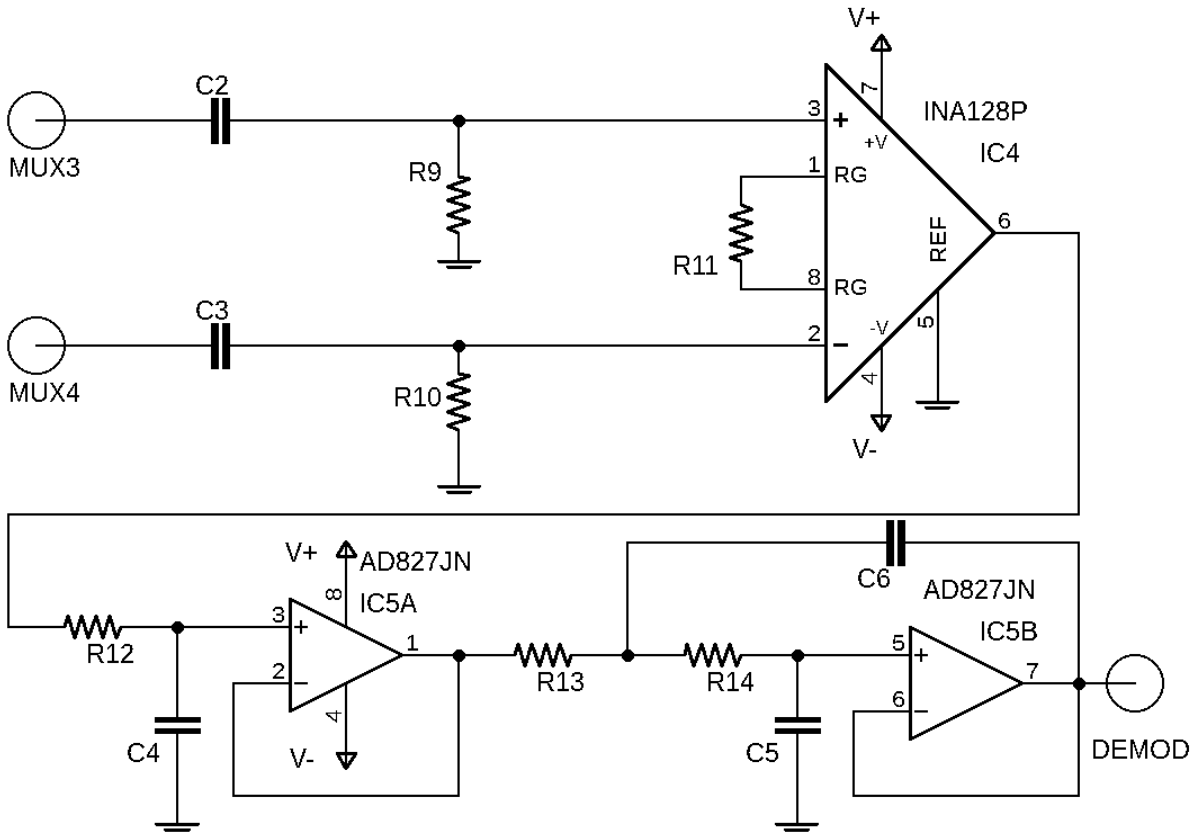

Figure 3.3: Circuit of the instrumentation amplifier and the Butterworth active low-pass filter.

This is the conventional form to apply the instrumentation amplifier, which utilizes 1 stage to operate the voltages differentially. Recently, Shi et al. [27] utilized a topology to increase CMRR with three in-amps in two stages of gain, which is intended to incorporate in the posterior versions of the equipment. In the design of the equipment is used the third-order active low-pass filter to reject the noise that degrades the signal, Figure 3.3. It is a Butterworth filter with a 90 kHz cutoff and 200 kHz band-stop frequency. The choice of this cutoff frequency is related to the operation of the equipment, which suffers increased errors for high frequencies due to the parasitic capacities [28]. Thus, the maximum possible frequency for the equipment presented in this work is 90 kHz.

3.3.3 Demodulator

To obtain the signal amplitude information, the sinewave must be demodulated efficiently. To this end, the IC AD536 is used because of its simplicity of application, as the signal does not require digital processing, Figure 3.4. This integrated circuit works with an implicit computation of the RMS signal value, outputting a DC signal proportional to the value RMS of the input

signal. On the other hand, this simplicity necessarily comes with the cost of a relatively low image acquisition rate, when compared to other methods. This is due to the internal low-pass filter in IC6 (Figure 3.4) introducing a settling time dependent on the selected C7 capacitor, Figure 3.4. Capacitor C10 was selected at the output of the demodulator after the follower with low value, of an order of pF. This has been done to prevent it from significantly influence the system settling time. Thus, the capacitor that dominates the process remains the demodulator capacitor C7. It is important to analyze the frequency and settling time in this IC to provide a signal with a low error [29, 30]. Notice that at lower frequencies the error increases and produces a poor quality signal. Therefore, the minimum frequency for the displayed system is 20 kHz. This type of demodulation only retrieves the real part of the impedance because it is insensitive to changes of the sinewave phase.

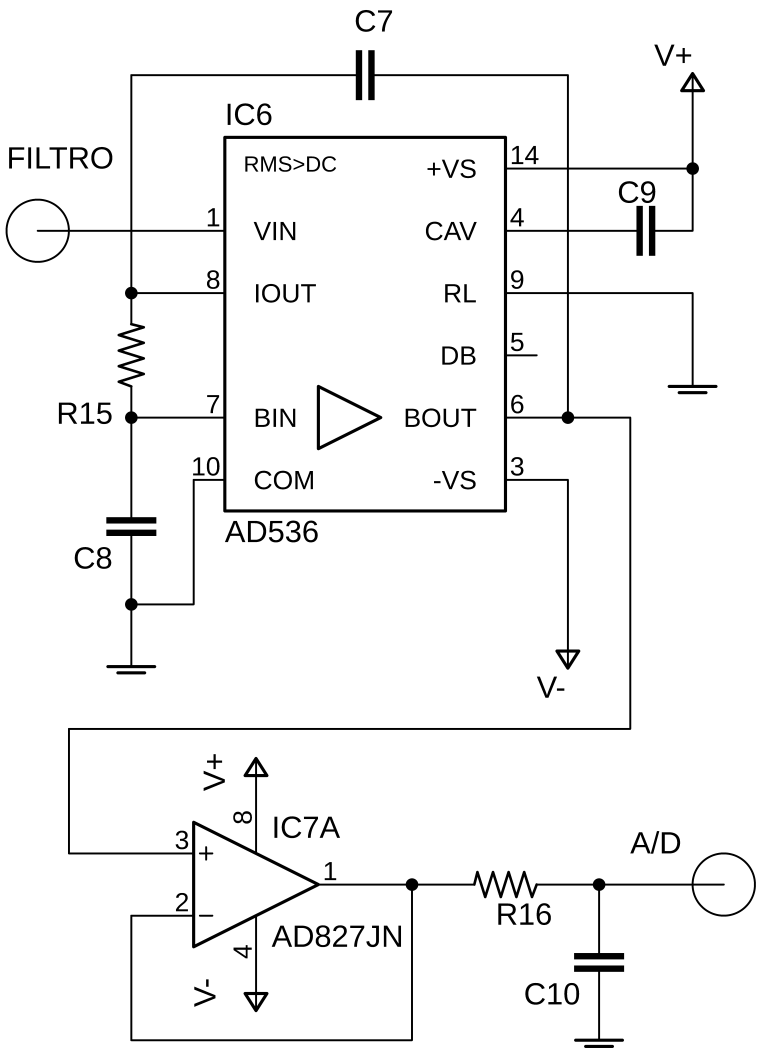

Figure 3.4: Circuit of the demodulator RMS-to-DC converter.

3.3.4 Microcontroller and Multiplexers

The multiplexers used as switches to inject current and measure voltages are the ADG506 ICs. The choice is due to its dynamic range greater than 30V differential and its relatively low parasitic capacities [31]. The use of multiplexers gives the design simplicity, although with the addition of non-idealities such as the on-resistance of the switches and parasitic capacitance. The 16 ports of all multiplexers are connected directly to the sensors. The inputs of the first two multiplexers are connected to the ground and the current source output. The output of the other two is connected to the in-amp inputs.

In the project, it is used the Arduino Due, which is a microcontroller prototyping platform. This platform uses the Atmel SAM3X8E ARM Cortex-M3 microcontroller [16, 32], which operates at a clock speed of 84 MHz. The ADC has 12 bits of resolution and a conversion frequency of up to 1 MHz [32], which is sufficient for the desired application. The microcontroller is responsible for controlling the injection current frequencies, current injection position, voltage distribution in the sensors through the multiplexers, and communication between computer and equipment. The measured analog signals are converted to digital in the ADC. These signals are used for image reconstruction on the computer.

3.4 Software Structure

The software written in Octave performs the communication between Arduino Due and the computer, which transfers all data relating to a complete image to the program memory. After performing data acquisition within a defined interval of time or number of images, the software performs the reconstruction using the routines from the software Electrical Impedance Tomography and Diffuse Optical Reconstruction Software (EIDORS), written in Matlab easily converted to Octave. It offers several possibilities of reconstruction algorithms, with many features [33]. The image to be reconstructed depends on the resolution of the forward problem and the inverse problem.

3.4.1 Forward Problem

The forward problem consist in a bidimensional domain Ω with an electrical conductivity σ, with a scalar potential distribution u in the domain, potential U_l in the boundary electrodes $\partial\Omega$, where a current I_l is injected. The equations that represents the phenomenon, known as the Complete

Electrode Model, are described by Eq. 6.1-6.4 [24]:

$$\nabla \cdot (\sigma \nabla u) = 0 \quad em\ \Omega \tag{3.4}$$

$$u + \bar{z}_l \sigma \frac{\partial u}{\partial n} = U_l \quad em\ e_l,\ l = 1, 2, ..., L \tag{3.5}$$

$$\int_{e_l} \frac{\partial u}{\partial n} dS = I_l \quad em\ e_l,\ l = 1, 2, ..., L \tag{3.6}$$

$$\sigma \frac{\partial u}{\partial n} = 0 \quad em\ \partial\Omega \setminus \cup_{l=1}^{L} e_l \tag{3.7}$$

where n is the normal direction from the boundary $\partial\Omega$, $\bar{z}_l$ is the contact impedance, e_l is the l-esimal electrode in the boundary $\partial\Omega$. To confer the existence and uniqueness of the solution, two additional conditions are necessary. Thus, the conservation of charges is given by Eq. 6.5

$$\sum_{l=1}^{L} I_l = 0 \tag{3.8}$$

and the determination of a reference node is given by Eq. 6.6

$$\sum_{l=1}^{L} U_l = 0 \tag{3.9}$$

The model is implemented directly on the software EIDORS, which is discretized by the Finite Element Method. The mesh with triangular elements is obtained by the free software Gmsh, which is then solved to provide the results.

3.4.2 Inverse Problem

The inverse problem consists in solving the regularization functions to obtain the estimations of the electrical conductivity in the domain. To perform this task, the one-step Gauss-Newton minization can be utilized, Eq. 3.10-3.11, [24, 34]:

$$\delta V = V_{meas} - V_{calc} \tag{3.10}$$

$$\delta\sigma = \left(J^T J + \alpha^2 \tilde{L}^T \tilde{L}\right)^{-1} \left(J^T \delta V + \alpha^2 \tilde{L}^T \tilde{L} \left(\sigma_{ref} - \sigma_0\right)\right) \tag{3.11}$$

where V_{meas} is the set of voltage measurements, V_{calc} is the set of voltages calculated by the forward problem, J is the Jacobian, $\delta\sigma$ is the estimated conductivity, σ_{ref} is the reference conductivity, σ_0 is the initial conductivity, $\tilde{L}$ is the regularization matrix and α is the regularization parameter. The method is implemented in EIDORS. The regularization matrix utilized in image reconstruction is known as Newton's One-Step Error Reconstructor (NOSER). This matrix considers that the diagonal of the approximate Hessian matrix $(J^T J)$ is utilized as regularization. [35]. The regularization parameter is 0.001.

3.5 Assembling and Sensors

The equipment was developed and soldered on a universal printed circuit board for testing. A vessel is assembled with electrodes, in a way that minimizes the differences between the real and computational domain. The vessel is made of acrylic with a total diameter of 14.4 cm and 16 equally spaced circumferential holes. In these holes, the sensors are positioned for injecting electrical current and measuring of electrical voltages. The sensors are made of stainless steel and are hemispherically shaped with a diameter of 18 mm. The test medium is water with an electrical conductivity of 74 $\mu S/cm$, although the equipment has been tested and works with values as high as 1129 $\mu S/cm$. Figure 3.5 shows the details of the mounted printed circuit boards and the vessel.

3.6 Results and Discussion

To evaluate the equipment performance, we considered: i) the maximum error produced by the measurements when compared to the forward problem, ii) the signal-to-noise ratio (SNR) of the equipment, and iii) the acquisition capability quantified by the number of images per second. These parameters are shown in Table 3.1, considering a conductivity value of 74 uS/cm measured for the tap-water. It is important to notice that the error increase for 16 electrodes is related to factors such as the correct electrode position and injection magnitude of current injection. The higher the number of electrodes, the more sensitive the positioning of the electrodes is and the low magnitude of the current negatively impacts the SNR, increasing the density of random errors.

Tests were performed to evaluate the correct functioning of the developed equipment. It is evaluated reconstructions with the object moving radially within the reservoir. The sensitivity of the resulting voltage related to the conductivity of inclusion varies from the highest point near

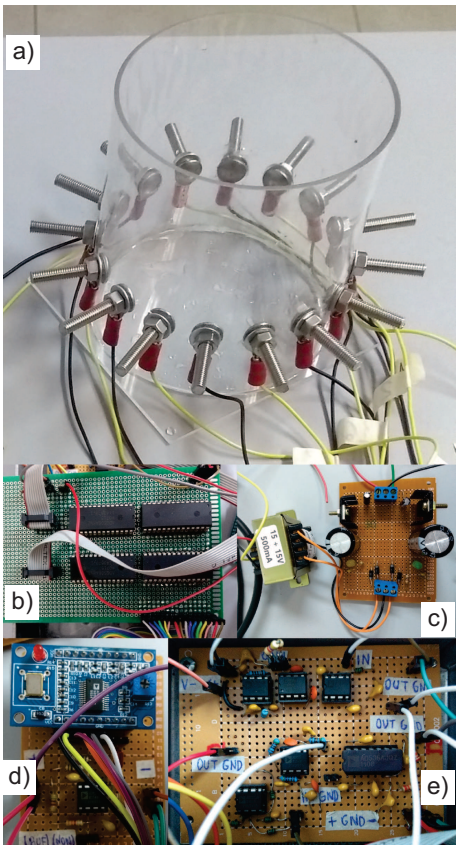

Figure 3.5: Assembling of the equipment prototype for tests, (a) the test vessel, (b) the multiplexers, (c) the voltage source, (d) the sinewave generator and conditioning circuit, (e) current source, low-pass filter e demodulator RMS-to-DC converter.

the wall to the lowest in the center of the reservoir, employing the adjacent pattern [11]. Thus, the reconstructed images are investigated in the direction of the variation of sensitivity. The first reconstructions were tested in the region of least sensitivity, in the central point, to the region of greater sensitivity near the wall. The first test was made with a 51 mm diameter phantom made of a non-conductive material, which corresponds to 12.54% of the vessel area. The results, Figure 3.6, shows that the method presented correctly positioned images, Figure 3.6a, for both 8-electrode reconstruction, Figure 3.6b, and for 16 electrodes, Figure 3.6c.

Table 3.1: Performance values measured in the equipment.

Performance	8 Eletrodes	16 Eletrodes
Max Error (%)	3.79	9.11
S/N (dB)	57.47	47.20
Images/s	30.61	6.41

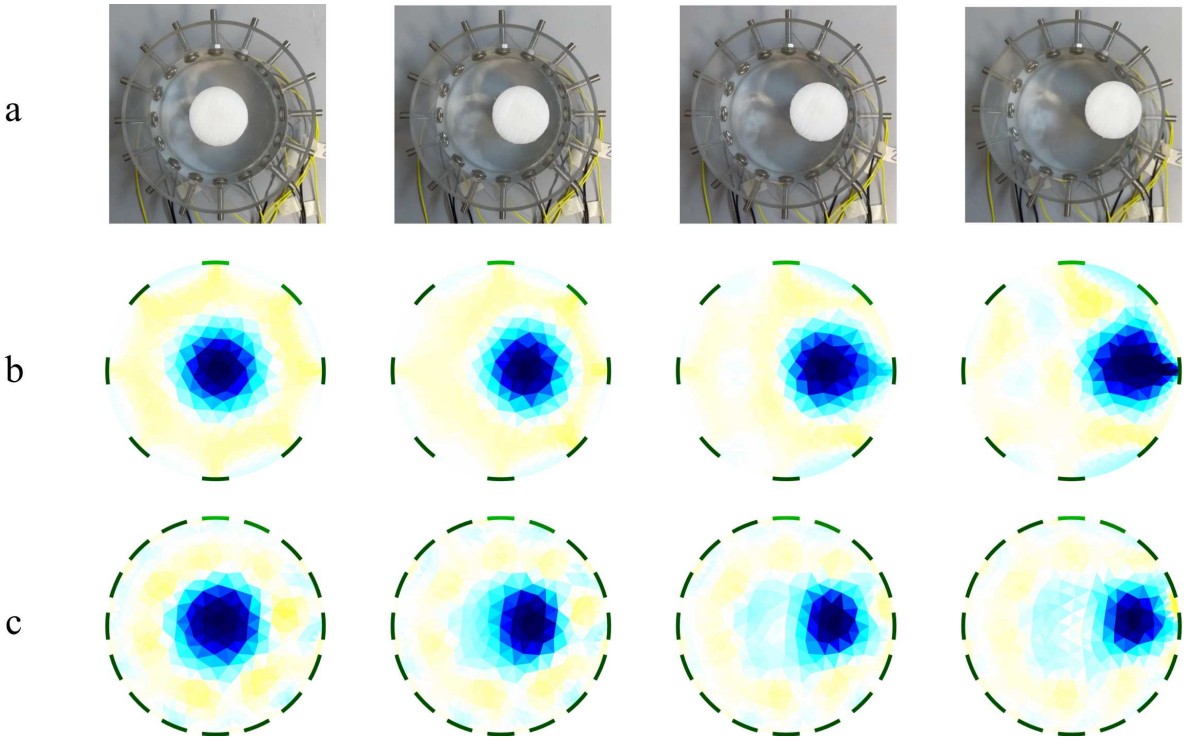

Figure 3.6: Reconstruction of a non-conductive phantom, in blue, in the test vessel. (a) Positioning of the phantom inside the vessel, (b) Image reconstruction utilizing 8 electrodes, (c) Image reconstruction utilizing 16 electrodes.

The second test is a phantom made of conductive material with a 49 mm diameter, which corresponds to 11.57% of the vessel area. Similarly, the image reconstructed with the algorithm showed a good contrast and positioned according to the real position, Figure 3.7a, for 8 electrode acquisitions, Figure 3.7b, and 16 electrodes, Figure 3.7c. It is noticed that there is a larger diameter image for the conductive and non-conductive test bodies using 8 electrodes compared to reconstruction with 16 electrodes. This is expected since the accuracy of the inverse problem solution increases with the use of an increased number of independent measurements[11].

In the third test, it is evaluated the reconstruction capacity with smaller diameters. A test was performed with a non-conductive material with a diameter of 21 mm, which corresponds to 2.12% of the vessel area, Figure 3.8a. Both reconstructions presented images with satisfactory positioning, but the diameter of the reconstructed image with 8 electrodes is overestimated, Figure 3.8b. The 16-electrode image showed low contrast, Figure 3.8c. However, these points do not prevent the correct interpretation of the image.

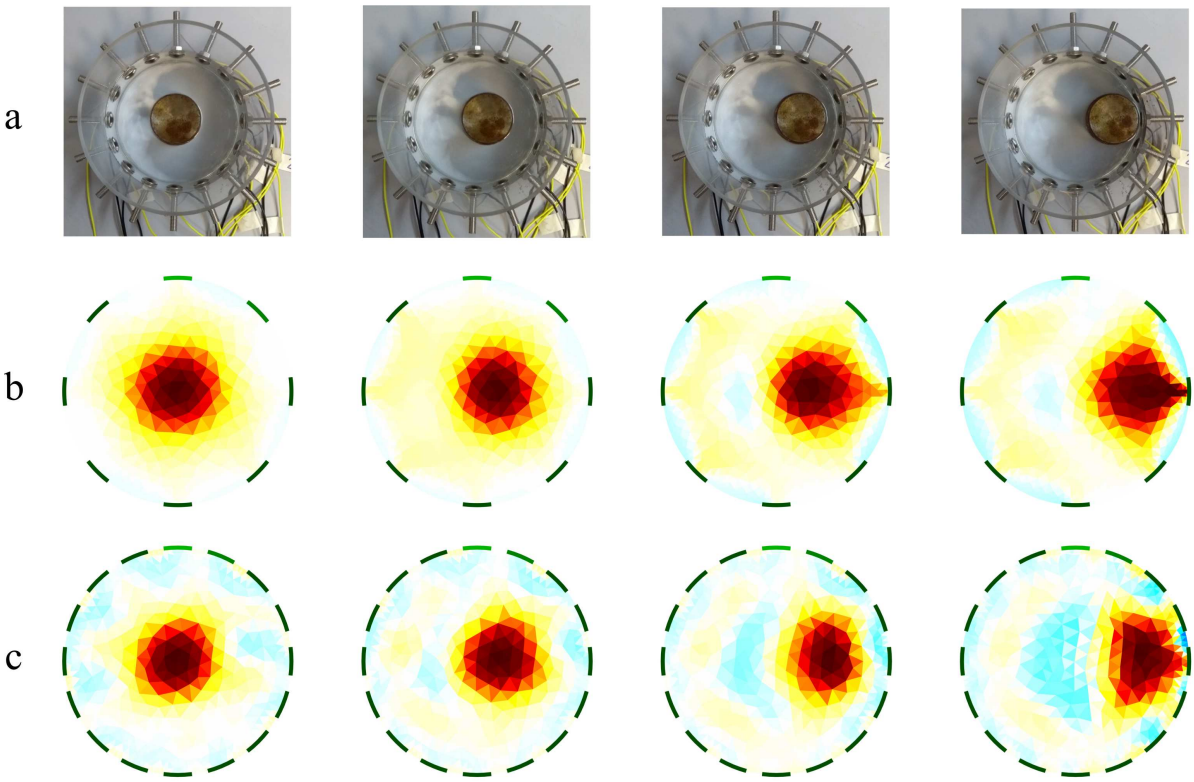

Figure 3.7: Reconstruction of a conductive phantom, in red, in the test vessel. (a) Positioning of the phantom inside the vessel, (b) Image reconstruction utilizing 8 electrodes, (c) Image reconstruction utilizing 16 electrodes.

3.7 Conclusion

A circuit of an experimental acquisition module, responsible for providing measurements that enable the reconstruction of images related to the electrical conductivity in the medium, through the technique of electrical impedance tomography is proposed in the present work. The instrumentation consists of seven modules responsible for injecting the electric currents and measuring the voltages, transforming the analog signal into digital in the process. These modules are the signal generator, the current source, the multiplexers, the instrumentation amplifier, the low-pass filter, the demodulator RMS-to-DC converter, and Arduino with an ADC. A test vessel was assembled and images in accordance are obtained in three different configurations. The equipment can reconstruct 30.61 images/s with 8 electrodes and 6.41 images/s with 16 electrodes presenting an SNR of 57.47 dB and 47.20 dB respectively. For future versions of the equipment, intended changes focus primarily to the current source, which with matched resistances at 0.1% tolerance or less) and changes in topography (balanced pair single-ended to inject equal positive and negative current), can reduce the error associated with the output impedance and common-mode signal; in the instrumentation amplifier, which using two stages can significantly increase the

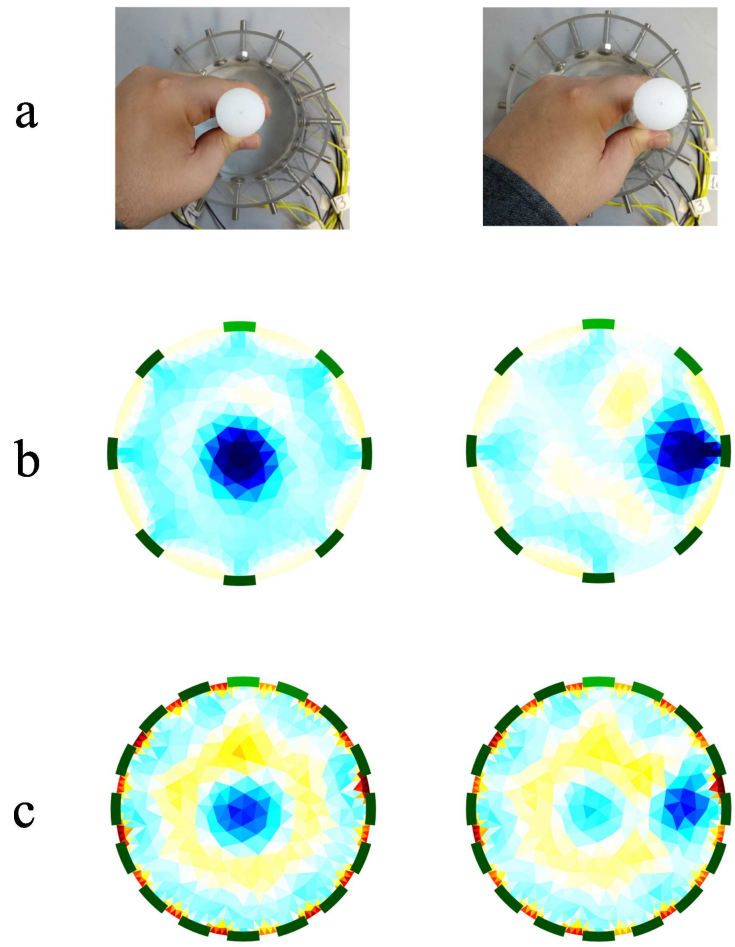

Figure 3.8: Reconstruction of a non-conductive phantom, in blue, with a decreased section area in the test vessel. (a) Positioning of the phantom inside the vessel, (b) Image reconstruction utilizing 8 electrodes, (c) Image reconstruction utilizing 16 electrodes.

module CMRR; in the implementation of digital demodulation that significantly decreases the acquisition time and enables the acquisition of sinewave phase information, the imaginary part of the impedance (synchronous demodulation); and implementing injection through the opposite pattern.

References

[1] R. Giguère, L. Fradette, D. Mignon, and P.A. Tanguy. ERT algorithms for quantitative concentration measurement of multiphase flows. *Chemical Engineering Journal*, 141(1): 305 – 317, 2008. ISSN 1385-8947. doi: https://doi.org/10.1016/j.cej.2008.01.011.

[2] Bong Seok Kim, Anil Kumar Khambampati, Yoon Jeong Hong, Sin Kim, and Kyung Youn Kim. Multiphase flow imaging using an adaptive multi-threshold technique in electrical resistance tomography. *Flow Measurement and Instrumentation*, 31:25 – 34, 2013. ISSN 0955-5986. doi: https://doi.org/10.1016/j.flowmeasinst.2012.11.003.

[3] M. Bodenstein, M. David, and K. Markstaller. Principles of electrical impedance tomography and its clinical application. *Critical Care Medicine*, 37(2):713 – 724, 2009.

[4] A Romsauerova, A McEwan, L Horesh, R Yerworth, R H Bayford, and D S Holder. Multi-frequency electrical impedance tomography (EIT) of the adult human head: initial findings in brain tumours, arteriovenous malformations and chronic stroke, development of an analysis method and calibration. *Physiological Measurement*, 27(5):S147–S161, 2006.

[5] Charles R. Carrigan, Xianjin Yang, Douglas J. LaBrecque, Dennis Larsen, David Freeman, Abelardo L. Ramirez, William Daily, Roger Aines, Robin Newmark, Julio Friedmann, and Susan Hovorka. Electrical resistance tomographic monitoring of CO2 movement in deep geologic reservoirs. *International Journal of Greenhouse Gas Control*, 18:401 – 408, 2013. ISSN 1750-5836. doi: https://doi.org/10.1016/j.ijggc.2013.04.016.

[6] William Daily, Abelardo Ramirez, Douglas LaBrecque, and John Nitao. Electrical resistivity tomography of vadose water movement. *Water Resources Research*, 28(5):1429–1442, 1992. doi: 10.1029/91WR03087.

[7] Mi Wang, Jiabin Jia, Yousef Faraj, Qiang Wang, Cheng gang Xie, Gary Oddie, Ken Primrose, and Changhua Qiu. A new visualisation and measurement technology for water

continuous multiphase flows. *Flow Measurement and Instrumentation*, 46:204 – 212, 2015. ISSN 0955-5986. doi: https://doi.org/10.1016/j.flowmeasinst.2015.06.022.

[8] Zhenzhen Meng, Zhiyao Huang, Baoliang Wang, Haifeng Ji, Haiqing Li, and Yong Yan. AirâĂŞwater two-phase flow measurement using a Venturi meter and an electrical resistance tomography sensor. *Flow Measurement and Instrumentation*, 21(3):268 – 276, 2010. ISSN 0955-5986. doi: https://doi.org/10.1016/j.flowmeasinst.2010.02.006.

[9] A. Parvareh, M. Rahimi, A. Alizadehdakhel, and A.A. Alsairafi. CFD and ERT investigations on two-phase flow regimes in vertical and horizontal tubes. *International Communications in Heat and Mass Transfer*, 37(3):304 – 311, 2010. ISSN 0735-1933. doi: https://doi.org/10.1016/j.icheatmasstransfer.2009.11.001.

[10] B H Brown and A D Seagar. The Sheffield data collection system. *Clinical Physics and Physiological Measurement*, 8(4A):91–97, nov 1987. doi: 10.1088/0143-0815/8/4a/012.

[11] Fraser Dickin and Mi Wang. Electrical resistance tomography for process applications. *Measurement Science and Technology*, 7(3):247–260, mar 1996. doi: 10.1088/0957-0233/7/3/005.

[12] A J Wilson, P Milnes, A R Waterworth, R H Smallwood, and B H Brown. Mk3.5: a modular, multi-frequency successor to theMk3a EIS/EIT system. *Physiological Measurement*, 22 (1):49–54, feb 2001. doi: 10.1088/0967-3334/22/1/307.

[13] A. J. Wilkinson, E. W. Randall, J. J. Cilliers, D. R. Durrett, T. Naidoo, and T. Long. A 1000-measurement frames/second ERT data capture system with real-time visualization. *IEEE Sensors Journal*, 5(2):300–307, April 2005. ISSN 1530-437X. doi: 10.1109/JSEN.2004.842445.

[14] Mi Wang, Yixin Ma, N. Holliday, Yunfeng Dai, R. A. Williams, and G. Lucas. A high-performance EIT system. *IEEE Sensors Journal*, 5(2):289–299, April 2005. ISSN 1530-437X. doi: 10.1109/JSEN.2005.843904.

[15] Jiabin Jia, Mi Wang, H. Inaki Schlaberg, and Hua Li. A novel tomographic sensing system for high electrically conductive multiphase flow measurement. *Flow Measurement and Instrumentation*, 21(3):184 – 190, 2010. ISSN 0955-5986. doi: https://doi.org/10.1016/j.flowmeasinst.2009.12.002.

[16] Arduino. https://www.arduino.cc/, 2019. Accessed: 2019-08-27.

[17] Giovanni Bitella, Roberta Rossi, Rocco Bochicchio, Michele Perniola, and Mariana Amato. A novel low-cost open-hardware platform for monitoring soil water content and multiple soil-air-vegetation parameters. *Sensors*, 14(10):19639–19659, 2014. ISSN 1424-8220. doi: 10.3390/s141019639.

[18] Petteri Teikari, Raymond P. Najjar, Hemi Malkki, Kenneth Knoblauch, Dominique Dumortier, Claude Gronfier, and Howard M. Cooper. An inexpensive arduino-based led stimulator system for vision research. *Journal of Neuroscience Methods*, 211(2):227 – 236, 2012. ISSN 0165-0270. doi: https://doi.org/10.1016/j.jneumeth.2012.09.012.

[19] Luis J. Claros-Marfil, J. Francisco Padial, and Benito Lauret. A new and inexpensive open source data acquisition and controller for solar research: Application to a water-flow glazing. *Renewable Energy*, 92:450 – 461, 2016. ISSN 0960-1481. doi: https://doi.org/10.1016/j.renene.2016.02.037.

[20] Yang Zhang, Robert Xiao, and Chris Harrison. Advancing hand gesture recognition with high resolution electrical impedance tomography. In *Proceedings of the 29th Annual Symposium on User Interface Software and Technology*, pages 843–850, New York, NY, USA, 2016. ACM. doi: 10.1145/2984511.2984574.

[21] Amin Mahnam, Hassan Yazdanian, and Mohsen Mosayebi Samani. Comprehensive study of howland circuit with non-ideal components to design high performance current pumps. *Measurement*, 82:94 – 104, 2016. ISSN 0263-2241. doi: https://doi.org/10.1016/j.measurement.2015.12.044.

[22] A. S. Tucker, R. M. Fox, and R. J. Sadleir. Biocompatible, high precision, wideband, improved howland current source with lead-lag compensation. *IEEE Transactions on Biomedical Circuits and Systems*, 7(1):63–70, Feb 2013. ISSN 1932-4545. doi: 10.1109/TBCAS.2012.2199114.

[23] Pedro Bertemes-Filho, Alexandre Felipei, and Volney Coelho Vincence. High accurate Howland current source: Output constraints analysis. *Circuits and Systems*, 4(7):451–458, 2013. doi: 10.4236/cs.2013.47059.

[24] D.S. Holder. *Electrical Impedance Tomography: Methods, History and Applications*. Series in Medical Physics and Biomedical Engineering. CRC Press, 2004. ISBN 9781420034462.

[25] Lew Counts and Charles Kitchen. *A Designer's Guide to Instrumentation Amplifiers*. Analog Devices, 3rd edition edition, 2006.

[26] *INA12x Precision, Low-Power Instrumentation Amplifiers datasheet (Rev. E)*. Texas Instruments, 2019.

[27] X. Shi, W. Li, F. You, X. Huo, C. Xu, Z. Ji, R. Liu, B. Liu, Y. Li, F. Fu, and X. Dong. High-precision electrical impedance tomography data acquisition system for brain imaging. *IEEE Sensors Journal*, 18(14):5974–5984, July 2018. ISSN 1530-437X. doi: 10.1109/JSEN.2018.2836336.

[28] K G Boone and D S Holder. Current approaches to analogue instrumentation design in electrical impedance tomography. *Physiological Measurement*, 17(4):229–247, nov 1996. doi: 10.1088/0967-3334/17/4/001.

[29] *AD536A: Integrated Circuit True RMS-to-DC Converter Data Sheet (Rev. G)*. Analog Devices, 2019.

[30] Dan Sheingold, editor. *RMS-to-DC Application Guide*. Analog Devices, second edition, 1986.

[31] *ADG506A/ADG507A: CMOS 8-/16-Channel Analog Multiplexers Data Sheet (Rev. C)*. Analog Devices, 1998.

[32] *SAM3X/SAM3A Series Datasheet*. Microchip, 2015.

[33] Andy Adler and William R B Lionheart. Uses and abuses of EIDORS: an extensible software base for EIT. *Physiological Measurement*, 27(5):S25–S42, apr 2006. doi: 10.1088/0967-3334/27/5/s03.

[34] William R B Lionheart. EIT reconstruction algorithms: pitfalls, challenges and recent developments. *Physiological Measurement*, 25(1):125–142, feb 2004. doi: 10.1088/0967-3334/25/1/021.

[35] M. Cheney, D. Isaacson, J. C. Newell, S. Simske, and J. Goble. NOSER: An algorithm for solving the inverse conductivity problem. *International Journal of Imaging Systems and Technology*, 2(2):66–75, 1990. doi: 10.1002/ima.1850020203.

Chapter 4

Errors Assessment and Modeling to Develop a Data Acquisition System for Electrical Impedance Tomography

The present chapter has been submitted to the journal "Measurement" on March 13th, 2020.

4.1 Abstract

Electrical Impedance Tomography (EIT) is a technique that enables the reconstruction of the impedance distributions inside a vessel in a multiphase flow of industrial processes. Such a technique combines a data acquisition (DAQ) system to inject a current and to measure the voltages on the sensors and an inverse problem technique to reconstruct the image properly. This problem is highly ill-conditioned, causing errors that produce instabilities in the solution. Therefore, when performing the acquisition, the DAQ system must have sufficient accuracy to allow the reconstruction of images with good quality. To avoid these measurement inaccuracies, this paper introduces a methodology that aids in the process of new system development. It consists of investigating the errors in the current version of the system by measuring the voltages using a ring of resistors and a water vessel to identify their causes and, further, predicts the systematic errors caused by the non-idealities of each subsystem by modeling its frequency response by SPICE. From this information, it is possible to perform a critical analysis that aids the design decisions towards developing new hardware. The methodology is demonstrated in the system designed by the authors.

Keyword: Electrical Impedance Tomography (EIT), Data Acquisition Design, Error Analysis, Instrumentation, Measurement.

4.2 Introduction

Electrical Impedance Tomography (EIT) is a technique that is currently attracting the interest of researchers, especially when dealing with multiphase flow measurements [1]. Through the use of observations, it is possible to solve an inverse problem that reconstructs an image of the domain. These observations are obtained by a system that injects a bidirectional current through a specific pattern and measures the potential voltage from an electrical field formed inside a vessel. From this potential, it is possible to reconstruct the field of electrical conductivity. In the reconstructed image, due to the difference of conductivity, it becomes possible to visualize different zones, which can be associated with different phases of fluid or different bodies in the domain in question [2]. The attention being given to this technique arises from the advantage that is a non-intrusive process since the electrodes that receive the stimulus are attached to the inner surface of the vessel, of relatively low-cost, is free of ionizing radiation and has high temporal resolution when compared to other image applications.

Several research groups have presented designs for a data acquisition (DAQ) system to reconstruct images, such as one of the pioneer systems, the Mk1 [3], designed by the Sheffield group. This system injects a single current at a specific frequency and measures the voltage serially. A latter design, the Mk3.5 [4], utilizes a multi-frequency design that is able to reconstruct images at several frequencies since the conductivity of in-vivo tissues varies with this parameter. The KHU Mark 2 [5] is updated from the first version [6], which is a multi-frequency fully parallel EIT system capable of 100 images/s. It presented additional features with an improved layout and components, impacting the CMRR when compared with the previous version. The above mentioned systems were designed for biomedical purposes. For industrial process applications, other design parameters become important. A higher time resolution with adequate accuracy is the primary goal for this type of system, allowing the method to evaluate dynamic changes and higher velocities in fluid flow and mixing processes. Thus, one of the systems developed is the design proposed by Wilkinson et al. [7], capable of acquiring 1000 images/s, and based on a current pulse injection method, with a fully parallel acquisition. Wang et al. [8] developed a dual-plane system of over 1000 images/s/plane for flow measurements. Jia et al. [9] developed an EIT system capable of reconstructing images in a highly conductive medium, by using a voltage source design. For these systems, the process of development to achieve the required

accuracy is not explicitly demonstrated. The best components might be chosen by trial and error and/or a posteriori by optimization, such as the method demonstrated by [10].

The process of inversion to obtain an image from the conductivities is highly ill-posed. Therefore, errors from computational modeling and measurement error, including noise, can cause significant anomalies in these images [11]. Kolehmainen et al. [12] investigated the impact of several computational modeling errors on the reconstruction, such as the contact impedance mismatch, electrode size, electrode localization, and the boundary shape of the domain. Dehghani and Soleimani [13] demonstrated the importance of the correct meshing. Methods to compensate for these computational errors are given in [14].

Regarding the measurements, it is important to minimize the systematic and random errors present in the system. The performance is intrinsically related to each electronic subsystem that comprises the DAQ system. A comprehensive method to model a channel of the system, which considers each of the systematic errors associated with the subsystems and their non-idealities is given by the following researchers: Boone and Holder [15], Jennings and Schneider [16]. According to these authors, the primary characteristics that must be accountable to avoid major error are the stray capacitance present in the circuit and multiplexers, the common-mode signal that affects the instrumentation amplifier, and the output impedance of the current source. For instance, Jennings et al. [16] consider a threshold value of 0.1% error for a system to achieve a good image, considering a static imaging reconstruction.

There is no established methodology in the literature that presents a deeper and detailed process to design a new prototype given these errors of measurement. Thus, it is important to outline the influence of each electronic subsystem and its operational parameters in the accuracy of the measurement of the designed EIT DAQ system. These data are extremely relevant when designing a new prototype, as they leads to an optimal selection of the components and the best configurations of the subsystems based on the design guidelines. From that perspective, the objective of the present work is to propose a new methodology that guides the process of system development. This is achieved by evaluating the occurrence of random and systematic errors, due to the non-idealities of each electronic subsystem and the incorrect selection of operational parameters. This methodology is given in four steps: i) evaluating the errors caused by design decisions of the current system version by inspecting measurements in a ring of resistors and a water solution vessel; ii) modeling by SPICE the DAQ system measurement channel and further validating the results; iii) investigating different configurations of the subsystems and sensors in the model to assist the decision making process; iv) modeling the new design, and evaluating

the quality of the static reconstruction of this system.

4.3 Hardware Architecture

The electrical impedance tomography system developed has the following subsystems: sine wave generator, voltage-controlled current source, multiplexers, sensors, instrumentation amplifier, low-pass filter, demodulator, and a microcontroller with an analog-to-digital converter (ADC), as shown in Fig. 4.1. The injection pattern adopted by the current design is known as the adjacent protocol. It consists of performing injections between two adjacent electrodes and the remaining ones that are not on duty, measuring the boundary voltages in each measurement cycle. Due to reciprocity, the number of measurements, N_{meas}, is related to the number of electrodes, L, by the relationship $N_{meas} = L(L-3)$, of which half of these are independent [11].

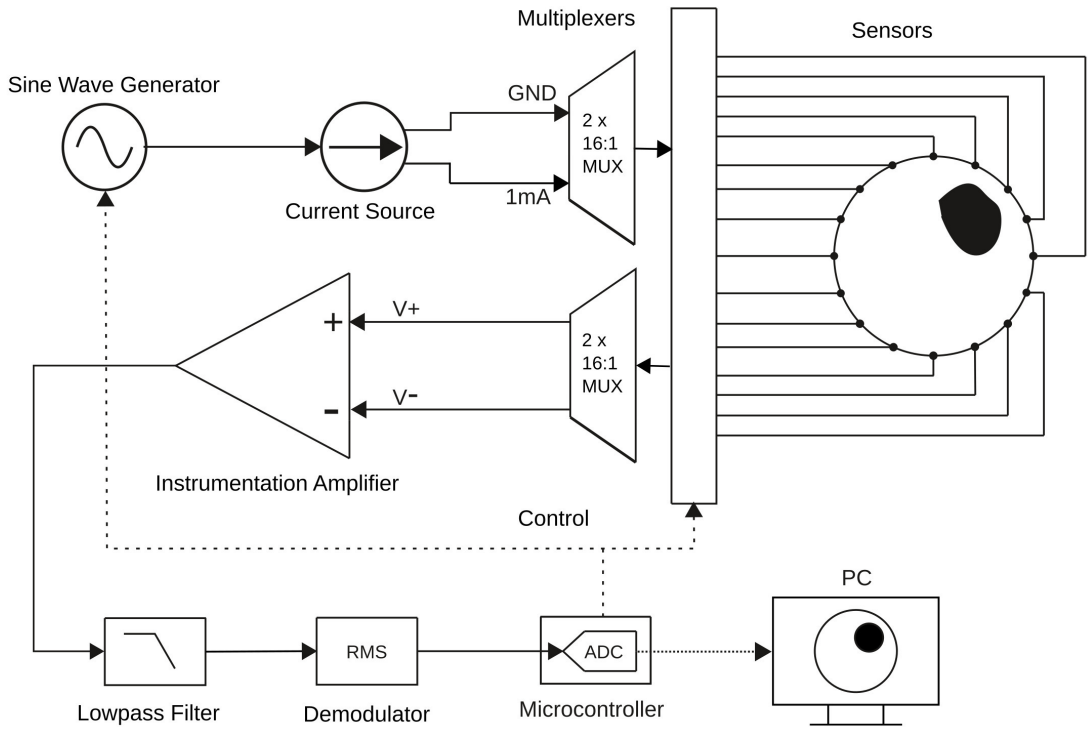

Figure 4.1: Block diagram of the developed tomography.

The acquisition can be performed using 8 or 16 electrodes. The decisions towards the design of this system prioritized the simplicity of the hardware, knowing that it would have a performance cost in terms of the speed of acquisition and the accuracy of the measurements.

The sine wave generator comprised the integrated circuit (IC) AD9850, which utilizes a Direct Digital Synthesis (DDS) technology to synthesize the waves with a digitally programmed frequency [17]. This subsystem can output signals with frequency over 1 MHz, which is sufficient bandwidth for the current design.

The voltage-controlled current source (VCCS) provides a bidirectional constant current controlled by the input voltage. The standard Howland current source comprised of an operational amplifier (op-amp) with both positive and negative feedback [18, 19]. For the presented design, a modification is implemented containing an extra op-amp buffer in the positive feedback, thus producing a higher output impedance [20]. The single-ended topology is chosen for the VCCS. Resistors with 1% tolerance are utilized for both positive and negative feedback. The gain setting resistor is set with 1% tolerance resistors, with a value chosen to achieve a 1 mA RMS.

The multiplexers are the IC ADG506, due to the relative low parasitic capacitance [21]. Even with the non-ideal behavior introducing errors in the measurement, with the on-resistance and parasitic capacitance, its use is desirable when it is necessary to simplify the hardware design.

It is important to implement an instrumentation amplifier (in-amp) to reduce the dynamic range of the signal by measuring it differentially. Also, it is important to emphasize that, in EIT applications, there is a high common-mode voltage (CMV). This signal is caused by the impedance distribution inside the vessel, and it needs to be rejected to decrease the error of the measurements. For this purpose, the INA128 is selected, an in-amp that presents a common-mode rejection ratio (CMRR) that is adequate for medium frequencies [22].

The third-order active low-pass filter is used to reject the noise which degrades the equipment signal. It is a Butterworth filter with a cutoff frequency of 90 kHz and a bandstop of 200 kHz. The choice of the cutoff frequency is related to the increase in error attributed to the parasitic capacitances present in the equipment, which becomes considerable at higher frequencies [15] and the frequency response from the demodulator [23].

The sine wave must be demodulated to efficiently measure the signal amplitude in the ADC. The IC AD536 is selected to perform the task, an RMS-to-DC converter, which is used due to the simplicity of the application. On the other hand, this simplicity limits the speed of acquisition. This occurs due to the settling time of the low-pass filter that is present in the implicit computation of the RMS-to-DC converter [23]. Therefore, the system is built considering the settling time of this filter from the IC.

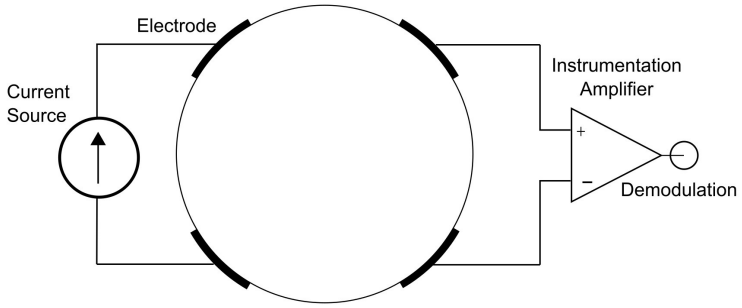

Figure 4.2: The ideal 4-electrode measuring procedure.

The Arduino Due is an open-hardware prototyping platform based on the microcontroller Atmel SAM3X8E ARM Cortex-M3, which has a clock operating with a speed of 84 MHz. The ADC has 12 bits of resolution and the conversion rate can reach 1 MHz [24]. In this design, this microcontroller is responsible for controlling the injected and measured signals from the sensor, which are transferred through the switches of the multiplexers. Additionally, it is responsible for converting the analog signal to digital.

4.4 Sources of Error

The EIT DAQ system utilizes the four-electrode method to inject current and measure voltages. This type of measurement is chosen to avoid the polarization effect [25]. The ideal method to inject and measure the signal is shown in Fig. 4.2.

However, the real circuit deviates from the ideal due to the non-idealities present in the circuit [15, 16]. These elements introduce errors that affect the accuracy of the DAQ system. The sources of these errors include the current source, the multiplexers, the cables, the electrodes, and the voltmeter.

4.4.1 Howland Current Source

Three effects contribute to the output impedance in the current source which must be accounted to quantify the error: the imbalance in the positive and negative feedback, $RO1$; the finite open-loop gain of the op-amp, $RO2$; and the op-amp finite bandwidth, CO [19, 20]. These elements effectively shunt part of the current from the load, Z_L, causing errors in the output current. The buffered feedback Howland current source, the output impedance model, and the dual version of the VCCS output impedance model [18] are shown in Fig. 4.3(a), Fig. 4.3(b), and Fig. 4.3(c) respectively.

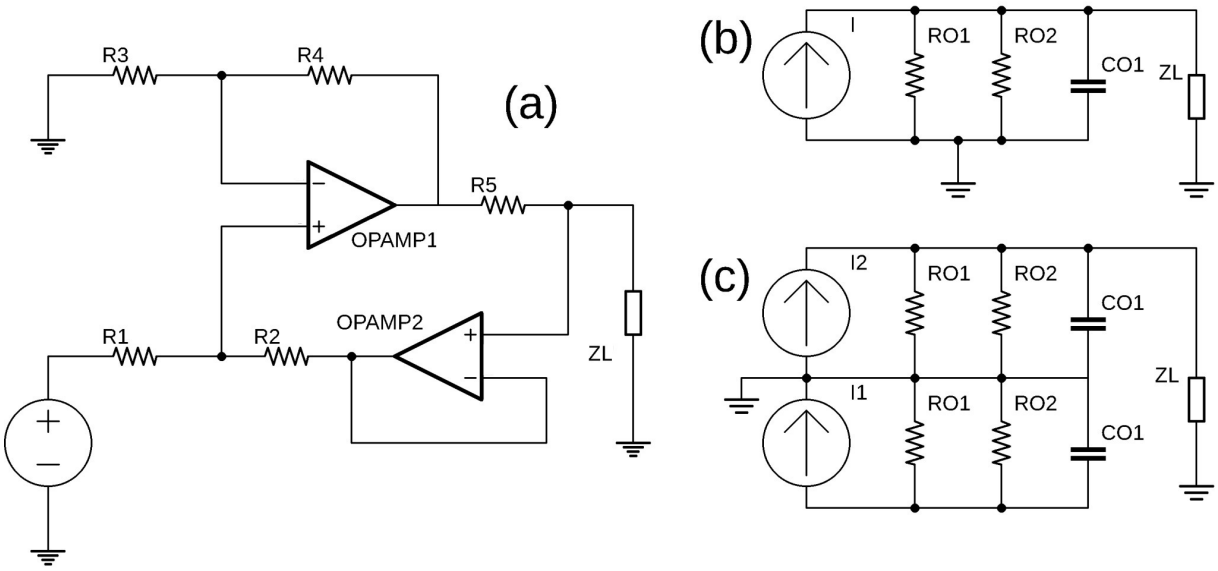

Figure 4.3: (a) Positive feedback buffered Howland current source, (b) Output impedance model of the current source, (c) Output impedance of the dual current source.

The resistors from the inverting and non-inverting feedback must match to prevent the loss of accuracy, satisfying, for this topology, (4.1).

$$\frac{R_4}{R_3} = \frac{R_2}{R_1} \tag{4.1}$$

Therefore, the resistance must possess a tight tolerance or a good match between the nominal values. In addition, a trimming scheme is desirable to perform a fine adjustment. The effect of the tolerance T in the current source output resistance, R_{O1}, for the chosen topology is given by (4.2), [20].

$$R_{O1} = \frac{1}{4T}\frac{R_5}{1-\beta_{fb}} \tag{4.2}$$

R_5 is the gain setting resistor connected to the output of the OPAMP1 and the non-inverting input of the OPAMP2 in the current source, and β_{fb} is the feedback ratio.

By applying the feedback circuit analysis, considering the positive feedback buffered topology of the current source, the relationship for the finite open-loop gain output resistance, R_{O2}, is given by (4.3) [20].

$$R_{O2} = \frac{R_5(1+Aol_1\beta_{fb})}{(\frac{Aol_1 Aol_2}{1+Aol_2}\beta_{fb} - Aol_1\beta_{fb} - 1)} \tag{4.3}$$

where Aol_1 is the open-loop gain of the OPAMP1 and Aol_2 is the open-loop gain of the OPAMP2.

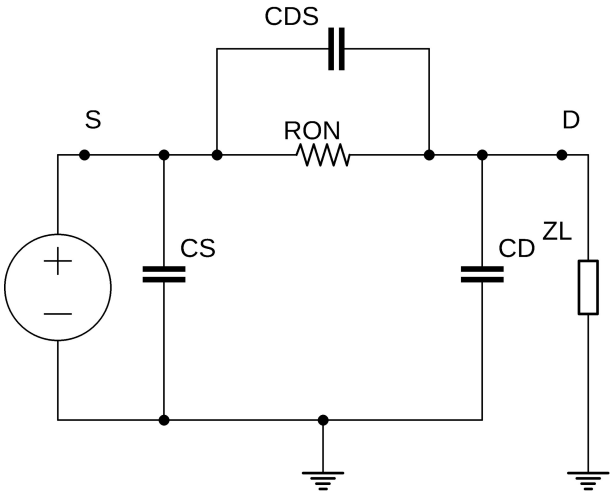

Figure 4.4: Model of the AC performance of an on-state analog CMOS switch.

The open-loop gain depends on the bandwidth of the op-amp. Considering that the system operates at medium to high frequencies, the roll-off of this parameter cannot be neglected. Thus, the capacitor C_{O1} is added to model this behavior. Considering $R_1 = R_2 = R_3 = R_4 = R$ and the finite gain bandwidth of the op-amp, f_{gbw}, this output capacitance, C_{O1}, can be calculated by (4.4) [19].

$$C_{O1} = \frac{2R}{2\pi f_{gbw} R(2R||R_5)} \tag{4.4}$$

4.4.2 Multiplexer

Multiplexers are common types of switches based on Complementary MOSFET (CMOS) technology. The ideal characteristics of multiplexers include a zero on-resistance and an infinite off impedance, zero switching time, zero leakage switching, and zero power dissipation [26]. The MOSFET presents a non-linear behavior of the voltage-controlled resistance that increases with the signal voltage. To minimize this effect, an N-type MOSFET is combined with a P-type MOSFET [26].

There are some characteristics present on the multiplexers that affect the DC signal, whereas others affect the AC signal. Additionally, some non-idealities affect both the AC and DC signals. Since a sinusoidal signal is expected in the channels of the multiplexer, the AC performance of the multiplexer is considered in the error analysis. Therefore, the model of these error sources that affect the on-state of the multiplexers is shown in Fig. 4.4.

These characteristics are the on-resistance, R_{ON}, which changes non-linearly with the power

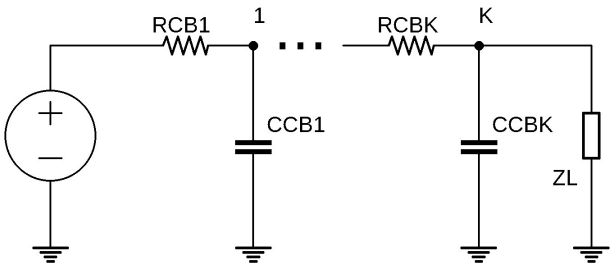

Figure 4.5: Model of the signal delay caused by the distributed RC circuit in cables.

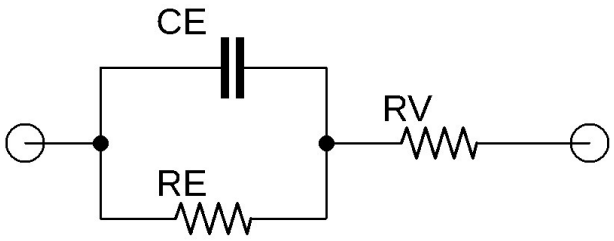

Figure 4.6: Model of the electrode-electrolyte interface.

supply, the parasitic capacitances from source and drain, C_S, C_D, which shunt current or forms a voltage divider with the signal, and the non-ideal isolation, C_{DS}, when the multiplexer switches are off.

4.4.3 Cable

Ideally, a cable must possess a zero impedance path to transmit the signal from point to point. However, a signal delay is present in the cable due to parasitic capacitances present in the system [27]. A method to model this effect is by considering a network of RC circuits from node 1 to K, as shown in Fig. 4.5.

4.4.4 Electrodes

When a potential is applied to the electrolyte by an electrode, there is an ionic movement towards the direction of the electrodes. This phenomenon leads to the formation of an ionic double layer [25]. Therefore, three effects are observable in this system: the charge transfer resistance, the double-layer capacitance, and the bulk resistance [28]. The equivalent circuit of an electrode-electrolyte interface is given in Fig. 4.6.

The charge transfer is the effect of transferring ions from the electrode to the electrolyte, which presents resistance to this process. Considering the current density, j, and the overpotential η,

and by analogy with Ohm's Law, the charge transfer resistance, R_E, is given by (4.5) [28].

$$R_E = \frac{\partial \eta}{\partial j} = \frac{GT}{j_0 F} = \frac{E_T}{j_0} \tag{4.5}$$

where G is the gas constant, F is the Faraday constant, T is temperature, j_0 is the exchange current density, E_T is the temperature voltage. The value for the E_T at $298K$ is $0.026V$.

The double-layer formed in the interface between the electrode and the electrolyte stores electrical charges. Experiments and theory support that these charges vary according to the potential between this layer. A way to represent and model these charges is by considering the capacitance of two parallel plates, the first being the electrode surface and the opposite plate being electrolyte. The Helmholtz double-layer capacitance, C_E, is given by (4.6).

$$C_E = \frac{dq_m}{dV} = \frac{\varepsilon_T \varepsilon_0}{\delta_H} \tag{4.6}$$

where q_m is the excess charge on the metal, ε_0 is the permittivity of a vacuum, ε_T is the relative permittivity of the material between plates, and δ_H is the distance between the plates formed by the electrolyte and electrode. However, the double layer is not constant with potential and practical values, considering the small applied potential from outside the system, can be estimated as 10 $\mu F/cm^2$ [28].

The bulk resistance models the effect of transferring the electrodes from the bulk solution to the interface of the system. The value of this resistance can be modeled considering a hemispherically shaped electrode immersed in an electrolyte with a vessel far larger than the electrode. Considering that the current density from this electrolyte must be the same as the current from the electrode, and using Ohm's Law, the relationship for the bulk resistance, R_V, is given by (4.7) [28].

$$R_V = \frac{1}{2\pi\sigma r_{elec} p} \tag{4.7}$$

where σ is the electrolyte conductivity, r_{elec} is the radius of the electrode, p is the shape factor. The shape factor for electrodes hemispherically shaped is $p = 1$, for metal spheres $p = 2$ and for a flat-cut disk shape $p = 0.66$.

4.4.5 Voltmeter

The in-amp is a circuit comprising op-amps to perform the differential measurement. It is common to use the 3 op-amp topology. This consists of two op-amp buffers in the input and an

op-amp receiving the signals at the inverting and non-inverting input. The reason for the op-amps in the buffer configuration is to improve the input impedance of the circuit [29]. The ideal behavior of the in-amp is to measure differentially the voltage, according to (4.8) and (4.9).

$$V_D = (V_+ - V_-) \tag{4.8}$$

$$V_{IAideal} = A_D V_D \tag{4.9}$$

where $V_{IAideal}$ is the ideal output voltage, V_D is the differential voltage, V_+ is the non-inverting input and V_- is the inverting input. However, an additional term is added to the output in a real system, the CMV, defined in (4.10).

$$V_{CM} = \frac{(V_+ + V_-)}{2} \tag{4.10}$$

This CMV is present in the measurement and the real voltage output, V_{DReal}, is given according to (4.11).

$$V_{IAreal} = A_D V_D + A_{CM} V_{CM} \tag{4.11}$$

where A_{CM} is the common-mode gain. The parameter that indicates the ability to reject the common-mode voltage is the CMRR, of which the definition is given by (4.12).

$$CMRR = 20 \cdot log_{10} \left| \frac{A_D}{A_{CM}} \right| \tag{4.12}$$

An ideal voltmeter has an infinite CMRR. To improve further the CMRR of the in-amp, Shi et al. [30] proposed a design with 2-stages of amplification, with 3 in-amps, which is shown in Fig. 4.7.

The voltage output of the circuit is given by (4.13) [30]

$$\begin{aligned} V_{IA} = &\left[(A_{D1} + A_{D2}) A_{D3} + \frac{A_{D1} - A_{D2}}{2} A_{CM3} \right] V_D \\ + &\left[(A_{CM1} - A_{CM2}) A_{D3} + \frac{A_{CM1} + A_{CM2}}{2} A_{CM3} \right] V_{CM} \end{aligned} \tag{4.13}$$

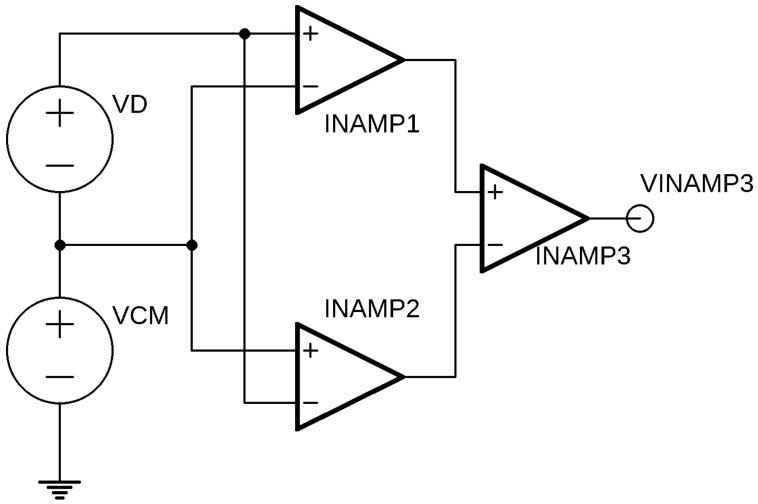

Figure 4.7: Circuit of the 2-stages voltmeter.

Considering that the INAMP1 matches the INAMP2 ($CMRR_1 = CMRR_2 = CMRR$), the CMRR of the 2-stage in-amp is given by (4.14).

$$CMRR_{total} = 2 \cdot CMRR \cdot CMRR_3 \tag{4.14}$$

Equation (4.14) shows the CMRR for the ideal case. Mismatches between the in-amps may be present and it is reported that, even with a 10% mismatch between in-amps, the CMRR is improved by 26 dB [30].

4.5 Image Reconstruction

The focus of the EIT acquisition system developed by the authors is to reconstruct an image to analyze the flow in multiphase flow applications. The image reconstruction proceeds by solving an inverse problem. The forward problem consists in a bidimensional domain Ω with an electrical conductivity σ and a scalar potential distribution u in the domain, and potential U_l at the electrodes in the contour $\partial\Omega$ where a current I_l is injected. The equations that represent the phenomenon, known as the Complete Electrode Model, are described by (6.1)-(6.4) [11, 31].

$$\nabla \cdot (\sigma \nabla u) = 0 \quad in\ \Omega \tag{4.15}$$

$$u + z_l \sigma \frac{\partial u}{\partial n} = U_l \quad in\ e_l,\ l = 1, 2, ..., L \tag{4.16}$$

$$\int_{e_l} \frac{\partial u}{\partial n} dS = I_l \quad in\ e_l,\ l = 1, 2, ..., L \tag{4.17}$$

$$\sigma \frac{\partial u}{\partial n} = 0 \quad in\ \partial\Omega \setminus \cup_{l=1}^{L} e_l \tag{4.18}$$

where n is the normal of the contour $\partial\Omega$, z_l is the contact impedance, e_l is the l-esimal electrode in the contour $\partial\Omega$. To confer existence and uniqueness to the solution, two additional conditions are necessary. Thus, the charge conservation is given by (6.5).

$$\sum_{l=1}^{L} I_l = 0 \tag{4.19}$$

and the determination of a reference point is given by (6.6).

$$\sum_{l=1}^{L} U_l = 0 \tag{4.20}$$

The forward problem is implemented and discretized by the Finite Element Method.

The inverse problem is solved by Gauss-Newton optimization. This procedure is responsible for reconstructing the static images by minimizing the norm of the difference between the measurements and the forward problem output. It is described by (6.16)-(6.17) [11, 31].

$$\delta V = V_{meas} - V_{fwd} \tag{4.21}$$

$$\sigma_k = \sigma_{k-1} + \left(J^T J + \alpha^2 \tilde{L}^T \tilde{L}\right)^{-1} \left(J^T \delta V + \alpha^2 \tilde{L}^T \tilde{L} \left(\sigma_{ref} - \sigma_0\right)\right) \tag{4.22}$$

where J is the Jacobian, V_{meas} is the voltage measurements from the DAQ, V_{fwd} is the voltages simulated by the forward problem, σ is the estimated conductivity, σ_{ref} is a reference conductivity, σ_0 is an initial conductivity, $\tilde{L}$ is the regularization matrix, and the α is the regularization parameter, for which the value chosen in this work is 0.0005. An open-source software is utilized for the reconstructions, the Electrical Impedance Tomography and Diffuse Optical Tomography Reconstruction Software (EIDORS) [32]. The regularization matrix chosen is the main diagonal of the approximated Hessian $(J^T J)$, the NOSER prior.

4.6 Results and Discussion

4.6.1 Errors in the Ring of Resistors

To evaluate the errors in the system, measurements are performed in a ring of 16 resistors connected in series. Between each node of the ring, the current is injected and the voltages are measured according to the adjacent pattern. The voltage is measured at 18 different frequencies, from 5 kHz to 100 kHz. 500 sets of measurements, corresponding to an image for each set when reconstructing the conductivities, are used to evaluate the repeatability of the equipment. To reproduce signals of different magnitude, three different load resistors, of 100 Ω, 511 Ω, and 1000 Ω, with 1% of tolerance, are used with an in-amp gain of 7.25. Since the resistors set in the ring present the same nominal specification, the voltage drops are the same between each resistor. This value is calculated with SPICE simulations and it is used as a reference. The voltage value on the input of the demodulation is expected to be 44.2 mV for the ring with 100 Ω resistors, whereas the signal for the 511 Ω and 1000 Ω is expected to be a voltage of 226.0 mV and 442.4 mV respectively.

The frequency response is shown in Fig. 4.8. Compared with the reference, there is an error dependence on the signal magnitude, since the measurements with 511Ω resistors presented measurements closer to the reference than the 100 Ω resistor, although both presented an observable error. However, measurements with 1000 Ω presented a good match between 20 kHz and 50 kHz. This behavior is as expected and reported in the datasheet [23]. Utilizing a correct gain to input a voltage compatible with the dynamic range of the ADC should decrease this error. Also, there is an observably increasing error caused by the limited bandwidth. At lower frequencies, the AD536 produces a frequency-dependent average error caused by the settling time of the demodulation that becomes prominent as the frequency decreases. On the other hand, at higher frequencies, the error is dependent not on the demodulator, but instead on the stray capacitances in the acquisition system and the active low-pass filter before the input of the demodulation.

To calculate the error in each set of measurements, an RMS measurement is utilized, which is defined in (4.23), [8]:

$$RMS = 100\% \times \sqrt{\frac{1}{L\,(L-3)} \sum_{i=1}^{L(L-3)} \left(\frac{V_{meas_i} - V_{ref_i}}{V_{ref_i}} \right)^2} \tag{4.23}$$

where RMS is the RMS error, L is the number of electrodes, V_{meas} is the measured voltage, V_{ref} is the reference voltage calculated from SPICE. This measurement indicates the level of

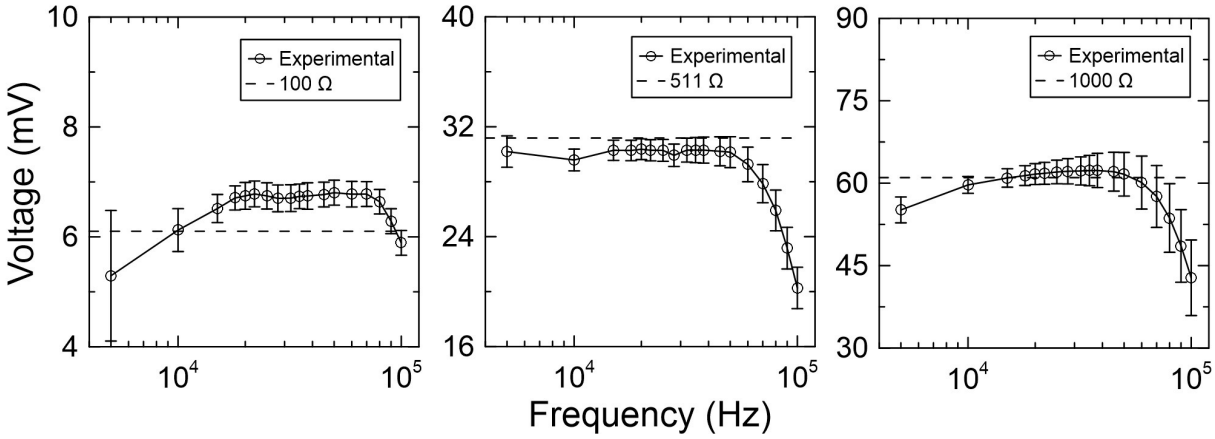

Figure 4.8: The measured and reference frequency response in the output of the demodulator for 100 Ω, 511 Ω and 1000 Ω load resistor.

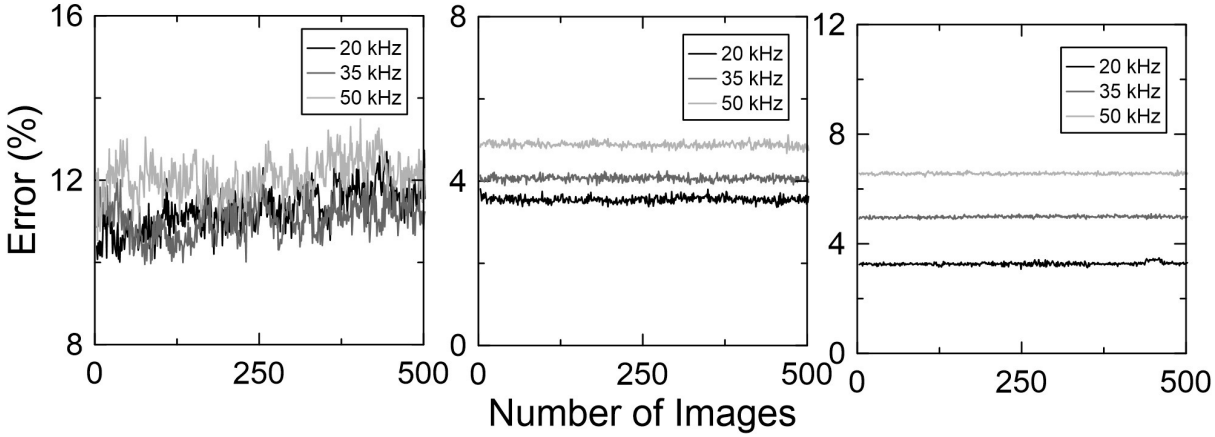

Figure 4.9: Random errors observed when measuring with a ring of resistor with 100 Ω, 511 Ω and 1000 Ω load resistor.

repeatability shown in the equipment.

The RMS error is evaluated in Fig. 4.9. The signal magnitude influences the random errors present at the demodulator. Considering the higher voltages, for 511 Ω and 1000 Ω, the error is constant regardless of the number of images, and it increases with frequency due to the ripple present in the output of the demodulation, shown in Fig. 4.10. This ripple is more pronounced at higher frequencies, which is also represented by the standard deviation of Fig. 4.8. Even though the RMS-to-DC converter demodulates the wave properly in a simple manner, a considerable amount of error is introduced in this subsystem.

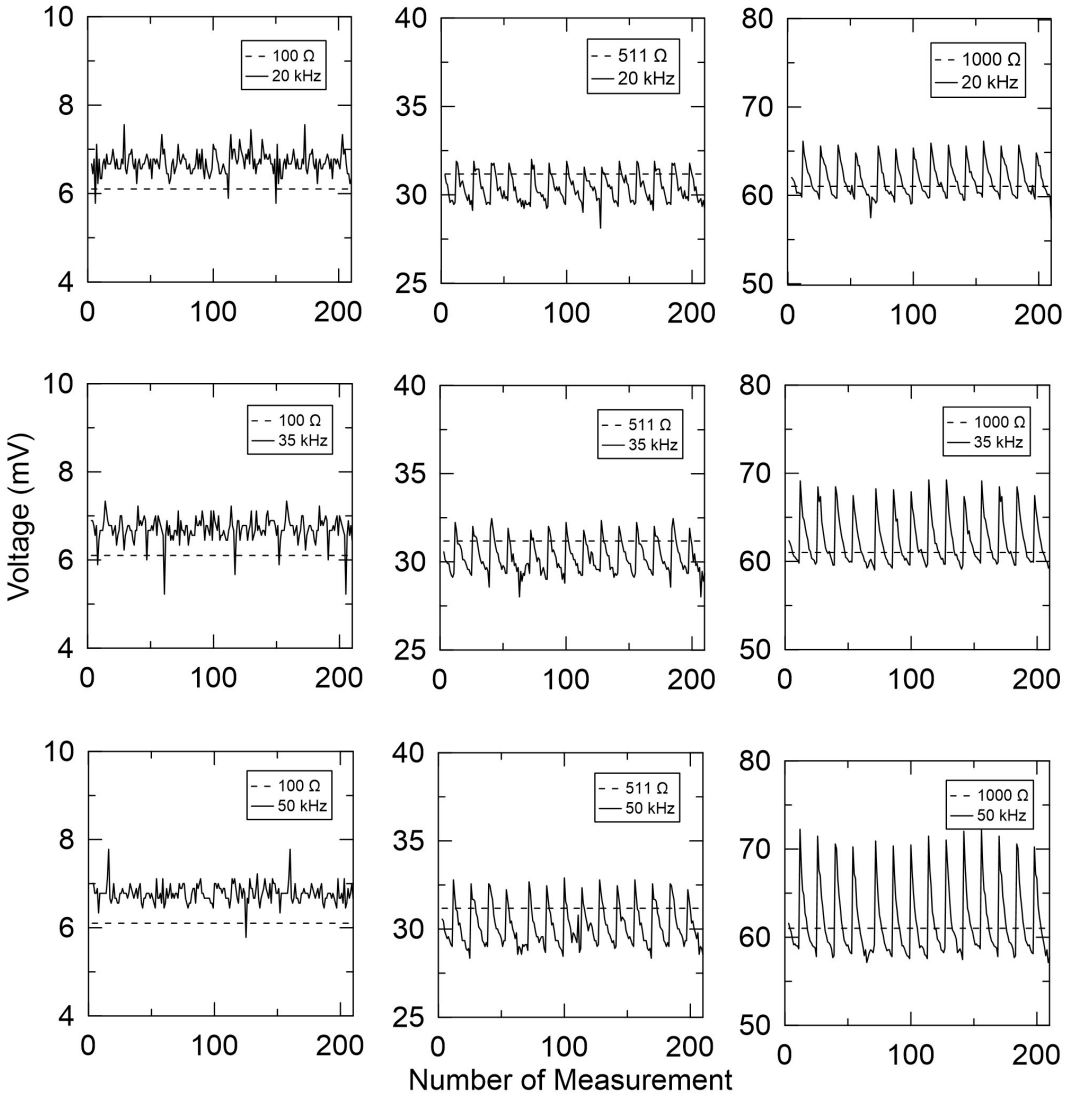

Figure 4.10: The voltage for each measurement in a ring of resistors with a nominal load resistance of 100 Ω, 511 Ω, 1000 Ω, from left to right, varying between 20 kHz, 35 kHz and 50 kHz from top to bottom.

4.6.2 Errors in the Water Vessel

The measurements and the error calculation in a saline solution are performed according to Wilkinson et al. [7] and Wang et al. [8]. The measurements from the DAQ system are compared with the homogeneous solution of the forward problem. With this data, the performance of the developed DAQ is evaluated by the calculation of the error and the signal-to-noise ratio (SNR). To evaluate the influence of the electrical conductivity on the measurements, a 1 L aqueous solution of tap water is prepared with 5 different conductivities by increasing the salinity of the water. Measurements were taken of 500 sets of data from 5 kHz to 100 kHz. The conductivity range is restricted to 74-1129 μS/cm. The gain of the DAQ is changed to take advantage of the dynamic

range from the ADC. A 14.4 cm diameter acrylic container is used as the phantom vessel. The 16 sensors are hemispherically shaped with a radius of 18 mm stainless steel, positioned at 40 mm from the bottom.

The error present at each frequency, when measuring in the vessel, is shown in Fig. 4.11(a). There is a major discrepancy between the forward model and the measured data. This error is attributed to the fact that the actual vessel is treated as a 2D phenomenon, a simplification that impacts directly on the magnitude of the simulated signals [33]. Ma et al. [34] reported over 80% error when comparing 3D simulations with 2D analytic results.

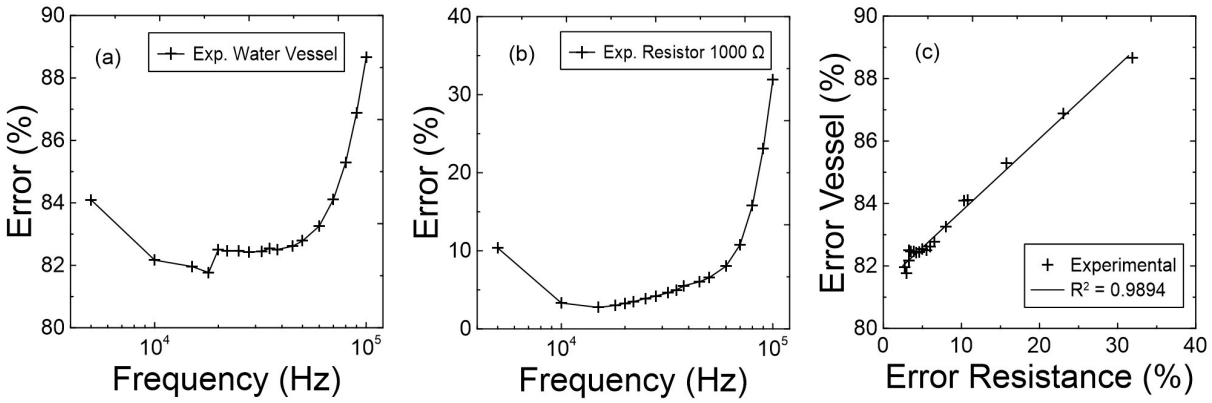

Figure 4.11: (a) Measurement error obtained in a vessel of water, with a water conductivity of 74μS/cm, (b) Correlation between the measurements obtained in the ring of resistors and the water vessel.

The errors obtained in the water vessel (Fig. 4.11(a)) and the ring of resistors (Fig. 4.11(b)) are compared in Fig. 4.11(c). There is a linear correlation between the two measurements, indicating that a linear adjustment could eliminate the error caused by the domain simplification. The offset and gain to adjust the forward model considering the electrical conductivity range tested are shown in Fig. 4.12. The variability of the measurements corresponds to the standard deviation concerning the working frequency, from 20-50 kHz. As it is shown, there is a minor influence caused by the frequency, although there is a non-linear variation concerning the electrical conductivity. This is expected since the model is a non-linear problem, represented by (6.1). Measurements for 16 electrodes are shown in Fig. 4.13, after the adjustment.

The SNR is the parameter that indicates the level of noise that is corrupting the signal, as given in (4.24).

$$SNR_i = 20 \cdot log\left(\frac{|E\left(V_{meas_i}\right)|}{STD\left(V_{meas_i}\right)}\right) \tag{4.24}$$

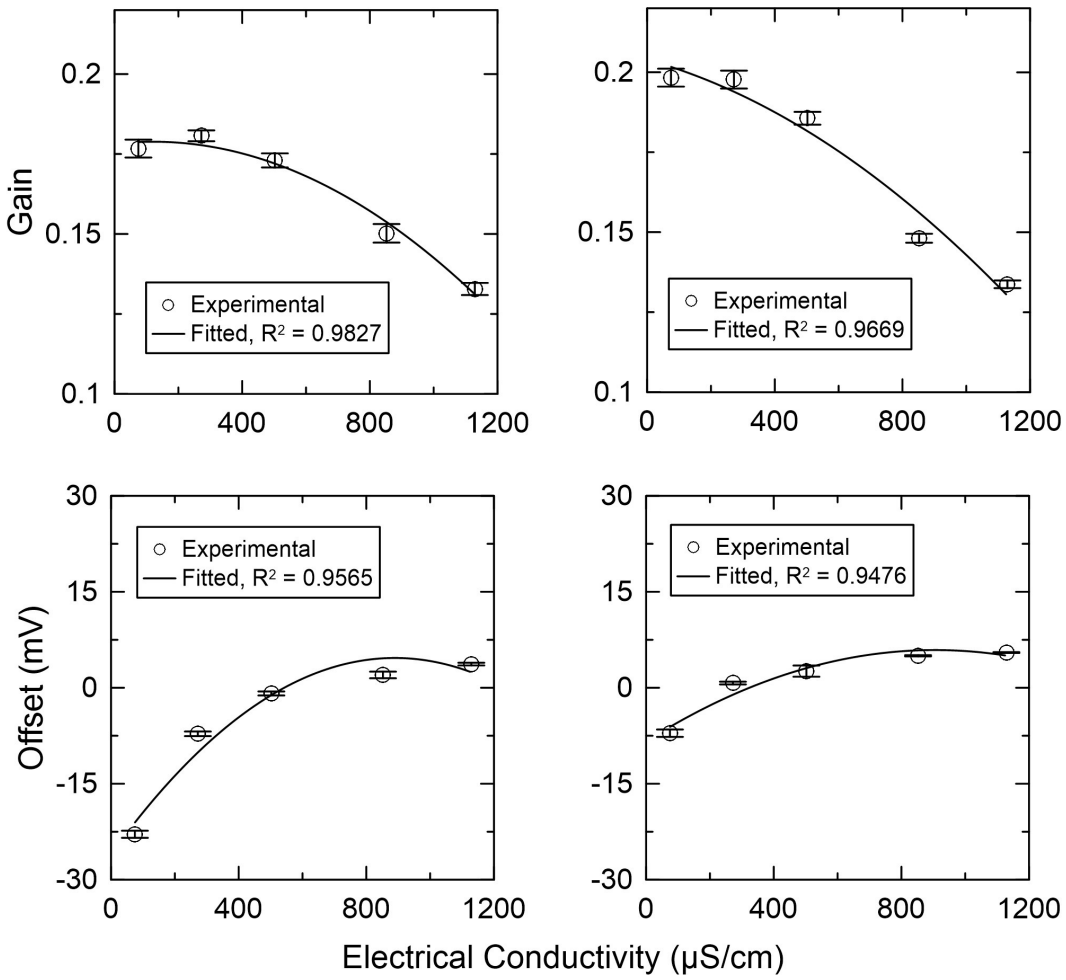

Figure 4.12: Gain and offsets error observed in the forward problem with 8 electrodes, left, and 16 electrodes, right.

where $E(.)$ is the expected measurement value, and $STD(.)$ is the standard deviation of the measurement value.

It is evident, analyzing Fig. 4.14, that the noise has a direct impact on the error when measuring with 16 electrodes, by observing that there is a linear relationship between them. The signal strength is decreased due to the smaller distance between the electrodes, representing a smaller resistance, and is thus more susceptible to noise. To overcome this situation, a current source with an adjustable current magnitude could be implemented to provide a signal with sufficient strength when the medium presents higher conductivities. Considering the measurements with 8 electrodes, the error remains constant, without significant noise variation. This behavior is observed since the electrodes are well spaced for the current magnitude.

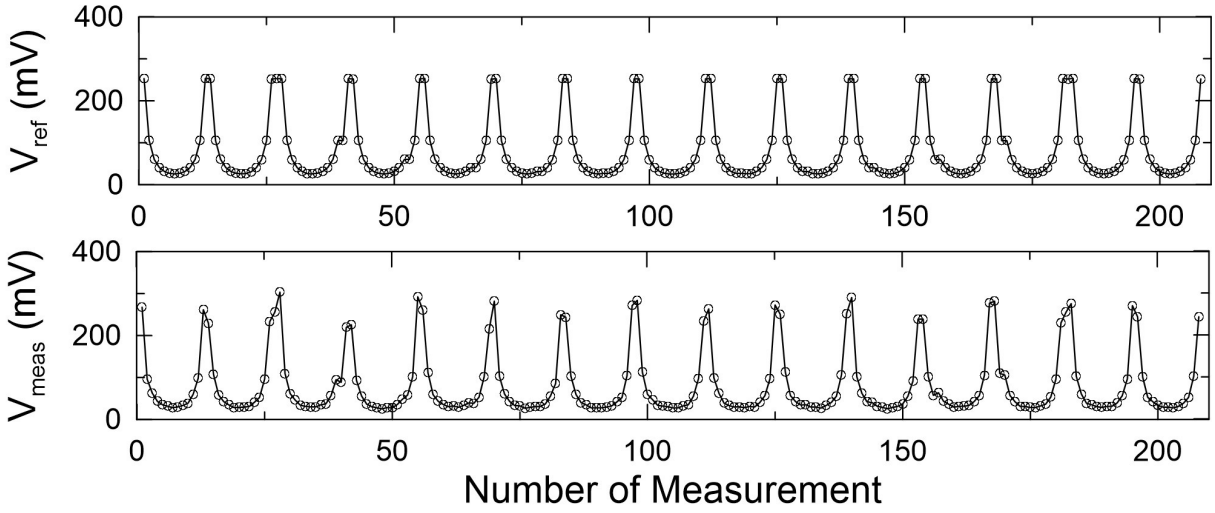

Figure 4.13: The reference voltages using 16 electrodes from the forward problem considering a homogeneous solution (top) and the voltages for each measurement in the acquisition system in the vessel after the adjustment (bottom).

4.6.3 Modeling the Errors

Combining the models of the real processes, the DAQ channel is modeled in SPICE according to Fig. 4.15(a). The circuit is modeled considering the ring of resistors and the water vessel with the electrodes. The influence of noise, including from the demodulator, the ADC and other sources, is neglected. The signal is compared with the ideal 4-electrodes model in Fig. 4.15(b), considering an ideal current source and voltmeter. An AC sweep analysis is performed to evaluate the frequency response of the system regarding the error and the voltage from 1kHz to 100kHz. The error is evaluated by (4.25).

$$\epsilon = \frac{|V_{out} - V_{ideal}|}{V_{ideal}} \tag{4.25}$$

where ϵ is the error, V_{out} is the output from the DAQ model, and V_{ideal} is the output from the ideal 4-electrode model.

The equivalent component values are given in Table 4.1. The output resistances from the VCCS are calculated by (4.2) and (4.3), considering a tolerance of 1% and the open-loop gain of 75 dB from the op-amp AD827. The output capacitance is calculated by (4.4), considering a gain bandwidth of 50 MHz. The parasitic capacitances and on-resistance from the multiplexers, C_S, C_D, R_{ON}, are given by the datasheet of the ADG506 [21]. The non-ideal isolation capacitor is neglected since medium frequencies are being considered. The values for the cable capacitance are considered for less than 1-meter length [11] and 1 node only. The electrodes components are

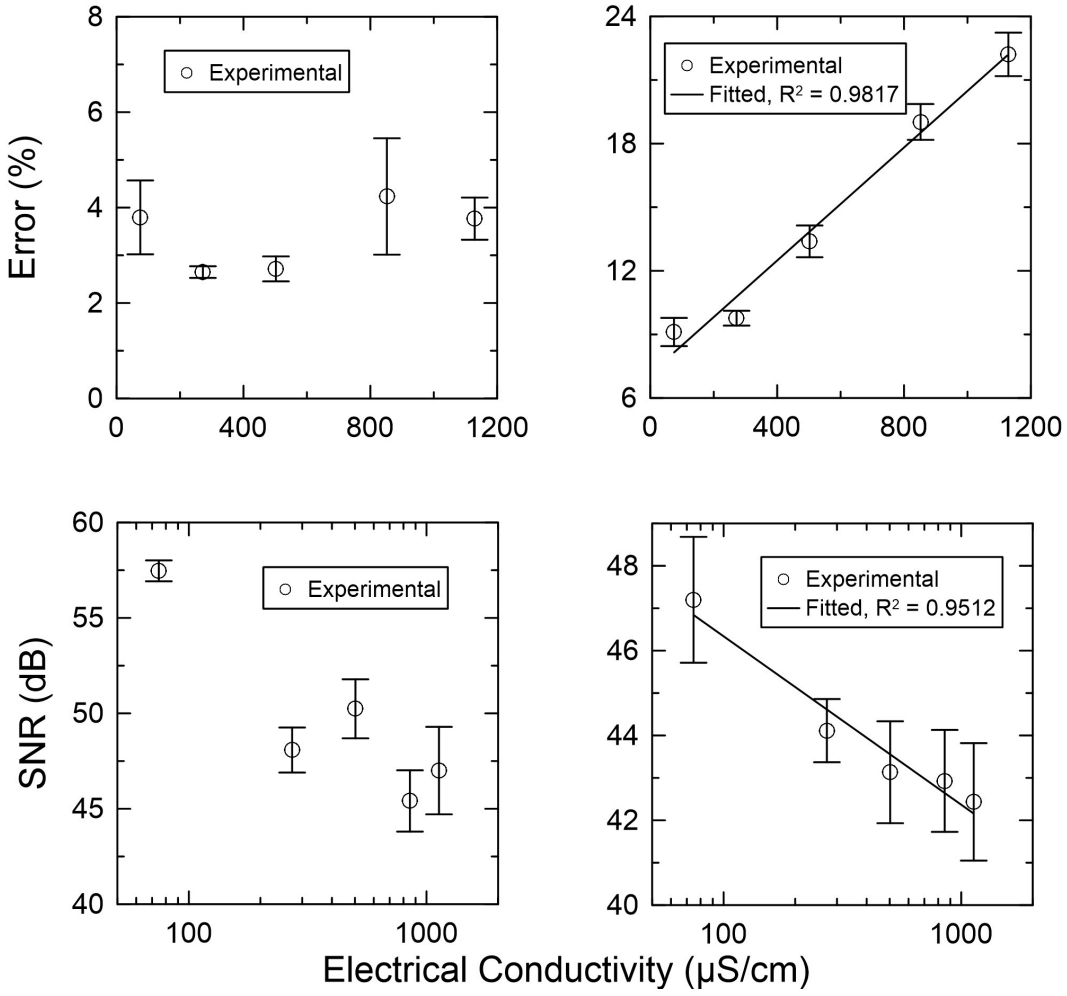

Figure 4.14: Error and SNR observed in voltage measurements acquisition with 8 electrodes, (left) and 16 electrodes (right).

given by (4.5) and 10 $\mu F/cm^2$ for the charge transfer resistance and double-layer capacitance respectively. The load resistance for the ring of resistors model is 1 $k\Omega$, and the bulk resistance for the electrode modeling is given by (4.7). A value of 1 MΩ is assumed for the voltmeter, which is the resistor from the coupling circuit that limits the input resistance of the voltmeter. The input capacitance is given by the datasheet of the voltmeter [22].

The voltmeter is modeled with an in-amp SPICE model, presenting a CMRR corresponding to the behavior shown in Fig. 6.4(a). It is compared to the experimental values from the datasheet and the results presents good agreement between the real circuit and the model.

The error and the voltage between the experiment and the model are compared to further validate the model. The results are considered from the ring of resistors with 1000 Ω load resistor and the 8 electrodes with 74 $\mu S/cm$ since these experiments are less influenced by noise and errors

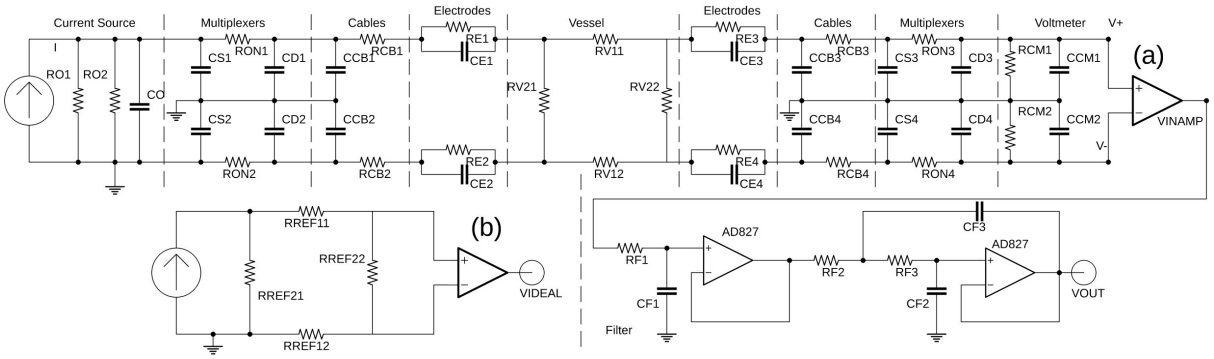

Figure 4.15: (a) The equivalent circuit that includes the sources of error modeled in SPICE, (b) The equivalent circuit modeled in SPICE representing the ideal 4-electrodes model.

Table 4.1: Values considered in the error evaluation equivalent circuit.

Subsystem	Component	Resistor	Vessel
Current Source	Ro1 (Ω)	50k	50k
	Ro2 (Ω)	1.875 M	1.875 M
	Co (pF)	9	9
Multiplexers	Cs (pF)	44	44
	Ron (Ω)	600	600
	Cd (pF)	5	5
Cables	Rcb (Ω)	0.053	0.053
	Ccb (pF)	33	
Electrode	Re (Ω)	-	10.2k
	Ce (nF)	-	254
Resistor/Vessel	Rv1 (Ω)	1k	2.4k
	Rv2 (Ω)	7k	2.4k
Voltmeter	Rcm (Ω)	1M	1M
	Ccm (pF)	9	9

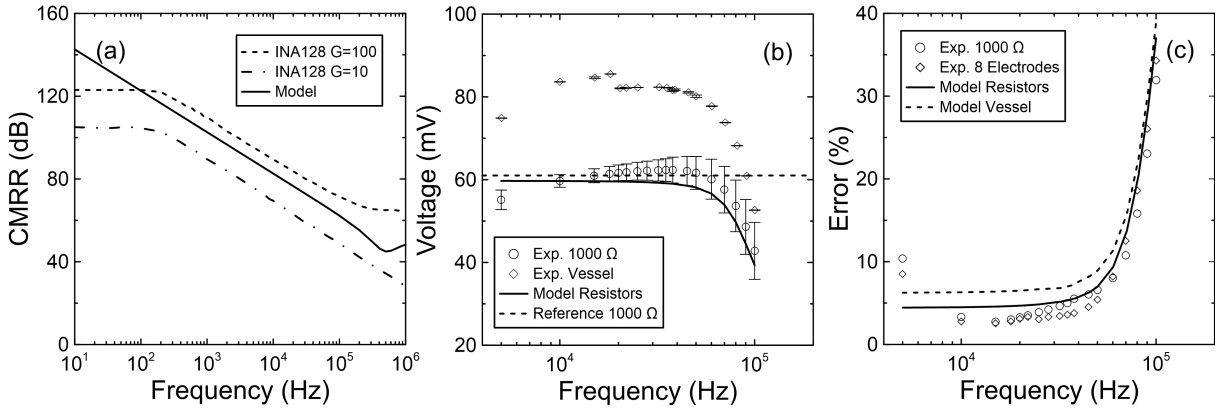

Figure 4.16: Validation of the model. (a) CMRR modeled by the in-amp SPICE model compared to the experimental values provided in the datasheet [22]. (b) Output voltage of the SPICE model and the voltage measured in the ring of resistors with 1000 Ω. (c) Experimental error for the ring of resistors with 1000 Ω and the error for 8 electrodes compared with the response modeled in SPICE.

from the demodulation. The voltage is shown in Fig. 6.4(b). The results for the ring of resistors showed good accordance between the model and the experimental values. On the other hand, the results for the water vessel are not shown since the voltage is greatly overestimated, in the order of 0.7 V. Despite these discrepancies, the modeled error for both the ring of resistors and the vessel showed good agreement, in Fig. 6.4(c). There are discrepancies at lower frequencies due to the unaccounted errors in the demodulation subsystem.

4.6.4 Investigation of Different Configurations for the Subsystem and Sensors

Analyzing the resistance SPICE model, some aspects are relevant to improve the design. The output resistance of the current source exhibits a relevant influence in the error. The goal is to obtain a current source output impedance that is nearly infinite, so that the current remains unchanged. Fig. 4.17(a) shows the error dependence on the output resistance of this system relative to the matching between resistors. The tolerance must be well-matched to improve the accuracy of the system. If a tolerance of 0.1% by is assured matching and trimming the feedback resistors to satisfy (4.1), a substantial reduction further of the error is observed, from 4.69% to 1.05% at 20 kHz. Increasing the tolerances to 0.01% would decrease the error to 0.67%. The open-loop gain of the op-amp has an impact, although it is much less sensitive than the matching of the current source resistances. The dominant part of the output resistance is the one representing the matching of the resistors. The actual effect of the open-loop gain of the

op-amp in the current source is to reduce the output resistance of the subsystem by a certain amount related to $R_{o1}||R_{o2}$. With a higher tolerance design, 1% for instance, this resistance has less effects the equivalent resistance, reducing the total output resistance from 2.5% to about 0.004% considering an open-loop gain of 75 dB and 120 dB. However, as the tolerances are tighter, the effect becomes more evident. There is a reduction of 21% to 0.048% considering 75 dB and 120 dB in a VCCS design with a 0.1% tolerance match. Despite these changes, the error decreases from 4.69% to 4.58% in 20 kHz when tolerances match 1% and considering 0.1% tolerance, there is a reduction from 6.98% to 6.89% for 75 dB and 120 dB respectively. But it is important to prioritize the op-amp with high open-loop gain as a guideline for high accuracy devices to achieve a higher output impedance in the current source.

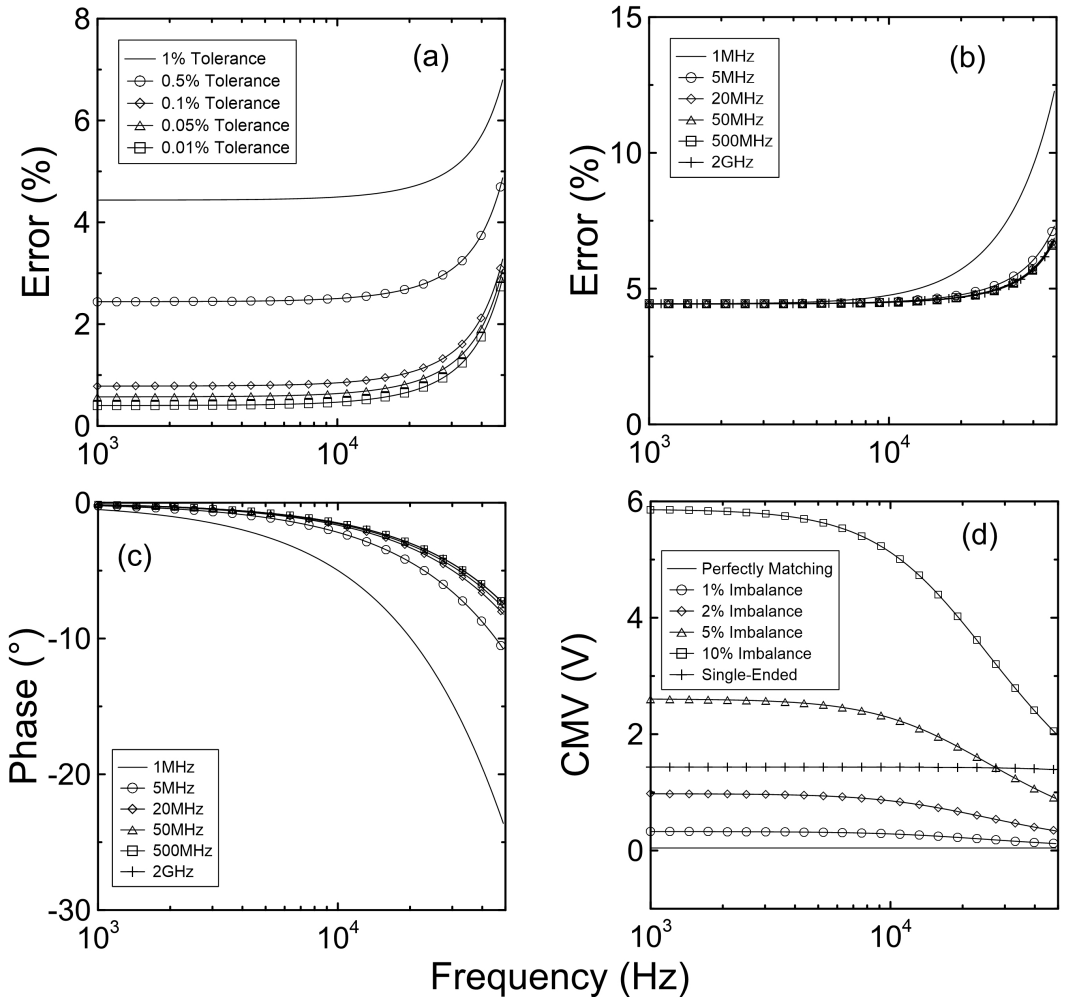

Figure 4.17: Comparison of different aspects and configurations for the VCCS. (a) The matching between resistances, (b) Op-amp bandwidth of the current source, (c) Phase delay before the filter considering different op-amp bandwidths, (d) Common-mode voltage considering imbalance between the current sources of a dual configuration.

At higher frequencies, the error is dominated by the reactive parts, the stray capacitances. The bandwidth of the op-amp is directly related to the output capacitance of the VCCS. The error and the phase delay after the in-amp caused by this bandwidth limitation are given in Fig. 4.17(b) and (c). A low bandwidth would be detrimental to the design, introducing considerable error, as is seen for 1 MHz. The current design utilizes the op-amp AD827, which presents a bandwidth of 50 MHz, a good threshold to avoid further errors in lower bandwidth designs.

Another topology frequently utilized is the mirrored Howland current source. This is a combination of two single-ended currents sources to form a dual source. The primary consequences are the addition of the two output impedances from the two single-ended current sources [18] and the reduction of the CMV, from 1.43 V to 86 mV at 20 kHz, shown in Fig. 4.17(d). With a single-ended topology the error is 6.82% whereas in the differential topology it is 2.41%, which is a significant decrease. The imbalance between the two currents injected causes a frequency-dependent increase in the CMV for this topology, shown in Fig. 4.17(d), although the design presents lower CMV even with 2% imbalance. There is no observable decrease in error, although, at higher frequencies, the CMRR from the in-amp reduces substantially and may cause errors.

The multiplexers are important to provide simplicity to the hardware but this is at the expense of accuracy since the non-idealities are responsible for introducing errors in the acquisition system [15, 16]. The on-resistance varies with the supply voltage, which could add non-linearities and potentially cause additional errors. Also, the source and drain capacitance present in the multiplexer affect the measurement greatly at medium-to-high frequencies. It is important to select a multiplexer with lower values of these two parameters. A comparison of the error between the currently adopted multiplexer and two commercially available multiplexers is shown in Fig. 4.18(a). The ADG1206, which reduces on-resistance, source and drain capacitance, presents an error of 3.28% at 20 kHz, whereas the current design presents 4.69% at 20 kHz. The other multiplexer, the ADG1406, has a lower on-resistance with higher stray capacitances. This combination provides a decrease in error at lower frequencies, from 4.69% to 2.62%, although it increases to 5.79% at 50 kHz. As expected, the CMV is directly related to the on-resistance whereas the phase is directly related to the stray capacitances, shown in Fig. 4.18(b) and (c).

The implementation of a 2-stage voltmeter is investigated for the design. It is possible to visualize a reduction of the error at higher frequencies, shown in Fig. 4.18(d), considering single-ended and dual VCCS. This error is reduced from 3.94% to 2.74% at 50 kHz for a dual configuration. The CMV presents a frequency-dependent behavior with this voltmeter. At 50 kHz, the CMV increases from 43 mV to 47 mV.

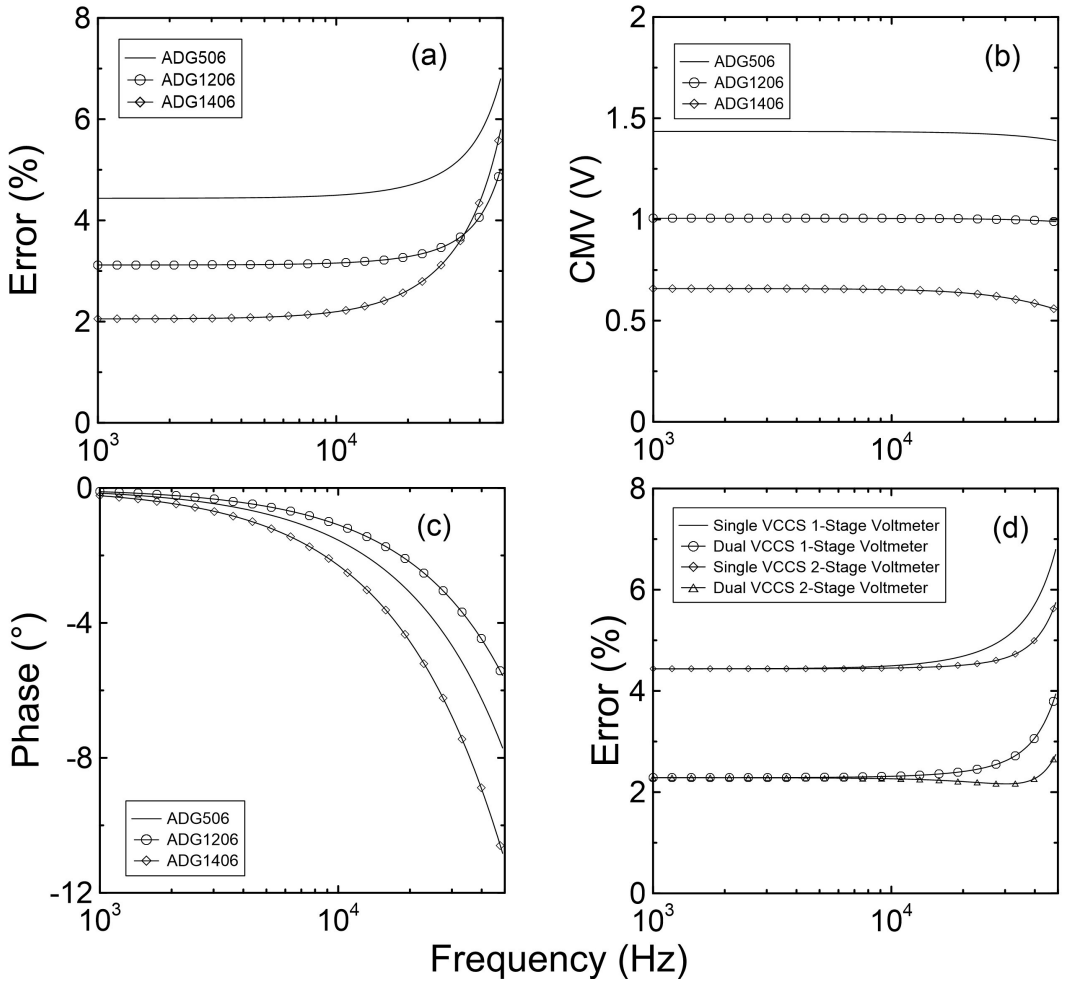

Figure 4.18: Comparison between different multiplexers and voltmeter configurations. (a) Error with different selected multiplexers, (b) Common-mode voltage considering these different multiplexers, (c) Phase delay caused by the multiplexers, (d) Error considering single-stage and dual-stage voltmeter.

The influence of the electrode area and the mismatch between its impedances are investigated by using the electrode model. It is shown in Fig. 4.19(a) that the electrode area must be as large as possible. By increasing by 20% the area of contact, the error decreases from 6.51% to 6.16% and decreasing it in by present significant changes, as shown in Fig. 4.19(b). In the same manner, mismatches in the impedances of the electrodes (Fig. 4.19(c) and Fig. 4.19(d)) do not influence the errors in the DAQ measurements, although it is well known that these mismatches may influence the image reconstruction [12].

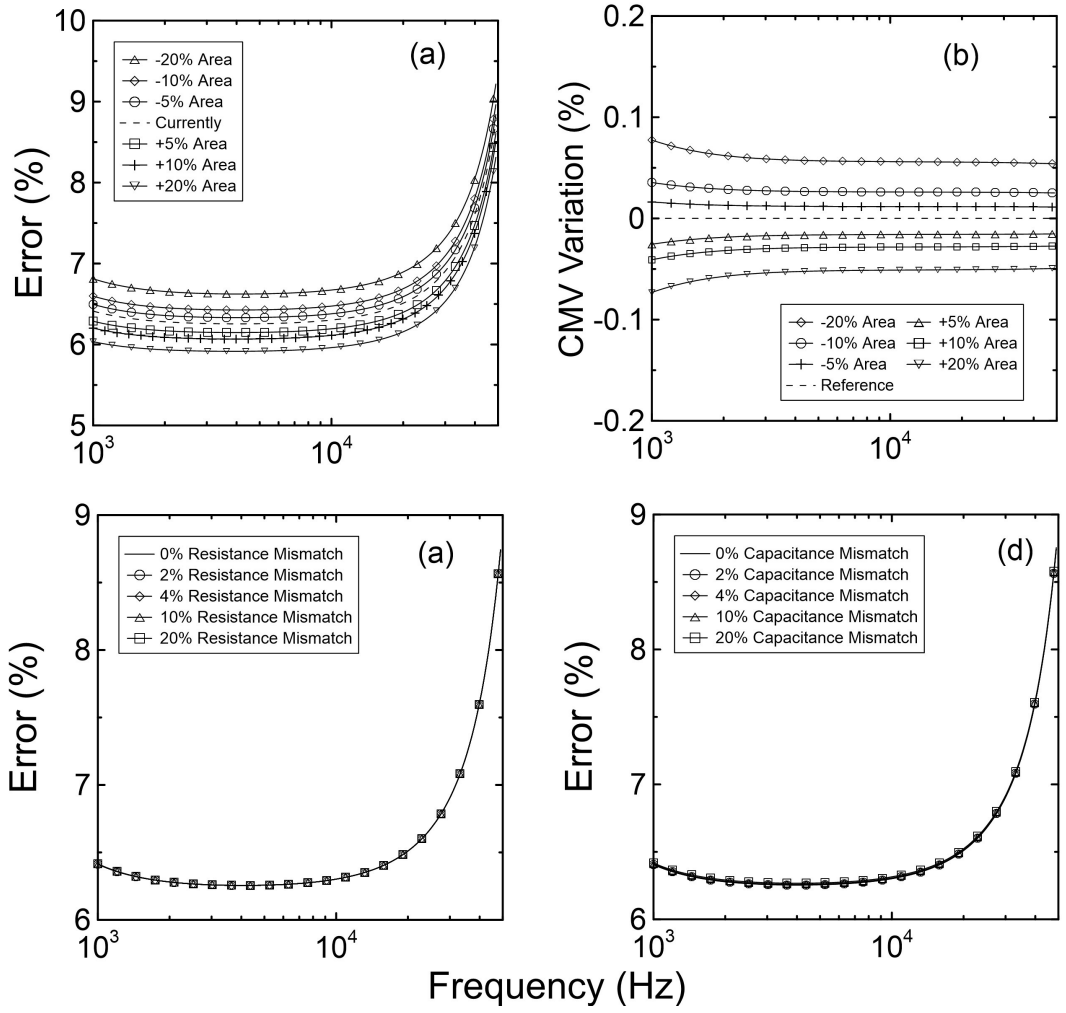

Figure 4.19: Comparison between different aspects of electrode selection. (a) The matching between resistances, (b) Increase and reduction of the area of the electrode, (c) The CMV considering the area variation, (d) The matching between contact capacitance.

4.6.5 Model of the New Design

For the proposed new design of a low-cost system, the following improvements are chosen after evaluating each contribution to the error of the subsystems:

1. The Howland current source is a dual VCCS that matches the resistors with 0.1% tolerance, utilizing op-amps with a bandwidth of 140 MHz and open-loop gain of 126 dB with 0.1% of imbalance between the current sources.

2. Designing a Generalized Impedance Converter (GIC) to cancel output and parasitic capacitances from the VCCS [35].

3. The multiplexers utilized are the IC ADG1206.

4. The cables' parasitic capacitances are neglected due to the driven shields considered in the design [36].

5. The 2-stage voltmeter with the IC AD8421 is adopted to improve the CMRR and the frequency bandwidth [30].

6. The bandwidth of the design considered is 1 kHz to 1 MHz.

7. A digital phase-sensitive detector is adopted, which can retrieve the signals with higher SNR without significant bandwidth limitation as to the RMS-to-DC converter [37]. The measurement bandwidth is limited only by the sampling frequency from the ADC.

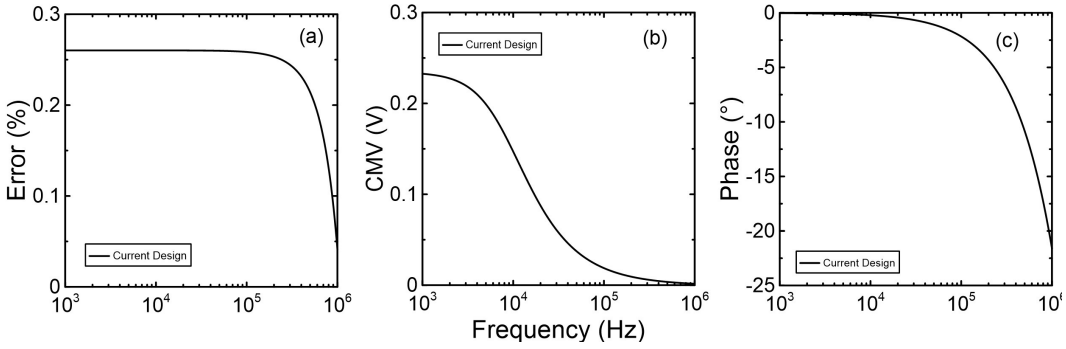

Figure 4.20: The performance of the new design. (a) The error, (b) The CMV, (c) Phase delay.

It is shown in Fig. 4.20(a) that the new design simulation presents an error lower than 0.3%. A fine calibration by trimming the resistors from the VCCS should help achieve the target of 0.1% error. There is a reduction of the error at higher bandwidths, which is caused by the non-ideal behavior of the in-amp. This is because the CMV is not rejected properly, adding to the total attenuated signal by the non-idealities, and momentarily raising the output voltage near the reference signal. For frequencies over the system bandwidth, the error should increase greatly. The common-mode and the phase before the in-amp are shown in Fig. 4.20(b) and (c).

The image from the current design and the new design are evaluated to investigate the influence of these errors in the reconstruction. The position of the phantoms is shown in Fig. 4.21(a) and the experimental reconstruction in Fig. 4.21(b). The homogeneous voltage V_{hom} is calculated considering the forward problem and the conductivity of the saline solution of 74 $\mu S/cm$ and a ratio of $1/100$ for the inclusion conductivity. The error influence is obtained from the normal distribution $V_{syst} \sim \mathcal{N}(0, V_{hom} \cdot \epsilon)$. The white noise influence is obtained from $V_{rand} \sim \mathcal{N}(0, \sigma_{noise})$, where σ_{noise} is the standard deviation from (4.24). The noise is considered to be the same for both reconstruction images, the value of 47.20 dB. Therefore, from these components, the image

reconstruction signal V_{rec} is given by (4.26).

$$V_{rec} = V_{hom} + V_{rand} + V_{syst} \tag{4.26}$$

Reconstructions from fabricated measurements for the current design, in Fig. 4.21(c), presented more influence from error and noise than the experimental measurements, shown in Fig. 4.21(d). Despite these influences, it is clear that the reduced error in the new design improves the image reconstruction, presenting a better image, with more contrast, when compared to the current design.

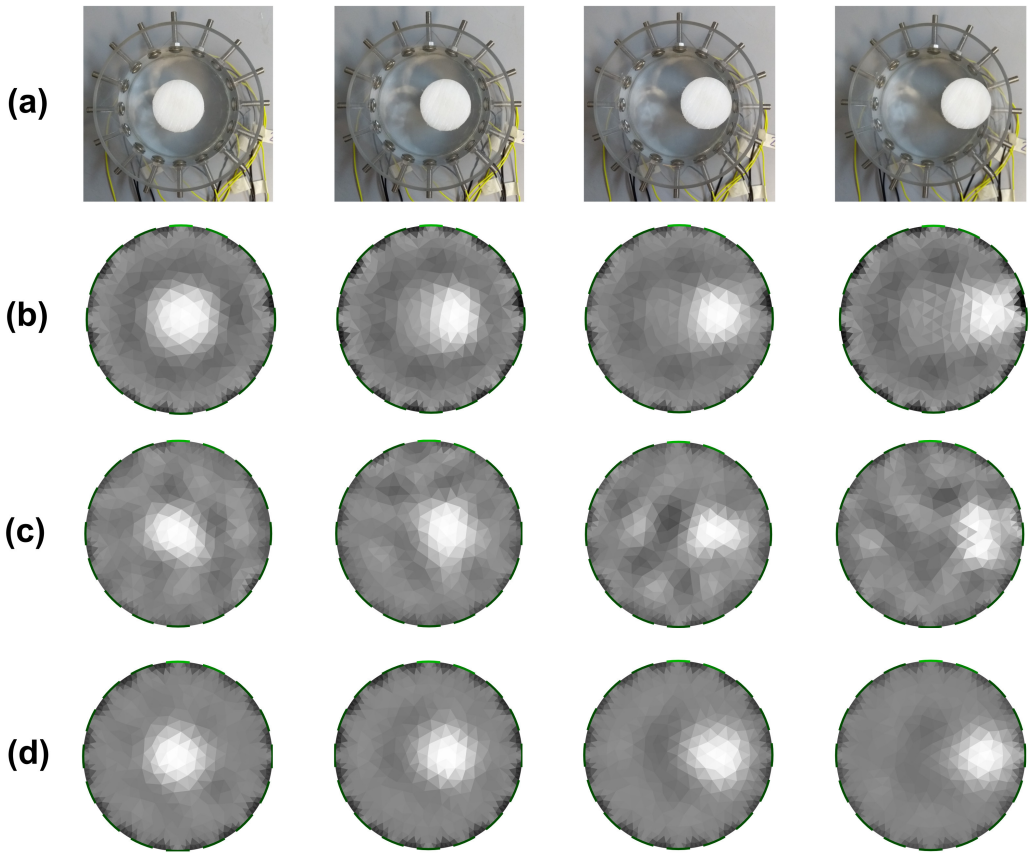

Figure 4.21: Static image reconstruction of a non-conductive inclusion with 16 electrodes. (a) The real position of the non-conductive phantoms, (b) The reconstruction from experimental measurements with the current design, (c) The reconstruction from measurements fabricated computationally for the current design, (d) The reconstruction from measurements fabricated computationally for the new design.

4.7 Conclusion

A methodology to aid in the process of developing a new design of an EIT DAQ system is developed in this work and tested for a low-cost system. This approach consists in outlining the sources of random error by measurement, and the systematic errors by modeling the DAQ channel as their equivalent impedance. From the results, it is possible to understand the impact of each subsystem and design parameter in the error of the system. By inspecting the influence of the SNR in the error of the developed system, it is observed that the magnitude of the current injected is directly related to the noise that corrupts the signal. The influence of each subsystem's non-idealities in the design is evaluated, such as the effect of the output impedance and tolerance mismatching of the current source, cables' stray capacitance, and multiplexer non-idealities. The SPICE model agrees with the experimental data and, by selecting the components appropriately for a new design through this method, the error is expected to reduce from 4.69% to less than 0.3% at 20 kHz. To assess the impact on a static reconstruction, the signal is modeled as a contribution of both random and systematic error. It is demonstrated that the quality of the image reconstruction would greatly improve by this new design.

References

[1] A. Parvareh, M. Rahimi, A. Alizadehdakhel, and A.A. Alsairafi. CFD and ERT investigations on two-phase flow regimes in vertical and horizontal tubes. *International Communications in Heat and Mass Transfer*, 37(3):304 – 311, 2010. ISSN 0735-1933. doi: https://doi.org/10.1016/j.icheatmasstransfer.2009.11.001.

[2] Mi Wang, Jiabin Jia, Yousef Faraj, Qiang Wang, Cheng gang Xie, Gary Oddie, Ken Primrose, and Changhua Qiu. A new visualisation and measurement technology for water continuous multiphase flows. *Flow Measurement and Instrumentation*, 46:204 – 212, 2015. ISSN 0955-5986. doi: https://doi.org/10.1016/j.flowmeasinst.2015.06.022.

[3] B H Brown and A D Seagar. The Sheffield data collection system. *Clinical Physics and Physiological Measurement*, 8(4A):91–97, nov 1987. doi: 10.1088/0143-0815/8/4a/012.

[4] A J Wilson, P Milnes, A R Waterworth, R H Smallwood, and B H Brown. Mk3.5: a modular, multi-frequency successor to theMk3a EIS/EIT system. *Physiological Measurement*, 22 (1):49–54, feb 2001. doi: 10.1088/0967-3334/22/1/307.

[5] Tong In Oh, Hun Wi, Do Yub Kim, Pil Joong Yoo, and Eung Je Woo. A fully parallel multi-frequency EIT system with flexible electrode configuration: KHU mark2. *Physiological Measurement*, 32(7):835–849, jun 2011. doi: 10.1088/0967-3334/32/7/s08.

[6] Tong In Oh, Eung Je Woo, and David Holder. Multi-frequency EIT system with radially symmetric architecture: KHU mark1. *Physiological Measurement*, 28(7):S183–S196, 2007. doi: 10.1088/0967-3334/28/7/s14.

[7] A. J. Wilkinson, E. W. Randall, J. J. Cilliers, D. R. Durrett, T. Naidoo, and T. Long. A 1000-measurement frames/second ERT data capture system with real-time visualization. *IEEE Sensors Journal*, 5(2):300–307, April 2005. ISSN 1530-437X. doi: 10.1109/JSEN.2004.842445.

[8] Mi Wang, Yixin Ma, N. Holliday, Yunfeng Dai, R. A. Williams, and G. Lucas. A high-performance EIT system. *IEEE Sensors Journal*, 5(2):289–299, April 2005. ISSN 1530-437X. doi: 10.1109/JSEN.2005.843904.

[9] Jiabin Jia, Mi Wang, H. Inaki Schlaberg, and Hua Li. A novel tomographic sensing system for high electrically conductive multiphase flow measurement. *Flow Measurement and Instrumentation*, 21(3):184 – 190, 2010. ISSN 0955-5986. doi: https://doi.org/10.1016/j.flowmeasinst.2009.12.002.

[10] Alzbeta Elizabeth Hartinger, Hervé Gagnon, and Robert Guardo. A method for modelling and optimizing an electrical impedance tomography system. *Physiological Measurement*, 27(5):S51–S64, 2006. doi: 10.1088/0967-3334/27/5/s05.

[11] D.S. Holder. *Electrical Impedance Tomography: Methods, History and Applications*. Series in Medical Physics and Biomedical Engineering. CRC Press, 2004. ISBN 9781420034462.

[12] V Kolehmainen, M Vauhkonen, P A Karjalainen, and J P Kaipio. Assessment of errors in static electrical impedance tomography with adjacent and trigonometric current patterns. *Physiological Measurement*, 18(4):289–303, 1997. doi: 10.1088/0967-3334/18/4/003.

[13] Hamid Dehghani and Manuchehr Soleimani. Numerical modelling errors in electrical impedance tomography. *Physiological Measurement*, 28(7):S45–S55, 2007. doi: 10.1088/0967-3334/28/7/s04.

[14] A Nissinen, L M Heikkinen, and J P Kaipio. The bayesian approximation error approach for electrical impedance tomography—experimental results. *Measurement Science and Technology*, 19(1):015501, 2007. doi: 10.1088/0957-0233/19/1/015501.

[15] K G Boone and D S Holder. Current approaches to analogue instrumentation design in electrical impedance tomography. *Physiological Measurement*, 17(4):229–247, nov 1996. doi: 10.1088/0967-3334/17/4/001.

[16] D. Jennings and I. D. Schneider. Front-end architecture for a multifrequency electrical impedance tomography system. *Medical and Biological Engineering and Computing*, 39 (3):368–374, May 2001. ISSN 1741-0444. doi: 10.1007/BF02345293.

[17] *AD9850: CMOS, 125 MHz Complete DDS Synthesizer Data Sheet (Rev. H)*. Analog Devices, 2004.

[18] Pedro Bertemes-Filho, Alexandre Felipei, and Volney Coelho Vincence. High accurate Howland current source: Output constraints analysis. *Circuits and Systems*, 4(7):451–458, 2013. doi: 10.4236/cs.2013.47059.

[19] A. S. Tucker, R. M. Fox, and R. J. Sadleir. Biocompatible, high precision, wideband, improved howland current source with lead-lag compensation. *IEEE Transactions on Biomedical Circuits and Systems*, 7(1):63–70, Feb 2013. ISSN 1932-4545. doi: 10.1109/TBCAS.2012.2199114.

[20] Amin Mahnam, Hassan Yazdanian, and Mohsen Mosayebi Samani. Comprehensive study of howland circuit with non-ideal components to design high performance current pumps. *Measurement*, 82:94 – 104, 2016. ISSN 0263-2241. doi: https://doi.org/10.1016/j.measurement.2015.12.044.

[21] *ADG506A/ADG507A: CMOS 8-/16-Channel Analog Multiplexers Data Sheet (Rev. C)*. Analog Devices, 1998.

[22] *INA12x Precision, Low-Power Instrumentation Amplifiers datasheet (Rev. E)*. Texas Instruments, 2019.

[23] *AD536A: Integrated Circuit True RMS-to-DC Converter Data Sheet (Rev. G)*. Analog Devices, 2019.

[24] *SAM3X/SAM3A Series Datasheet*. Microchip, 2015.

[25] Paul Ben Ishai, Mark S Talary, Andreas Caduff, Evgeniya Levy, and Yuri Feldman. Electrode polarization in dielectric measurements: a review. *Measurement Science and Technology*, 24(10):102001, 2013. doi: 10.1088/0957-0233/24/10/102001.

[26] N. Kularatna. *Electronic Circuit Design: From Concept to Implementation*. CRC Press, 2017. ISBN 9781351837606.

[27] J. Rubinstein, P. Penfield, and M. A. Horowitz. Signal delay in RC tree networks. *IEEE Transactions on Computer-Aided Design of Integrated Circuits and Systems*, 2(3):202–211, 1983. doi: 10.1109/TCAD.1983.1270037.

[28] M. Wang. Electrode models in electrical impedance tomography. *Journal of Zhejiang University-SCIENCE A*, 6(12):1386–1393, 2005.

[29] Lew Counts and Charles Kitchen. *A Designer's Guide to Instrumentation Amplifiers*. Analog Devices, 3rd edition edition, 2006.

[30] X. Shi, W. Li, F. You, X. Huo, C. Xu, Z. Ji, R. Liu, B. Liu, Y. Li, F. Fu, and X. Dong. High-precision electrical impedance tomography data acquisition system for brain imaging. *IEEE Sensors Journal*, 18(14):5974–5984, July 2018. ISSN 1530-437X. doi: 10.1109/JSEN.2018.2836336.

[31] M. Vauhkonen, D. Vadasz, P. A. Karjalainen, E. Somersalo, and J. P. Kaipio. Tikhonov regularization and prior information in electrical impedance tomography. *IEEE Transactions on Medical Imaging*, 17(2):285–293, April 1998. ISSN 0278-0062. doi: 10.1109/42.700740.

[32] Andy Adler and William R B Lionheart. Uses and abuses of EIDORS: an extensible software base for EIT. *Physiological Measurement*, 27(5):S25–S42, apr 2006. doi: 10.1088/0967-3334/27/5/s03.

[33] E Fransolet, M Crine, G L'Homme, D Toye, and P Marchot. Electrical resistance tomography sensor simulations: comparison with experiments. *Measurement Science and Technology*, 13(8):1239–1247, jul 2002. doi: 10.1088/0957-0233/13/8/311.

[34] Yixin Ma, Hao Wang, Ling-An Xu, and Changzhen Jiang. Simulation study of the electrode array used in an ert system. *Chemical Engineering Science*, 52(13):2197 – 2203, 1997. ISSN 0009-2509. doi: https://doi.org/10.1016/S0009-2509(97)00045-6.

[35] Alexander S Ross, G J Saulnier, J C Newell, and D Isaacson. Current source design for electrical impedance tomography. *Physiological Measurement*, 24(2):509–516, 2003.

[36] K Sakamoto, T J Yorkey, and J G Webster. Some physical results from an impedance camera. *Clinical Physics and Physiological Measurement*, 8(4A):71–76, nov 1987. doi: 10.1088/0143-0815/8/4a/009.

[37] R W M Smith, I L Freeston, B H Brown, and A M Sinton. Design of a phase-sensitive detector to maximize signal-to-noise ratio in the presence of gaussian wideband noise. *Measurement Science and Technology*, 3(11):1054–1062, 1992.

Chapter 5

Estimating the Parasitic Capacitances of an Electrical Impedance Tomography Data Acquisition by MAP and MCMC

The present chapter has been submitted to the journal "International Journal of Electronics and Communications" on March 31th, 2020.

5.1 Abstract

The Electrical Impedance Tomography (EIT) technique is proving to be desirable when multi-phase flow measurements are required. The injection of current followed by the measurements of the resulted voltages is combined with an inverse problem to estimate the conductivity distribution inside the vessel. Since the problem is severely ill-posed, due to the number of measurements being inferior to the dimension of the problem, errors and noise can lead to instabilities in the solution, leading to anomalies in the image. Therefore, the system must be well designed to avoid such errors. One of the main sources of these errors is the parasitic capacitances, that shunts the current and signal to ground in high frequencies. These non-idealities are present in integrated circuits, in cables, printed circuit vias, and others. Thus, it is important to determine the quantity of these parasitic capacitances present in the circuit.

Given these reasons, the objective of this work is to estimate statistically the parasitic capacitances from the data acquisition system developed combined with the output impedance. This

is proceeded utilizing the Maximum a Posteriori (MAP) Estimate and the Monte Carlo Markov Chain (MCMC). Results are compared with the calculated from the literature.

Keywords: Electrical Impedance Tomography; Parasitic Capacitance Estimation; Data Acquisition Modeling; EIT System Development

5.2 Introduction

Through Electrical Impedance Tomography (EIT), it is possible to reconstruct the image by capturing electrical signals from electrodes to reconstruct the conductivity distribution inside a given region. The influence of the electrical circuit of the EIT equipment must be considered in the system because the real behavior of the hardware itself is responsible for a portion of the errors when computing the impedances from the medium [1, 2]. McEwan et al. [3] pointed out that, at higher frequencies, the responsible for introducing errors into the measurement system is the parasitic capacitances present in components, cables [4, 5], and connections. It is also a problem in printed circuit vias [6, 7] and interconnections in integrated circuits [8, 9, 10]. The presence of such a problem causes coupling between the lines and ground, effectively shunting the signal and electric currents.

Halter et al. [11] proposed a system to perform multi-frequency measurements. One of the challenges of developing such a system is performing measurements in higher frequencies. According to the authors, the methods to decrease effectively the parasitic capacitances is to optimize the circuit layout and minimize the lengths from the cables by keeping the electronics close. To evaluate the quantity of these parasitic capacitances, it is possible to measure it in the literature for several applications. Cook et al. [12] introduced a technique to measure the output resistance of a current source for an EIT system together with the stray capacitance from this subsystem. Although the measurement is made for this subsystem, no information is given regarding the other sources of stray capacitance. Ferri et al. [13] present a circuit that is capable of estimating the parasitic capacitances in resistive gas sensors.

Frequently, we are faced with the problem of retrieving quantities that are difficult or impossible to obtain by direct measuring [14]. To this matter, it is important to utilize the inverse problem technique, which enables the possibility of measuring the quantity indirectly, by an easily quantified measurement. It consists of solving the least-squares problem, minimizing the residual between measurements and a model. By using this approach, Scharfetter et al. [15] utilizes the Levenberg-Marquadt method to estimate using mathematical modeling for the bioimpedance

spectroscopy measurements based on an inverse problem and faced the challenge of an ill-posed system, not effectively estimating the parasitic capacitance. Another method of indirect estimation of parasitic capacitances is proposed by Lee and Kim [16], which utilizes the address power consumption to retrieve the values.

As it is mentioned, it is required a model to describe the phenomenon, named as the forward problem. To model the data acquisition (DAQ) system, Jennings et al. [2] and Boone and Holder [17] utilize impedances to represent the non-idealities of the system, that it is easily solved by SPICE, although the results are not easily implemented as a forward problem since it requires post-processing. Hartinger et al. [18] proposed a method for modeling electronic circuits in an EIT system utilizing a combination of SPICE and symbolic approach, based on the Kirchhoff's current law.

The inverse problem can be seen as a problem of statistical inversion [19], treating the parameters as stochastic as opposed to the deterministic problems, which are dependent on the initial value and have limited possibility regarding the election of the prior information [20]. From the statistical framework, more specifically the Bayesian framework, it is possible to obtain a point estimate by Maximum a Posteriori (MAP) or estimate the posterior density by a more robust approach, the Markov Chain Monte Carlo method [21]. By evaluating the posterior density, it is possible to estimate the uncertainty regarding the estimation, which is desirable to known when developing methods to compensate for these quantities.

From that perspective, the objective of this paper is to model the system by a modified Kirchhoff's current law to use as a forward problem to perform statistical inference of the parasitic capacitances of the system. Two different methods are used to obtain the quantities, the MAP estimate, and the MCMC method. From these algorithms, it is possible to investigate whether the MAP estimate, a less computationally complex solution, is sufficient. Additionally, the output impedance of the current source of the system is estimated to investigate whether the method can be used as an alternative to its measurement.

5.3 Electrical Impedance Tomography

5.3.1 Design

The data acquisition system consists of the following modules: sinewave generator, voltage-controlled current source, multiplexers, sensors, voltmeter, low-pass filter, demodulator, micro-

controller, and analog-to-digital converter. The sinewave generator is built based on the integrated circuit (IC) AD9850, capable of delivering a wave over 1 MHz. The voltage-controlled current source is a Howland type, with the non-inverting input buffered, details in [22]. The multiplexers are the IC ADG506 since the parasitic capacitances are relatively low. The voltmeter is an instrumentation amplifier to reduce the dynamic range of the application and reject the common-mode signal, comprised of the IC INA128. The active low-pass filter is a Butterworth with 90 kHz cut-off. The demodulation is performed with an RMS-to-DC converter, the IC AD536, retrieving the information about the amplitude of the wave. The system is digitized by the ADC, a peripheral from the microcontroller Atmel SAM3XE. Additionally, the microcontroller is utilized to control the sinewave generator and the multiplexers.

5.3.2 Modeling

The Electrical Impedance Tomography is responsible for injecting currents and measuring voltages inside the domain, utilizing the four-electrode method to avoid the polarization effect [23]. The differential channel of the ideal circuit is an injection of the current source and measurement by the voltmeter. However, the real circuit deviates from the ideal due to the non-idealities present in the circuit. Boone et al. and Jennings et al. present the modeling using this approach [17, 2]. These elements introduce errors that affect the accuracy of the Data Acquisition (DAQ) system. The sources of these errors include the current source, the multiplexers, the cables, the electrodes, and the voltmeter. Considering all these subsystems in the DAQ, the model that describes the behavior of the differential channel of the system is modeled in Chapter 4 according to Fig. 5.1.

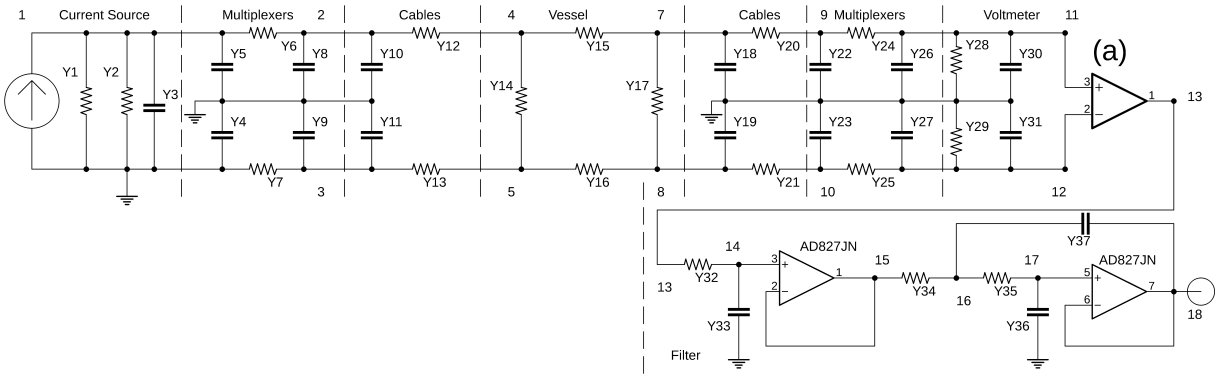

Figure 5.1: The modeling of the developed DAQ system.

To solve the circuit and obtain the voltages in each node comprised, the method proposed by Hartinger et al. [18] is employed, based on the Kirchhoff's current law. It consists of assembling

a matrix of the admittances, by considering all the currents that flow through the node, Eq. 5.1

$$\sum_{x=1}^{N} I_x = 0 \tag{5.1}$$

Each node has a corresponding equation. From these equations, the circuit is given by:

$$YV = I_N \tag{5.2}$$

where Y is the admittance matrix, V and I are the voltage and current vectors for the circuit in every node N. The amplifiers and instrumentation amplifiers are considered to be ideal. Considering that the circuit known parameter is only the current from the voltage source, the solution is given by inverting the admittance matrix from Eq. 5.2.

The nodes containing an ideal operational amplifier is given by Eq. 5.3,

$$A_g(V_+ - V_-) = V_{out} \tag{5.3}$$

and containing an ideal instrumentation amplifier is given by Eq. 5.4

$$(V_+ - V_-) = V_{out} \tag{5.4}$$

The details of the algorithm to assemble the admittance matrix considering the node's location is given by [18]. The admittances and nodes are shown in Fig. 5.1. The admittances that must be estimated are the output impedance, given by $Y1$, $Y2$ and $Y3$; and the parasitic capacitances, given by Y10, Y11, Y18, Y19. Therefore, the parameters to be estimated are respectively given by Eq. 5.5.

$$Y_{sys} = (R1, R2, C1, C2, C3, C4, C5) \tag{5.5}$$

The observation model is, shown in Eq. 5.6, dependent by the parameters, given in Eq. 5.5, and also afflicted by a noise v.

$$V_{sys} = h(Y_{sys}, v) \tag{5.6}$$

5.4 Bayesian Inference

From the Bayes Theorem, it is possible to observe how the a posteriori probability ($p(V_{sys}|Y_{sys})$) can be changed by new evidence [25, 19, 26, 21]. Therefore, Bayesian inference allows the

assessment of hypotheses from a likelihood function ($p(Y_{sys}|V_{sys})$), or the conditional probability of the parameters given the voltages, as in the Eq. 5.7. The a priori ($p(V_{sys})$) gives the information known prior the estimation and the marginal probability density ($p(Y_{sys})$), which plays the role of a normalizing constant [25, 21]. Therefore, the relationship between each is given from the Bayes Theorem in Eq. 5.7.

$$p(Y_{sys}|V_{sys}) = \frac{p(V_{sys}|Y_{sys})p(Y_{sys})}{p(V_{sys})} \tag{5.7}$$

For each of the parameters, the prior is considered to be a multivariate lognormal distribution and can be calculated by Eq. 5.8.

$$p(Y_{sys}) \propto \exp(-0.5(ln(Y_{sys}) - \mu_{Y_{sys}})^T \Sigma_{prior}^{-1}(ln(Y_{sys}) - \mu_{Y_{sys}})) \tag{5.8}$$

where Σ_{prior} is the covariance of the prior distribution and $\mu_{Y_{sys}}$ is the expected value for the prior distribution of the parameters.

The likelihood function relates the simulated measurements from the forward problem and the experimental measurements and can be calculated by Eq. 6.22.

$$p(V_{sys}|Y_{sys}) \propto \exp(-0.5(V(Y_{sys}) - z)^T \Sigma_{likelihood}^{-1}(V(Y_{sys}) - z)) \tag{5.9}$$

where Σ_{prior} is the covariance of the likelihood distribution and z is the observations.

5.4.1 Maximum a Posteriori Estimate

A commonly used estimate process based on the Bayesian framework is to consider the Maximum a Posteriori (MAP) estimate [25, 19, 26, 21, 27]. The method consists in solving, for a point estimate, the optimization process described in Eq. 5.10.

$$Y_{MAP} = argmax_{Y_{MAP}} p(Y_{sys}|V_{sys}) \tag{5.10}$$

Writing the posterior as a non-normalized form, in Eq. 5.11,

$$p(Y_{sys}|V_{sys}) \propto p(V_{sys}|Y_{sys})p(Y_{sys}) \tag{5.11}$$

and substituting Eq. 5.8 and 5.9 into 5.11 and 5.10, it is given the objective function in Eq. 5.12 [25, 27].

$$\begin{aligned} Y_{MAP} = argmin_{Y_{MAP}} \{ & [(V(Y_{sys}) - z)^T \Sigma_{likelihood}^{-1}(V(Y_{sys}) - z)] \\ & + (ln(Y_{sys}) - \mu_{Y_{sys}})^T \Sigma_{prior}^{-1}(ln(Y_{sys}) - \mu_{Y_{sys}}) \} \end{aligned} \tag{5.12}$$

5.4.2 Markov Chain Monte Carlo

In Monte Carlo methods, integration is necessary to calculate the probability density. The Markov Chain Monte Carlo (MCMC) method proposes to generate samples from the probability density, which represents accurately the distribution. From these points then, an approximate integration is calculated. One of the most commonly used algorithms is the Metropolis-Hastings, which is based on a transition kernel to sample the chain $(Y_{sys,1}, Y_{sys,2}, ..., Y_{sys,P})$, where P are the number of samples [19, 27].

The Metropolis-Hastings algorithm is performed in the following steps.

- Step 1: Select the initial value $Y_{sys,0}$ and set $k = 1$.
- Step 2: Disturb the sample to change to $p(Y^*_{sys}|V_{sys})$, using the random-walk process. Calculate the acceptance rate $\hat{\alpha}$.

$$\hat{\alpha}\left(Y_{sys,k}, Y^*_{sys}\right) = min\left(1, \frac{p(Y^*_{sys}|V_{sys})}{p(Y_{sys,k}|V_{sys})}\right). \tag{5.13}$$

- Step 3: Define $t \in [0, 1]$ from the uniform probability density.
- Step 4: If $\left(Y_{sys,k}, Y^*_{sys}\right) \geq t$, accept $Y_{sys,k+1} = Y^*_{sys}$, else $Y_{sys,k+1} = Y_{sys,k}$.
- Step 5: If $k = P$, the desired sample size has been reached and the algorithm is stopped. Else, $k = k + 1$ and return to step 2.

5.5 Results and Discussion

5.5.1 Methodology

The algorithms to solve the MAP Estimate and MCMC was implemented in Matlab to estimate the output resistance and the parasitic capacitance of the DAQ system. The optimization procedure utilized is the Nelder-Mead Simplex Method, described in detail in [28]. The random walk process is drawn from $Y^*_{sys} \sim \mathcal{N}(Y_{sys}, 0.3 \cdot Y_{sys})$, a value to maintain a accept ratio adequate. The measurements are considered for a 1 mA current in a ring of resistors with 1000 Ω load. For the MCMC method, it is important to burnout results until convergence when computing the expected value. It was tested 10000, 25000, and 50000 samples. The forward problem modeling is achieved by calculating R1, R2 by the relationship provided by Mahnam et al. [22] considering the tolerance of the resistors 1% and the open-loop gain of the op-amp AD827 and C1 is

obtained considering the gain-bandwidth of the op-amp AD827 by the relationship provided by Tucker et al. [29], shown in Table 5.1. The capacitances C2, C3, C4, C5 is considered in Table 5.1. The results are shown and validated in Chapter 4.

Table 5.1: Forward modeling of the DAQ system.

Forward Modeling	
$R1\ (\Omega)$	5.00×10^{3} [22]
$R2\ (\Omega)$	2.00×10^{6} [22]
$C1\ (F)$	9.00×10^{-11} [29]
$C2\ (F)$	3.30×10^{-11}
$C3\ (F)$	3.30×10^{-11}
$C4\ (F)$	3.30×10^{-11}
$C5\ (F)$	3.30×10^{-11}

5.5.2 Prior Distribution

The prior distribution considered for both methods is described in Table 5.2.

Table 5.2: Prior distribution of the inference.

	Prior - Lognormal Distribution	
	Expected Value	Standard Deviation
$R1\ (\Omega)$	5.00×10^{3}	2.50×10^{3}
$R2\ (\Omega)$	2.00×10^{6}	1.20×10^{7}
$C1\ (F)$	9.00×10^{-11}	4.50×10^{-11}
$C2\ (F)$	3.30×10^{-10}	2.64×10^{-10}
$C3\ (F)$	3.30×10^{-10}	2.64×10^{-10}
$C4\ (F)$	3.30×10^{-10}	2.64×10^{-10}
$C5\ (F)$	3.30×10^{-10}	2.64×10^{-10}

The probability density function (pdf) and the histogram related to the prior distribution is given by Fig. 5.2. It is important to emphasize that $R1$ is considered distributed between the worst-case considering a 1% tolerance resistor for the current source, which would be 5×10^{4} and the case with tolerance 0.66%, which would be 1.32×10^{5} considering $1 < P < 0.95$. Since C1 is calculated, we considered the prior near this value, while C2-C5 is considered to be almost an order higher.

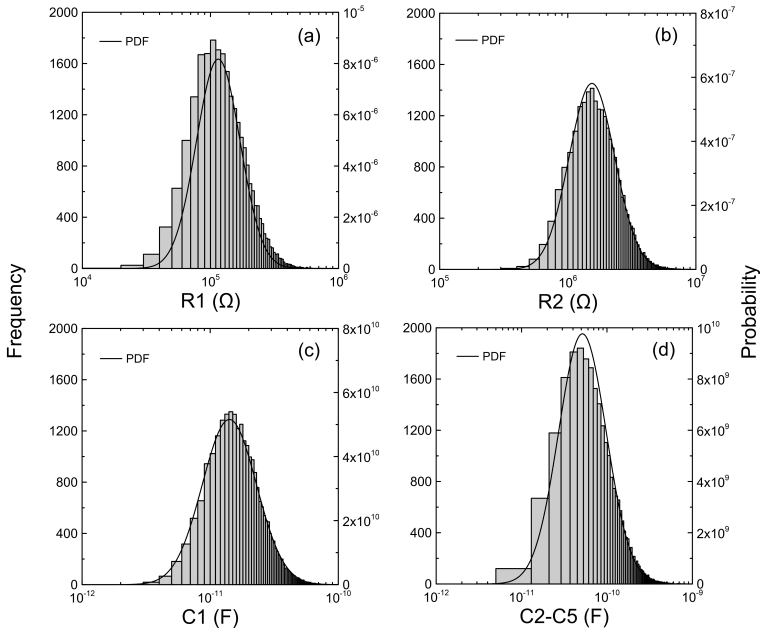

Figure 5.2: The histogram and fitting of the prior information.

5.5.3 Voltage Estimation and Posterior Distribution

The voltage estimation is given in Fig 5.4. As it is shown, for both estimations the voltage agrees well with the experimental measurements. The forward problem deviates more in the lower frequencies for the resistive part, as it is possible to observe that the roll-off of the signal is adequate. Nevertheless, the result is considered inside the confidence interval from the MCMC estimation. For the MAP estimate, the deviation is 1.60%, while the deviation of the MCMC is 3.12% from the true value.

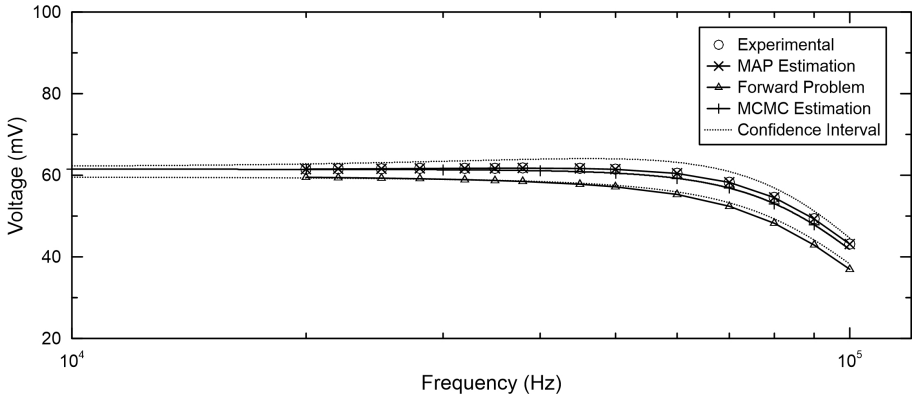

Figure 5.3: The output voltage for the parameters considering the MAP estimation, forward problem, MCMC estimation and its confidence interval, and the experimental measurements.

Results for each parameter is given in Table 5.3. Considering the results regarding the samples, it was observed some differences between 10000 and 25000, although no observable difference

between 25000 and 50000. The acceptance rate is 35.85%. The MAP estimation compensates greatly regarding the parasitic capacitances, also noticed in Fig. 5.4. It is well known that the resistive part is more sensitive at lower frequencies and the capacitances at higher frequencies. The MAP estimate is more sensitive to those parameters presenting more sensitivity in this region. The capacitances do not deviate greatly from the prior distribution. Another trend worth mentioning is the prior and posterior that do not change for R1. This confirms the correct prior utilized to model R1.

Table 5.3: MAP estimate and posterior distribution by MCMC of the inference.

	Posterior - Lognormal Distribution		
	MAP	Expected Value (MCMC)	Standard Deviation
$R1\ (\Omega)$	1.48×10^{5}	1.44×10^{5}	5.91×10^{4}
$R2\ (\Omega)$	5.13×10^{5}	1.58×10^{6}	7.22×10^{5}
$C1\ (F)$	1.79×10^{-11}	1.42×10^{-11}	7.08×10^{-12}
$C2\ (F)$	7.72×10^{-11}	4.51×10^{-11}	3.47×10^{-11}
$C3\ (F)$	7.83×10^{-11}	4.24×10^{-11}	3.16×10^{-11}
$C4\ (F)$	6.34×10^{-11}	2.96×10^{-11}	1.93×10^{-11}
$C5\ (F)$	1.32×10^{-10}	7.93×10^{-11}	3.61×10^{-11}

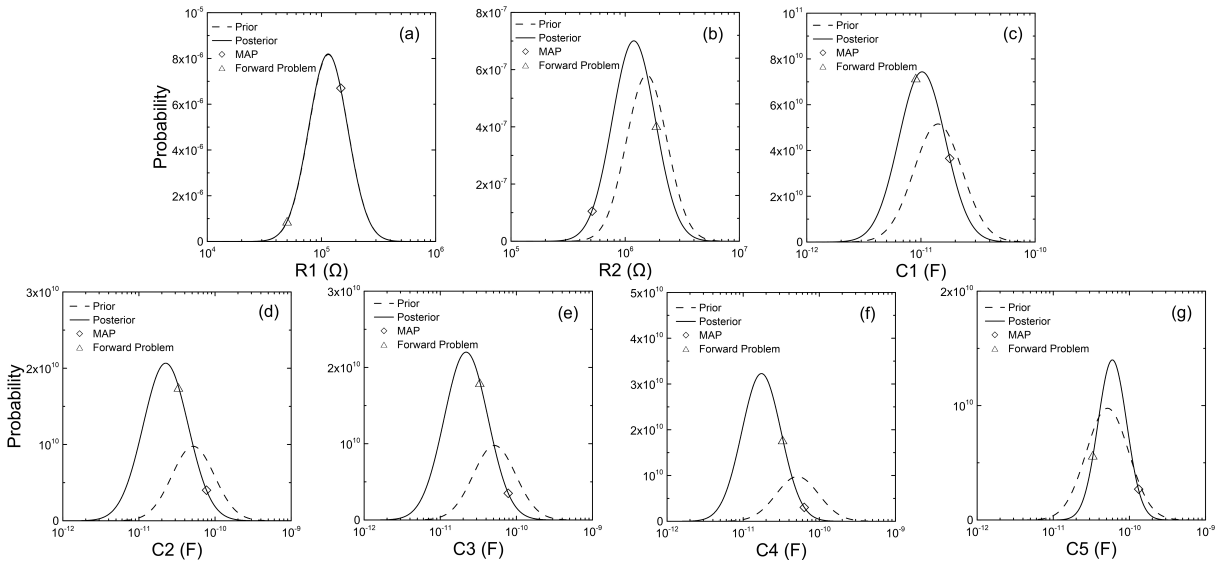

Figure 5.4: The pdf for the posterior density and the point estimate considering each of the estimated parameters.

The histogram for the parameters is given in Fig. 5.5. The posterior information of each parameter follows a lognormal distribution, except for the C5, which deviates from this distribution. The traces and convergence are shown in Fig. 5.6. Since the prior information is calculated from

Chapter 3 4, the results seem to be in the region of high probability, chain 1, in the first step of the algorithm. Dislocating the initial sample from this higher probability region demonstrated to converge to the same region after 1500 samples of the chain for 4 different initial positions. Therefore, there is no necessary need for burnout of the samples for chain 1.

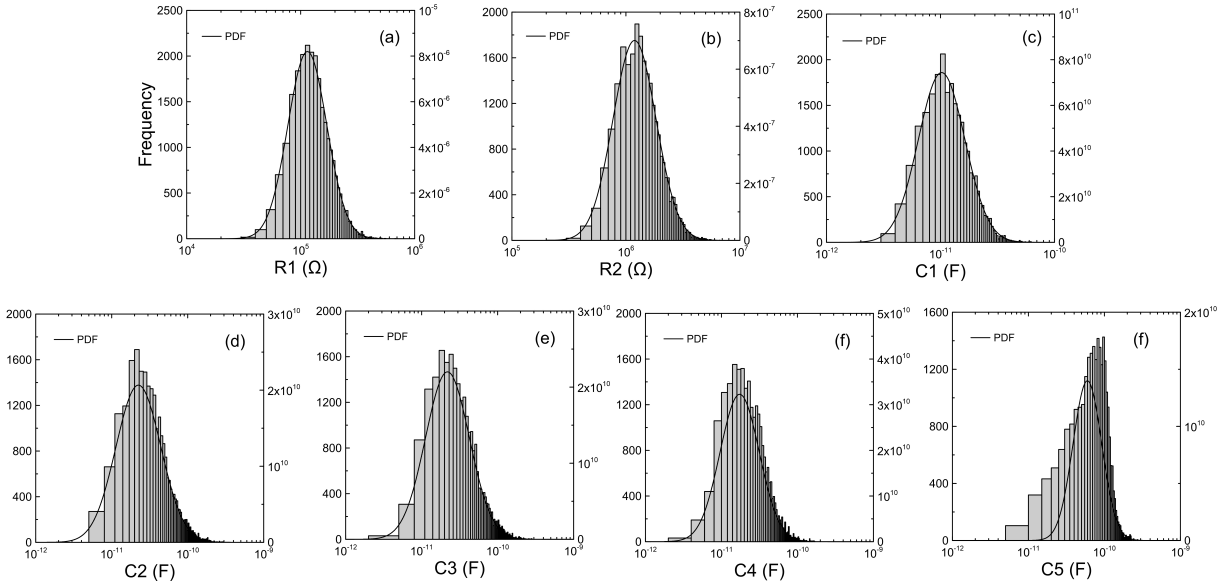

Figure 5.5: The histogram obtained by MCMC method for each parameter.

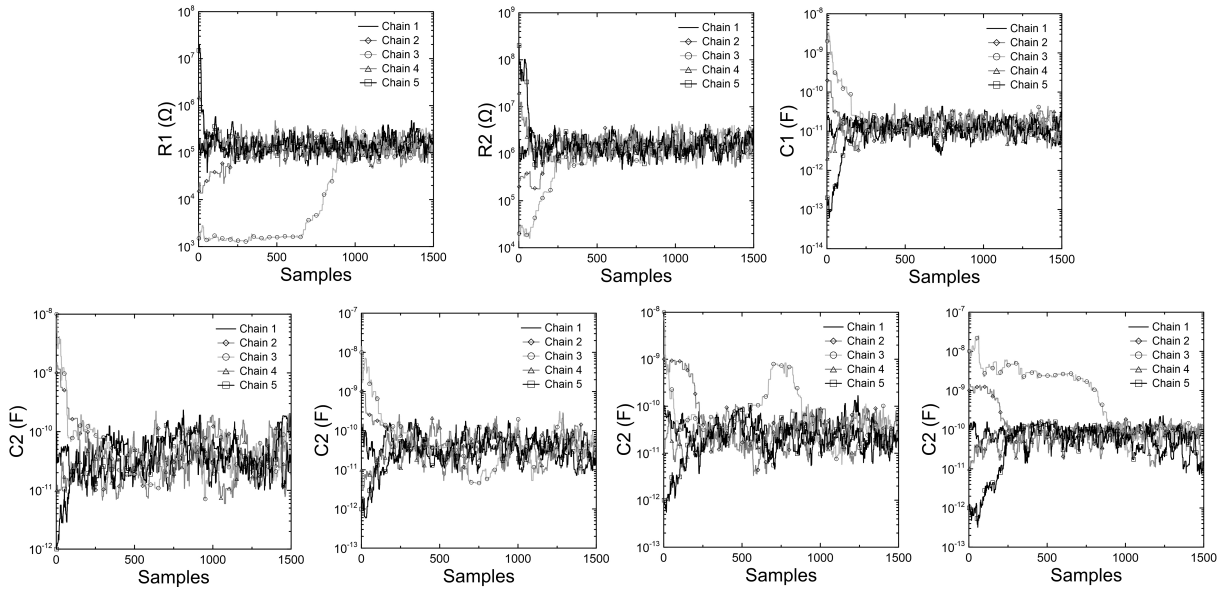

Figure 5.6: The trace obtained by MCMC method for each parameter for different initial position.

The output impedance of the current source, combined with the parasitic capacitance of the line, is shown in Fig. 5.7. The calculated for the forward model presents a lower influence of the resistive part and less influence in the reactive part. MAP and MCMC presented the same trends on the resistive part, whilst the reactive part is more pronounced in MAP estimate. Notice that

all results remain inside the confidence interval of the MCMC method.

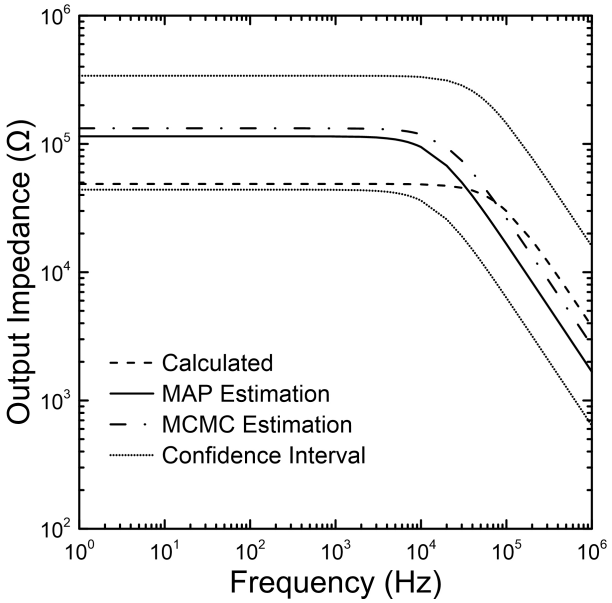

Figure 5.7: Output impedance of the current source with addition to the parasitic capacitance of the line.

5.6 Conclusion

A method to statistically estimate the parasitic capacitance of an EIT DAQ system is developed in this work. Additionally, the output impedance of the current source can be estimated in combination and used to check whether the results are in agreement. It was presented two methods, the MAP estimate, and the MCMC Metropolis-Hastings algorithm. Whilst the MAP estimate is a point estimate technique, the MCMC procedure is capable of obtaining the full probability distribution, using more computational resources. The methods were compared to evaluate if the MAP estimate obtains estimates according to the MCMC. Both methods could estimate properly the results, matching closely the measured voltages. The estimation showed that the MAP estimate prioritized the resistive part, even so, the result is within the probability distribution of the MCMC results.

References

[1] D.S. Holder. *Electrical Impedance Tomography: Methods, History and Applications*. Series in Medical Physics and Biomedical Engineering. CRC Press, 2004. ISBN 9781420034462.

[2] D. Jennings and I. D. Schneider. Front-end architecture for a multifrequency electrical impedance tomography system. *Medical and Biological Engineering and Computing*, 39 (3):368–374, May 2001. ISSN 1741-0444. doi: 10.1007/BF02345293.

[3] A McEwan, G Cusick, and D S Holder. A review of errors in multi-frequency EIT instrumentation. *Physiological Measurement*, 28(7):S197–S215, jun 2007. doi: 10.1088/0967-3334/28/7/s15.

[4] S M Huang, A L Stott, R G Green, and M S Beck. Electronic transducers for industrial measurement of low value capacitances. *Journal of Physics E: Scientific Instruments*, 21 (3):242–250, 1988.

[5] D Marioli, E Sardini, and A Taroni. High-accuracy measurement techniques for capacitance transducers. *Measurement Science and Technology*, 4(3):337–343, 1993. doi: 10.1088/0957-0233/4/3/012.

[6] K. S. Oh, J. E. Schutt-Aine, R. Mittra, and Bu Wang. Computation of the equivalent capacitance of a via in a multilayered board using the closed-form green's function. *IEEE Transactions on Microwave Theory and Techniques*, 44(2):347–349, 1996.

[7] M. Pajovic, J. Yu, and D. Milojkovic. Analysis of via capacitance in arbitrary multilayer pcbs. *IEEE Transactions on Electromagnetic Compatibility*, 49(3):722–726, 2007.

[8] V. W. C. Chan, P. C. H. Chan, and Mansun Chan. Three-dimensional cmos soi integrated circuit using high-temperature metal-induced lateral crystallization. *IEEE Transactions on Electron Devices*, 48(7):1394–1399, 2001.

[9] Y. Li, S. Yan, X. Xu, P. Lyu, and Z. Ren. 3-d ic interconnect parasitic capacitance extraction with a reformulated pgd algorithm. *IEEE Transactions on Magnetics*, 53(6):1–4, 2017.

[10] I. Ciofi, A. Contino, P. J. Roussel, R. Baert, V. Vega-Gonzalez, K. Croes, M. Badaroglu, C. J. Wilson, P. Raghavan, A. Mercha, D. Verkest, G. Groeseneken, D. Mocuta, and A. Thean. Impact of wire geometry on interconnect rc and circuit delay. *IEEE Transactions on Electron Devices*, 63(6):2488–2496, 2016.

[11] R. J. Halter, A. Hartov, and K. D. Paulsen. A broadband high-frequency electrical impedance tomography system for breast imaging. *IEEE Transactions on Biomedical Engineering*, 55(2):650–659, 2008.

[12] R. D. Cook, G. J. Saulnier, D. G. Gisser, J. C. Goble, J. C. Newell, and D. Isaacson. Act3: a high-speed, high-precision electrical impedance tomograph. *IEEE Transactions on Biomedical Engineering*, 41(8):713–722, 1994.

[13] Giuseppe Ferri, Vincenzo Stornelli, Andrea De Marcellis, Alessandra Flammini, and Alessandro Depari. Novel cmos fully integrable interface for wide-range resistive sensor arrays with parasitic capacitance estimation. *Sensors and Actuators B: Chemical*, 130 (1):207 – 215, 2008. ISSN 0925-4005. doi: https://doi.org/10.1016/j.snb.2007.08.001.

[14] Alistair B. Forbes (eds.) Franco Pavese (auth.), Franco Pavese. *Data modeling for metrology and testing in measurement science*. Modeling and simulation in science, engineering and technology. BirkhÃd'user Basel, 1 edition, 2009. ISBN 0817645926,9780817648046,9780817645922,0817648046. URL http://gen.lib.rus.ec/book/index.php?md5=D8776FC050F3CBE6AA5E4BA605C118E8.

[15] H Scharfetter, P Hartinger, H Hinghofer-Szalkay, and H Hutten. A model of artefacts produced by stray capacitance during whole body or segmental bioimpedance spectroscopy. *Physiological Measurement*, 19(2):247–261, 1998. doi: 10.1088/0967-3334/19/2/012.

[16] J. . Lee and Y. . Kim. Panel capacitance estimation method for three-electrode ac-pdp. *Electronics Letters*, 42(12):685–687, 2006.

[17] K G Boone and D S Holder. Current approaches to analogue instrumentation design in electrical impedance tomography. *Physiological Measurement*, 17(4):229–247, nov 1996. doi: 10.1088/0967-3334/17/4/001.

[18] Alzbeta Elizabeth Hartinger, Hervé Gagnon, and Robert Guardo. A method for modelling and optimizing an electrical impedance tomography system. *Physiological Measurement*, 27(5):S51–S64, 2006. doi: 10.1088/0967-3334/27/5/s05.

[19] Jari P Kaipio, Ville Kolehmainen, Erkki Somersalo, and Marko Vauhkonen. Statistical inversion and monte carlo sampling methods in electrical impedance tomography. *Inverse Problems*, 16(5):1487–1522, 2000. doi: 10.1088/0266-5611/16/5/321.

[20] Jose Pujol. The solution of nonlinear inverse problems and the levenberg-marquardt method. *Geophysics*, 72:W1–W16, 07 2007. doi: 10.1190/1.2732552.

[21] Jari Kaipio and Erkki Somersalo. *Statistical and Computational Inverse Problems*. Springer, Dordrecht, 2005. doi: 10.1007/b138659.

[22] Amin Mahnam, Hassan Yazdanian, and Mohsen Mosayebi Samani. Comprehensive study of howland circuit with non-ideal components to design high performance current pumps. *Measurement*, 82:94 – 104, 2016. ISSN 0263-2241. doi: https://doi.org/10.1016/j.measurement.2015.12.044.

[23] Paul Ben Ishai, Mark S Talary, Andreas Caduff, Evgeniya Levy, and Yuri Feldman. Electrode polarization in dielectric measurements: a review. *Measurement Science and Technology*, 24(10):102001, 2013. doi: 10.1088/0957-0233/24/10/102001.

[24] Fraser Dickin and Mi Wang. Electrical resistance tomography for process applications. *Measurement Science and Technology*, 7(3):247–260, mar 1996. doi: 10.1088/0957-0233/7/3/005.

[25] A Nissinen, L M Heikkinen, and J P Kaipio. The bayesian approximation error approach for electrical impedance tomography—experimental results. *Measurement Science and Technology*, 19(1):015501, 2007. doi: 10.1088/0957-0233/19/1/015501.

[26] Robert G. Aykroyd and Brain A. Cattle. A flexible statistical and efficient computational approach to object location applied to electrical tomography. *Statistics and Computing*, 16 (4):363–375, 2006. ISSN 1573-1375. doi: 10.1007/s11222-006-9619-x.

[27] Helcio R. B. Orlande. Inverse Problems in Heat Transfer: New Trends on Solution Methodologies and Applications. *Journal of Heat Transfer*, 134(3), 01 2012. doi: 10.1115/1.4005131.

[28] Jeffrey C. Lagarias, James A. Reeds, Margaret H. Wright, and Paul E. Wright. Convergence properties of the nelder–mead simplex method in low dimensions. *SIAM J. on Optimization*, 9(1):112âĂŞ147, 1998. doi: 10.1137/S1052623496303470.

[29] A. S. Tucker, R. M. Fox, and R. J. Sadleir. Biocompatible, high precision, wideband, improved howland current source with lead-lag compensation. *IEEE Transactions on Biomedical Circuits and Systems*, 7(1):63–70, Feb 2013. ISSN 1932-4545. doi: 10.1109/TBCAS.2012.2199114.

Chapter 6

A Novel Algorithm Combining Gauss-Newton Optimization with Image Processing and Particle Filter for Recursive Shape Determination in Electrical Impedance Tomography

The present chapter has been submitted to the journal "Inverse Problem in Science and Engineering" on November 18th, 2019.

6.1 Abstract

Electrical Impedance Tomography (EIT) is a technique that is utilized to perform flow measurements and investigating flow patterns in multiphase flow. Through an injection of an electric current inside a vessel, an electric field is formed and enables a set of boundary voltage measurements to be performed. These measurements are used as an input in an inverse problem technique to reconstruct the electric conductivity distribution of that domain. Recently, attention to statistical inversion has increased by researchers, due to its ability to easily assimilate priors in combination with the possibility to fully describe the statistical information. The particle filters are an option for recursively estimating the state variables, in this case, the shapes of the boundaries. In the literature, the estimation of these shapes by particle filters are scarce and

considers only a static reconstruction. To address this issue and allow a recursive estimation, the Gauss-Newton Optimization Sequential Importance Resampling (GNOSIR) filter is proposed. It combines the Gauss-Newton Optimization with an Image Processing algorithm to improve the prior information when the posterior density is far from the region of high probability. Results shown demonstrate that the GNOSIR filter improves the estimation when initially tracking and when there is a large displacement of the inclusion between states.

Keywords: Electrical Impedance Tomography; Particle Filter; Shape Estimation; Elliptic Contours; Image Processing

6.2 Introduction

The Electrical Impedance Tomography (EIT) method is attracting the attention of researchers nowadays. The method consists in attaching invasive but not intrusive electrodes in the inner walls of a vessel to inject a current and measure the corresponding voltage formed by this injection. These voltages measurements are used to compute an electrical conductivity distribution inside the domain of the vessel by an inverse problem technique.

A natural application for this technique is the industrial environment, more specifically when dealing with a multiphase flow. Many researchers utilize EIT to the identification of the flow patterns since it is critical to optimize, design and operate these industrial processes [1, 2, 3]. An important aspect is the calculation of the void-fraction of a flow, which is specifically required to measure flow-rate. Through the information of the conductivity field in the fluid flow, it is possible to calculate such parameters [3, 4, 5]. Nevertheless, to allows a good estimative of this parameter, good information of the contour shape of the interface between two fluids, considering a two-phase flow, is necessary to provide correct information regarding the void-fraction.

Several different approaches to deterministically compute this conductivity field have been proposed in the literature. At the beginning of EIT technique development, Barber and Brown [6] proposed the utilization of the Linear Back Projection (LBP). The idea behind the algorithm is to approximate the Jacobian through a proposition based on algorithms utilized in x-ray tomography. By calculating the so-called LBP operator and inverting this matrix, it was possible to compute the conductivities values. An extensively used alternative to the LBP operator is to adopt the transpose of the Jacobian matrix instead of [7]. Another way to solve the least-square problem is the Gauss-Newton method. To deal with the ill-posedness of the solution, the Tikhonov regularization term is added to the solution. This penalty term is considered as

prior information, aiding the stabilization of the solution [8, 9, 10]. Other deterministic iterative methods have been proposed such as the Landweber [11], Conjugate Gradient [12]. The commonly chosen regularization matrices to these methods consider a smooth and slowly changing prior, therefore the conductivity images estimated do not present sharp boundaries [9]. There are in the literature alternatives to prevent the blur of the images by estimating discontinuities of conductivity properly, such as the Total Variation regularization [13]. Another approach is to include prior knowledge of the physical boundaries into the computational domain [14, 9].

The previously presented algorithms are focused on the cases where there is no significant variation (static reconstruction) of the conductivity field in time. There is a crescent interest on dynamic reconstructions since the acquisition systems nowadays can acquire a set of voltage measurements with high speed of acquisition [15, 16]. A way to perform this estimation is by using recursive methods, such as the extended Kalman filter [17, 18, 19]. The conductivity is treated as a state estimation problem and the process noise is taken into consideration. In industrial applications, there are processes that the conductivities are known beforehand. Ijaz et al. [20, 21] use this information as a prior to estimating recursively the shapes of open and closed contours utilizing the Unscented Kalman filter.

A desirable alternative for process tomography is to use Bayesian statistical inference, to allow the incorporation of the prior information more precisely [22]. Therefore, regarding the image, the full statistical information is obtained, such as the reliability of the inference. Aykroyd and Cattle [23] combined the Boundary Element Method (BEM) with the Markov chain Monte Carlo (MCMC) to estimate a set of radii related to the parametrization of an inclusion. The drawback of the MCMC method, considering the applications described before, is its non-recursively feature and the high computational cost. To dynamically reconstruct the images, a recursive filter option is available, the particle filters. This filter is being applied to several areas of knowledge, such as industrial [24, 25] and medical [26] By this technique, the posterior distribution is described by a set of random particles and propagated recursively [27, 28, 29]. Using the particle filters, Watzenig et al. [30] present a method to estimate the boundaries of inclusion inside a vessel, utilizing a high order dimension representation of a closed contour, such as splines and Fourier descriptors.

The dynamic reconstruction algorithms estimate the contours considering only a small displacement, without the presence of large distances between each state, or stationary phantom [20, 30]. Another point that must be emphasized is the fact that the reconstruction presents a transient response from the initial state, where no good prior is known, to the convergence point. There-

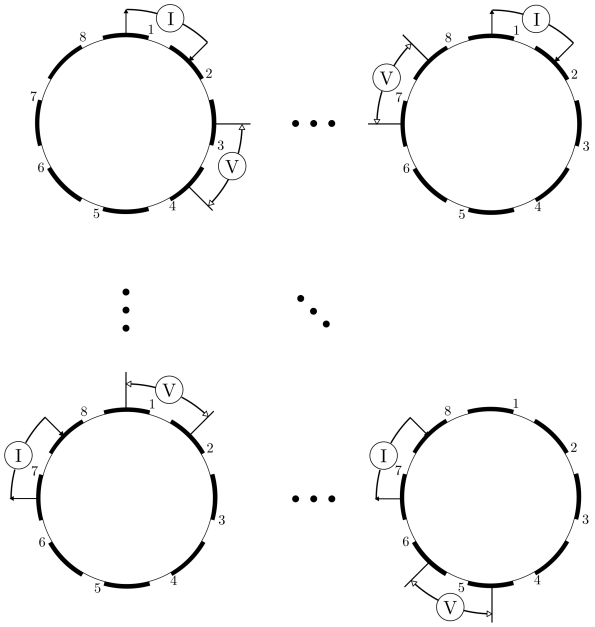

Figure 6.1: The adjacent protocol. From left to right, the measurement cycle in each adjacent pair is read from the first to the last non-injecting pair. From top to bottom, at the end of the measurement cycle, the adjacent injection is changed to the next pair until the last is used as the working pair.

fore, it should fail to estimate recursively the processes that suddenly or fastly move inside the domain (creating a discontinuity into the displacement path). Thus, the present work proposes a filter to address the gap of such methods in recursive shape determination of the EIT technique. It combines the use of the Gauss-Newton minimization with an image processing algorithm to provide better information about the prior distribution. This deterministic procedure only starts if the posterior density is far from the true position, determined by a calibration procedure.

6.3 Electrical Impedance Tomography

Electrical Impedance Tomography is responsible for injecting currents and measuring voltages inside the domain. The injection pattern chosen to the acquisition and reconstructions is the adjacent pattern. It consists of the injection of current through neighboring electrodes, i.e. adjacent, and its subsequent voltage measurement through neighboring electrodes that are not in operation in a differential form. This cycle repeats until all the electrodes are treated as the working electrode as it is shown in Fig. 6.1. The method presents $L(L-3)$, which L is the number of electrodes, where half of these measurements are independent [31, 10].

6.4 Algorithm of the Gauss-Newton Optimization Sequential Importance Sampling Resampling

It is known that the estimation of the contours can take several iterations to converge from the initial state using the Kalman filter or the particle filter [20, 30]. There is no good prior information in the initialization, so it is necessary to search throughout the entire domain to find a good match. To overcome that problem, a comprehensive optimization search step by the GNO, similarly on the algorithm proposed by da Silva et al. [32], is implemented in the Sequential Importance Resampling (SIR) filter in a way that these several evolutions in the time necessary to converge are avoided. This procedure allows the filter to generate particles from a proposal distribution to search in the region near the prior distribution after the evolution. The optimization step is activated if the proposal distribution is in regions of low or zero probability, more specifically in the initialization to provide good prior information and after a large displacement from a previous state to the next. Therefore, the Gauss-Newton Optimization Sequential Importance Resampling (GNOSIR) filter algorithm for the EIT technique is presented in Fig. 6.2. The following sections depict each stage of the filter.

6.4.1 Forward Problem

The forward problem consists in a bidimensional domain Ω with an electrical conductivity σ and a scalar potential distribution u in the domain, potential U_l at the electrodes in the contour $\partial\Omega$ where a current I_l is injected. The equations that represents the phenomenon, known as the Complete Electrode Model, are described by Eq. 6.1-6.4 [10, 9, 17]:

$$\nabla \cdot (\sigma \nabla u) = 0 \quad in\ \Omega \tag{6.1}$$

$$u + \bar{z}_l \sigma \frac{\partial u}{\partial n} = U_l \quad in\ e_l,\ l = 1, 2, ..., L \tag{6.2}$$

$$\int_{e_l} \frac{\partial u}{\partial n} dS = I_l \quad in\ e_l,\ l = 1, 2, ..., L \tag{6.3}$$

$$\sigma \frac{\partial u}{\partial n} = 0 \quad in\ \partial\Omega \setminus \cup_{l=1}^{L} e_l \tag{6.4}$$

where n is the normal of the contour $\partial\Omega$, $\bar{z}_l$ is the contact impedance, e_l is the l-esimal electrode in the contour $\partial\Omega$. To confer existence and uniqueness to the solution, two additional conditions

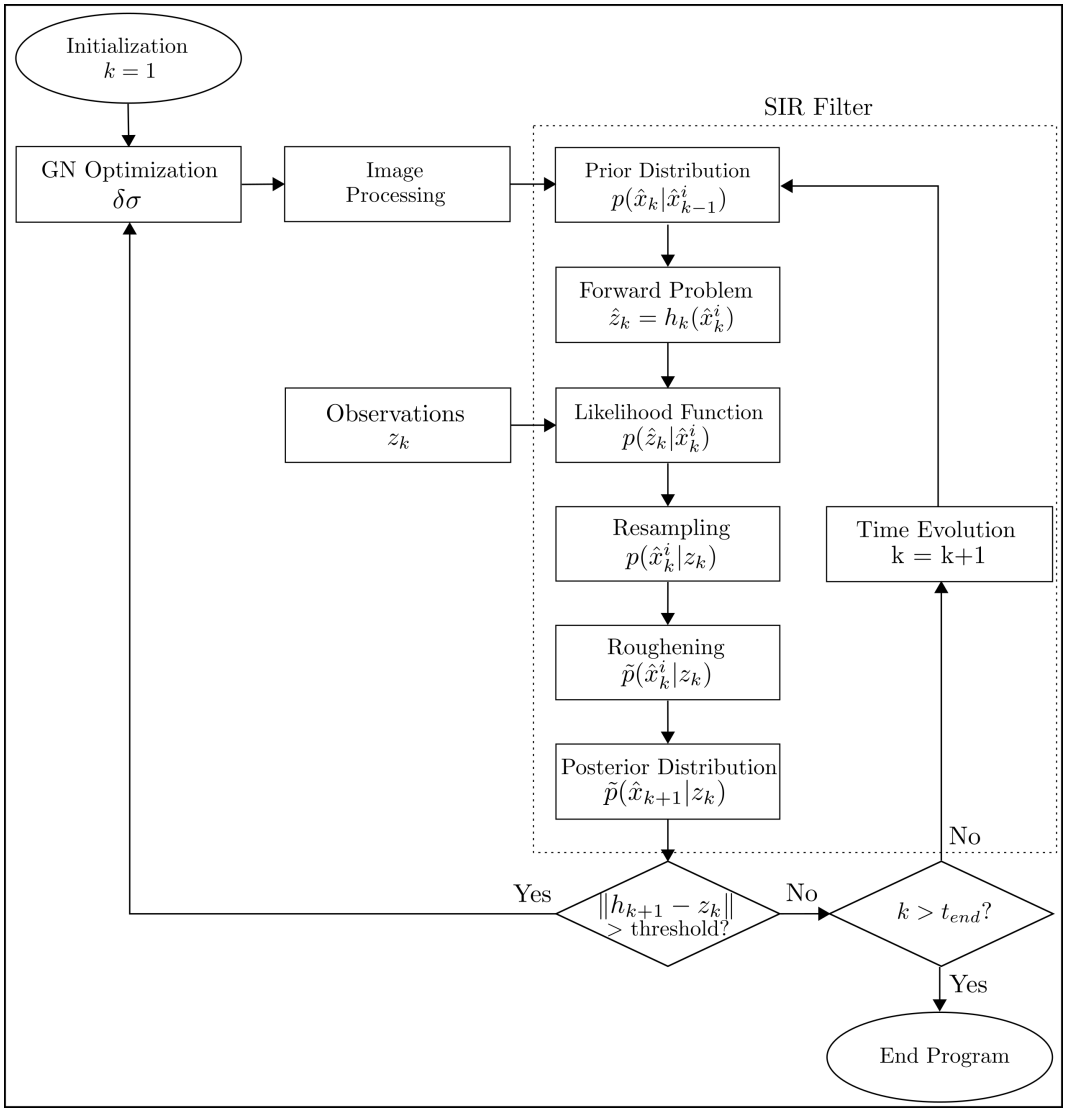

Figure 6.2: Fluxogram of the GNOSIR filter for EIT contour reconstruction application.

are necessary. Thus, the charge conservation is given by Eq. 6.5

$$\sum_{l=1}^{L} I_l = 0 \tag{6.5}$$

and the determination of a reference point is given by Eq. 6.6

$$\sum_{l=1}^{L} U_l = 0 \tag{6.6}$$

The model is implemented and discretized by the Finite Element Method. The domain Ω is fractionated into simplices, turning the domain into a finite number of elements Ω_k. The mesh is formed by the sum of those elements, which will have K elements and N vertices, i.e. nodes. To approximate the potential on the mesh, it is used specific functions, the basis function [33]. It is considered that the electrical conductivity inside each element is considered constant. After applying the weak form to Eq. 6.1, a system of equation must be solved, Eq. 6.7 [10, 33]:

$$A_M u_{sol} = I_M \tag{6.7}$$

where I_M=(0, I_{patt})^T, 0 $\in \mathbb{R}^{1,N}$, $I_{patt} = (I_1, I_2, ..., I_L)^T \in \mathbb{R}^{1,L}$ is the vector containing the injected currents. The matrix $A_M \in \mathbb{R}^{N+L,N+L}$ is formed by Eq. 6.8

$$A_M = \begin{pmatrix} B_M & C_M \\ C_M^T & D_M \end{pmatrix} \tag{6.8}$$

where the matrices B_M, C_M, D_M are calculated by Eq. 6.9-6.11

$$B_M(i,j) = \int_\Omega \sigma \nabla\phi_i \cdot \nabla\phi_j dxdy + \sum_{l=1}^{L} \frac{1}{\bar{z}_l} \int_{e_l} \phi_i \phi_j dS \quad i,j = 1,2,...,N \tag{6.9}$$

$$C_M(i,j) = -\frac{1}{\bar{z}_l} \int_{e_j} \phi_i dS \quad i = 1,2,...,N; j = 1,2,...,L \tag{6.10}$$

$$D_M(i,j) = \begin{cases} 0, & i \neq j \\ \frac{|e_j|}{\bar{z}_j} & i = j \end{cases} \quad i,j = 1,2,...,L \tag{6.11}$$

The Eq. 6.6 can be satisfied by designating in a arbitrary node i $u_i = 0$ [10].

6.4.1.1 Ellipse Representation of the Closed Contour

Considers that an inclusion is a closed contour, such as a bubble that flows inside a pipe that presents an interface between air and water. Further, the conductivities of the medium and the inclusion are both known. The problem becomes to estimate the boundaries of the inclusion. A way to treat these boundaries is to consider an ellipse form to represent the image in terms of its variables [34, 35, 36]. The Eq. 6.12, which represents an ellipse, is given

$$\frac{((x-x_c)cos(\rho)+(y-y_c)sin(\rho))^2}{r_a^2}+\frac{((x-x_c)sin(\rho)+(y-y_c)cos(\rho))^2}{r_b^2}=1 \quad (6.12)$$

where x_c is the x-coordinate of the center of the ellipse, y_c is the y-coordinate of the center of the ellipse, r_a is the radius related to the x-axis, r_b is the radius related to the y-axis, ρ is the angular orientation of the axis.

In that form, the elements of the mesh inside this ellipse are given a value of conductivity, while the elements outside of that contour are set to be the conductivity of the medium. The representation of such images as boundaries is a way to reduce the dimension of the problem to avoid the curse of dimensionality when dealing with particle filters [37]. Therefore, the estimation vector is given by Eq. 6.13

$$\hat{x}=(x_c, y_c, r_a, r_b, \rho) \quad (6.13)$$

6.4.2 Inverse Problem

6.4.2.1 Gauss-Newton Optimization

To estimate the conductivity in each pixel of the mesh, i.e. elements, one can solve the Eq. 6.14 [9, 8, 10]:

$$argmin_\sigma(\|z-h\|^2) \quad (6.14)$$

where z is the set of voltage measurements, h is the set of calculated voltages from the forward problem.

It occurs that this minimization of voltages is an ill-posed problem. To provide a unique solution, one must provide some sort of prior information. The Tikhonov regularization is an additional

term that allows the minimization to proceed without instabilities in the solution. Thus, the problem seeks to minimize the following Eq. 6.15 [9, 8, 10]:

$$argmin_{\sigma}(\|z-h\|^2+\alpha^2\|L(\sigma-\sigma_{ref})\|^2) \tag{6.15}$$

The one-step Gauss-Newton Optimization (GNO) proceeds with the linearized minimization necessary and is described by Eq. 6.16-6.17 [10, 9, 8]:

$$\delta V = z-h \tag{6.16}$$

$$\delta\sigma = \left(J^TJ+\alpha^2\tilde{L}^T\tilde{L}\right)^{-1}\left(J^T\delta V+\alpha^2\tilde{L}^T\tilde{L}\left(\sigma_{ref}-\sigma_0\right)\right) \tag{6.17}$$

where J is the jacobian, $\delta\sigma$ is the estimated conductivity, σ_{ref} is a reference conductivity, σ_0 is an initial conductivity, $\tilde{L}$ is the regularization matrix, and the α is the regularization parameter, which the value chosen to this work is 0.001. Note that the details regarding the forward problem can be seen in [10, 9, 17]. A free software is responsible for the solution of the Eq. 6.17, the Electrical Impedance Tomography and Diffuse Optical Tomography Reconstruction Software (EIDORS) [38]. The regularization matrix chosen is the one called Newton's One-Step Error Reconstructor (NOSER) prior. It consists of considering the main diagonal of the approximated Hessian (J^TJ) as the regularization matrix [39].

6.4.2.2 Sequential Importance Resampling Filter

The estimation of the boundaries of the inclusions with different electrical conductivity in the domain is considered as a state estimation problem [27, 28, 29]. Consider that the set of variables necessary to describe fully the image is defined by Eq. 6.18-6.19

$$\hat{x}_{k+1} = f_k(\hat{x}_k,\hat{w}_k) \tag{6.18}$$

$$\hat{z}_k = h_k(\hat{x}_k,\hat{v}_k) \tag{6.19}$$

where $f_k(.)$ is the system transition function that is dependent on the state variable $\hat{x}_k$, $\hat{w}_k$ is a zero mean, white-noise that afflict the system, $h_k(.)$ is the observation model dependent on the state variables $\hat{x}_k$, also afflicted by a noise $\hat{v}_k$. The state variable $\hat{x}_k$ is modelled as a Markovian process, where the initial distribution $p(\hat{x}_0)$, the transition state is $p(\hat{x}_k|\hat{x}_{k-1})$. The observations $\hat{z}_k$ is modelled as independent of the process and of marginal distribution $p(\hat{z}_k|\hat{x}_k)$. The state

evolution problem becomes to predict $p(\hat{x}_k|z_{k-1})$ from the transition state $p(\hat{x}_k|\hat{x}_{k-1})$, thus, Eq. 6.20

$$p(\hat{x}_k|z_{1:k-1}) = \int p(\hat{x}_k|\hat{x}_{k-1})p(\hat{x}_{k-1}|z_{1:k-1})d\hat{x}_{k-1} \tag{6.20}$$

and update the $p(\hat{x}_k|\hat{z}_k)$ by the marginal distribution $p(\hat{z}_k|\hat{x}_k)$ recursively, applying the Bayes' theorem in Eq. 6.21

$$p(\hat{x}_k|z_{1:k}) = \frac{p(\hat{z}_k|\hat{x}_k)p(\hat{x}_k|z_{1:k-1})}{\int p(\hat{z}_k|\hat{x}_k)p(\hat{x}_k|z_{1:k-1)}}d\hat{x}_k \tag{6.21}$$

Since the aforementioned complex high-dimensional integrals are not commonly tractable analytically, a numerical method called Monte Carlo (MC) integration is used to obtain the needed solution [27, 28, 29]. The method relies on generating stochastic samples distributed randomly in the region chosen according to the state space. Since it is a difficult process to sample directly from the posterior density $p(x_{0:k}|z_{1:k})$ at any time, the importance sampling technique is used as a solution. It consists of basically assign weights for each sample based on how close the arbitrary importance sampling distribution represents the posterior density. To compute the weights, assuming the process to be a multi-variate Gaussian distribution, the likelihood function is given by Eq. 6.22

$$p(\hat{z}_k|\hat{x}_k) \propto \exp(-0.5(h_k - z_k)^T\mathbf{\Sigma}^{-1}(h_k - z_k)) \tag{6.22}$$

where $\mathbf{\Sigma}$ is the covariance matrix of the process. The process of weight assimilation assures the estimation of the posterior density of a state variable recursively. The resulting algorithm is named as Sequential Importance Sampling (SIS), which enables to estimate non-Gaussians state variables recursively. At the end of a time step, it is given P random particles with its weights, which allows the computation of the posterior density, Eq. 6.23,

$$p(\hat{x}_k|z_{1:k}) \approx \sum_{i=1}^{P} w_k^i \delta(\hat{x}_k - \hat{x}_k^i) \tag{6.23}$$

where w_k^i corresponds to the weight related to each sample and δ is the Dirac delta. Since a probability distribution is available and represented by the weighted samples, it is possible to

estimate the expected value and the confidence interval of the state variable. The expected value is given by Eq. 6.24

$$E(\hat{x}_k|z_k) \approx \sum_{i=1}^{P}(w_k^i \hat{x}_k^i) \tag{6.24}$$

It was found that the SIS filter had a major issue. After some evolution in time, the weight becomes increasingly skewed, and later only one particle would present a non-zero weight. This phenomenon is called degeneracy [27, 28, 29]. To overcome this problem, Gordon et al. [40] introduce a step into the SIS filter. The resampling step rejects samples with low importance weight, and then selects and multiplies the samples with high importance weight. The assigned normalized weights are uniform after the resampling step. The filter originated from this step is called SIR filter or the Bootstrap Filter [40].

The SIR filter has a drawback that occurs when particles has the same and significant weight and the particles with small weight are abandoned . This problem is called impoverishment and can be treated by a process called roughening [41, 40]. It consists of adding an independent Gaussian jitter noise in the update procedure after resampling, with zero mean and covariance, $\tilde{J}_k$. Considering $p(\hat{x}_k|z_{1:k})$ is a Gaussian with mean $\tilde{x_k}$ and covariance $\tilde{P}_k$, then from Eq. 6.25 [41, 40]:

$$\tilde{p}(\hat{x}_k|\hat{z}_{1:k}) \approx N(\hat{x}_k : \hat{x}_k, \hat{J}_k + \tilde{P}_k) \tag{6.25}$$

According to Gordon et al. [40], the representation of the covariance J_k is given by Eq. 6.26

$$\tilde{J}_k = \sigma_{rough}\tilde{I} \tag{6.26}$$

where $\tilde{I}$ is the identity matrix.

The standard deviation of the roughening process is given by Eq. 6.27 [40]

$$\sigma_{rough} = \hat{K}\hat{L}P^{-1/d} \tag{6.27}$$

where $\hat{L} = max(0.001, \hat{l})$, $\hat{l}$ is the length of the interval between the maximum and the minimum samples (before roughening), d is the dimension of the state space, $\hat{K}$ is a constant tuning

Table 6.1: Image processing to obtain the state variables from the Gauss-Newton optimization.

Image Processing Algorithm
1: Find the centroid of the element with a minimum value of σ_k to obtain the coordinates x_c and y_c.
2: Find the centroid of the elements that have a σ_k value within an arbitrary contour range.
3: Calculate the distance from the ellipse center point to each element centroid obtained previously within the range.
4: Find the max distance from the center to the centroid of the element, which corresponds to r_a.
5: Calculate the angle ρ between the line formed by the two points.
6: Find the centroid of the element within the range that has the min of $\lvert\rho - \frac{\pi}{2}\rvert$ to obtain r_b.

parameter, and P is the number of particles. This procedure is responsible for augmenting the diversity of the particles, allowing the SIR filter to estimate the confidence interval properly when there is an impoverishment.

6.4.3 Image Processing

The Image Processing (IP) procedure is the step that obtains a better estimation of the state vector prior information. An image is reconstructed from the GNO, Eq. 6.17, thus obtaining a set of electrical conductivity values within the domain. Each element presents a constant value of conductivity, which is normalized to aid in the next step. To obtain the estimation for the state vector from the acquired image, a simple algorithm of Image Processing is presented in Tab. 6.1.

Since the solution from the GNO is a continuous surface and does not present a clear boundary, the algorithm depends on tuning a range to be considered a closed contour of the image. Fig. 6.3 shows the contours of a typical image reconstruction solution and the process of choosing this range. The normalized conductivity considered as the range of the contour is 0.35 ± 0.05.

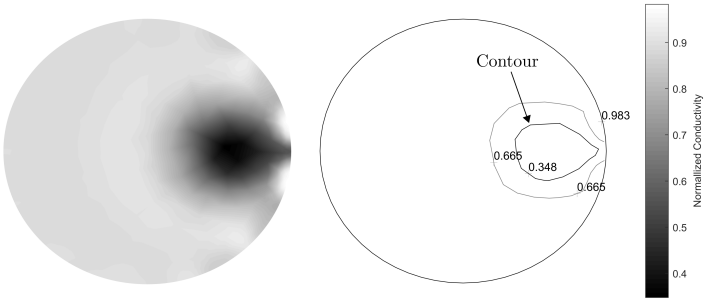

Figure 6.3: Contour plot of the image to aid the election of the range to be considered the contour.

Table 6.2: Image processing to obtain the state variables from the Gauss-Newton optimization.

	Image Processing Algorithm							
	Optimization 1		Optimization 2		Optimization 3		Optimization 4	
	True	Simulated	True	Simulated	True	Simulated	True	Simulated
x_c (mm)	0	-2.5	0	-2.9	0	-2.9	-25	-32.3
y_c (mm)	0	-4.3	0	3.7	0	3.7	-10	-11.9
r_a (mm)	40	34.8	40	36.7	20	38.4	25	24
r_b (mm)	20	17.9	20	19.9	40	19.3	25	17.4
ρ (rad)	0.7854	1.0518	1.5708	1.5579	0.7854	-0.8208	0	0.8684

6.5 Results and Discussion

6.5.1 Validation of the Image Processing Algorithm

To evaluate the accuracy of the estimation performed by the Image Processing algorithm, some known inclusions are fabricated with a conductivity of the medium set as $\sigma_{hom} = 0.01S/m$ and the $\sigma_{inc} = 0.0001S/m$. The diameter of the domain is 14.4cm. A total of 15% of random noise is added to the measurements. The meshes are obtained by the Gmsh software with 4 different refinements, given in Tab. 6.3. The true geometric parameters and the estimated are displayed in Tab. 6.2, considering Mesh 3. The algorithm can estimate the inclusions properly. There are some discrepancies between the true and estimated data. However, the Image Processing Algorithm aim is to get better prior distribution, not a final estimation. To perform this estimation, a coarser mesh would present results faster, in detriment of the accuracy. The mesh influence in the estimated parameters is shown in Fig. 6.5 and Tab. 6.3. The estimated parameters with Mesh 2 is satisfactory, although there is improvement between Mesh 2 and Mesh 3, 4.

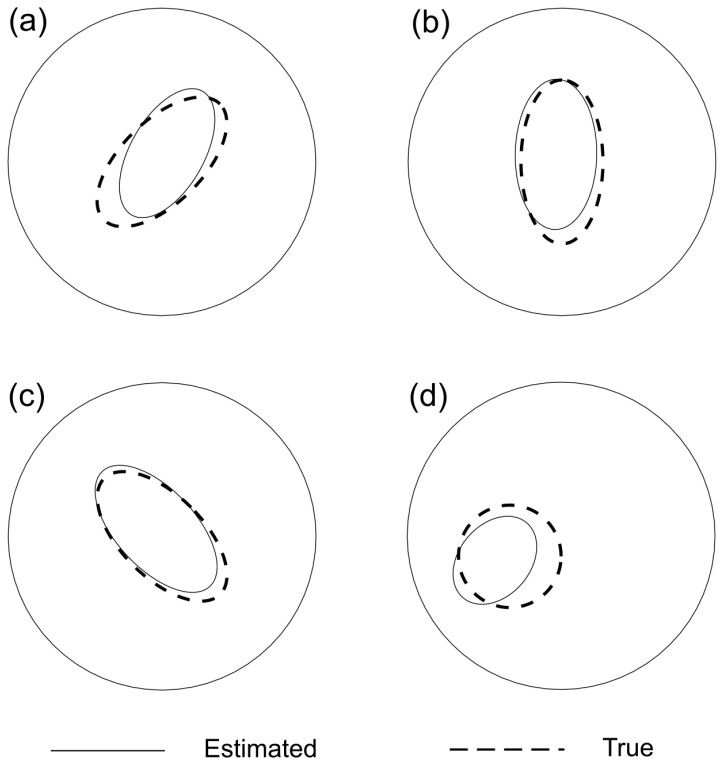

Figure 6.4: Validation of the Image Processing Algorithms. (a) Optimization 1. (b) Optimization 2. (c) Optimization 3. (d) Optimization 4.

Table 6.3: Image processing to obtain the state variables from the Gauss-Newton optimization.

	Image Processing Algorithm				
	True	Mesh 1	Mesh 2	Mesh 3	Mesh 4
Nodes	-	269	454	720	1032
Elements	-	488	858	1358	1966
x_c (mm)	-20	9.3	25.7	23.0	20.5
y_c (mm)	-10	-15.1	-8.3	-2.6	-10.4
r_a (mm)	30	30	34.3	33.5	25.9
r_b (mm)	15	20.8	14.4	19.3	15.7
ρ (rad)	0.4363	0.8320	0.4308	0.7028	0.2291

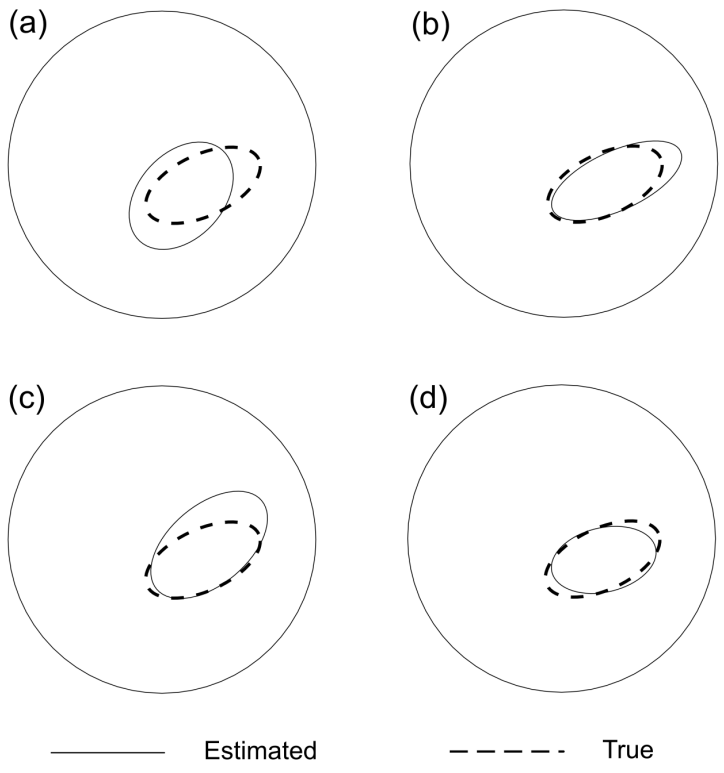

Figure 6.5: Mesh validation. (a) Mesh 1. (b) Mesh 2. (c) Mesh 3. (d) Mesh 4.

6.5.2 Sensitivity Coefficient

To check the influence of each state variable in the model, the normalized sensitivity coefficient is evaluated. The definition of the normalized coefficient is given as follows [42, 43]:

$$\varphi_i = \frac{\partial Y_{ind}}{\partial X_{dep,i}} \left(\frac{X_{dep,i}}{Y_{ind}} \right) \tag{6.28}$$

where φ_i is the sensitivity parameter, Y_{ind} is the independent variable, $X_{dep,i}$ are the dependent variables, and $\frac{X_{dep,i}}{Y_{ind}}$ is introduced to normalize the sensitivity.

The effect of each variable is given in Fig. 6.6. It is important to emphasize that only one coordinate in the plane is considered due to symmetry and both radii are considered since its shape in the domain changes. As it is expected, the variable presenting considerable amount of sensitivity is x_c and y_c. As the adjacent pattern is chosen, the position near the boundaries present high values of sensitivity in detriment of the center of the domain [31]. It is important to highlight that the r_a, r_b and ρ of the inclusion has significantly lesser sensitivity, being harder to estimate properly.

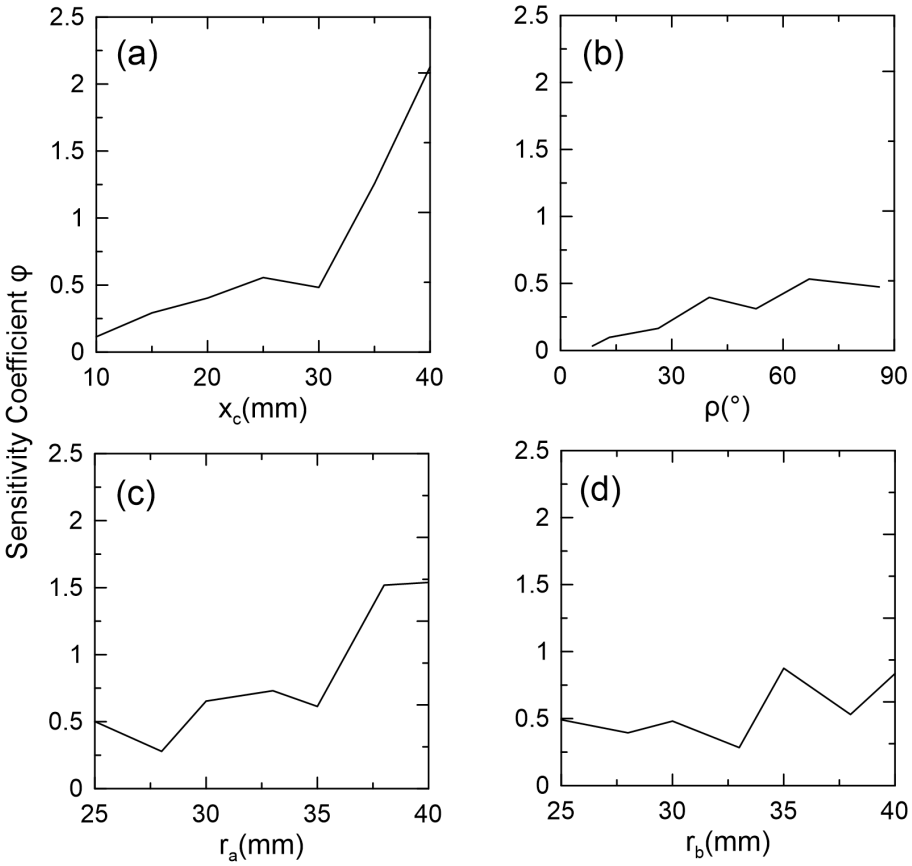

Figure 6.6: Dimensionless sensitivity coefficient. (a) Sensitivity of the distance from the center x_c considering $y_c = 0$, $r_a = 25mm$, $r_b = 25mm$ and $\rho = 0$. (b) Sensitivity of the angle ρ considering $x_c = 20mm$, $y_c = 0$, $r_a = 38mm$ and $r_b = 25mm$ (c) Sensitivity of the form r_a considering $x_c = 20mm$, $y_c = 0$, $r_b = 25mm$ and $\rho = 0$. (d) Sensitivity of the form r_b considering $x_c = 20mm$, $y_c = 0$, $r_a = 25mm$ and $\rho = 0$.

Table 6.4: The standard deviation and tuning parameters of the roughening process choose for the GNOSIR filter.

GNOSIR Filter Parameters		
	Std	K
x_c	15mm	0.8
y_c	15mm	0.8
r_a	5mm	0.3
r_b	5mm	0.3
ρ	0.15rad	0.2

6.5.3 Computational Phantoms

The algorithm is tested with computational phantoms. The measurements are obtained utilizing Mesh 4 and a 15% Gaussian noise is added to avoid inverse crime [8]. The solution of the forward problem used as an observational model, from Eq. 6.7-6.11, are implemented in Octave. The mesh utilized the image processing code and to reconstruct the image is Mesh 3. The standard deviation and tuning parameters of the roughening process are displayed in Tab. 6.4. The procedure to verify whether the result is in a high probability region is similar to the prior editing presented in [40]. The parameter to observe is the minimization of the norm between measurements and model $\|h_{k+1} - z_k\|$. The threshold for this case should be $\|h_{k+1} - z_k\| > 6\sigma_{std}$. However, the EIT signal is multivariate and it occurs that for the cases where the estimated is far from a probability region only a few measurements from the set may satisfy this inequality. Therefore, this relationship is not considered and a calibration procedure is developed to set this threshold.

The condition for Test Computational 1 is a stationary phantom with the true position of radius of $r_a = 25mm$, $r_b = 25mm$, and $\rho = 0$ is at $x_c = 40mm$, $y_c = 0mm$. Results are shown in Fig. 6.7. The minimization parameter are given for each state. The algorithm takes 3 to 4 steps to converge, which is also observed from the minimization parameter. This procedure is important to calibrate the threshold for the GNOSIR filter, calibrated to a value of 0.28 (dashed line). Furthermore, the SIR filter presents good estimations after converging.

In Test Computational 2, different numbers of particles are tested to determine the necessary effort to estimate the boundaries. To evaluate the quality of the image, the Mean Absolute Error

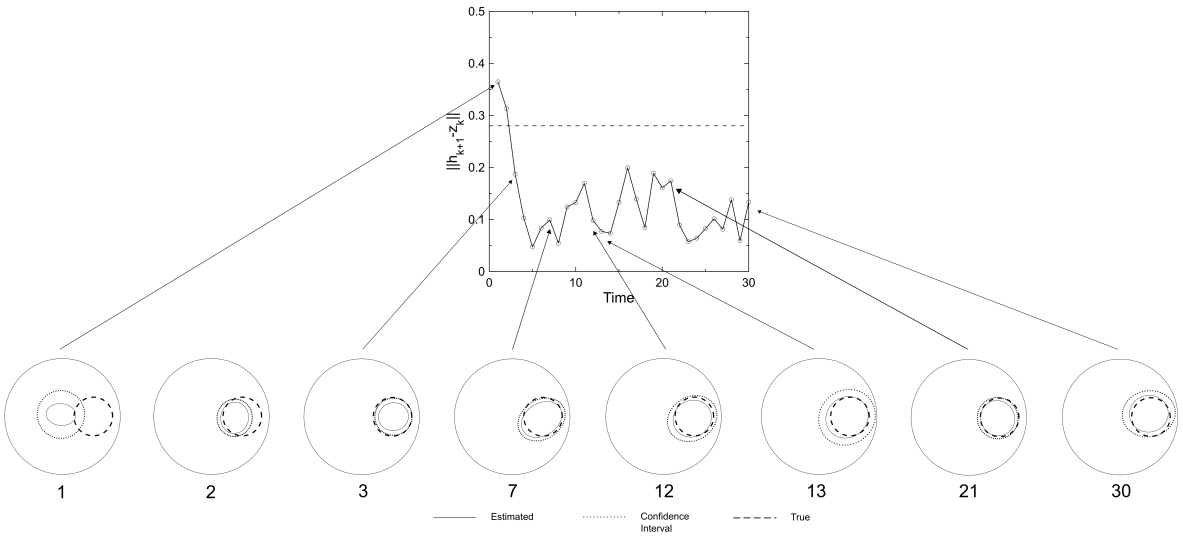

Figure 6.7: Test Computational 1: The estimation of the contours by the SIR filter. From left to the right, the convergence into the true position. The dashed line represents the threshold of the GNOSIR filter.

(MAE) is calculated between the true measurement and the estimated measurement, Eq. 6.29.

$$MAE = \frac{1}{K}\sum_{i=1}^{K}\left(\left|\frac{\sigma_i - \sigma_{true,i}}{\sigma_{hom} - \sigma_{inc}}\right|\right) \tag{6.29}$$

where σ_{true} is the element value of electrical conductivity in the true image. If $MAE = 1$, it indicates that there is a total mismatch between the estimated and true position, while if $MAE = 0$ indicates there is a total match.

The results for each number of particles are evaluated in Fig. 6.8. As it is shown in Fig. 6.8(a), the evolution path of the inclusion inside the domain begins with equal radii $r_a = r_b$ at the top of the domain, expanding one of the radii and rotating nearly the middle of the domain. After that, it contracts until the inclusion reaches the bottom of the domain and obtain equal radii. By inspecting Fig. 6.8(b), it becomes evident that there are poorer results in the region of less sensitivity, the middle of the mesh, for all estimated shapes despite the different number of particles of each test. Further investigation shows that the increase in the number of particles is not sufficient to increase the quality of the image, as the results with 150 particles between 19-22 provide a worse quality when compared with the results with 100 particles. To the other positions, the algorithm estimated with good precision. A random variation of the quality is observed and it is accounted for by the stochastic nature of the particle filters.

The GNOSIR filter does not utilize the optimization step in Test 2 since the evolution is steady

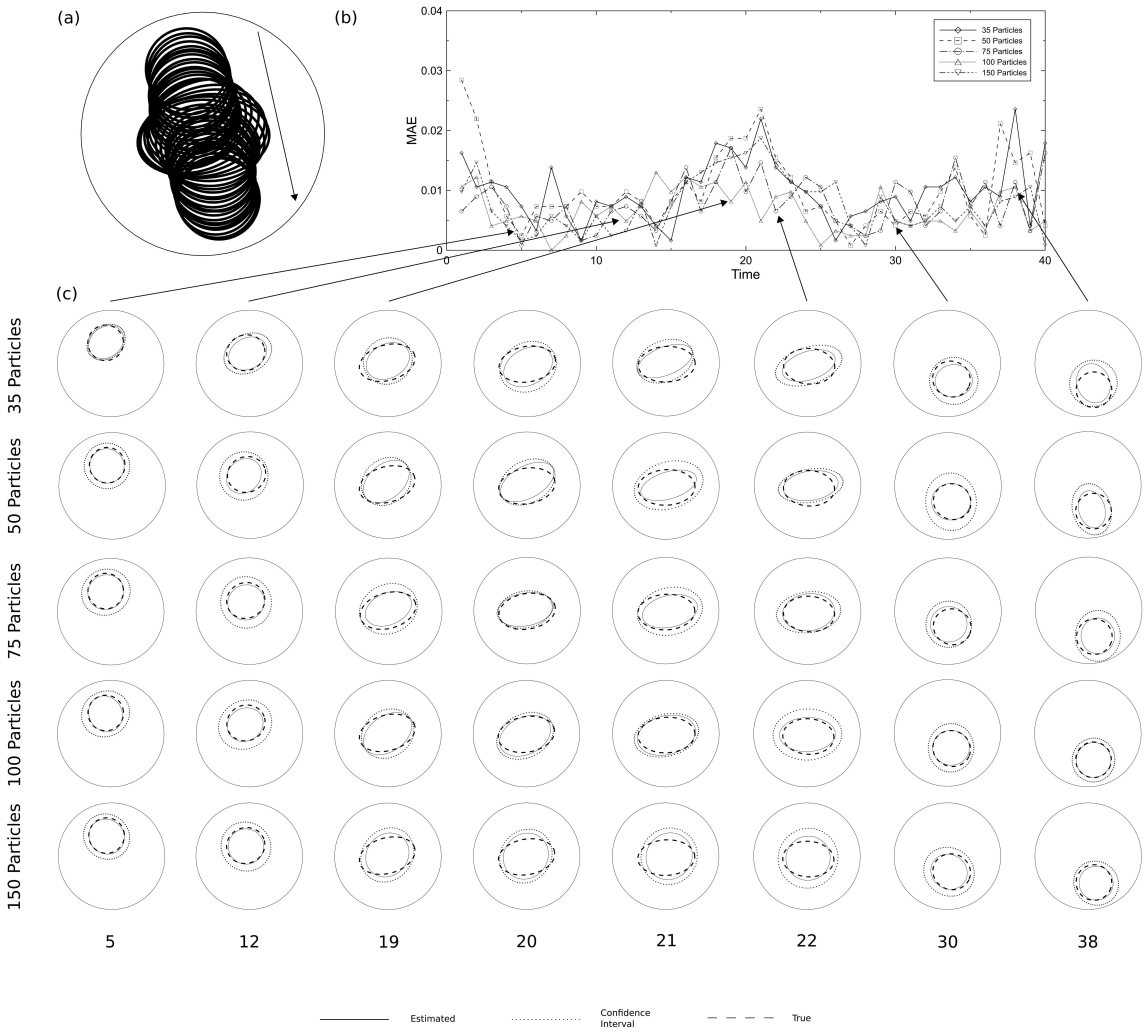

Figure 6.8: Test Computational 2: Estimation of the contours considering a different number of particles. (a) The path of evolution in time. (b) The MAE for each image considering a different number of particles. (c) The images for the selected time.

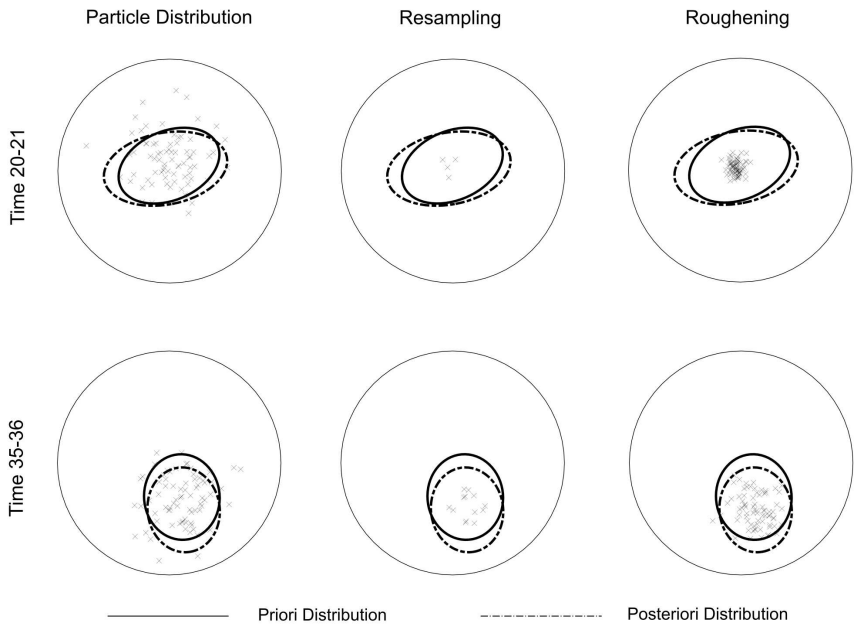

Figure 6.9: Estimation of the contours considering a discontinuity of the true position between states. (a) The path of evolution in time. (b) The MAE for each state. (c) The images for each state.

and slow-paced. This behavior is intended, as the generation of particles stands near the prior distribution, Figure 6.9. To avoid the search throughout the entire domain, the GNOSIR filter focus on generating particle in the regions closer to this region, thus increasing the particle density in the desired area.

The mean time for the evolution of the state and its standard deviation is given in Tab. 6.5. As it is shown, the procedure is fast since it is not required a high amount of particles to perform good estimations. The particles are efficiently generated in the region of interest, thus a lower computational time is required. The optimization time is given in Tab. 6.5. Considering it is assured a maximum of one optimization each time, the total time of the complete reconstruction is given by Eq. 6.30

$$t_{tot} = (k + \tilde{n}_{opt})t_k + t_{opt}(1 + \tilde{n}_{opt}) \tag{6.30}$$

where t_k is the evolution time, t_{opt} is the optimization time, k is the number of state variables, and $\tilde{n}_{opt}$ is the number of optimizations. The fastest case is when the filter does not engage in optimization, and the slowest is when all states optimize. The time for the best and worst-case scenario is given in Tab. 6.5 considering the 40 states. This corresponds to a total of 2.30 increase for 35 particles and a 2.069 increase for 150 particles. It is expected, since the iteration must

Table 6.5: Time elapsed by the GNOSIR filter per evolution and total time considering 40 states.

Time Elapsed per Evolution					
Particles	Mean (s)	Std (s)	Total Best (s)	Total Worst (s)	Ratio
Opt.	2.82	0.06	-	-	-
35	9.17	0.31	369.62	849.22	2.30
50	13.49	0.30	542.42	1194.82	2.20
75	27.32	2.47	1095.62	2301.22	2.10
100	30.11	3.35	1207.22	2524.42	2.09
150	39.9	2.16	1598.82	3307.62	2.07

be restarted from the beginning, doubling the time. The effort necessary to the optimization is diminished as the number of particles increases, becoming negligible with a high number of particles.

Test Computational 3 evaluates the capability of the GNOSIR filter in estimating inclusions with a discontinuity between the states. The initial guess for the SIR filter considering the following tests is: position $x_c = -40mm$, $y_c = 0mm$, radius of $r_a = 10mm$, $r_b = 10mm$, and $\rho = 0$. The number of particles utilized in the following tests is 50. It is shown in Fig. 6.10(a) the path of evolution in time. The inclusion dislocates from top to bottom when a discontinuity happens in Time 5. From that point, the inclusion steadily moves and expands. It is noticed in Fig 6.10(b) and Fig. 6.10(c) that the SIR filter fails to track initially from a poor initial guess, resulting in an increased MAE value. It begins to track properly in Time 4. Due to the conditions discussed previously, the SIR filter tracks slowly in Time 5. On the other hand, the GNOSIR filter proceeds to optimize, obtaining a good estimation and a lower MAE when comparing with the SIR filter.

Test Computational 4 further evaluates the performance of the GNOSIR filter in estimating inclusions with a high-speed evolution. From Fig. 6.11(a), it is observed that the inclusion evolves faster and rotating near the boundary while expanding and contracting until Time 5. From that point, the inclusion rotates, expands, and moves faster, turning into a circle in the end. Inspecting Fig. 6.11(b) and Fig. 6.11(c), it becomes evident that the SIR filter slowly converges, and finally tracks the true position at Time 6. To reach that point, notice that at Time 5 the SIR filter position is dislocated to the left, closer to the true position in Time 6. This position facilitates the estimation since the generation of the particles can reach closer to the true easier. The GNOSIR filter initiates converged already until it reaches Time 6, in which the estimation is tracking but becomes far from the true position. To compensate for this issue, an optimization

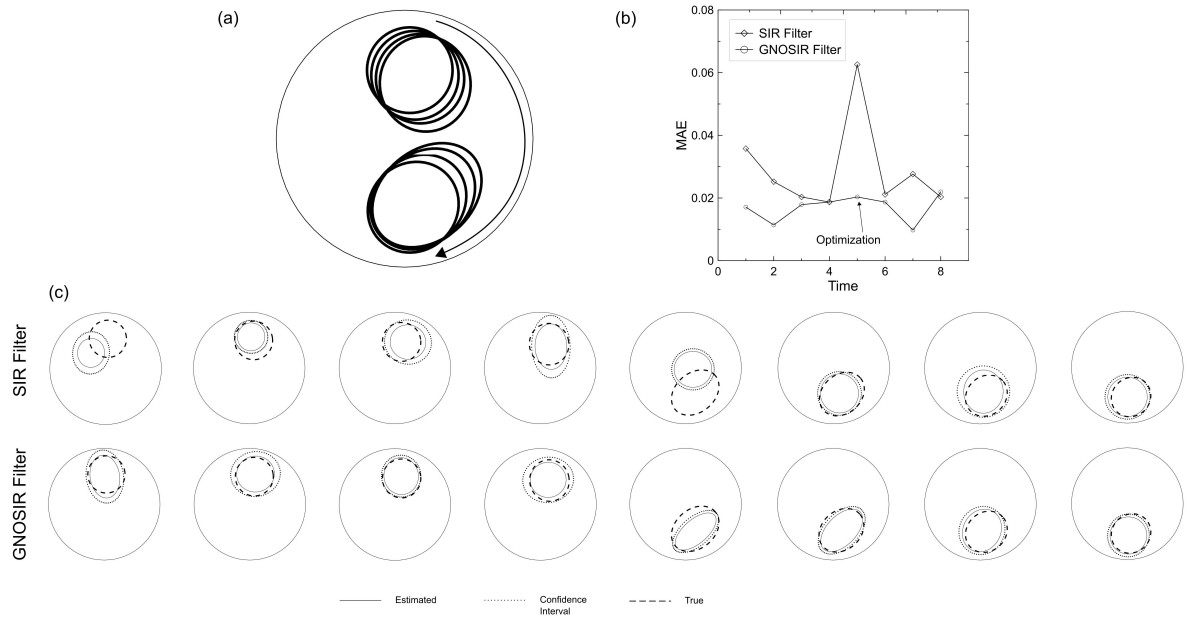

Figure 6.10: Test Computational 3: Estimation of the contours considering a discontinuity. (a) The path of evolution in time. (b) The MAE for each state. (c) The images each state.

is performed in Time 7, estimating well at that point.

6.5.4 Experimental Phantoms

The algorithm is tested with experimental phantoms. A non-conductive cylinder of 51mm diameter is inserted inside a vessel with a diameter of 44cm with a saline solution of $77.09 \pm 0.47 uS/cm$. The SIR filter is used to calibrate the conductivity of the homogeneous medium. The estimated value of the homogeneous conductivity is $76.69 uS/cm$ and it is used in the algorithm as the conductivity of the medium. The conductivity of the inclusion is $15 uS/cm$. The tuning parameters are the same as the results of the computational phantom, in Tab. 6.4. A comprehensive analysis of the error present in the measurements is previously done, thus generating the covariance matrix of the filter.

In Test Experimental 1, the threshold is adjusted by a stationary phantom placed in $x_c = 40mm$ and $y_c = 0$, as shown in Fig. 6.12(b). It must be emphasized that the position contains measurement uncertainties that must be accounted for. The measurements and model output minimizes and converges further in Time 1-4, until it reaches a minimum, Fig. 6.12(a). From that point, the convergence is assured, as it is shown in Fig. 6.12(c). The threshold calibrated for the GNOSIR filter is shown in the dotted line, considered 0.13.

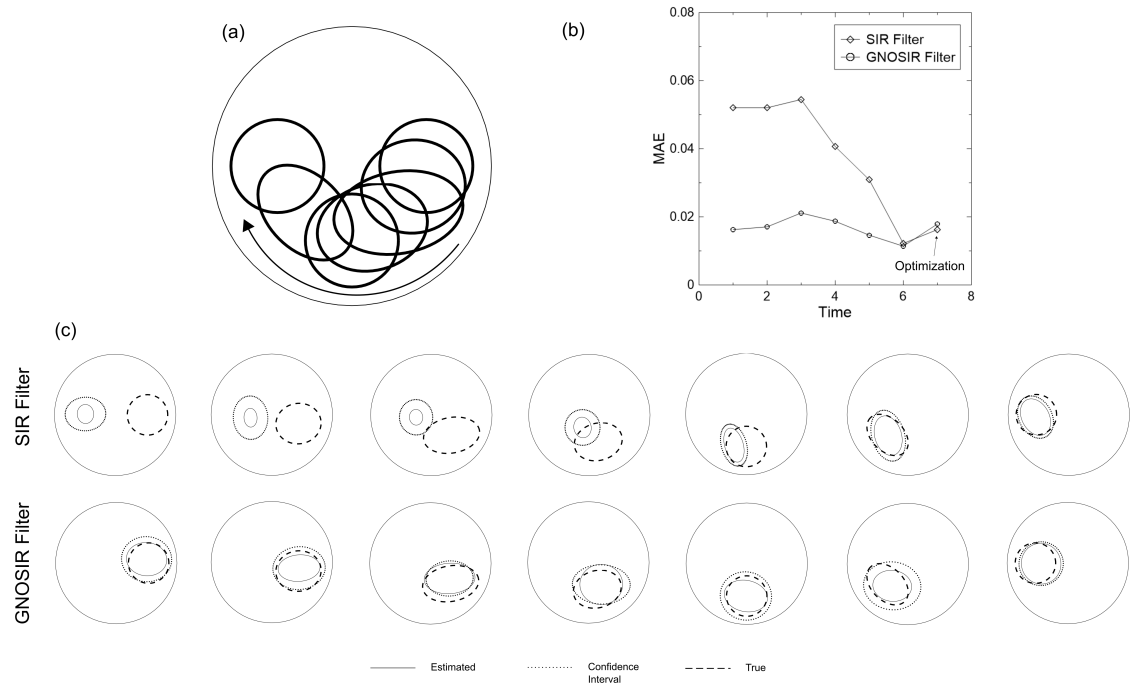

Figure 6.11: Test Computational 4: Estimation of the contours considering a high-speed evolution. (a) The path of evolution in time. (b) The MAE for each state. (c) The images each state.

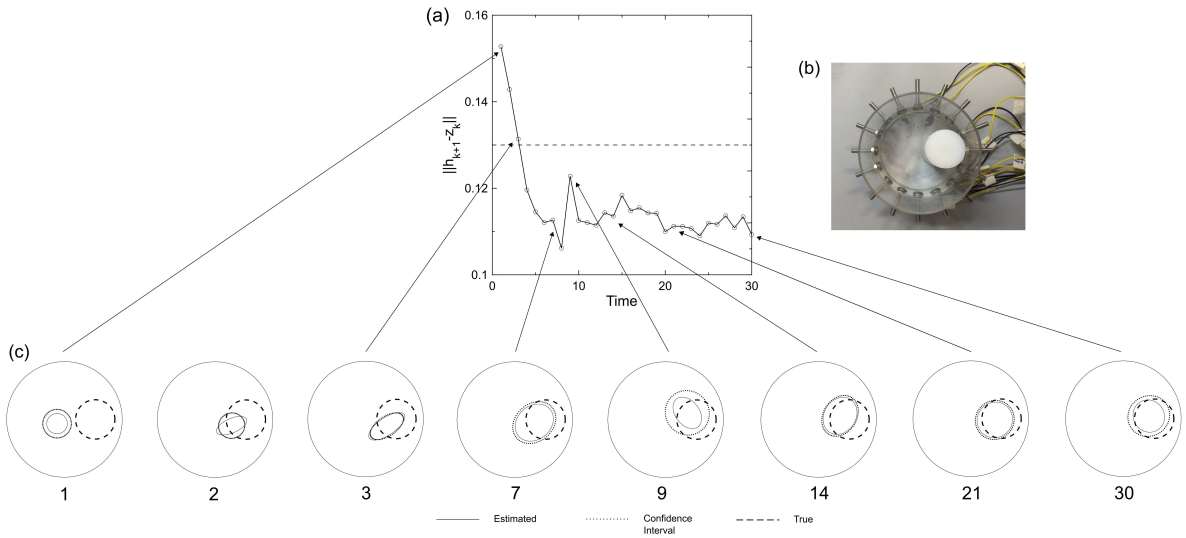

Figure 6.12: Test Experimental 1: The estimation of the contours by the SIR filter. From left to the right, the convergence into the true position. The dashed line represents the threshold of the GNOSIR filter.

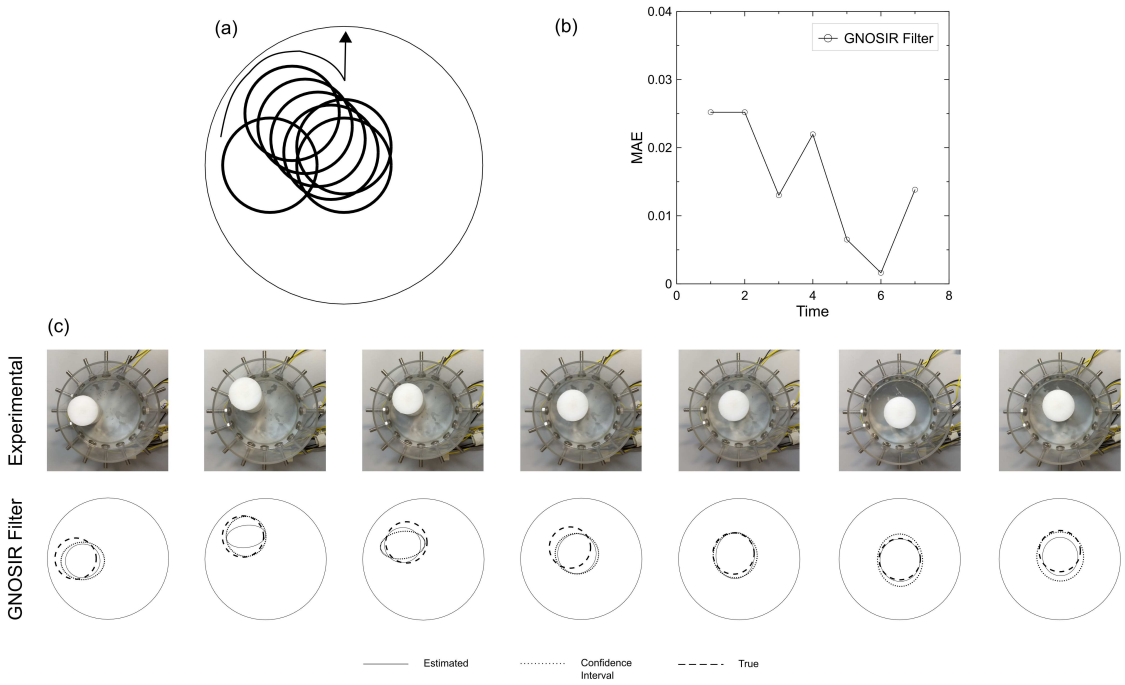

Figure 6.13: Test Experimental 2: Estimation of the contours considering a high-speed evolution. (a) The path of evolution in time. (b) The MAE for each state. (c) The images each state.

The algorithm is evaluated in Test Experimental 2. The path consists of 7 states, initiating in the left region of the domain, Fig. 6.13(a). From that point, it moves faster to the northwest region and continues to move towards the central region slower through the radial direction. Furthermore, it moves one last time north. The reconstruction is shown in Fig. 6.13(c) and the image quality is shown in Fig. 6.13(b). From Time 1-2, it is possible to observe that the estimation of the contour becomes elliptic, while the true object has a circular form. This occurs due to the increased distance between true images 1 and 2. The density of particles in the region becomes decreased, thus the estimation becomes harder. The GNOSIR filter was tested 20 times for the evolution from Time 1 to 2 and in 35% of the tests, the optimization procedure initiates, corroborating the elucidation described before. After this time, the filter adjusts further, until it estimates properly.

6.6 Conclusion

An algorithm to estimate the contours of an elliptic inclusion by the Electrical Impedance Tomography technique is presented in the present work. The GNOSIR filter is based on the SIR filter with an optimization procedure performed by the Gauss-Newton Optimization. This extra step improves the prior information when it is far from the region of high probability, thus ob-

taining a prior dislocated from the actual search region. When the optimization is necessary, the minimization parameter is greater than an adjusted threshold, the values of the state variables are obtained by an image processing algorithm. This threshold is determined by a stationary test both for computational and experimental phantoms. The GNOSIR filter proved to obtain good results for recursive estimations and requiring low computational cost when there are discontinuities in the image evolution and fast speed movement. Further development is necessary, such as utilizing higher complexity models to describe the shapes of the inclusion, improved algorithms of image processing, and the possibility of reconstructing multiple inclusions. Additionally, implementation of a faster forward model discretization, such as the BEM, would decrease the computational cost of the filter.

References

[1] Nicholas P Ramskill and Mi Wang. Boolean logic analysis for flow regime recognition of gas–liquid horizontal flow. *Measurement Science and Technology*, 22(10):104016, 2011. doi: 10.1088/0957-0233/22/10/104016.

[2] A. Parvareh, M. Rahimi, A. Alizadehdakhel, and A.A. Alsairafi. CFD and ERT investigations on two-phase flow regimes in vertical and horizontal tubes. *International Communications in Heat and Mass Transfer*, 37(3):304 – 311, 2010. ISSN 0735-1933. doi: https://doi.org/10.1016/j.icheatmasstransfer.2009.11.001.

[3] Zhenzhen Meng, Zhiyao Huang, Baoliang Wang, Haifeng Ji, Haiqing Li, and Yong Yan. AirâĂŞwater two-phase flow measurement using a Venturi meter and an electrical resistance tomography sensor. *Flow Measurement and Instrumentation*, 21(3):268 – 276, 2010. ISSN 0955-5986. doi: https://doi.org/10.1016/j.flowmeasinst.2010.02.006.

[4] Jiabin Jia, Mi Wang, and Yousef Faraj. Evaluation of EIT systems and algorithms for handling full void fraction range in two-phase flow measurement. *Measurement Science and Technology*, 26(1):015305, dec 2014. doi: 10.1088/0957-0233/26/1/015305.

[5] Claudio Olerni, Jiabin Jia, and Mi Wang. Measurement of air distribution and void fraction of an upwards air–water flow using electrical resistance tomography and a wire-mesh sensor. *Measurement Science and Technology*, 24(3):035403, feb 2013. doi: 10.1088/0957-0233/24/3/035403.

[6] D C Barber and B H Brown. Applied potential tomography. *Journal of Physics E: Scientific Instruments*, 17(9):723–733, 1984.

[7] C J Kotre. A sensitivity coefficient method for the reconstruction of electrical impedance tomograms. *Clinical Physics and Physiological Measurement*, 10(3):275–281, 1989. doi: 10.1088/0143-0815/10/3/008.

[8] William R B Lionheart. EIT reconstruction algorithms: pitfalls, challenges and recent developments. *Physiological Measurement*, 25(1):125–142, feb 2004. doi: 10.1088/0967-3334/25/1/021.

[9] M. Vauhkonen, D. Vadasz, P. A. Karjalainen, E. Somersalo, and J. P. Kaipio. Tikhonov regularization and prior information in electrical impedance tomography. *IEEE Transactions on Medical Imaging*, 17(2):285–293, April 1998. ISSN 0278-0062. doi: 10.1109/42.700740.

[10] D.S. Holder. *Electrical Impedance Tomography: Methods, History and Applications*. Series in Medical Physics and Biomedical Engineering. CRC Press, 2004. ISBN 9781420034462.

[11] W Q Yang, D M Spink, T A York, and H McCann. An image-reconstruction algorithm based on landweber's iteration method for electrical-capacitance tomography. *Measurement Science and Technology*, 10(11):1065–1069, 1999. doi: 10.1088/0957-0233/10/11/315.

[12] M Wang. Inverse solutions for electrical impedance tomography based on conjugate gradients methods. *Measurement Science and Technology*, 13(1):101–117, 2001. doi: 10.1088/0957-0233/13/1/314.

[13] McLeod C N Borsic A and Lionheart W R B. Total variation regularisation in eit reconstruction. In *2nd World Congress on Industrial Process Tomography*, pages 433–441, 2001.

[14] A. Borsic, W. R. B. Lionheart, and C. N. McLeod. Generation of anisotropic-smoothness regularization filters for eit. *IEEE Transactions on Medical Imaging*, 21(6):579–587, 2002. doi: 10.1109/TMI.2002.800611.

[15] Mi Wang, Yixin Ma, N. Holliday, Yunfeng Dai, R. A. Williams, and G. Lucas. A high-performance EIT system. *IEEE Sensors Journal*, 5(2):289–299, April 2005. ISSN 1530-437X. doi: 10.1109/JSEN.2005.843904.

[16] A. J. Wilkinson, E. W. Randall, J. J. Cilliers, D. R. Durrett, T. Naidoo, and T. Long. A 1000-measurement frames/second ERT data capture system with real-time visualization. *IEEE Sensors Journal*, 5(2):300–307, April 2005. ISSN 1530-437X. doi: 10.1109/JSEN.2004.842445.

[17] P.J. Vauhkonen, Marko Vauhkonen, and Jari Kaipio. Fixed-lag smoothing and state estimation in dynamic electrical impedance tomography. *International Journal for Numerical Methods in Engineering*, 50:2195 – 2209, 03 2001. doi: 10.1002/nme.120.

[18] A Seppänen, M Vauhkonen, P J Vauhkonen, E Somersalo, and J P Kaipio. State estimation with fluid dynamical evolution models in process tomography - an application to impedance tomography. *Inverse Problems*, 17(3):467–483, 2001. doi: 10.1088/0266-5611/17/3/307.

[19] Andy Adler, Tao Dai, and William R B Lionheart. Temporal image reconstruction in electrical impedance tomography. *Physiological Measurement*, 28(7):S1–S11, 2007. doi: 10.1088/0967-3334/28/7/s01.

[20] Umer Zeeshan Ijaz, Anil Kumar Khambampati, Jeong Seong Lee, Sin Kim, and Kyung Youn Kim. Nonstationary phase boundary estimation in electrical impedance tomography using unscented kalman filter. *Journal of Computational Physics*, 227(15): 7089 – 7112, 2008. ISSN 0021-9991. doi: https://doi.org/10.1016/j.jcp.2007.12.025.

[21] Umer Zeeshan Ijaz, Soon Il Chung, Anil Kumar Khambampati, Kyung Youn Kim, and Sin Kim. Electrical resistance imaging of a time-varying interface in stratified flows using an unscented kalman filter. *Measurement Science and Technology*, 19(6):065501, 2008. doi: 10.1088/0957-0233/19/6/065501.

[22] Jari P Kaipio, Ville Kolehmainen, Erkki Somersalo, and Marko Vauhkonen. Statistical inversion and monte carlo sampling methods in electrical impedance tomography. *Inverse Problems*, 16(5):1487–1522, 2000. doi: 10.1088/0266-5611/16/5/321.

[23] Robert G. Aykroyd and Brain A. Cattle. A flexible statistical and efficient computational approach to object location applied to electrical tomography. *Statistics and Computing*, 16 (4):363–375, 2006. ISSN 1573-1375. doi: 10.1007/s11222-006-9619-x.

[24] Bruno Furtado de Moura, Wellington Betencurte da Silva, Marcelo Camargo Severo de MacÃłdo, and MÃąrcio Ferreira Martins. A statistical approach to estimate state variables in flow-accelerated corrosion problems. *Inverse Problems in Science and Engineering*, 26(7):966–995, 2018. doi: 10.1080/17415977.2017.1372434.

[25] T. de J. Mateo Sanguino and F. Ponce GÃşmez. Toward simple strategy for optimal tracking and localization of robots with adaptive particle filtering. *IEEE/ASME Transactions on Mechatronics*, 21(6):2793–2804, 2016. doi: 10.1109/TMECH.2016.2531629.

[26] Bernard Lamien, Helcio Rangel Barreto Orlande, Leonardo Antonio Bermeo VarÃşn, Rodrigo Leite Queiroga Basto, Guillermo Enrique EliÃğabe, Dilson Silva dos Santos, and Renato Machado Cotta. Estimation of the temperature field in laser-induced hyperthermia experiments with a phantom. *International Journal of Hyperthermia*, 35(1):279–290, 2018. doi: 10.1080/02656736.2018.1496283.

[27] M. S. Arulampalam, S. Maskell, N. Gordon, and T. Clapp. A tutorial on particle filters for online nonlinear/non-gaussian bayesian tracking. *IEEE Transactions on Signal Processing*, 50(2):174–188, 2002. doi: 10.1109/78.978374.

[28] B. Ristic, S. Arulampalam, and N. Gordon. *Beyond the Kalman Filter: Particle Filters for Tracking Applications*. Artech House, 2003. ISBN 9781580538510.

[29] Zhe Chen. Bayesian filtering: From kalman filters to particle filters, and beyond. *Statistics*, 182, 01 2003. doi: 10.1080/02331880309257.

[30] D Watzenig, M Brandner, and G Steiner. A particle filter approach for tomographic imaging based on different state-space representations. *Measurement Science and Technology*, 18 (1):30–40, 2006. doi: 10.1088/0957-0233/18/1/004.

[31] Fraser Dickin and Mi Wang. Electrical resistance tomography for process applications. *Measurement Science and Technology*, 7(3):247–260, mar 1996. doi: 10.1088/0957-0233/7/3/005.

[32] Wellington Betencurte da Silva, Julio Cesar Sampaio Dutra, José Mir Justino da Costa, Luiz Alberto da Silva Abreu, Diego Campos Knupp, and Antônio José Silva Neto. *A Hybrid Estimation Scheme Based on the Sequential Importance Resampling Particle Filter and the Particle Swarm Optimization (PSO-SIR)*, chapter 13, pages 247–261. Springer International Publishing, Cham, 2019. doi: 10.1007/978-3-319-96433-1_13.

[33] T.J.R. Hughes. *The Finite Element Method: Linear Static and Dynamic Finite Element Analysis.* Series in Medical Physics and Biomedical Engineering. Prentice-Hall, 2004. ISBN 9781420034462.

[34] John Porrill. Fitting ellipses and predicting confidence envelopes using a bias corrected kalman filter. *Image and Vision Computing*, 8(1):37 – 41, 1990. ISSN 0262-8856. doi: https://doi.org/10.1016/0262-8856(90)90054-9.

[35] Si-Cheng Zhang and Zhi-Qiang Liu. A robust, real-time ellipse detector. *Pattern Recognition*, 38(2):273 – 287, 2005. ISSN 0031-3203. doi: https://doi.org/10.1016/j.patcog.2004.03.014.

[36] O Isaksen and J E Nordtvedt. A new reconstruction algorithm for process tomography. *Measurement Science and Technology*, 4(12):1464–1475, 1993. doi: 10.1088/0957-0233/4/12/024.

[37] F. Daum and J. Huang. Curse of dimensionality and particle filters. In *2003 IEEE Aerospace Conference Proceedings*, volume 4, pages 1979–1993, 2003. doi: 10.1109/AERO.2003.1235126.

[38] Andy Adler and William R B Lionheart. Uses and abuses of EIDORS: an extensible software base for EIT. *Physiological Measurement*, 27(5):S25–S42, apr 2006. doi: 10.1088/0967-3334/27/5/s03.

[39] M. Cheney, D. Isaacson, J. C. Newell, S. Simske, and J. Goble. NOSER: An algorithm for solving the inverse conductivity problem. *International Journal of Imaging Systems and Technology*, 2(2):66–75, 1990. doi: 10.1002/ima.1850020203.

[40] N. J. Gordon, D. J. Salmond, and A. F. M. Smith. Novel approach to nonlinear/non-gaussian bayesian state estimation. *IEE Proceedings F - Radar and Signal Processing*, 140 (2):107–113, 1993. doi: 10.1049/ip-f-2.1993.0015.

[41] Tiancheng Li, Shudong Sun, Tariq Pervez Sattar, and Juan Manuel Corchado. Fight sample degeneracy and impoverishment in particle filters: A review of intelligent approaches. *Expert Systems with Applications*, 41(8):3944 – 3954, 2014. ISSN 0957-4174. doi: https://doi.org/10.1016/j.eswa.2013.12.031.

[42] D. M. Hamby. A review of techniques for parameter sensitivity analysis of environmental models. *Environmental Monitoring and Assessment*, 32(2):135–154, 1994. doi: 10.1007/BF00547132.

[43] M.N. Ozisik and H.R.B. Orlande. *Inverse Heat Transfer: Fundamentals and Applications*. Taylor & Francis, 2000. ISBN 9781560328384.

Chapter 7

Conclusion

7.1 Summary

This work aims to develop the Electrical Resistance Tomography data acquisition and to present an algorithm responsible for reconstructing the shape of the boundary of the inclusions recursively.

First, it was designed by the research group a data acquisition system, consisting of a single-ended Howland current source, multiplexers to distribute the injected current and the measured voltage, an instrumentation amplifier to measure differentially the resulting voltages, a low-pass filter to reject the noise in the signal, an RMS-to-DC demodulation scheme to acquire the amplitude information and an Arduino board, with a microcontroller and an ADC. The system obtains a maximum of 30.61 images/s with a maximum SNR of 57.47dB.

The accuracy of the system was tested and it presented errors due to the low current injected when using 16 electrodes, due to the proximity between these sensors. The forward problem presents an error that must be tractable. The system was modeled by SPICE and the results were evaluated, such as the influence of the output impedance of the current source, multiplexers, cables in the accuracy of the measurements. Some directives are summarized regarding the development of a new version.

The estimation of the parasitic components is performed by a statistical method, the MAP estimate, and MCMC. Both the results from the MAP and the forward problem showed to be inside the confidence interval of MCMC. Although the MAP estimate presented more changes

in the resistive part, there is good accordance between them. Further, measurements from the output impedance can validate the results and is yet to be performed.

To conclude, it is developed a new algorithm to estimate the boundaries of the inclusion inside a vessel. The algorithm is a particle filter that obtains better prior information if necessary to estimate recursively the shapes of the inclusions. The procedure repeats the iteration when the estimation is poor and the prior information is obtained by an Image Processing algorithm after the estimation is performed by the Gauss-Newton optimization. It was tested in cases that the recursive algorithms fail to estimate and it presented better estimations when there is sudden or fast movement.

7.2 Recommendations for Future Work

For further consideration, the following points are described:

1. Development of the Data Acquisition System

    - Include a floating topology to the current source. This modification would not only increase the output impedance by adding the corresponding output impedances of both the single-ended, but also the common-mode voltage which is reduced causing less error in the measurements.

    - Provide matching resistors and a trimming scheme to the current source. This modification increases the output impedance as it depends greatly on assuring the matching condition of the resistors.

    - Design a current source with digital controlled gain to increase the magnitude of the input current. It was concluded that this magnitude is of greater importance for obtaining a higher accuracy signal.

    - Select a multiplexer with lower parasitic capacitance or even a parallel measurement. The multiplexers aids in the simplicity penalizing the accuracy, thus its use must be considered for a new design.

    - Include a 3-in-amp for the voltmeter section. The utilization of this topology was demonstrated to increase considerably the CMRR of the system.

    - Development of the digital demodulation scheme by the phase-sensitive detection

method. The utilization of this digital approach can increase greatly the speed of acquisition of the system since this speed is limited by the current demodulation scheme. Additionally, it is possible to obtain information regarding the phase of the signal.

- Design an Impedance Converter circuit to cancel the stray capacitances from the system and the output capacitance of the current source.

2. Development of the Algorithm for Shape Determination

   - Represent the shapes of the inclusion in the algorithm by high dimensional model, such as the splines or Fourier descriptors. The representation by an ellipse is limited considering the many forms an air phase can be in a multiphase flow.

   - Utilize new methods of Image Processing. For the representation of the shapes using a higher dimension, a new and optimized algorithm would present better results.

3. Tests in a Flow Loop

   - Test different airflow rates to establish different flow patterns and perform the identification of these patterns through the images or the signals.

   - Acquire images in a multiphase flow loop test to perform the calculation of the void-fraction with the current developed system for these different flow rates.